

NORTHWESTERN UNIVERSITY

Basal Ganglia Population Activity in Innate and Learned Behaviors

A DISSERTATION

SUBMITTED TO THE GRADUATE SCHOOL  
IN PARTIAL FULFILLMENT OF THE REQUIREMENTS

for the degree

DOCTOR OF PHILOSOPHY

Northwestern University Interdepartmental Neuroscience Program (NUIN)

By

Samuel Minkowicz

EVANSTON, ILLINOIS

June 2023

## Abstract

Vertebrate brains evolved to facilitate a diverse array of behaviors and internal cognitive processes. Theories of neural function have proposed that neural computation is organized within populations or ensembles of neurons. Here, we identify ensembles of neurons in the striatum, the main input nucleus of the basal ganglia, in which units show correlated activity during grooming. Ensembles are comprised of putative striatal projection neurons and fast spiking interneurons. These ensembles encode grooming duration as well as transitions into and out of grooming. In a collaborative study utilizing fiber photometry, we record bulk population activity of ventral tegmental area dopaminergic neurons during aversive learning. We find that dopaminergic activity consistently varies across learning. A single dose of ketamine—a rapidly acting antidepressant—is sufficient to restore changes in behavior and dopaminergic neuron activity. Further, we identify the medial prefrontal cortex as the locus for ketamine’s effects on behavior and the dopaminergic system. Finally, we describe the development of fully implantable, miniaturized wireless devices for optogenetic manipulation of neuronal activity. These devices provide real-time user programmability over multiple independent light sources, in head-mounted and back-mounted designs. These devices facilitate the study of natural, ethological behaviors without the mechanical constraints imposed by a tethered configuration. Overall, these studies improve our understanding of how populations of neurons control innate and learned behaviors and provide tools to interrogate neural control of behavior.

## Acknowledgments

My academic career has been greatly enhanced by the support I received and the relationships I had with many faculty and friends. I would first like to thank my advisor Dr. Yevgenia (Genia) Kozorovitskiy for her support and guidance throughout my time in graduate school. Genia's emphasis on clear scientific writing and accessible, thorough, and engaging presentations significantly improved my scientific communication skills. My graduate training was enriched by Genia's enthusiasm for science, scientific rigor, and personable mentor style. I would also like to thank my collaborator Dr. Ann Kennedy for sharing her expertise in behavioral and neural data analysis. Thank you, Ann, for challenging me, for the engaging discussions, and for demonstrating how technical writing can be simultaneously rigorous, accessible, and enjoyable.

I would like to thank the members of the KLab for their friendship and camaraderie. My training was enhanced by the diverse expertise and widely varying projects led by the scientists in our lab including Lindsey Butler, Meghan Masotti, Sara Freda, Isabelle Rieth, Giulia Hinderman-Soto, Deanna Badong, and Drs. Vasin Dumrongprechachan, Mingzheng Wu, Michael Priest, Pushpa Kumari, Neto Canton, Manish Kumar, and Nicholas Bannon. I am grateful for the junior researchers that assisted me: Mychaela Matthews, Felicia Mou, Ethan Cui, and Hyoseo Yoon and am excited to see their careers evolve.

I would like to thank my committee members Drs. Ann Kennedy, Dan Dombeck, and Malcolm MacIver for their perspective and their insightful recommendations that helped shape and improve my research. I would also like to thank Andrew Miri and the rest of the Miri Lab for helpful discussions on in vivo electrophysiology and discussions on method details that are not usually included in research papers.

I would like to thank Drs. Takashi Ueda and Yinghong Sheng at Florida Gulf Coast University for providing me with my first opportunities to work in research labs as an undergraduate. My time working with them shaped my thinking about research and facilitated my later research career. I was fortunate enough to be introduced to neuroscience by Dr. Bob (A.R.) Martin who did foundational work on the nature of synaptic transmission. Our numerous conversations opened me up to the world of neuroscience and the intriguing questions being addressed by neuroscientists. I am grateful that Dr. Achim Klug took a chance on me, an undergraduate student from across the country, and gave me my first opportunity to work in a neuroscience lab. Thank you Achim for teaching me the fundamentals of neuroscience and giving me the space and support to grow as a young neuroscientist. Thank you to Klug Lab members Liz McCullagh, Anna Dondzillo, and Otto Albrecht for taking me under your wing.

Most importantly, I would like to thank my family and friends for supporting me on this path. Thank you, Brett, Alex, Mauricio, Maite, Rogan, Oscar, Ted, Zach, and Jonathan for all the stimulating conversations we had and wonderful moments we shared. Thank you, Chana Leah, for always believing in me and encouraging me to create the life that I want. Thank you, mom, for your unwavering support and for serving as the ultimate role model for how to be constantly evolving and how create a life on your own terms. Thank you for empowering me to choose my own path. I am eternally grateful for you.

Lastly, I would like to thank my partner Miranda for building a life with me and being by my side throughout the roller coaster that was graduate school.

*To Mom*

## Table of Contents

Abstract .....	2
Acknowledgments.....	3
Table of Contents .....	6
List of Figures .....	10
Chapter 1 – Introduction .....	14
1.1 Self-grooming behavior.....	14
1.1.1 Innateness of self-grooming .....	14
1.1.2 Function of self-grooming.....	14
1.1.3 Grooming variability .....	16
1.1.4 The decision to groom .....	17
1.2 Neural control of self-grooming.....	19
1.3 Basal Ganglia .....	20
1.3.1 The striatum .....	22
1.3.3 Disease relevance .....	23
1.4 Neural ensembles .....	24
1.4.1 Terminology of neural ensembles .....	24
1.4.2 Overview of identified ensembles .....	25
1.4.3 Striatal ensembles.....	26

	7
1.4.5 Quantitative identification of neural ensembles .....	27
1.5 Thesis overview.....	28
Chapter 2 – Striatal ensemble activity in an innate naturalistic behavior .....	30
2.1 Introduction .....	31
2.2 Results and discussion.....	32
2.2.1 Mouse spontaneous self-grooming behavior .....	32
2.2.2 Striatal SPNs and FSIs encode grooming transitions .....	35
2.2.3 Striatal activity is organized into ensembles .....	41
2.2.4 Striatal ensembles encode features of self-grooming .....	46
2.2.5 Discussion.....	49
2.3 Methods.....	53
2.3.1 Striatal in-vivo electrophysiology in freely moving mice .....	53
2.3.2 Video capture of mouse grooming .....	56
2.3.4 Striatal ensemble characterization .....	58
2.3.5 Additional details beyond published methods.....	64
2.4 Reviewer-requested analyses .....	67
Chapter 3 – Attenuated dopamine signaling after aversive learning is restored by ketamine to rescue escape actions .....	69
3.1 Introduction .....	70

	8
3.2 Results and discussion.....	72
3.2.1 VTA DA neuron activity during aversive learning .....	72
3.2.2 Outcome-specific VTA DA dynamics during weaker aversive learning and after ketamine treatment .....	78
3.2.3 DA neuron activity is necessary for behavioral effects of ketamine after LH .....	87
3.2.4 Ex vivo local effects of ketamine on VTA DA neurons.....	90
3.2.5 Local mPFC ketamine infusion rescues VTA Ca <sup>2+</sup> transients and escape actions after LH.....	93
3.2.6 mPFC Drd1 <sup>+</sup> neurons mediate behavioral effects of ketamine .....	96
3.2.7 Discussion.....	102
3.3 Methods.....	108
Chapter 4 – Wireless multilateral devices for optogenetic studies of individual and social behaviors .....	
	121
4.1 Introduction.....	122
4.2 Results and discussion.....	123
4.2.1 Head mounted and back mounted multilateral optogenetic devices .....	123
4.2.2 Mechanical characterization for multilateral optogenetic devices .....	127
4.2.3 Biocompatibility characterization for multilateral optogenetic devices.....	132
4.2.4 Dynamically programmable multichannel operation .....	134

4.2.6 Applications of bilateral stimulation and subject-specific programmability for wireless control of place preference and social behavior .....	145
4.2.7 Discussion.....	156
4.3 Methods.....	157
Chapter 5 – Conclusions and future directions .....	176
References.....	179
Appendix.....	244
A.1 Collaboration: Ketamine rapidly enhances spinogenesis through dopaminergic mechanisms .....	244
A.1.1 Introduction .....	245
A.1.2 Results and discussion.....	247
A.1.2.1 Ketamine rapidly enhances glutamate-evoked spinogenesis in mPFC pyramidal neurons.....	247
A.1.2.2 Rapid enhancement in evoked spinogenesis requires Drd1-PKA signaling .....	250
A.1.2.3 Bidirectional manipulation of mPFC DA release controls behavioral effects of ketamine.....	258
A.1.2.4 Discussion.....	263
A.1.3 Methods .....	266

## List of Figures

Figure 2.1	3D tracking and characterization of the structure of mouse spontaneous grooming	34
Figure 2.1 Supplement 1	Manual refinement of grooming identification	35
Figure 2.2	Striatal cell type specific activity mapped to spontaneous self-grooming	37
Figure 2.2 Supplement 1	Probe placement and firing rate characteristics	38
Figure 2.3	Emergent motifs in SPN and FSI activity around grooming transitions	40
Figure 2.4	Identification and characterization of striatal grooming ensembles	43
Figure 2.4 Supplement 1	Statistics of identified clusters and activity patterns	45
Figure 2.5	Striatal ensembles encode features of self-grooming	47
Figure 2.5 Supplement 1	Patterns of cluster engagement	49
Figure 3.1	Ketamine rescues escape behavior and dampened DA neuronal activity after aversive learning	73
Figure 3.1 Supplement 1	Characterization of behavior after learned helplessness.	76
Figure 3.1 Supplement 2	VTA DA neuron responses to anesthesia, foot shock, and motion transitions	77
Figure 3.2	Weak learning analysis links DA activity, behavioral outcomes, and response to ketamine	79
Figure 3.2 Supplement 1	Characterization of behavioral sequences and dampened VTA DA activity in weak learned helplessness (wLH) paradigm	81

Figure 3.2 Supplement 2	Outcome-specific VTA DA responses in wLH paradigm	83
Figure 3.2 Supplement 3	Outcome-specific VTA DA responses in control mice without wLH induction	84
Figure 3.2 Supplement 4	Outcome-specific VTA DA responses in wLH mice with saline treatment	85
Figure 3.2 Supplement 5	Trace distance of GCaMP transients between escape and failure trials	86
Figure 3.3	Ketamine behavioral effects in aversive learning require VTA DA activity	88
Figure 3.4	Ex vivo ketamine application does not alter GCaMP6f transients, neuronal firing, and synaptic inputs of VTA DA neurons	92
Figure 3.5	Local ketamine infusion in mPFC rescues escape behavior and VTA DA activity after LH	94
Figure 3.5 Supplement 1	VTA DA activity after local ASCF infusion in mPFC	95
Figure 3.6	Activation of mPFC Drd1 <sup>+</sup> neurons rescues escape actions	97
Figure 3.6 Supplement 1	Activity of Drd1 <sup>+</sup> neurons in mPFC after in vivo ketamine treatment	99
Figure 3.6 Supplement 2	Inhibition of Drd1 <sup>+</sup> neurons in mPFC blocks the behavioral effects of ketamine.	100
Figure 3.6 Supplement 3	Behavioral outcomes and viral expression distributions	101
Figure 4.1	Device layout and implantation	125
Figure 4.1 Supplement 1	Electrical circuit implemented in the NFC-enabled platform	126
Figure 4.2	Characterization of mechanical properties and effects on animal locomotor behavior	128

Figure 4.2 Supplement 1	Mechanical deformations for head mounted devices	130
Figure 4.2 Supplement 2	Device longevity and behavioral outcomes for head mounted devices	131
Figure 4.2 Supplement 3	Biocompatibility of injectable probes and back mounted implants	133
Figure 4.3	Designs, operational features and use cases for dynamically programmable NFC electronics	135
Figure 4.3 Supplement 1	Dynamically programmable platform operation with intensity control	138
Figure 4.4	Characterization of optical and thermal properties	141
Figure 4.4 Supplement 1	Thermal power, irradiance, illumination volume, and penetration depth of $\mu$ -ILEDs	143
Figure 4.4 Supplement 2	Temperature increment vs irradiance and duty cycle at 20 Hz frequency	144
Figure 4.5 Supplement 1	Bilateral burst wireless stimulation of midbrain dopaminergic neurons regulates place preference	146
Figure 4.5	Bilateral stimulation and subject-specific programmability for wireless optogenetic control of social behavior	148
Figure 4.5 Supplement 2	Increased excitability of mPFC pyramidal neurons after stimulation	151
Figure 4.5 Supplement 3	Wireless control of social behavior in dyads and triads	154
Figure A.1.1	Ketamine regulates mPFC plasticity through a DA-dependent mechanism	248
Figure A.1.1 Supplement 1	De novo glutamate-induced spinogenesis on pyramidal neurons in mPFC.	250
Figure A.1.1 Supplement 2	Drd1a mRNA expression and distribution in mPFC	251

Figure A.1.2	Ketamine rescues mPFC plasticity after stressful experience through Drd1 receptor	253
Figure A.1.2 Supplement 1	Spinogenesis in mPFC is regulated by stress and correlates with behavioral outcomes.	255
Figure A.1.3	Drd1 activation promotes glutamate-induced spinogenesis in mPFC pyramidal neurons through PKA signaling.	257
Figure A.1.4	Activity of local DA terminals and Drd1+ neurons in mPFC mediates ketamine effects on behavior after stress.	259
Figure A.1.4 Supplement 1	Effects of local inhibition of DA terminals in mPFC	261

## Chapter 1 – Introduction

### 1.1 Self-grooming behavior

Self-grooming is an evolutionarily conserved, ethologically relevant, and innate behavior. Self-grooming behavior is found in insects<sup>1–12</sup>, crustaceans<sup>13–16</sup>, birds<sup>17–24</sup>, and mammals<sup>25–38</sup>. In general, cephalocaudal progression of grooming is a conserved feature of self-grooming in many animals<sup>6,27,28,34,35,39</sup> including humans<sup>40</sup>.

#### 1.1.1 Innateness of self-grooming

Self-grooming is an innate behavior<sup>35,38,41–44</sup>, with mice showing primitive forms of facial grooming as early as postnatal day 1 (p1)<sup>41</sup>. From p4-8, the kinematics of grooming movements become more tightly coordinated. After p9, mice start to perform movements similar to those performed by adults. Guinea pig grooming is remarkably complete from p1<sup>35</sup>. By p3 guinea pigs already perform all the grooming movements seen in adults<sup>35</sup>. Rat pups begin to exhibit functional face grooming at p6-8<sup>35</sup>, but do not perform long sequences of grooming until p14-21<sup>38,42,43</sup>, the time of development when many complex motor programs begin to emerge<sup>45,46</sup>.

#### 1.1.2 Function of self-grooming

The most readily apparent function of self-grooming is to care for the outer body surface<sup>1,47–49</sup>. In addition to this primary function, grooming also serves multiple secondary roles, including

aiding in the removal of pathogens<sup>50</sup> and defending against parasitism<sup>8,51-54</sup>. Experiments in a wide range of animals reported a higher rate of parasitic infections in animals restrained from grooming compared to those allowed to groom freely<sup>13,36,52,55-59</sup>. To explain differences in the rates of grooming among several species of ungulates, a model was proposed where species grooming rates evolved to balance the risks of exposure to parasites with the costs of grooming<sup>33,60</sup>. The costs of grooming include both energetic costs as well as the increased risk of predation while grooming. The model predicts that species with a larger body size would have a lower grooming rate and higher average parasite load than those with smaller body sizes, since their higher body surface-to-mass ratio means they cannot sustain as many parasites per unit of body area.

Self-grooming in some mammals often includes spreading saliva, fatty acids, and radiation-absorbing pigments over their bodies. Saliva-spreading is important for thermoregulation, communication, and water economy. Rodents and marsupials regulate their temperature by spreading saliva over their bodies for the purposes of evaporative cooling<sup>61-67</sup> and can spread fatty acids and radiation absorbing pigments from the harderian gland<sup>68-71</sup> to protect against cold<sup>49,72-74</sup>. In the absence of heat stress, the water loss due to the saliva-spreading during grooming makes up one third of a rat's total evaporative water loss<sup>75</sup>.

In addition to thermoregulation, secretions spread during grooming often play a role in olfactory communication<sup>76-81</sup>. Self-grooming has also been shown to maintain olfactory acuity in insects through the removal of native lipids and foreign chemicals from the olfactory sensilla<sup>82</sup>.

Diminished olfactory responses were observed in the non-groomed antenna of cockroaches restrained from grooming one of their antennae<sup>82</sup>. A role for grooming in olfactory

communication was also reported in rodents where male voles groom more when around female voles suggesting a role in the attraction of a mate<sup>76</sup>. Secretions spread during grooming can also serve as an agonistic signal towards animals of the same sex that they should not approach one's mate<sup>77</sup>.

### 1.1.3 Grooming variability

While many aspects of self-grooming are stereotyped and present across the animal kingdom, grooming varies both among groups of animals as well as within individuals. Among groups, consistent variations in the set of movements used during grooming were observed in 14 hymenopteran superfamilies<sup>2</sup>. Further, these differences followed a sequence paralleling the proposed phylogeny of these superfamilies, suggesting that grooming behavior may be useful for phylogenetic comparisons. Variations in the set of movements used during grooming have also been reported for 38 coleopteran families<sup>10</sup>, 23 species of Blattodea<sup>7</sup>, and 6 rodent species<sup>34</sup>. As in the hymenopteran superfamilies, the grooming variations in Blattodea<sup>7</sup>, Decapoda<sup>14</sup>, and Rodentia<sup>34</sup> are consistent with and can help interpret phylogenetic relationships. For example, a consistent difference was observed in how roaches from the Blaberidae family clean their antennae compared to all other roaches, consistent with other evidence that this family forms a group separate from other roaches<sup>7</sup>. In rodents, individuals from the three classic rodent suborders Hystricormorpha, Sciurormorpha, and Myomorpha were compared<sup>34</sup>. A set of shared grooming traits, for example the structure of grooming sequences, was present within all six species. Then, more specific grooming features such as the relative frequencies of grooming actions and the number of strokes within some grooming actions traits were shared amongst

more phylogenetically related species. The four Myomorpha species were more similar to one another than to those from the other two families. Within the Myomorphs, the Muridae and Cricetidae were more similar amongst themselves than to each other<sup>34</sup>.

Within individuals, variations in grooming are observed depending on context and age. After eating, rats direct more of their grooming to their paws and face<sup>26,83</sup>. However, this does not seem to be for the purpose of cleaning their paws, since this was also observed in rats fed through a stomach tube<sup>83</sup>. Grooming evoked by water droplets often results in a larger proportion of body grooming and more attention directed towards the wet region<sup>84</sup>. Differences were reported in the amount of grooming exhibited by young and old rats after being placed in a novel chamber<sup>85-87</sup>.

#### **1.1.4 The decision to groom**

What causes animals to self-groom? Grooming was originally thought to be a *displacement activity*, where animals were observed to perform seemingly irrelevant grooming bouts during other activities. For example, birds would stop fighting to groom in middle of a fight and then continue<sup>17,88,89</sup>. They were also observed to pause courtship for brief grooming bouts<sup>89,90</sup>. It was hypothesized that this occurs when a powerful drive or urge, such as fighting or mating, cannot be expressed and this urge then gets displaced to generate another behavior, such as grooming. The seemingly irrelevant behaviors were therefore labeled ‘displacement’ behaviors<sup>91-93</sup>. In addition to birds, displacement grooming has been characterized in insects<sup>94</sup>, crustaceans<sup>95</sup>, rodents<sup>96-99</sup>, and primates<sup>100,101</sup>.

The original proposed explanation for displacement behaviors was rejected following evidence from a quantitative study on displacement grooming<sup>88</sup>. Displacement grooming was found to occur most often when the tendency to perform two primary behaviors was equally strong. Further, grooming rarely occurred when the animal was engaged in just one behavior. Thus, the authors instead proposed a disinhibition model where the necessary stimuli for grooming are constantly present, as previously suggested<sup>89</sup>, but grooming is inhibited by other more pressing behaviors. When these more pressing behaviors, for example brooding and fleeing from a predator, are mutually inhibiting or incompatible, it would lead to the disinhibition of grooming giving rise to displacement grooming<sup>88</sup>. This was supported by later experiments<sup>17,102</sup>.

The disinhibition model of grooming evolved to account for regular forms of grooming. Within a hierarchy of needs, grooming is considered a low-priority behavior since—although broadly important—it is not often an immediate concern. Thus, grooming is inhibited when other higher priority behaviors are occurring and then disinhibited once these other behaviors are complete<sup>27,28,49</sup>.

In addition to the disinhibition model, the ability of stressful stimuli to evoke grooming<sup>103–105</sup> has led some to hypothesize that grooming serves to aid in de-arousal<sup>49,99,103</sup>. With a role in de-arousal, displacement grooming may be interpreted as a result of the common displacement scenarios being stressful in nature. Then, the subsequent displacement grooming occurs not as a result of being disinhibited, but rather to aid in de-arousal<sup>98,99,106</sup>.

## 1.2 Neural control of self-grooming

The presence of self-grooming behavior in a wide variety of species demonstrates its fundamental importance. How are the movements within self-grooming behaviors generated? Further, given the ubiquity of self-grooming across animals, is self-grooming controlled through a conserved mechanism? The first hypothesis for the control of self-grooming was analogous to Sherrington's proposal for the control of locomotion where sensory input from one's foot touching the ground during each step triggers reflexive stepping<sup>107</sup>. Similarly, during grooming, sensory input during each grooming movement was hypothesized to control the sequence of movements in a self-grooming bout<sup>108,109</sup>. Evidence that sensory input is not necessary for normal grooming movements comes from experiments in birds<sup>24</sup> and rodents<sup>108-110</sup> where denervation of normally groomed body regions did not alter grooming behavior. Further, mice will continue to make grooming movements in the air after one of their paws is pulled away from their face<sup>41</sup> and mice with one or both forelimbs amputated from birth develop normal grooming movements<sup>111</sup>, providing further evidence that sensory input is not necessary for normal grooming behavior. Overall, these findings demonstrate that self-grooming is not controlled by a sensory input triggered reflex and suggests that grooming may be centrally controlled.

The striatum is the main input nucleus of the basal ganglia, an evolutionarily conserved group of subcortical nuclei involved in motor control (see **Section 1.3** for an overview of the basal ganglia and its functions). The striatum has been implicated in the production of self-grooming behavior. Lesions of the striatum<sup>112</sup> and the substantia nigra<sup>113</sup>, which sends dopaminergic projections to the striatum, result in abnormal grooming behaviors. Isolating the relevant region within the striatum, lesions of the dorsolateral striatum recapitulate the broader striatal lesion effects on

grooming<sup>114</sup>. Additionally, neurons of the dorsolateral striatum<sup>115,116</sup> and nearby central striatal regions<sup>117</sup> display grooming-related activity. Yet, how populations or functional ensembles of neurons in the striatum encode self-grooming remains unclear.

### 1.3 Basal Ganglia

The basal ganglia are a group of evolutionarily conserved subcortical nuclei involved in motor control, motor learning, and decision-making. The striatum, the main input nucleus of the basal ganglia, receives topographical cortical and thalamic excitatory projections<sup>118–122</sup>. The basal ganglia output nuclei, the globus pallidus internal segment (GPi) and the substantia nigra pars reticulata (SNR) project to the thalamus. Cortical projections from the thalamus complete the cortico-basal ganglia-thalamo-cortical loop. Anatomical and physiological data support the segregation of the striatum into a dorsolateral sensorimotor motor region, a dorsomedial associative region, and a limbic ventral region<sup>118,119,123</sup>. For example, the dorsolateral striatum receives inputs from premotor, motor, and sensorimotor cortices while the ventral striatum receives inputs from the medial prefrontal cortex, hippocampus, entorhinal cortex, and amygdala<sup>120,124–126</sup>. Further, dopaminergic input varies between striatal subregions. Ventral striatum primarily receives dopamine from the ventral tegmental area<sup>127,128</sup> and regions within the dorsal striatum receive input from different genetically defined subpopulations of neurons within the substantia nigra pars compacta<sup>129</sup>. In sum, each striatal subregion primarily receives inputs from and projects back to distinct cortical and thalamic regions, forming segregated cortico-thalamic-basal ganglia-cortical loops<sup>120</sup>.

Within the basal ganglia, activity is segregated along two functionally opposing pathways, the direct and indirect pathways<sup>130,131</sup>. The direct pathway is formed by projections from the striatum directly to the basal ganglia output nuclei, the GPi and SNR. Within the indirect pathway, striatal output neurons project to the globus pallidus external segment, which projects to the subthalamic nucleus, targeting the basal ganglia output nuclei. Striatal activity along the direct pathway, being two inhibitory synapses from the thalamus, increases thalamic and cortical activity, while activity along the indirect pathway, being an additional inhibitory synapse from the thalamus, decreases thalamic and cortical activity. While the direct and indirect pathways were originally hypothesized to be strongly functionally opposed<sup>132</sup>, evidence suggests that direct and indirect pathway striatal neurons are often co-active and these pathways work together to control behavior<sup>133–137</sup>.

The organization of the basal ganglia in mammals is similar to that in cyclostomes (lampreys and hagfishes)<sup>138</sup>, the oldest group of living vertebrates, suggesting that the basal ganglia were present in the last common ancestor of all vertebrates<sup>139</sup>. The cyclostomes diverged from the evolutionary line leading to mammals approximately 560 million years ago<sup>140</sup> and yet have a basal ganglia with the similar component nuclei, output pathways, neurotransmitters and neuromodulators as in the vertebrate basal ganglia<sup>139,141</sup>.

### 1.3.1 The striatum

The primary neurons of the striatum, the striatal projection neurons (SPN; also referred to as spiny projection neurons or medium spiny neurons), can be subdivided into two categories based on their projection targets and dopamine receptor expression<sup>142,143</sup>. SPNs of the direct pathway (dSPN) project to the basal ganglia output nuclei and selectively express Drd1 receptors while SPNs of the indirect pathway (iSPN) project to the GPe and selectively express Drd2 dopamine receptors. These dopaminergic receptors are activated by dopaminergic input from the substantia nigra pars compacta (SNc), crucial for normal striatal function<sup>144–146</sup>. Chronic depletion of striatal dopamine following a loss of SNc dopaminergic neurons results in Parkinson's disease<sup>147,148</sup>. In addition to modulation from dopamine, the activity of striatal SPNs is sculpted by a variety of neuromodulators including acetylcholine<sup>149,150</sup>, adenosine<sup>151</sup>, serotonin<sup>152–154</sup>, and histamine<sup>155,156</sup> that modulate striatal plasticity and function<sup>157</sup>.

Approximately 95% of the neurons in the striatum are SPNs with the remaining 5% comprised of interneurons<sup>158–160</sup>. Striatal interneurons include both cholinergic and GABAergic neurons. The cholinergic interneurons are tonically active and thus are known as “tonically active neurons” or TANs<sup>161,162</sup>. TANs have large cell bodies, widespread dendritic trees, receive thalamic inputs, and co-release glutamate<sup>163–165</sup>. TANs regulate dopamine release in the striatum<sup>166</sup> and through their thalamic inputs TANs can gate cortical inputs to the striatum<sup>167–169</sup>. Three primary classes of GABAergic interneurons have been identified in the striatum: fast-spiking interneurons (FSI), somatostatin-expressing low-threshold spiking interneurons (LTSI), and calretinin positive interneurons<sup>159,160</sup>. FSIs are parvalbumin-positive neurons<sup>170</sup> coupled together by gap-junctions<sup>171</sup> that provide coordinated widespread inhibition to SPNs<sup>172</sup>. LTSIs exhibit Ca<sup>2+</sup>-

dependent low-threshold spikes and express somatostatin, nitric oxide synthase, and neuropeptide Y. Both FSIs and LTSIs receive direct cortical input<sup>158,173</sup>. The final class of striatal interneurons, the calretinin-positive interneurons, are the least studied in part due to their low abundance in mouse striatum<sup>174</sup>.

The dorsolateral striatum controls the selection and initiation of actions<sup>132,133,136,175–178</sup> and encodes action space<sup>134</sup>. Supporting a hypothesized role for the basal ganglia in chunking of cognitive and motor elements<sup>179</sup>, the striatum has been shown to flexibly combine behavioral motifs into actions<sup>136</sup> and to represent the start and end of learned action sequences<sup>180,181</sup>. Striatal cell-type specific recordings in mice during the learning and performing of action sequences showed hierarchical control of action sequences by the striatum<sup>182</sup>. SPNs of both pathways were involved in controlling the component actions. However, the start and end of the action sequences was preferentially encoded by the direct pathway while the indirect pathway encoded the switch between subsequences<sup>182</sup>.

### **1.3.3 Disease relevance**

Dysfunction in the basal ganglia has been implicated in several neurological and psychiatric disorders, including Parkinson's disease, Huntington's disease, Tourette's syndrome<sup>183–186</sup>, schizophrenia, and obsessive-compulsive disorder<sup>123,187</sup>. Further, deficits in movement sequences are present in people with diseases related to the basal ganglia. People with Parkinson's disease, Huntington's disease and obsessive-compulsive disorder have deficits in performing movement sequences<sup>188–193</sup>. Additionally, people with Tourette's syndrome often have unwanted repetitive

movements during their voluntary movements<sup>194</sup>. Understanding how the striatum controls movement sequences can help those with diseases associated with the basal ganglia.

## **1.4 Neural ensembles**

In 1949, Donald Hebb proposed that neural computation is organized in groups of neurons called 'cell assemblies.'<sup>195</sup> Hebb's hypothesis was that following repeated activation of a group of neurons by some stimulus, the excitatory connections between these neurons would get strengthened forming a cell assembly in a process now called Hebbian plasticity. With strengthened excitatory connections among the assembly members, activity within the assembly could persist following a future presentation of the stimulus or following re-activation due to an internal process. With their self-sustaining activity, cell assemblies were proposed to underlie internal cognitive processes. At the time Hebb presented his theory, the presence of inhibitory neurons was not established. Once the existence of inhibitory neurons was demonstrated, the cell assembly hypothesis was extended to include inhibitory connections that could serve to limit the size of cell assemblies and could solve the paradox of how associations between two assemblies do not result in them merging together<sup>196</sup>.

### **1.4.1 Terminology of neural ensembles**

Beginning with the first simultaneous recordings from multiple neurons, the term 'ensemble' was used to denote the collection of simultaneously recorded units, and this usage is still common. Here, as many others do<sup>197–203</sup>, we define neural ensemble as groups of neurons with

correlated activity. In addition to neural ensemble, others have used multiple terms for this definition including neural clique<sup>204,205</sup>, cell assembly<sup>195,206–208</sup>, and neural assembly<sup>209–211</sup>.

#### 1.4.2 Overview of identified ensembles

Advances in electrophysiological<sup>212–221</sup> and optical<sup>222–232</sup> recording technologies, together with advances in acquisition<sup>233,234</sup> and spike sorting software<sup>235–242</sup>, have enabled the recording and identification of populations of neurons in freely moving animals. With these advances, neuronal ensembles have been identified in cockroach<sup>206</sup>, zebrafish<sup>243,244</sup>, and jelly fish<sup>245</sup> and in the mammalian retina<sup>246</sup>, visual cortex<sup>247,248</sup>, auditory cortex<sup>249</sup>, motor cortex<sup>250</sup>, hippocampus<sup>204,208,251,252</sup>, and striatum<sup>134,135,202,253–255</sup>. To provide a means to precisely manipulate neural ensembles, several laboratories developed optical approaches to simultaneously record and manipulate neural ensemble activity with single cell resolution<sup>256–259</sup>. Carrillo-Reid et al used simultaneous two-photon imaging and stimulation to artificially generate neural ensembles in mouse visual cortex that can subsequently become spontaneously active<sup>257</sup>. They showed that after generating an artificial ensemble, stimulation of a single neuron within the ensemble can recall the ensemble, demonstrating that cortical neurons can perform pattern completion. To non-invasively test molecular and developmental aspects of neuronal ensembles, Rabadan et al. recently developed an *in vitro* 3D cell-culture model of neuronal ensembles<sup>260</sup>.

### 1.4.3 Striatal ensembles

Cortical stimulation and bath application of N-methyl-D-aspartate result in synchronous firing among groups of striatal neurons<sup>255</sup>, suggesting that striatal activity is organized into neural ensembles. Striatal ensembles were able to transform tonic excitatory input into sequential activity among groups of ensembles. This was later confirmed *in vivo*, where correlated activity was observed within striatal ensembles that encoded features of mouse behavior<sup>134–136,202,253,254,261,262</sup>. After segmenting freely moving mouse behavior into subcomponents such as right turn, rear, forward walking, etc., striatal ensembles were identified that encoded the behavioral subcomponents<sup>134,136</sup>. Recording from populations of striatal fast-spiking interneurons in mice, Roberts et al. identified FSI ensembles that encode walking and head-movement speed<sup>262</sup>.

On the background of fast neurotransmission, neuromodulators are small molecules that can induce long-lasting changes in neuronal excitability and synaptic connectivity, providing a means to flexibly configure neural circuits<sup>263,264</sup>. Within the striatum, dopamine is a key neuromodulator necessary for normal striatal function<sup>144–146</sup>. Chronic reduction of dopaminergic input into the striatum results in Parkinson's disease<sup>147,148</sup>. To understand the role of dopamine in striatal neural ensembles, Carrillo-Reid et al. recorded *ex vivo* striatal population activity while manipulating dopamine receptors<sup>265</sup>. They found that activation of both dSPNS by application of the Drd1 receptor agonist SKF 81297 as well as application of the Drd2 receptor agonist quinolone increased the frequency of synchronous events. However, Drd1 receptor activation resulted in highly recurrent patterns of ensemble activation, while Drd2 receptor activation resulted in the successive activation of many different ensembles in a non-recurring pattern.

Recordings of dSPN and iSPN striatal ensembles *in vivo* while manipulating dopamine receptor activity found that dopamine tone influences the size of striatal SPN ensembles<sup>202</sup>. Simultaneous reduction of Drd1 and Drd2 receptor activity by systemic administration of Drd1 and Drd2 receptor antagonists SCH23390 and raclopride decreased the size of dSPN ensembles while increasing the size of iSPN ensembles. Interestingly, simultaneous elevation of Drd1 and Drd2 receptor activity by systemic administration of Drd1 and Drd2 receptor agonists SKF81297 and quinpirole altered SPN ensembles in a dose-dependent manner. At low concentrations, the size of dSPN ensembles increased but iSPN ensembles were unchanged, while at high concentrations the size of both dSPN and iSPN ensembles decreased. Overall, understanding how neuromodulators shape and configure neuronal ensembles will help us better understand neural control of behavior and can help provide insight into the many neurological disorders resulting from alterations in neuromodulatory signaling.

#### **1.4.5 Quantitative identification of neural ensembles**

The first method<sup>266</sup> developed to identify neural ensembles from neural population recordings was an algorithm based on gravitational clustering<sup>267</sup>. Since then, clustering algorithms have remained a common approach for identifying neural ensembles<sup>204,243,245,253,254,268–270</sup>. Clustering algorithms are a natural choice for identifying neural ensembles, as they are designed to identify groups of related variables within a dataset based on a given similarity metric. By varying the data used for clustering or the similarity metric, one can instantiate different definitions of ensembles. For example, clustering the activity of simultaneously recorded neurons based on their firing rates aligned to some behavioral event might yield ensembles specific to the given

behavioral event. Alternatively, clustering neural activity recorded during an entire session containing multiple behaviors could yield ensembles that encode multiple behaviors or perhaps the most commonly occurring behavior. Selecting a more specific definition of neural ensembles, Lin et al. first projected neural activity into a decoding subspace to separate units based on their encoding of task parameters and then identified ensembles by clustering neurons within this encoding subspace<sup>204</sup>. Clustering within this encoding subspace amounts to defining ensembles as groups of neurons that similarly encode task parameters. In addition to clustering methods, neural ensembles have been identified using dimensionality reduction methods<sup>198,201,265,271–280</sup>, template matching methods, and spike-timing based methods developed specifically for neural data<sup>209,281–289</sup>. Recently neural ensembles were identified using a generative model of neural activity constrained by ensemble organization<sup>210</sup>.

## 1.5 Thesis overview

Work over the last decade has highlighted the utility of thinking about neural function at the population level<sup>290–296</sup>. The overarching goal of this work is to improve our understanding of how populations of neurons within the basal ganglia control behavior.

In Chapter 2, I describe my primary research project that is published at *eLife*<sup>297</sup>. In this work we characterize striatal ensemble activity during spontaneous self-grooming behavior. We recorded single-unit extracellular activity from populations of striatal neurons in freely moving mice to capture striatal grooming related activity. To study self-grooming behavior, we developed a

semi-automated approach to detect grooming events from 117 hours of simultaneous multi-camera video recordings of mouse behavior.

In Chapter 3, I describe the first half of a collaboration with Dr. Mingzheng Wu where we studied changes in dopaminergic neuron activity and signaling following aversive learning. We characterized the effects of ketamine on behavior and the dopaminergic system. Further, we identified the medial prefrontal cortex as the locus of ketamine's actions. This work was published in 2021<sup>298</sup>.

In Chapter 4, I describe the development of wireless optogenetic devices to facilitate *in vivo* optogenetics studies of individual and social behaviors. These real-time programmable, wireless devices are fully implantable resulting in minimal interference with an animal's natural movements. This work was published in 2021<sup>299</sup> and was done in collaboration with members of the Kozorovitskiy Lab and members of Dr. John Rogers' research group at Northwestern University.

In the appendix, I describe the second part of my collaboration with Dr. Mingzheng Wu studying the dopaminergic system in an aversive learning paradigm. We characterized ketamine's effects on plasticity in the medial prefrontal cortex and identified dopaminergic mechanisms underlying ketamine's effects. This work was published in 2021<sup>300</sup>.

## Chapter 2 – Striatal ensemble activity in an innate naturalistic behavior

A version of this chapter is published in *eLife*.

Samuel Minkowicz, Mychaela Alexandria Mathews, Felicia Hoilam Mou, Hyoseo Yoon, Sara Nicole Freda, Ethan S Cui, Ann Kennedy, Yevgenia Kozorovitskiy. *eLife*, 2023. 12:RP87042. <https://doi.org/10.7554/eLife.87042.1>

### Abstract

Self-grooming is an innate, naturalistic behavior found in a wide variety of organisms. The control of rodent grooming has been shown to be mediated by the dorsolateral striatum through lesion studies and *in vivo* extracellular recordings. Yet, it is unclear how populations of neurons in the striatum encode grooming. We recorded single-unit extracellular activity from populations of neurons in freely moving mice and developed a semi-automated approach to detect self-grooming events from 117 hours of simultaneous multi-camera video recordings of mouse behavior. We first characterized the grooming transition-aligned response profiles of striatal projection neuron and fast spiking interneuron single units. We identified striatal ensembles whose units were more strongly correlated during grooming than during the entire session. These ensembles display varied grooming responses, including transient changes around grooming transitions or sustained changes in activity throughout the duration of grooming. Neural trajectories computed from the identified ensembles retain the grooming related dynamics

present in trajectories computed from all units in the session. These results elaborate striatal function in rodent self-grooming and demonstrate that striatal grooming-related activity is organized within functional ensembles, improving our understanding of how the striatum guides action selection in a naturalistic behavior.

## 2.1 Introduction

Self-grooming is an evolutionarily conserved, ethologically relevant, and innate behavior. Self-grooming is found in arthropods<sup>3,6</sup>, birds<sup>19,20,23</sup>, and mammals<sup>27,28,34,35,37</sup>. In mammals, grooming serves to care for the outer body surface, for de-arousal<sup>98,103</sup>, thermoregulation<sup>65-67</sup>, and water economy<sup>75</sup>. Rodent grooming is an innate behavior<sup>35,38,41-43</sup>, with mice showing primitive forms of facial grooming as early as postnatal day 1 (p1)<sup>41</sup>. From p4-8, the kinematics of grooming movements become more tightly coordinated. After p9, mice start to perform movements similar to those performed by adults. Rat pups begin to exhibit functional face grooming at p6-8<sup>35</sup>, but do not perform long sequences of grooming until p14-21<sup>38,42,43</sup>, the time of development when many complex motor programs begin to emerge<sup>45,46</sup>.

The selection and initiation of actions is controlled by the striatum<sup>132,133,136,175-177,180</sup>. The striatum has been shown to encode action space<sup>134</sup> and to flexibly combine behavioral motifs into actions<sup>136</sup>. Cells within the striatum, predominantly consisting of striatal spiny projection neurons<sup>158,301,302</sup>, are organized into functional clusters of co-active units; this clustering is considered to be important for striatal network dynamics<sup>255,303</sup> and behavioral control<sup>134,135,253,254,261,262</sup>. The striatum has been implicated in the production of self-grooming

behavior, and lesions of the striatum disrupt grooming bouts<sup>112</sup>. Within the striatum, neurons of the dorsolateral striatum<sup>115,116</sup> and nearby central striatal regions<sup>117</sup> display grooming-related activity. Yet, how populations or ensembles of neurons in the striatum—defined here as sets of neurons that are more likely than chance to be co-active—encode self-grooming remains unclear. Given the likely importance of ensemble activity in the striatum, elaborating whether grooming-associated neural activity maps onto striatal ensembles is significant, and it remains to be elucidated.

Here we recorded simultaneous activity of populations of neurons in the dorsolateral striatum of freely moving mice during spontaneous grooming using extracellular probes. Because grooming can be a relatively rare behavior, many hours of data must be acquired to capture an adequate sample of its neural correlates. To overcome this obstacle, we developed a semi-automated approach to detect grooming bouts from behavioral videos using 3D pose estimation and postural heuristics. We found striatal projection neurons (SPN) and fast spiking interneurons (FSI) with temporally diverse grooming-related activity. Furthermore, we identified striatal ensembles that encode core parameters of grooming bouts, including the transitions in and out of individual bouts, as well as bout duration.

## **2.2 Results and discussion**

### **2.2.1 Mouse spontaneous self-grooming behavior**

Mice were placed in a transparent, triangular arena with video recorded from each side to capture spontaneous behavior (**Figure 2.1A, B**). We identified mouse grooming bouts in a semi-

automated 4-step process (**Figure 2.1C**). First, mouse limb positions were tracked in 2D in each view using DeepLabCut<sup>304</sup> and triangulated to 3D using Anipose<sup>305</sup> (see Methods). The 3D limb positions were then used to isolate likely grooming times, using a set of postural heuristics including movement speed, whether the animal was rearing, and the hand-to-nose distance. These heuristics identified general windows during which grooming was likely to be occurring, but they did not capture the precise timing of the behavior. We therefore refined heuristic output using manual frame-by-frame annotation, to capture the precise start and stop times of grooming (**Figure 2.1 Supplement 1**). In 117 total hours of analyzed video, we observed 304.8 minutes of grooming behavior within 1,475 individual bouts of grooming; mice groomed for 4.1% of each session on average (**Figure 2.1D**,  $4.1 \pm 0.3\%$ , 63 sessions from 6 mice). Grooming bouts were on average 12.4 seconds long (**Figure 2.1E**,  $12.4 \pm 0.4$  seconds) and separated by 4.3 minutes (**Figure 2.1F**,  $4.3 \pm 0.1$  minutes).

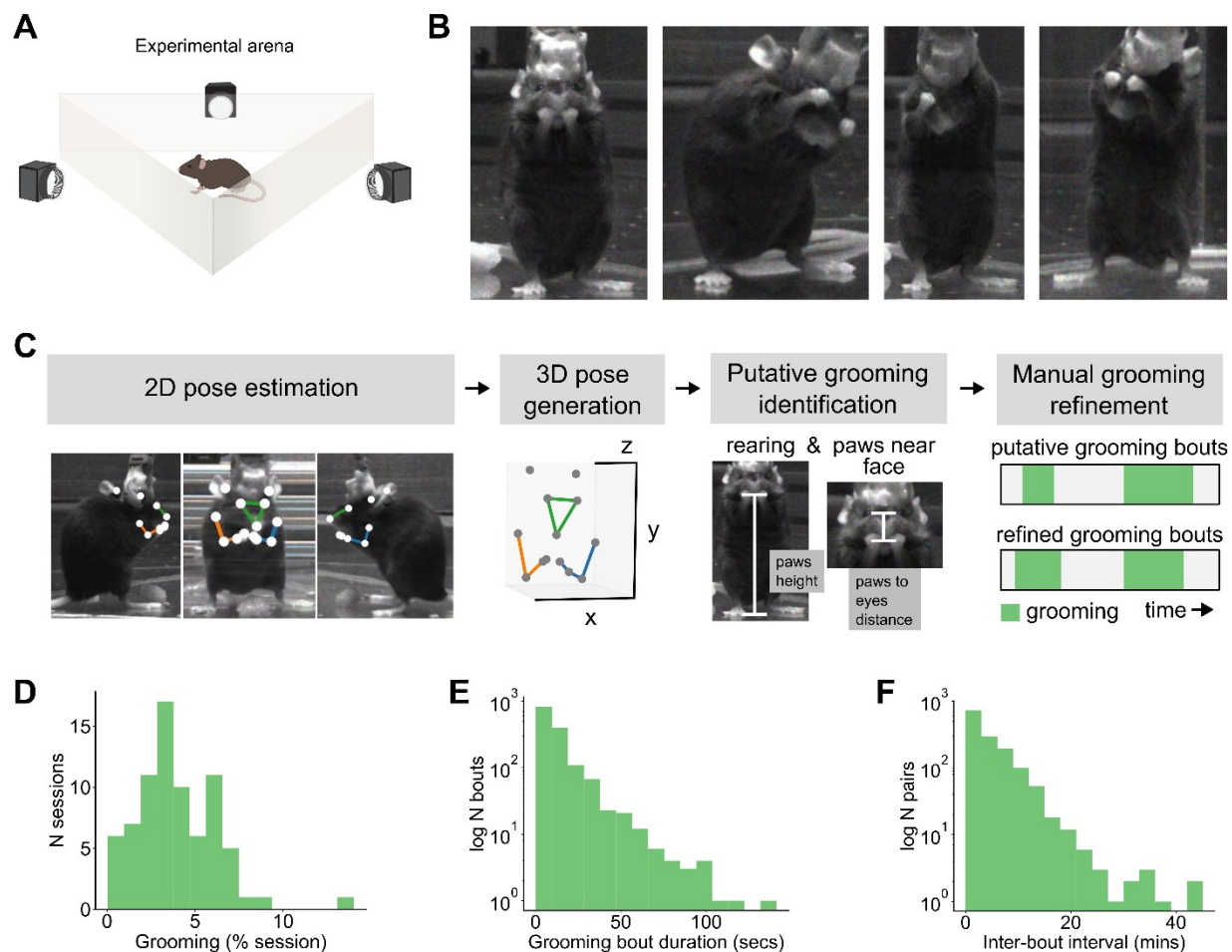


**Figure 2.1. 3D tracking and characterization of the structure of mouse spontaneous grooming.** **A.** Schematic of experimental setup. Mice were placed into an equilateral triangular arena made of transparent acrylic (12-inch sides and height) and their behavior was captured with three side view cameras. Schematic is not to scale. **B.** Example video frames of mice during spontaneous grooming. **C.** Overview of our 4-step grooming identification approach. **D.** Distribution of the percent of each session that mice spent spontaneously grooming (6 mice, 63 sessions, 117 experiment hours, 1,475 grooming bouts, 304.8 total minutes of spontaneous grooming). **E.** Distribution of spontaneous grooming bout durations in seconds (for the same dataset as in D). **F.** Distribution of inter-bout intervals in minutes (for the same dataset as in D).

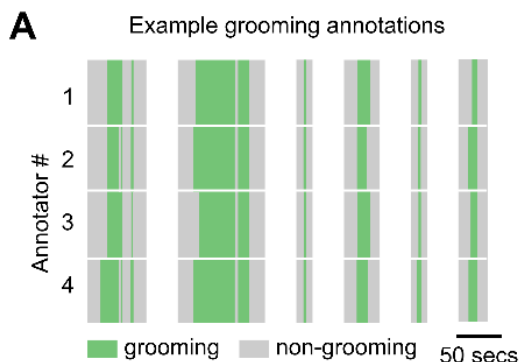


**Figure 2.1 Supplement 1. Manual refinement of grooming identification. A.** Example annotations of grooming behavior by four annotators. Green regions in each row denote times that the annotator labeled as grooming and gray regions denote times not annotated as grooming. Vertically aligned white spaces indicate breaks of variable time between individual grooming bouts. Average pairwise Jaccard Index (or Intersection over Union) computed on all annotations from a single 2-hour session was  $0.76 \pm 0.04$ .

### 2.2.2 Striatal SPNs and FSIs encode grooming transitions

To record striatal activity during mouse spontaneous grooming, we implanted 64-channel electrodes into the dorsolateral striatum of adult male and female mice (**Figure 2.2 Supplement 1A-D**,  $N=6$  mice). We classified well-isolated units as putative striatal spiny projection neurons (SPN) and putative fast spiking interneurons (FSI) on the basis of their firing rates and spike waveform, following established criteria<sup>306–308</sup>. Units that did not fit the criteria for SPNs or FSIs were labelled as ‘other’ and excluded from further analyses. (**Figure 2.2A**, SPN: 88.2% 2,755 units, FSI: 3.2% 100 units, other: 8.6% 269 units).

To identify example individual units with grooming-related activity, we isolated units whose activity within a two-second window around the start or end of grooming was two standard

deviations above mean activity during a grooming-free baseline period. All subsequent analyses were performed on the full dataset. Example SPNs and FSIs with grooming related activity are shown in **Figure 2.2B-E**. We observed units displaying diverse grooming-related responses, including increased activity at the start of grooming, end of grooming, and both start and end of grooming, as well as units that showed elevated activity for the duration of grooming, and units that showed reduced activity for the duration of grooming.

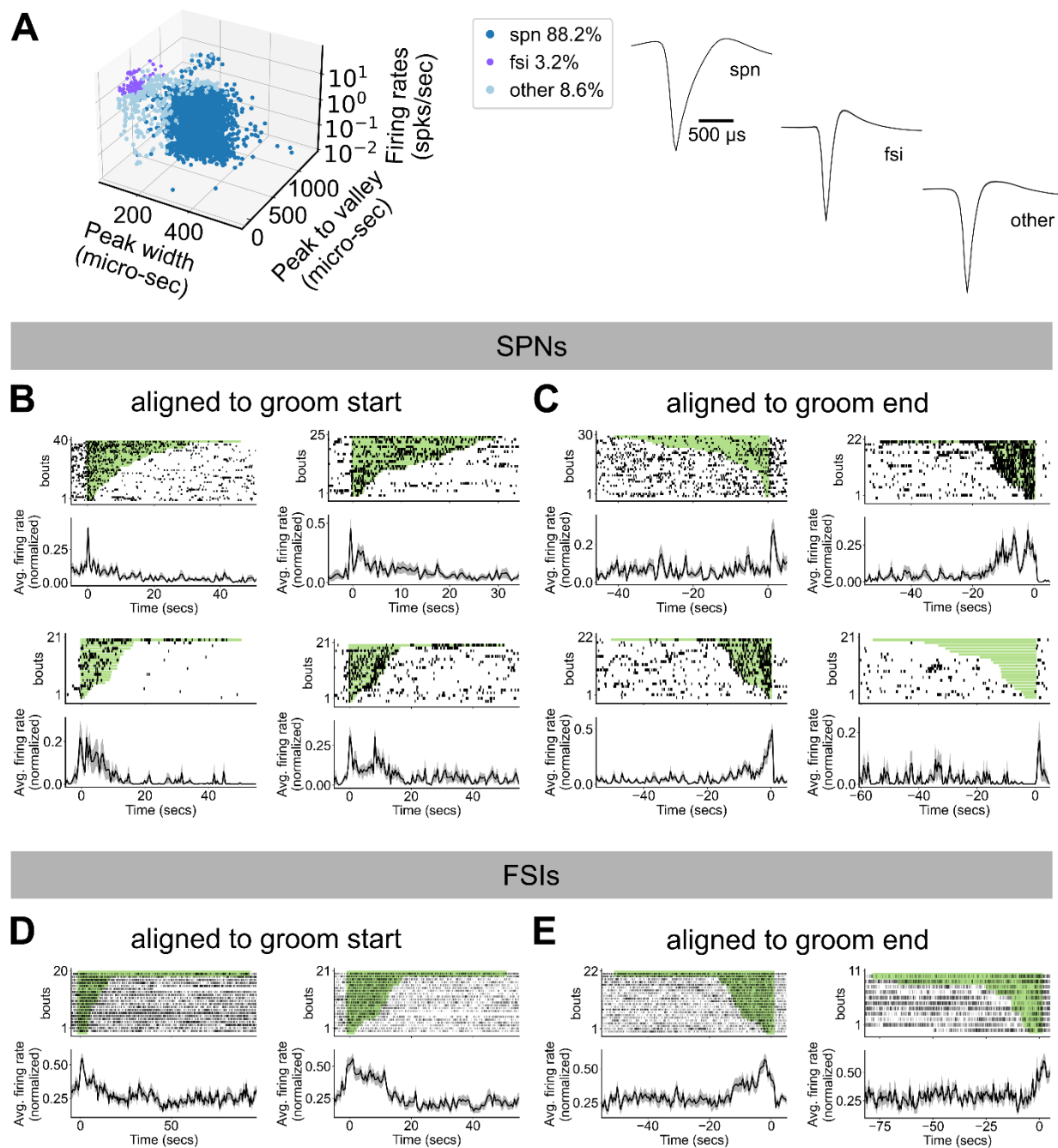


**Figure 2.2. Striatal cell type specific activity mapped to spontaneous self-grooming. A.** Classification of recorded units. Left: units were categorized as either SPNs, FSIs, or ‘other’ by their firing rates, spike waveform peak width, and duration between spike waveform peak to valley (SPN: 88.2% 2,755 units, FSI: 3.2% 100 units, other: 8.6% 269 units). Right: average  $\pm$  SEM

spike waveforms for units in each category. **B.** Activity of 4 example SPNs during grooming. Neural activity are aligned to the start of grooming bouts, denoted by  $t = 0$ . Top: spike raster plots for the example neuron during each grooming bout in the given session. Grooming bouts are sorted by grooming bout duration, denoted by the green rectangles. Bottom: unit average firing rate aligned to grooming start and normalized to  $[0, 1]$ . **C.** Activity of 4 example SPNs as in B but for aligned to groom end. **D.** Activity of 4 example units as in B but for FSIs aligned to groom start. **E.** Activity of 4 example units as in B but for FSIs aligned to groom end.

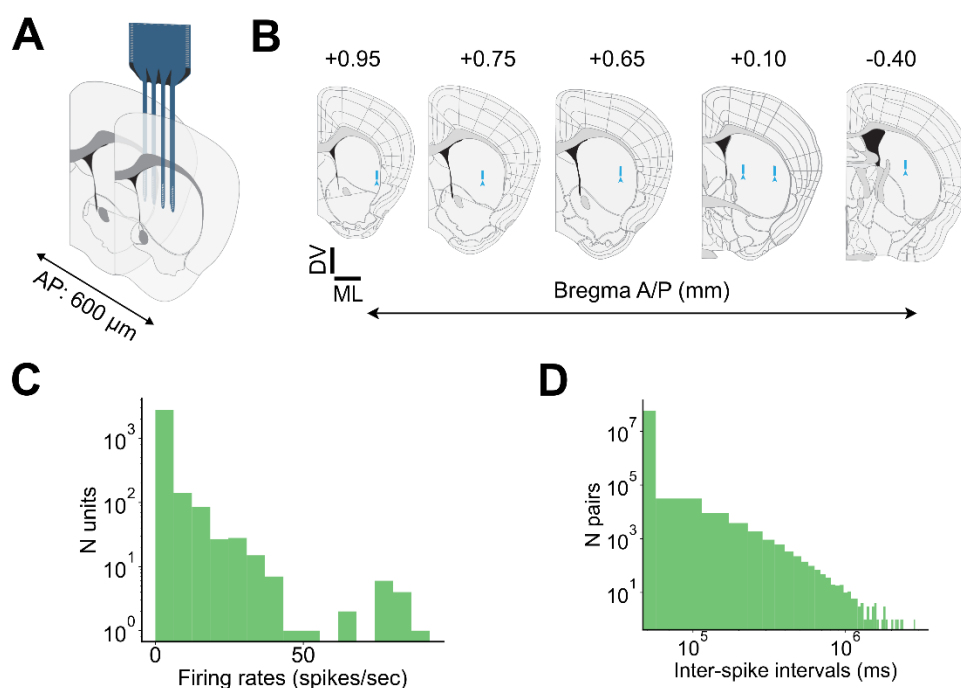


**Figure 2.2 Supplement 1. Probe placement and firing rate characteristics.** **A.** Schematic depicting how the four shanks within our recording electrodes were implanted along the anterior-posterior axis (shanks span  $600 \mu\text{m}$ ). **B.** Representative coronal slices of electrode placements. Coronal histological slices were obtained and registered to the Allen Common Coordinate Framework (CCFv3) using the WholeBrain software package. Blue arrows depict the most ventral electrode position for each mouse. Blue lines depict the region covered by sites in one shank of each electrode. Anterior-Posterior (A/P) coordinates from Bregma used for registration are depicted above each slice. (6 mice, scale bar DV and ML = 1 mm). **C.** Distribution of firing rates for all recorded units (3,124 units. 6 mice). **D.** Distribution of inter-spike intervals for all recorded units (3,124 units. 6 mice).

To characterize different grooming-associated responses in the recorded striatal units, we first performed principal components analysis (PCA)<sup>309</sup> on the grooming transition-triggered-average activity of all recorded SPNs and FSIs. We performed PCA separately on SPN activity aligned to groom start, SPN activity aligned to groom end, FSI activity aligned to groom start, and FSI activity aligned to groom end. The first principal component (PC) from each group reflects units that undergo a step-like increase or decrease in their activity at the grooming transition (**Figure 2.3A, B, F, G, K, L, P, Q**, SPNs aligned to groom start: 336 units with positive contributions to the first PC (denoted “> 0”), 640 < 0, SPNs aligned to groom end: 526 > 0, 424 < 0, FSIs aligned to groom start: 66 > 0, 1 < 0, FSIs aligned to groom end: 22 > 0, 44 < 0). The second PC from each group reflects units whose activity transiently peaks or decreases around the grooming transition (**Figure 2.3C, D, H, I, M, N, R, S**, SPNs aligned to groom start: 364 > 0, 292 < 0, SPNs aligned to groom end: 164 > 0, 518 < 0, FSIs aligned to groom start: 4 > 0, 19 < 0, FSIs aligned to groom end: 5 > 0, 19 < 0). Taken together, these results show that single unit SPNs and FSIs encode transitions into and out of an innate naturalistic behavior.

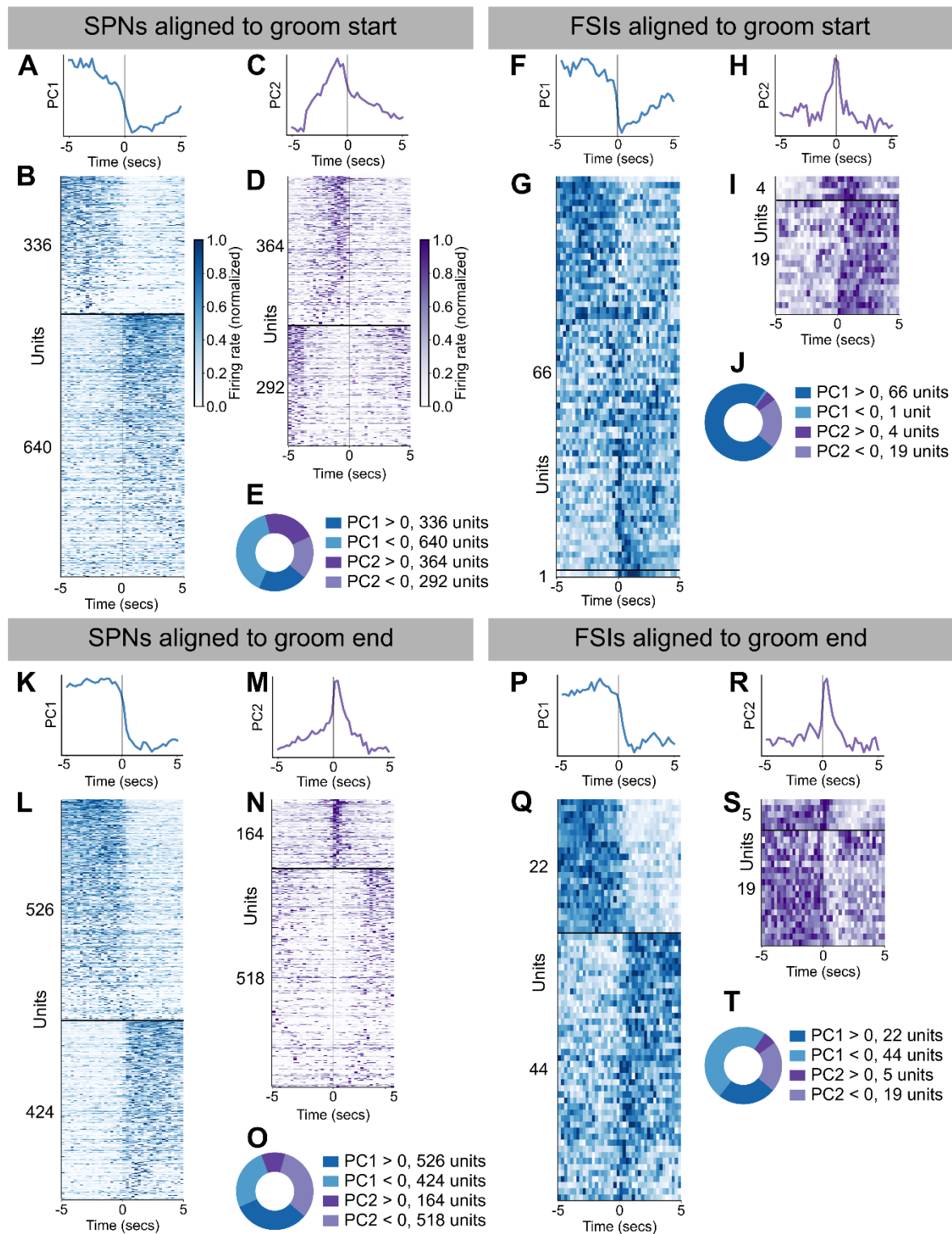


**Figure 2.3. Emergent motifs in SPN and FSI activity around grooming transitions. A.** First principal component from decomposing 10 seconds of SPN activity centered around grooming

bout start times (1,632 units, explains 9.3% of variance). **B.** Activity around grooming start for units that had the largest magnitude weight for the first principal component. Units with weight  $> 0$  are shown above the horizontal black line (336 units) followed by units with weight  $< 0$  (640 units). Units are sorted by their weight for PC1. Each unit's activity was normalized to the range from zero to one. **C.** Same as **A**, but for the second principal component (explains 5.1% of variance). **D.** Same as **B**, but for the second principal component (364 units with weight  $> 0$ , 292 units with weight  $< 0$ ). **E.** Donut plot depicting the number of units with positive and negative weights for the first two principal components. **F-J.** Same as **A-E**, but for FSIs aligned to groom start (66 units with PC1 weight  $> 0$ , 1 unit with PC1 weight  $< 0$ , 2 units with PC2 weight  $> 0$ , and 19 units with PC2 weight  $< 0$ . PC1 explains 21.2% of variance and PC2 explains 7.1% of the variance). **K-O.** Same as **A-E**, but for SPNs aligned to groom end (526 units with PC1 weight  $> 0$ , 424 units with PC1 weight  $< 0$ , 164 units for PC2 weight  $> 0$ , and 518 units with PC2 weight  $< 0$ . PC1 explains 12.9% of variance and PC2 explains 5.2% of the variance). **P-T.** Same as **A-E**, but for FSIs aligned to groom end (22 units with PC1 weight  $> 0$ , 44 units with PC1 weight  $< 0$ , 5 units with PC2 weight  $> 0$ , and 19 units with PC2 weight  $< 0$ . PC1 explains 34.6% of variance and PC2 explains 8.6% of the variance).

### 2.2.3 Striatal activity is organized into ensembles

The event-triggered average responses of striatal neurons reveal several patterns of firing rate modulation aligned with the start or end of grooming. However, because this analysis relies on trial-averaging, it cannot be used to determine whether the striatum contains ensembles of neurons that are consistently co-active. To address this question, we looked for functional clusters, or 'ensembles' of co-active striatal neurons with grooming related activity. To achieve this, we first constructed a matrix containing the grooming activity of all units in a given session, where the activity of each unit plus 5 seconds before and after grooming was concatenated. This matrix is shown for an example session in **Figure 2.4A**; dendrogram-based sorting of recorded units makes evident the presence of synchronous activity in groups of units. Synchrony among units is also suggested by the block-diagonal structure of the correlation matrix for this example session (**Figure 2.4B**). This synchrony is further suggested by comparison to a time-shuffled

version of the data (**Figure 2.4 Supplement 1A**) and its corresponding correlation matrix (**Figure 2.4 Supplement 1B**).

To test for the presence of ensembles and to estimate the number of potential ensembles within each session, we used an eigenvalue-based statistical method<sup>198,275</sup>, where we identify dimensions of the neural covariance matrix that capture more variance than expected by chance and found each session to have three to ten ensembles (**Figure 2.4C**,  $6.2 \pm 0.3$  ensembles, 33 sessions, see Methods for details). Next, using the meta- $k$ -means clustering algorithm<sup>310</sup>, we identified the ensembles present in each session. Meta- $k$ -means is an extension of  $k$ -means where one performs  $N$  iterations of  $k$ -means, keeping track of how many times each pair of units gets clustered together. The proportion of times that each pair gets clustered together is used to assign intermediate clusters before a final merging step. We chose to use meta- $k$ -means for two reasons. First, meta- $k$ -means does not always result in cluster assignment for all units, which is preferable because our recording configuration only samples a small subset of neurons in striatum and we do not expect all recorded units to belong to an identified striatal ensemble. Second, meta- $k$ -means allows for the final number of identified ensembles to be greater or less than the initial choice of  $k$ , which is preferable because we do not have *a priori* knowledge of ensemble numbers present in each session.

We found that 80% of recorded SPNs (1,074 units) and 70% of recorded FSIs (41 units) were clustered into ensembles of two or more units (**Figure 2.4 Supplement 1C**). A majority of clusters were composed of only SPNs, and FSIs were almost always assigned clusters together with SPNs (**Figure 2.4 Supplement 1D**; 88% (214 clusters) SPN only, 1% (1 cluster) FSIs only, 11% (28 clusters) SPN and FSIs). Within our identified ensembles, units in the same ensemble

tended to be spatially closer than units that are not within the same ensemble (**Figure 2.4D**), consistent with striatal ensembles detected using imaging techniques<sup>134,135,254</sup>. During grooming, the pairwise correlation between units within the same cluster is higher than for the correlation between units not in the same cluster, whether those units are unclustered or belong to a different cluster (**Figure 2.4E**). The distributions of pairwise correlations computed using data from the whole session are shown in **Figure 2.4F**. This in-versus-out of cluster difference is weaker when comparing unit activity during the whole session, rather than during grooming (**Figure 2.4G**, grooming AUC: 0.81, whole session AUC: 0.69).

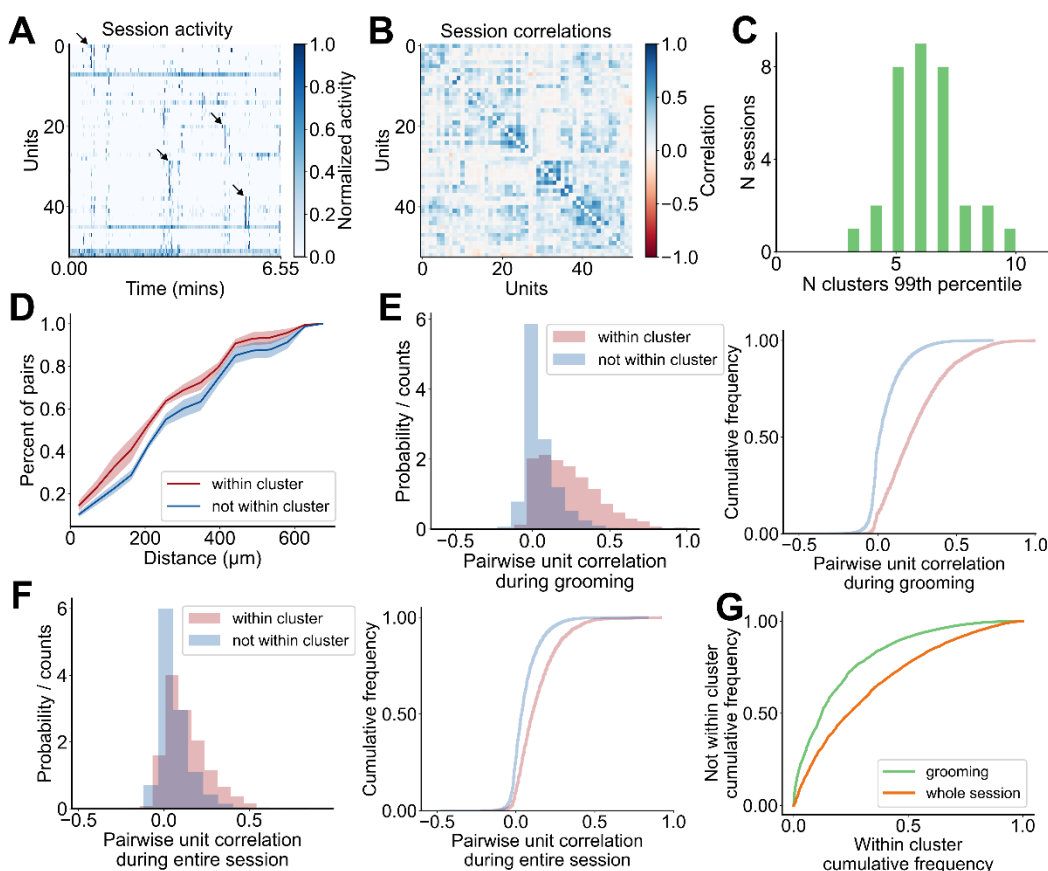


**Figure 2.4. Identification and characterization of striatal grooming ensembles.** A. Heatmap of activity during grooming for all units in an example session (53 units, 6.55 minutes). Arrows

point out a subset of synchronous events. Each unit's activity is normalized to [0, 1]. **B.** Correlation matrix for the activity shown in **A.** **C.** Distribution of statistical estimate for the number of ensembles within a given session (4 mice, 33 sessions). The estimate is obtained by computing the number of eigenvalues from the data that are above the 99<sup>th</sup> percentile of the distribution of eigenvalues from 5,000 random shuffles of the data. **D.** Average cumulative distribution of pairwise unit distances for each pair of units that are within the same cluster (red) and each pair of units that are not within the same cluster (blue). Plot depicts the mean  $\pm$  SEM of the cumulative distribution across mice (4 mice). **E.** Distribution of pairwise unit correlations during grooming for each pair of units that are within the same cluster (pink 2,747 pairs) and each pair of units that are not within the same cluster (blue 27,421 pairs). Left: histogram. Right: cumulative distribution. **F.** Same as in **E**, but for pairwise correlations computed from activity during the entire session including grooming times. **G.** Comparison between the difference in pairwise unit correlations for units within and not within the same cluster computed during grooming (green) and during the whole session (orange) (grooming AUC: 0.81, whole session AUC: 0.69).

The distribution of the number of ensembles identified in each session is shown in **Figure 2.4**

**Supplement 1E.** We found a significant positive relationship between the number of ensembles identified and the number of units in each session (**Figure 2.4 Supplement 1F**,  $R^2 = 0.239$ ,  $p =$

0.004). The distribution of the number of units within each cluster is shown in **Figure 2.4**

**Supplement 1G** (median cluster size = 4 units, mean =  $4.6 \pm 0.2$  units). Cluster size did not

increase with the number of units recorded in a given session (**Figure 2.4 Supplement 1H**,  $R^2 =$

0.01,  $p = 0.582$ ). The distribution of the percent of clustered units in each session is shown in

**Figure 2.4 Supplement 1I** with half of sessions having at least 82% clustered units.

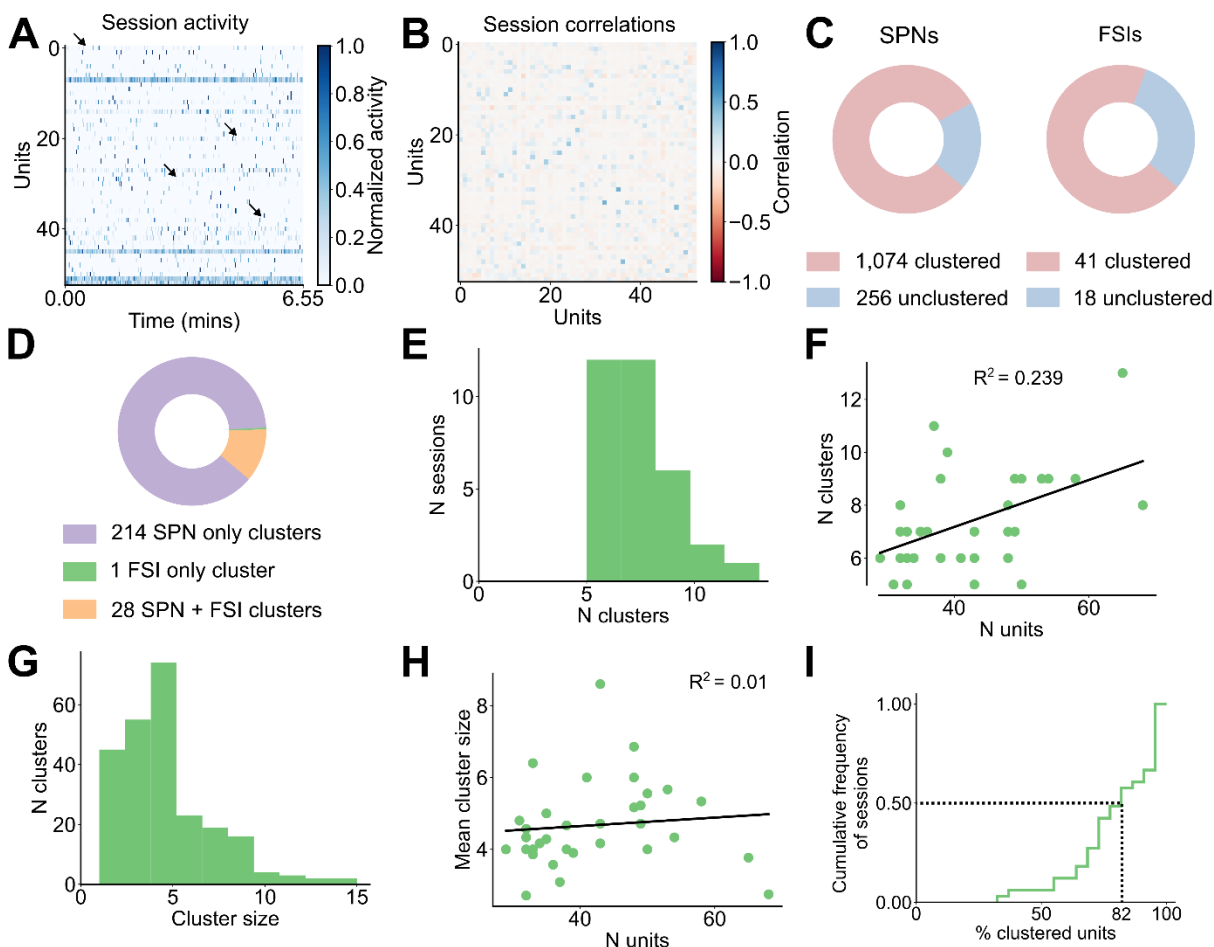


**Figure 2.4 Supplement 1. Statistics of identified clusters and activity patterns.** **A.** Heatmap of activity during grooming with shuffled time bins for all units in the example session shown in **4A** (53 units, 6.55 minutes). Arrows are in the same position as in **Figure 4A** highlighting the absence of synchrony after shuffling. Each unit's activity is normalized to the range from zero to one. **B.** Correlation matrix for the shuffled activity shown in **A**. **C.** Total number of SPNs and FSIs that were clustered (pink) and unclustered (blue) (4 mice, 33 sessions, 243 clusters). **D.** Total number of clusters that comprised of only SPNs (purple), only FSIs (green), and of both SPNs and FSIs (orange) (data as in **C**). **E.** Distribution of the number of clusters in each session. **F.** Relationship between the number of clusters found in each session and the number of units in that session ( $R^2 = 0.239$ ,  $p = 0.004$ ). **G.** Distribution of the number of units in each cluster (data as in **C**). **H.** Relationship between the average cluster size in each session and the number of units in that session ( $R^2 = 0.01$ ,  $p = 0.582$ ). **I.** Cumulative distribution of the percent of clustered units in each session. Dashed lines denote that half the sessions have at least 82% clustered units (data as in **C**).

### 2.2.4 Striatal ensembles encode features of self-grooming

Having demonstrated the existence of ensemble activity during grooming, we next asked whether ensemble activity was enriched during specific timepoints during grooming. A heatmap displaying the average grooming activity for all significant ensembles is shown in **Figure 2.5A** (112 ensembles, 4 mice, 33 sessions). To visualize the average grooming activity of ensembles across grooming bouts of varying duration, we first linearly time-warped ensemble activity during grooming. We found that ensemble peak activity is enriched around the transitions into and out of grooming (**Figure 2.5B**), but that the dynamics of grooming ensemble activation are diverse. For example, we found ensembles with higher activity during grooming, lower activity during grooming, and with peak activity at the start or end of grooming, with individual cluster examples of these patterns shown in **Figure 2.5C-F** and **Figure 2.5 Supplement 1C**. This finding was unchanged when we analyzed the percentage of active units within each ensemble rather than the ensemble-average firing rate (**Figure 2.5 Supplement 1A, B**).

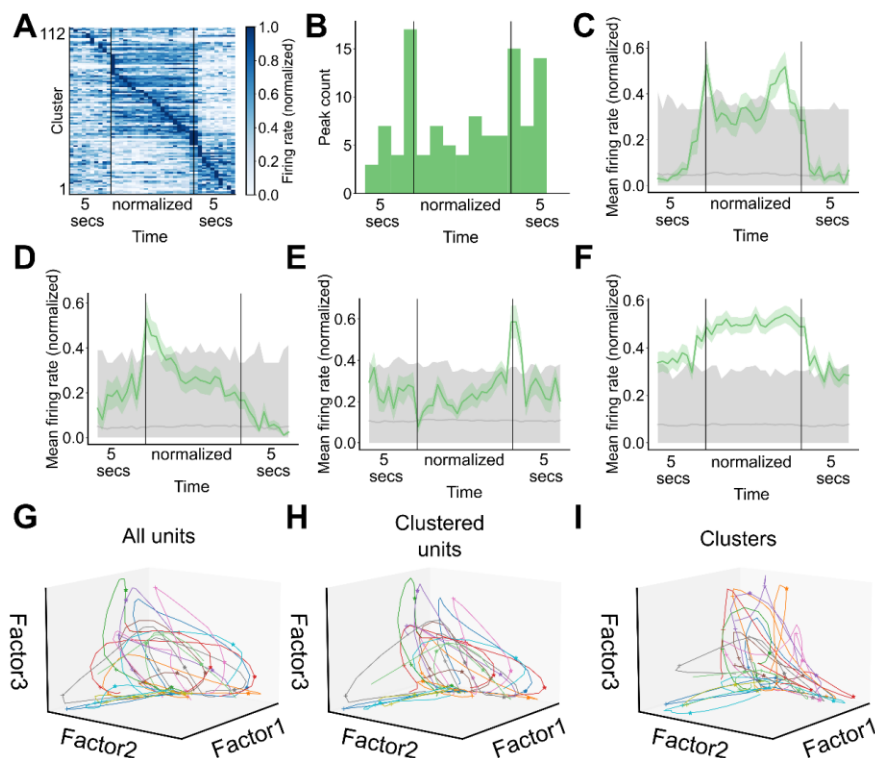


**Figure 2.5. Striatal ensembles encode features of self-grooming.** **A.** Heatmap depicting the grooming-aligned average activity of all striatal ensembles. Ensemble averages are normalized to the range from zero to one. Prior to averaging across grooming bouts, ensemble activity during each grooming bout, excluding the 5 seconds before and after grooming, was linearly time warped to a fixed duration. Ensembles are sorted by peak time (112 ensembles, 4 mice, 33 sessions). **B.** Distribution of time at which ensemble average activity peaked (data as in **A**). **C.** Representative example of an ensemble with increased average activity around grooming transitions. Grey region denotes the range of activity for shuffled ensemble activity. Bottom of the range depicts the 2.5<sup>th</sup> percentile of the shuffled activity, top of the range depicts the 97.5<sup>th</sup> percentile of the shuffled activity, and grey line depicts the average shuffled activity. **D.** Representative example of an ensemble with increased average activity at the start of grooming (grey region as in **C**). **E.** Representative example of an ensemble with increased average activity at the end of grooming (grey region as in **C**). **F.** Representative example of an ensemble with increased average activity throughout the duration of grooming (grey region as in **C**). **G.** Neural trajectories traced out in factor space by the population of units recorded during all grooming bouts in an example session (65 units, 22 grooming bouts). Colors depict different grooming bouts, pluses denote the start of grooming, and asterisks denote the end of grooming. **H.** Neural trajectories traced out in factor space by the population of clustered units during all grooming bouts in an example session (49 units, 22 grooming bouts). Visualization elements as in **G**. **I.** Ensemble trajectories traced out in

factor space by the striatal ensembles during all grooming bouts in an example session (13 ensembles, 22 grooming bouts). Visualization elements as in **G**.

To contrast the encoding of grooming-related activity in ensembles vs unclustered units, we used nonnegative matrix factorization to perform dimensionality reduction on the neural activity during grooming within a single session. The trajectories traced out by the population activity of all units during all grooming bouts in an example session are shown in **Figure 2.5G** (65 units). During most grooming bouts the population activity moves out along factor 1, then up along factor 2, and finally returns toward the origin along factor 3, corresponding to population encoding of grooming onset, maintenance, and termination. The neural trajectories computed from unclustered units do not retain the dynamics present in the trajectories from all units or the clustered ones (**Figure 2.5 Supplement 1D**, 16 unclustered units; **Figure 2.5H**, 49 clustered units). Notably, the ensemble trajectories computed from the activity of ensembles retain most of the dynamics seen in the trajectories computed from the activity of single units (**Figure 2.5I**, 13 ensembles).

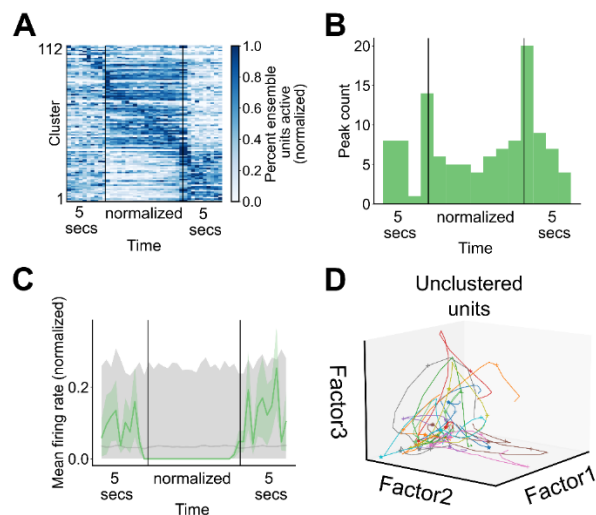


**Figure 2.5 Supplement 1. Patterns of cluster engagement.** **A.** Heatmap depicting the percent of units within each ensemble that are active during grooming averaged across all grooming bouts in a given session. Prior to averaging across grooming bouts, ensemble activity during each grooming bout was interpolated to a fixed duration, excluding the 5 seconds before and after grooming. Ensembles are in the same order as in **Figure 2.5A** and data is normalized to the range from **zero to one** (112 ensembles, 4 mice, 33 sessions). **B.** Distribution of times when the percent of active units in an ensemble peaked (data as in **A**). **C.** Representative example of an ensemble with decreased average activity throughout the duration of grooming (grey region as in **Figure 2.5C**). **D.** Neural trajectories traced out in factor space by the population of unclustered units during all grooming bouts in an example session (16 units, 22 grooming bouts). Visualization elements as in **Figure 2.5G**.

### 2.2.5 Discussion

Here, we developed a semi-automated approach to identify grooming events in mouse behavioral videos. We recorded population activity in the dorsolateral striatum of freely moving mice and found SPNs and FSIs with activity that encodes the start and end of spontaneous grooming bouts. Previous studies reported changes in striatal single unit activity around the start and end of naturalistic<sup>115,116,311</sup> and learned behaviors<sup>180–182</sup>. Our single unit data elaborate the changes in

striatal unit activity around the transitions of a naturalistic behavior. Single unit responses were heterogenous and included units with changes in activity at the start or end of grooming, as well as units that were active or silenced throughout the duration of grooming. We identified striatal ensembles with units that were more correlated during grooming than during the entire session. These striatal ensembles encoded grooming start time, end time, and bout duration. Single session trajectories computed from ensemble activity retain most of the dynamics present in trajectories computed from all units in the session.

The distribution of pairwise distances between units within an ensemble is shifted towards smaller distances, compared to the distribution of distances for units that do not belong to the same ensemble. This is consistent with striatal ensembles detected using imaging techniques<sup>134,135,254</sup> although our identified ensembles are less spatially compact than those previously reported. Notably, however, striatal 2-photon imaging approaches and microendoscopic imaging of genetically encoded calcium indicators yield a recording area that extends along the medial-lateral and anterior posterior axes (*i.e.*, horizontally), whereas our four-shank electrophysiological recordings yield a recording field that extends along the anterior-posterior and dorsal-ventral axes (*i.e.*, vertically), potentially accounting for this difference in findings. Together, the ensemble distances recorded via both methods suggest the possibility that striatal ensembles are isotropically organized, which is well-aligned with studies of cortical and thalamic projection patterns to the striatum<sup>118,121,312</sup>.

While the ensembles we characterized were identified during grooming behavior, it is possible that they are not grooming-specific. One possibility for the functional organization of striatal ensembles, is that ensemble membership is stable across different behaviors, and that ensemble

activation encodes some common movement motif or state that is present in multiple behavioral settings. However, the units within our identified striatal ensembles were more correlated during grooming than during the entire recording session. Our data therefore support an alternative to the stable membership hypothesis, wherein individual units can be members of multiple ensembles, such that when a given unit is active, the behavior the animal is performing can only be determined by looking at the population level. For example, a set of units might be members of a single ensemble that encodes the start of grooming, but each unit could also be part of different ensembles that encode aspects of other natural behaviors, such as eating or walking. This ‘mixed selectivity’ is broadly consistent with previously reported data on striatal activity patterns and cluster memberships that are not conserved across divergent behavioral motifs<sup>134,135</sup>.

Striatal FSIs are parvalbumin-containing GABAergic interneurons that make up approximately 1% of striatal neurons<sup>158,170,313</sup>. FSIs receive direct cortical input, form inhibitory synapses onto SPNs<sup>158,172,314</sup>, and are interconnected amongst themselves via gap junctions on their dendrites<sup>171</sup>. Previous studies found uncoordinated, idiosyncratic task-related changes in FSI activity<sup>315</sup>, as well as changes in FSI activity that correlated with movement features like velocity<sup>316</sup>, with one study showing grooming-related activity in a small number of recorded putative FSIs<sup>116</sup>. We recorded units that match spike waveform features and firing rates of FSIs<sup>306,313</sup> and found them to have grooming related activity. These units displayed decreased or increased activity during grooming, as well as transient activity changes at the transitions into and out of grooming. Consistent with strong connectivity present between FSIs and SPNs<sup>159</sup>, a majority of FSIs (70%) were part of identified ensembles and almost all FSIs were part of ensembles together with SPNs.

Striatal control of movement is mediated via two parallel pathways: the direct and indirect pathway, composed of dSPNs and iSPNs<sup>130,137,317</sup>. Previous recordings of direct and indirect pathway striatal ensemble activity have found that d- and iSPNs exhibit a similar time course of behavior-related changes in their activity<sup>132,134,254</sup> and have similar ensemble organization<sup>134</sup>, suggesting mixed pathway membership within ensembles. Indeed, simultaneous recording of direct and indirect pathway SPNs showed that striatal ensembles are composed of d- and iSPNs in equal proportions<sup>135</sup>. These prior data suggest that striatal ensembles encoding self-grooming might be composed of both d- and iSPNs, in similar proportions and with similar encoding of grooming, although this remains to be confirmed.

Within bouts of rodent self-grooming, animals perform highly stereotyped grooming sequences called syntactic grooming<sup>318,319</sup>. This sequence is comprised of four distinctive phases and found in a variety of species<sup>34,35,37</sup>. A large body of work has established a function for the striatum in the sequential ordering of syntactic grooming phases<sup>112-114,311</sup>. On a longer time scale, grooming is one of many behaviors an animal can perform at a given time. Since self-grooming, although broadly important, is not often an immediate concern, grooming is considered a low priority behavior<sup>49</sup>. Thus, the control of grooming has been characterized by a disinhibition model, in which grooming takes place in the time left over by other higher priority behaviors when grooming would be inhibited<sup>320</sup>. Previous studies have demonstrated a striatal role in behavioral sequencing on this longer time scale as well<sup>134,136</sup>. Thus, self-grooming represents an ethologically meaningful behavioral paradigm providing a path to study neural control of an innate, conserved behavior at multiple spatiotemporal scales<sup>321</sup>.

## **2.3 Methods**

### **2.3.1 Striatal in-vivo electrophysiology in freely moving mice**

#### Subjects

Animals were handled according to protocols approved by the Northwestern University Animal Care and Use Committee (protocol number: IS00009022). Adult male and female C57BL/6J mice (p57-105) were used in this study (The Jackson Laboratory, RRID:IMSR\_JAX:000664). All mice were group-housed in a humidity-controlled, ambient temperature facility, with standard feeding, 12 hr. light-dark cycle, and enrichment procedures.

#### Electrode implantation

Mice were anesthetized with isoflurane (3% for induction, 1.5-2% for maintenance) and placed on a small animal stereotax frame (David Kopf Instruments, Tujunga, CA). A 4-shank 64-channel silicon electrode (part #A4x16-Poly2-5mm-23s-200-177-H64LP\_30mm mounted on a dDrive-m, NeuroNexus Technologies, Ann Arbor, MI) was implanted into the dorsolateral striatum (0.5 mm AP, 2 mm ML, and lowered 0.25 mm) and secured with Vetbond (3M, Maplewood, MN) followed by dental cement (Micron Superior 2, Prevest DenPro, Jammu, India, or C&B Metabond, Parkell, Edgewood, NY). The electrode shanks were aligned with the brain's anterior-posterior axis. A skull screw was connected to the electrode ground wire and fastened to the skull above the ipsilateral cerebellum. The screw was secured with Vetbond followed by dental cement. Mice were monitored following the surgery to ensure a full recovery and were administered post-operative analgesics. Mice recovered for at least 5 days after implantation.

#### Electrophysiological recording

A 64-channel headstage (part #C3325 Intan Technologies, Los Angeles, CA) was connected to the implanted electrode. In the arena, the headstage was connected to a 12-channel commutator supported by a balance arm (Part # FL-12-C-MICRO-BAL Dragonfly Inc., Ridgeley, WV). Neural recordings were acquired at 30 kHz with an Open Ephys acquisition board<sup>233</sup> and the Open Ephys GUI<sup>233</sup> (GUI version 0.5.5, Open Ephys, Atlanta, GA). To facilitate alignment of videos and neural data, the video and neural recordings were simultaneously initiated by pressing a button connected to the microcontroller.

Neural recordings were spike sorted offline using KiloSort3<sup>236</sup> in MATLAB (MathWorks, Natick, MA). We only considered units labeled as ‘good’ by KiloSort. Additionally, we manually inspected the waveforms of all units labeled as ‘good’ and excluded units with waveform shapes that did not resemble an action potential. Recordings were performed from each animal until the number of ‘good units, as identified by KiloSort, stayed below 15 for 2 consecutive days ( $27.3 \pm 4.3$  days since implant).

### Unit classification

All recorded units were classified as either putative striatal projection neurons (SPN), fast-spiking interneurons (FSI), or ‘other’ based on their spike waveform and mean firing rate across the entire session following established criteria<sup>306–308</sup>. Units were classified as putative SPNs (88.2 %) if they had peak width  $> 150 \mu\text{s}$ , peak-valley interval  $> 500 \mu\text{s}$ , and mean firing rate  $\leq 10$  Hz. Units were classified as FSIs (3.2 %) if they had peak width  $\leq 150 \mu\text{s}$ , peak-valley interval  $\leq 500 \mu\text{s}$ , and mean firing rate  $\geq 0.1$  Hz. Units that were not identified as either putative SPNs or FSIs were labeled ‘other’ (8.6 %) and excluded from all analyses.

## Histology

After the recordings, coronal brain sections were obtained from all mice to determine electrode placement. Mice were deeply anesthetized with isoflurane and transcardially perfused with 4% paraformaldehyde (PFA) in 0.1 M phosphate buffered saline (PBS). Brains were post-fixed for 1-2 days and washed in PBS. Brains were then sectioned on a vibratome (Leica Biosystems, Wetzlar, Germany) at 60  $\mu\text{m}$  from frontal cortex to posterior striatum and then dried and cover slipped under glycerol:TBS (9:1) with Hoechst 33342 (2.5  $\mu\text{g}/\text{ml}$ , Thermo Fisher Scientific, Waltham, MA). Sections were imaged on an Olympus VS120 slide scanning microscope (Olympus Scientific Solutions Americas, Waltham, MA) with DAPI for localization of cell nuclei and FITC for background fluorescence to enable electrode localization.

## Electrode localization

Coronal slices containing electrode tracts were processed using WholeBrain software package<sup>322</sup> in R<sup>323</sup>. Histological slices were analyzed and registered to the Allen Mouse Brain Common Coordinate Framework (CCFv3)<sup>324</sup> as described previously<sup>325</sup>. Striatal sections with electrode tracts were analyzed at 60  $\mu\text{m}$  intervals and frontal lobe cortical sections, which rarely contained electrode tracts, were analyzed at 100-200  $\mu\text{m}$  intervals. A total of 6-18 section images were analyzed per mouse brain. Electrode placement for each brain section was denoted at the most ventral location that the electrode tract was observed. Medial-lateral and dorsal-ventral coordinates registered to the CCFv3 were obtained for each section and plotted on a representative coronal section using the WholeBrain package.

### 2.3.2 Video capture of mouse grooming

#### Behavioral recording

On the first day of experimentation, mice were acclimated to the experimental arena for 30 minutes. All subsequent experimental sessions were 120 minutes long. The experimental arena was an equilateral triangular arena constructed from transparent acrylic (**Figure 1A**. 12-inch sides and height, 1/8-inch thick. Part #8536K131, McMaster-Carr, Elmhurst, IL) fastened together with clear epoxy (Part #31345, Devcon, Solon, OH). While in the arena, mice were given DietGel (ClearH<sub>2</sub>O, Westbrook, ME) for food and hydration. One mouse was in the arena at a time. The arena was cleaned with 70% ethanol after each session. The arena was enclosed by a dark curtain and illuminated by infrared LEDs. Experiments were conducted during the animal's active phase.

Mouse behavior was captured with three side-view cameras at 125 fps using a custom fork of the campy Python package<sup>75</sup> (**Figure 2.1A**. image size 1440 x 608 pixels. Cameras: Part #BFS-U3-16S2M-CS Teledyne FLIR, Wilsonville, OR. Lenses: Part #8595755548 Yohii, China). To synchronize recordings from all cameras, each frame grab was triggered by a TTL pulse sent from a microcontroller (Arduino, Turin, Italy). To facilitate alignment of videos and neural data, each frame grab TTL pulse was also sent to the electrophysiology acquisition board and the video and neural recordings were simultaneously initiated by pressing a button connected to the microcontroller.

#### Grooming identification

We identified mouse grooming bouts in behavioral videos using a semi-automated 4-step procedure (**Figure 2.1C**). As detailed further below, first, we tracked the mouse limb positions in

2D; second, we triangulated to the 2D limb positions to 3D; third, the 3D limb positions were used to isolate likely grooming times; and fourth, using the likely times of grooming we manually identified grooming bout start and stop times.

For 2D pose estimation, we used DeepLabCut (version 2.2.0.5)<sup>304,326</sup> to detect 15 keypoint positions (snout, both paws, wrists, elbows, shoulders, eyes, ears, and hind paws) on the frames from each camera. We labeled the 15 keypoints in 1,627 frames from 14 videos, 3 animals, and all 3 cameras. We trained a ResNet-50-based neural network<sup>327,328</sup> with default parameters on 90% of the labeled frames for 300,000 iterations. We validated with 1 shuffle and got a train error of 3.88 pixels and test error of 6.64 pixels (image size: 1440 x 608 pixels). We used a p-cutoff of 0.6 to condition the x and y coordinates for future analyses. With the p-cutoff, the train error was 3.27 pixels and test error 5.06 pixels. This network was then used to analyze all videos from the same experimental setting.

For 3D triangulation of the 2D poses we relied on Anipose<sup>305</sup>. We calibrated our 3 cameras with a 3-minute video of a ChArUco board throughout the camera fields of view (125 FPS. Image size 1440 x 608 pixels). The ChArUco board was printed on paper and taped onto a stiff plastic board. The ChArUco pattern had 7x10 squares containing 4-bit markers and a dictionary size of 50 markers. Before triangulation, we applied a Viterbi filter to the 2D poses with  $F = 12$  frames. The triangulation was performed via an optimization constrained on the distance between the two eyes and the distance between each eye and the snout. We chose `scale_smooth = 5`, `scale_length = 2`, and `score_threshold = 0.3`.

To isolate times when the mouse was likely grooming, we identified frames where the mouse was rearing, and its paws were near its head. To identify frames where the mouse was rearing, we set thresholds on the snout height and the distance between the midpoint of the eyes and the midpoint of the hindlimbs. To identify frames where the mouse's paws were near its head, we set thresholds on the distance between the midpoint of the paws and the snout, the distance between the midpoint of the paws and the midpoint of the eyes, and height of the midpoint of the paws. Per-frame labels within 1.2 seconds were merged to form predictions over a window. Predicted grooming bouts less than 2 seconds long were discarded. Parameter values were evaluated by generating predictions for a set of videos and viewing the predictions aligned to the video in BENTO<sup>329</sup>.

Grooming bout start and stop times were manually refined by 4 trained annotators, with each annotator labeling a different subset of videos. Annotators used the predictions from the previous thresholding step to navigate the videos and score grooming behaviors. The videos were annotated in VLC media player<sup>330</sup> using the Time v3.2<sup>331</sup> and Speed controller<sup>332</sup> extensions. To assess inter-annotator reliability, all annotators were also given the same 2-hour session to annotate. The average pairwise Jaccard index (or Intersection over Union) computed on the annotations was  $0.76 \pm 0.04$ .

### **2.3.4 Striatal ensemble characterization**

#### Identification of units with grooming-related activity

To isolate units with grooming related activity, we first down sampled activity to 2 Hz, by summing spike counts within non-overlapping 500 ms bins. We defined units as having grooming-

related activity if their average activity at the start or end of grooming was 2 standard deviations above their average activity during a 3 second-long, grooming-free baseline period. For activity aligned to groom start, we used the activity from 5 to 2 seconds before grooming start as the baseline and compared that to the activity from 1 second before until 1 second after the grooming start time. For activity aligned to groom end, the activity from 2 to 5 seconds after grooming was chosen as the baseline and was compared to the average activity from 1 second before until 1 second after groom end. These selection criteria were only used to identify neurons to serve as examples in **Figure 2.2**; all subsequent analyses were performed on the full dataset.

#### Characterization of trial-averaged grooming responses

We characterized the grooming responses exhibited by the recorded units by computing each unit's event-triggered average response in a  $\pm 5$ -second window relative to the start and (separately) end of grooming. Responses were down sampled to 4 Hz, by summing spike counts within non-overlapping 250 ms bins. To simplify interpretation, we restricted averaging to grooming bouts that were 'well-isolated.' Specifically, because we included the 5 seconds before and after each bout in this analysis, grooming bouts that started within 10 seconds of the end of the previous bout were not included in this analysis. An exception to this is instances with less than 3 seconds between the end of one grooming bout and the start of the next, in which case we merged these two annotations into a single bout.

To better visualize and interpret grooming-associated activity we next performed principal component analysis (PCA)<sup>309</sup> on the set of event-triggered averages. Specifically, we performed PCA separately on SPN activity aligned to groom start, SPN activity aligned to groom end, FSI

activity aligned to groom start, and FSI activity aligned to groom end. For each cell type and condition combination, we concatenated the associated units to form a units-by-time matrix, relative to groom start/stop. The response of each unit in this matrix was then Z-scored, after which PCA was used to extract the first two principal components.

To group units into ‘response types’ for visualization, we examined the weight (or ‘score’) for each unit’s contribution to the largest and second-largest principal component. Units for which the absolute value of this weight was greater for the first principal component than the second formed the “PC1” response group, while those with greater-magnitude weights for the second principal component formed the “PC2” response group. Finally, we sorted the units within each group according to their contribution to the first (PC1) or second (PC2) principal component of the dataset (weight \* activity).

#### Grooming-associated striatal ensemble identification

To identify grooming-associated striatal ensembles within a given session, we took the neurons-by-time matrix of recorded spiking from the full two-hour recording session and excluded all frames that did not occur during grooming or within a 5-second window before or after grooming. Due to the low firing rate of SPNs, it was rare to find units that were co-active at high sampling rates. Therefore, to instead identify units that were frequently active at around the same time, we binned spike counts at a sampling rate of 0.667 Hz (bin size of 1.5 seconds). The spike counts for each unit were then normalized to between zero and one, and further smoothed by convolving with a Gaussian filter with a standard deviation of 3 seconds.

Using this smoothed and coarsened estimate of cell activity, we next applied meta- $k$ -means<sup>310</sup> to identify sets of cells that were often co-active. We chose to use meta- $k$ -means for clustering, because it does not force all units in a session to be assigned to a cluster, and it allows for the number of ensembles to be greater or less than the initial choice of  $k$ . Briefly, meta- $k$ -means employs repeated runs of standard  $k$ -means clustering to identify groups of units that are consistently clustered together. As with standard  $k$ -means, meta- $k$ -means requires the user specify an initial number of clusters  $k$ , which we set to be the square root of the number of units in the given session, as in Barbera et al<sup>38</sup>. We then ran 1,000 repeats of the  $k$ -means clustering algorithm on the matrix of filtered grooming-related activity described above, with units as variables and time bins as observations. Cluster centroids for each repeat were initialized using the greedy  $k$ -means++ algorithm<sup>333</sup>. As in prior work<sup>134,254,334</sup>, units that were assigned to the same cluster in >80% of  $k$ -means runs were considered to be part of the same meta- $k$ -means cluster.

When merging clusters as part of the meta- $k$ -means algorithm, we used the silhouette score<sup>335</sup> to evaluate the outcome of a potential cluster merge. To ensure adequate sample size for downstream analyses, ensemble identification was restricted to sessions with at least 30 SPNs and FSIs.

### Statistical analysis of striatal ensembles

To compute a statistical estimate on the number of ensembles present in each session we used an eigenvalue based statistical method from Peyrache et al<sup>198,275</sup>. Briefly, if two neurons have correlated firing, then we expect to observe common fluctuations in their spiking activity during recording. This can be visualized by plotting the firing rates of the two neurons against each other, in the form of a direction in neural activity space along which observations tend to be distributed.

Conversely, without any correlated firing, the variance in the dataset will be roughly equally distributed in all directions, and one would not expect to see structure when plotting the activity of two cells against each other. These relationships hold for any n-dimensional set of neurons, where structure emerges from correlated activity. The eigenvectors of the covariance matrix of a dataset represent the directions of maximally shared variance, thereby capturing the correlations present in the data. Each eigenvalue quantifies the variance of the data along the axis defined by its corresponding eigenvector. Thus, in a matrix of neurons-by-time, the eigenvalues of its covariance matrix capture the correlations among neurons (*i.e.*, ensembles) and comparing the eigenvalues to those computed from the covariance matrix of a shuffled version of the data provides a measure of the number of ensembles present.

To apply this method, we first binned spike counts at the same sampling rate as for clustering (0.667 Hz, bin size of 1.5 seconds) and Z-scored the activity of each neuron. Next, we shuffled the time bins for each neuron independently, and computed the maximal eigenvalue of the covariance matrix of the shuffled data. We repeated this 5,000 times to form a null distribution and counted the number of eigenvalues from the covariance matrix of the actual data that were above the 99<sup>th</sup> percentile of this null distribution.

#### Time-normalized grooming-related activity

To compare ensemble average activity during grooming across grooming bouts of varying duration, we linearly temporally rescaled the activity of each unit during each grooming bout to a single fixed length. We chose the length for the interpolated values from the distribution of grooming bout durations from all clustered sessions. To avoid ‘blurring’ activity associated with

the start and end of grooming bouts, the activity during the 5 seconds before and after each bout was not interpolated.

#### Bootstrap significance testing of grooming-related ensemble activity

To test for periods during grooming when the grooming ensemble average activity was significantly higher or lower than chance, we computed the mean, 2.5<sup>th</sup>, and 97.5<sup>th</sup> percentiles of the distribution of randomly sampled ensemble activity. To generate this distribution, we computed the population-average ensemble activity during 1,000 random duration windows of time sampled throughout the 2-hour recording session. Start times were sampled uniformly from 5 seconds into the recording session until 5 seconds before the end of the session. Window durations were sampled from the distribution of observed grooming bout durations across all sessions.

#### Neural trajectories

To visualize neural trajectories, neural activity during grooming was decomposed onto 3 components using non-negative matrix factorization<sup>336</sup>. For the neural trajectories, we decomposed a matrix containing each unit's activity during all grooming bouts within that session. For each unit, we concatenated its activity during all grooming bouts including the five seconds before and after each bout. For the ensemble trajectories, we averaged the activity of all units within each ensemble and concatenated each ensemble's activity during all grooming bouts including 5 seconds before and after each bout. We initialized using Nonnegative Double Singular Value Decomposition with zeros filled with the average neural activity and minimized the Frobenius norm of the loss.

## Statistical methods

All statistical tests were two-sided. Statistical significance was set to  $p = 0.05$ . Summary data in all figures are reported as mean  $\pm$  SEM.

## Software

All custom software was written in Python<sup>337</sup> unless stated otherwise. In addition to those mentioned elsewhere, we used the following Python packages: numpy<sup>338</sup>, scipy<sup>339</sup>, matplotlib<sup>340</sup>, scikit-learn<sup>341</sup>, and pandas<sup>342,343</sup>.

This research was supported in part through the computational resources and staff contributions provided for the Quest high performance computing facility at Northwestern University which is jointly supported by the Office of the Provost, the Office for Research, and Northwestern University Information Technology.

### **2.3.5 Additional details beyond published methods**

#### Frame rate of video capture

The frame rate of video recordings should be sufficiently high to adequately sample the behavior of interest. Paw movements during grooming can be as fast as 10 Hz. Our initial videos were recorded at 30 fps and as a result only had 2-3 frames captured during a given paw trajectory during one of these fast paw movements. Further, many of these fast paw movements are made from the snout to behind the ear where the paw gets occluded from a front facing camera. Thus, in the first

iteration of our video recordings, the low sampling rate together with occluded limbs resulted in poor tracking quality during our behavior of interest.

### Alignment of video and neural recordings

To facilitate alignment of video and neural recordings, both recordings were initiated by pressing a button that caused a TTL pulse to be sent to the electrophysiology acquisition box and a TTL pulse to be sent to all cameras. Initiating both recordings with the same trigger ensures that recordings start at the same time. However, if the sampling rate of either the video or neural recordings deviated, even slightly, from their specified sampling rate, then the recordings would go out of sync and downstream analyses of neural activity during a specific behavior could result in incorrect conclusions. For example, we recorded our videos at 125 Hz or 1 frame every 8 ms. To illustrate the sensitivity to misalignment, if 5% of frames took an extra 50  $\mu$ s so that there was 8 ms and 50  $\mu$ s between those frames and the one before them; then, by the end of a 2 hour recording session the video and neural recordings would be off by 2,250 ms or 67,500 neural samples. At 125 Hz we record 900,000 frames in 2 hours. 5% of frames recorded in 2 hours is 45,000 frames. With 50  $\mu$ s extra for each of the 45,000 frames we get a discrepancy of 2,250,000  $\mu$ s or 2,250 ms. Since we record neural data at 30 kHz or 30 samples per ms, a discrepancy of 2,250 ms would total 67,500 neural samples = 2,250 ms \* 30 samples / ms. To keep the video and neural recordings aligned throughout the entire session and be able to account for any deviations in either sampling rates, we used a hardware trigger to trigger each frame grab from each camera and then sent that trigger to the electrophysiology acquisition box as well. Thus, we

now have a timestamp in the neural recording system for each frame grab. The frame grab trigger is a square wave that alternates high and low for 4 ms each. The cameras are configured to grab a frame each time the wave goes high.

### Generating pose estimates in a practical amount of time

Across all experimental sessions we had 246 hours of video in each of our three cameras. Video recordings were saved in 6-minute video files and across all sessions and all cameras we had approximately 3,000 videos. Inference on each video took approximately 24 minutes on an NVIDIA A100 GPU. Thus, inference on all our videos was estimated to take approximately 1,200 GPU compute hours. To facilitate inference on all our videos in a reasonable amount of time we took advantage of the Quest computing facility at Northwestern University. Given the restrictions on Quest storage and job durations we ran two simultaneous compute jobs each running inference on 60 videos. We wrote a Python program to transfer videos to Quest using Globus<sup>344,345</sup>, monitor our jobs on Quest, submit new jobs after each ended, handle job failures, and transfer inferred poses back to our lab server using Globus.

### Pose estimation

Achieving reliable pose estimates for our videos was the most challenging component of this project. We spent a considerable amount of time labeling frames, exploring various model architectures, tuning hyperparameters, and choosing suitable pose estimation software packages.

The quality of pose estimates understandably varies with video quality. Luxem et al. present an overview of considerations for behavioral video analysis<sup>346</sup>. One factor that increased the amount of time it took for us to achieve adequate pose estimates was dealing with intricacies of existing pose estimation tools. Understandably, many researchers developing pose estimation tools publish their code primarily as proof of concept or have limited time to maintain their software. Initiatives such as the CZI's Essential Open Source Software for Science program provide support for researchers to maintain their projects. These initiatives will hopefully allow researchers to provide a more robust user experience improving overall scientific productivity for projects using advanced behavioral analytics.

## 2.4 Reviewer-requested analyses

To incorporate feedback from *eLife* reviewers—visible at <https://elifesciences.org/reviewed-preprints/87042/reviews>—we will complete the following analyses:

We will quantify the encoding of grooming start time, end time, and duration by striatal single units and ensembles. Additionally, we will determine whether the observed correlation between striatal activity and grooming is partially due to correlation with other aspects of movement.

One reviewer suggested that the striatum might actually be encoding grooming pose dynamics and not grooming boundaries. They proposed that our identification of changes in striatal activity at grooming transitions could result from averaging across grooming bouts with varying dynamics. To address this concern, we will group grooming bouts based on their pose dynamics and then re-run a subset of the analysis after accounting for variability in grooming dynamics.

Our data shown in **Figure 2.4A** suggests that ensembles probabilistically encode grooming since each ensemble is active during a subset of all grooming bouts. We will quantify the probability that a given ensemble is active during grooming. We will then attempt to determine whether we can predict whether a given ensemble will be active during a given grooming bout from aspects of grooming or other aspects of behavior (e.g., vigor, duration, or speed).

## **Chapter 3 – Attenuated dopamine signaling after aversive learning is restored by ketamine to rescue escape actions**

The work in this chapter was part of a collaboration with Mingzheng Wu, PhD. This work was published in:

Mingzheng Wu, Samuel Minkowicz, Vasin Dumrongprechachan, Pauline Hamilton, Yevgenia Kozorovitskiy. *eLife* 10 (2021): e64041. <https://doi.org/10.7554/eLife.64041>

### **Abstract**

Escaping aversive stimuli is essential for complex organisms, but prolonged exposure to stress leads to maladaptive learning. Stress alters neuronal activity and neuromodulatory signaling in distributed networks, modifying behavior. Here, we describe changes in dopaminergic neuron activity and signaling following aversive learning in a learned helplessness paradigm in mice. A single dose of ketamine suffices to restore escape behavior after aversive learning. Dopaminergic neuron activity in the ventral tegmental area (VTA) systematically varies across learning, correlating with future sensitivity to ketamine treatment. Ketamine's effects are blocked by chemogenetic inhibition of dopamine signaling. Rather than directly altering the activity of dopaminergic neurons, ketamine appears to rescue dopamine dynamics through actions in the medial prefrontal cortex (mPFC). Chemogenetic activation of Drd1 receptor positive mPFC neurons mimics ketamine's effects on behavior. Together, our data link neuromodulatory dynamics in mPFC-VTA circuits, aversive learning, and the effects of ketamine.

### 3.1 Introduction

Major depressive disorder (MDD) is a prevalent mental illness linked to diminished quality of life and increased mortality. Persistent changes in mood and emotional reactivity represent fundamental features of MDD, extensively investigated in human subjects<sup>347,348</sup>. Reduced reactivity to both positive and negative stimuli has been consistently observed in clinically depressed patients<sup>349,350</sup>, suggesting that MDD may involve systematic changes in the processing of reward and aversion. These changes in reward-based and aversive responses can be modeled in animals<sup>351–354</sup>. In animal models involving prolonged stress, the reactivity to positive valence (e.g., social stimuli) and negative valence (e.g., tail suspension) experiences is usually diminished<sup>355</sup>, suggesting that prolonged aversive experience induces maladaptive learning. One established model of aversive learning is learned helplessness (LH)<sup>356–358</sup>. Following prolonged inescapable stress exposure, animals learn that outcomes are independent of their behavioral actions; this learning eventually diminishes attempts to escape from avoidable stressful stimuli<sup>359</sup>. This form of aversive learning has been reproduced in humans and other animals, including rodents<sup>356,359,360</sup>. Reduced reactivity to aversive stimuli after LH is reversed by antidepressant treatments in animal models<sup>360–362</sup>. Several studies have implicated the involvement of neuromodulatory systems, including dopamine, norepinephrine, and serotonin in the acquisition of LH and its expression over time<sup>353,363–365</sup>.

Dopaminergic (DA) neurons in the ventral tegmental area (VTA) primarily encode reward and aversion, responding to both types of stimuli<sup>366–370</sup>. The activation of DA neurons is important in the development of aversive conditioning<sup>371</sup>, and the activity of DA neurons is differentially

modulated by acute and chronic stress<sup>372-374</sup>. Establishing a causal connection between DA neuron activity and depressive-like behavior, optogenetic activation of VTA DA neurons increases behavioral resilience to social defeat stress<sup>375</sup> and promotes active coping actions<sup>376</sup>. How VTA DA neurons adjust their activity during aversive learning and how these activity changes relate to reduced reactivity to aversive stimuli after learning remains unclear.

Widely used antidepressants, mostly targeting monoamine reuptake systems, are limited by delayed onset of efficacy, incomplete remission, and low remission rates<sup>377</sup>. Ketamine acts primarily as an antagonist at the glutamatergic N-methyl-D-aspartate (NMDA) receptors, showing rapid onset anti-depressant effects in depressed patients<sup>378,379</sup>. In addition, mechanisms beyond direct NMDAR antagonism likely participate in the rapid behavioral effects of ketamine, implicating other classes of glutamate receptors, neuromodulators, and emergent circuit-level dynamics<sup>380-385</sup>. Ketamine ameliorates depressive-like behaviors in animal models of acute and prolonged stress<sup>362,386-389</sup>, and rescues escape actions in response to aversive stimuli after LH induction<sup>361</sup>. A recently published meta-analysis suggests that acute sub-anesthetic doses of ketamine may increase DA levels in the cortex, dorsal striatum, and nucleus accumbens<sup>390</sup>. *In vivo* recordings from electrophysiologically identified VTA DA neurons in rats highlight ketamine's modulation of neuronal firing<sup>361</sup>. The medial prefrontal cortex (mPFC), essential for higher order cognitive functions including the control of emotional processing, is one key site for ketamine effects in the brain. Ketamine has been shown to modulate mPFC activity and plasticity to rescue depressive-like behaviors<sup>384,391-395</sup>. Given the bidirectional connectivity between VTA and mPFC<sup>396</sup>, ketamine may regulate VTA DA activity through actions in mPFC, proposed to potentiate the activity of pyramidal neurons rapidly through disinhibition by

suppressing inhibitory interneurons<sup>380,383,397</sup>. Despite some reported and suggested links between ketamine and DA systems, the causal relationship between the DA system and ketamine's effects on behavior remains to be elucidated.

Here, we use fiber photometry to record the responses of VTA DA neurons to aversive stimuli across different phases of learning in LH. By leveraging the tunability of LH induction parameters, we also design a modified, weaker LH paradigm to reveal the activity patterns of VTA DA neurons for distinct behavioral outcomes, correlating the activity signatures with future sensitivity to ketamine treatment. By using chemogenetic inhibition, we demonstrate that VTA DA activity and downstream signaling is necessary for the behavioral effects of ketamine. Finally, combining fiber photometry, anatomical tracing, and chemogenetics, we find that mPFC serves as an action site of ketamine to restore DA dynamics and escape actions.

## **3.2 Results and discussion**

### **3.2.1 VTA DA neuron activity during aversive learning**

To define the function of midbrain DA neurons during aversive learning, we used a variant of learned helplessness (LH)<sup>360</sup>. A shuttle box with two compartments connected by a door allows animals to escape from one side to the other when an electric foot shock is delivered to either compartment. Prior to LH induction, mice were exposed to 30 escapable shocks to test baseline escape behaviors. Initially, mice escape from electric foot shocks. However, following repeated exposure to inescapable foot shocks, mice reduce escapes from avoidable 10 second-long foot shocks (**Figure 3.1a, b**). Our data and prior publications<sup>361,398,399</sup> show that a single low dose of

racemic ketamine 4 hours prior to the test (10 mg/kg, b.w., i.p.) is sufficient to rescue escape behavior in this LH paradigm (**Figure 3.1b**). A separate group of mice that received saline instead of ketamine following the same experimental design did not decrease escape failures after LH (**Figure 3.1 Supplement 1a**). Thus, reduced failures to escape after ketamine treatment are not simply a function of time elapsed since LH induction (i.e. spontaneous fear extinction). Reduced escape behavior after LH induction, as well as its reversal by ketamine, are not strictly context-dependent, since the proportion of failures to escape was similar regardless of whether behavioral evaluation was carried out in the induction context or in a novel environment (**Figure 3.1 Supplement 1b**).

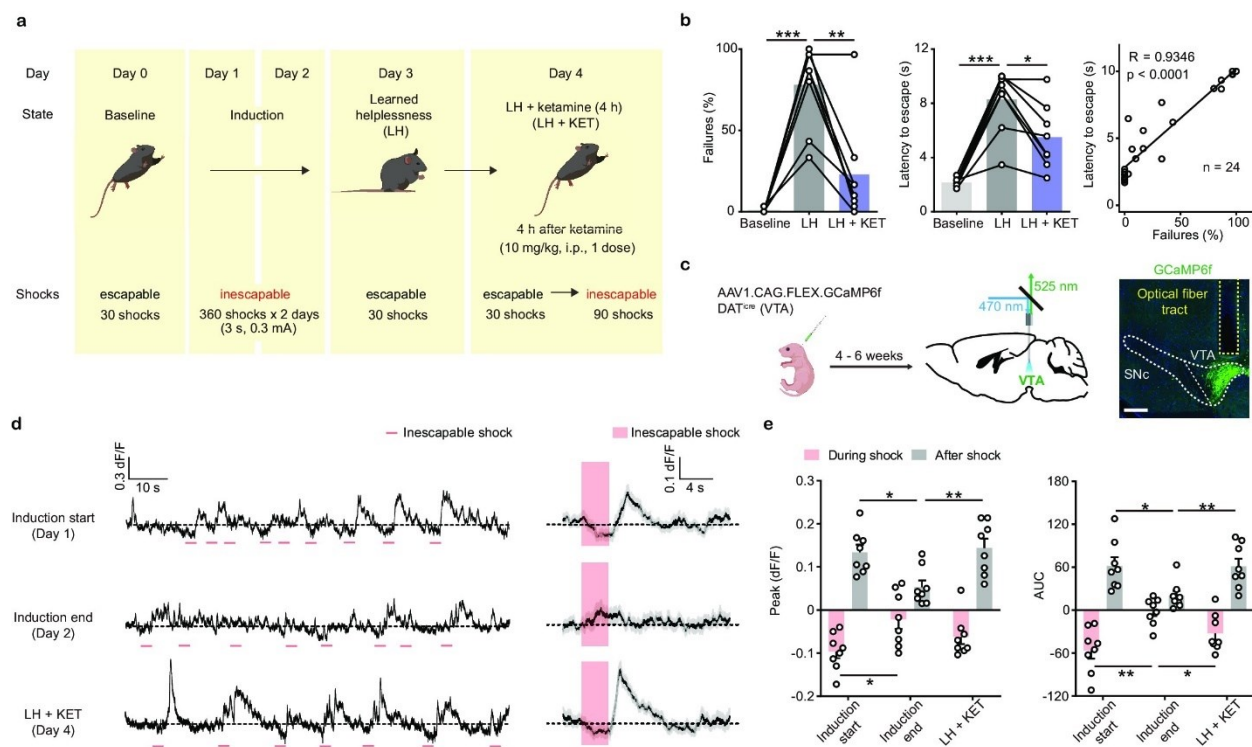


**Figure 3.1. Ketamine rescues escape behavior and dampened DA neuronal activity after aversive learning.** (a). Schematic illustrating the timeline of behavioral and pharmacological manipulations in the LH paradigm. (b). Left, summary data showing the percentage of failures to

escape an escapable aversive shock across phases of learning (Baseline, LH, and LH+ KET). Middle, same as left, but for latency to escape. Right, for all conditions, the correlation between percentage of failure to escape and escape latency (failure to escape trials scored as 10 sec latency).  $n = 24$  trials from eight mice. % Failures: repeated measures one-way ANOVA,  $F(1.89, 13.23) = 27.9$ ,  $p = 0.0001$ , Sidak's multiple comparison test, Baseline vs LH,  $p = 0.0001$ , LH vs LH+ KET,  $p = 0.0037$ . Latency to escape: repeated measure one-way ANOVA,  $F(1.96, 13.72) = 29.63$ ,  $p < 0.0001$ , Sidak's multiple comparison test, Baseline vs LH,  $p = 0.0003$ , LH vs LH+ KET,  $p = 0.0141$ . Pearson correlation:  $R = 0.9346$ ,  $p < 0.0001$ . **(c)**. Left, schematic for viral transduction in the VTA and subsequent fiber implant. Right, fiber placement verification. Green, GCaMP6f; blue, Hoechst nuclear stain. Scale bar: 500  $\mu\text{m}$ . **(d)**. Left, baseline adjusted raw traces of VTA DA neuron  $\text{Ca}^{2+}$  responses to inescapable foot shocks (3 s, pink) in one animal, at the start of induction, at the end of induction, and 4 hr following a single dose of ketamine (LH+ KET, 10 mg/kg i.p.). Right, average traces in the same subject aligned to shock start time (20 trials/condition, mean  $\pm$  SEM). **(e)**. Left, quantification of peak  $\text{Ca}^{2+}$  transient amplitude during and after foot-shock stimuli across conditions. Right, same but for area under the curve (AUC). Both positive and negative values are quantified.  $n = 8$  animals, repeated measures one-way ANOVA, Holm-Sidak's multiple comparison test, Peak: During shock,  $F(1.823, 12.76) = 5.387$ ,  $p = 0.0222$ , Induction start vs Induction end,  $p = 0.0458$ , Induction end vs LH + KET,  $p = 0.0788$ . After shock,  $F(1.693, 11.85) = 6.805$ ,  $p = 0.0132$ , Induction start vs Induction end,  $p = 0.0230$ , Induction end vs LH + KET,  $p = 0.0068$ . AUC: During shock,  $F(1.705, 11.94) = 8.942$ ,  $p = 0.0054$ , Induction start vs Induction end,  $p = 0.0058$ , Induction end vs LH + KET,  $p = 0.0258$ . After shock,  $F(1.437, 10.06) = 5.499$ ,  $p = 0.0318$ , Induction start vs Induction end,  $p = 0.0257$ , Induction end vs LH + KET,  $p = 0.0069$ . \* $p < 0.05$ , \*\* $p < 0.01$ , \*\*\* $p < 0.001$ . Error bars reflect SEM.

To understand the relationship between VTA DA neuron activity and ketamine's rescue of escape behavior, we used fiber photometry to monitor the activity of the genetically encoded calcium indicator GCaMP6f in VTA DA neurons. DAT<sup>icre</sup> neonates were virally transduced with Cre-dependent AAV1.CAG.FLEX.GCaMP6f. Four to six weeks after transduction, optical fibers were implanted in the VTA (**Figure 3.1c**), guided by real-time photometry (**Figure 3.1 Supplement 2a**). During fiber implant procedure, we observed that surgical anesthesia was associated with  $\sim 1$  Hz oscillations in VTA calcium transients (**Figure 3.1 Supplement 2b**). After mice recovered from surgery, we evaluated the activity of VTA DA neurons during

aversive learning in young adult mice (p40-60) of both sexes. We first recorded  $\text{Ca}^{2+}$  transients of VTA DA neurons in response to brief, inescapable foot shocks (3 sec, 0.3 mA) during the learning period and after ketamine treatment. At the start of learning (Induction start), the activity of VTA DA neurons first decreased during the aversive foot shocks and then rose after the termination of the shock (**Figure 3.1d, e**). This biphasic response is consistent with recently published observations of VTA DA activity during other forms of aversive conditioning<sup>371</sup>. Notably, the responses of VTA DA neurons to inescapable foot shocks were blunted at the end of the second-day induction (Induction end). A single low dose of racemic ketamine (10 mg/kg, b.w., i.p., LH+KET) largely restored the characteristic  $\text{Ca}^{2+}$  transient features, in parallel to the behavioral rescue (**Figure 3.1d, e; Figure 3.1 Supplement 2d, e**). Visualizing sequential  $\text{Ca}^{2+}$  traces from individual trials illustrates (1) the prevalence of after-shock peaks at the start of learning, (2) their decreased latency relative to shock onset during the second day of training, and (3) the recovery of  $\text{Ca}^{2+}$  transient latency to peak following ketamine administration (**Figure 3.1 Supplement 2f**). To quantify this temporal structure, we computed the latency to peak on sequential averaged trials ( $n = 10$  trials/avg) and plotted the data as a scatter plot and cumulative distribution (**Figure 3.1 Supplement 2g**). No significant transients were observed in GFP-expressing controls in this behavioral assay (**Figure 3.1 Supplement 2c**).

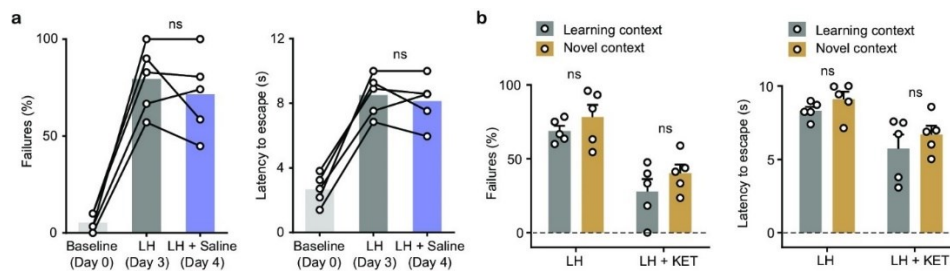


**Figure 3.1 Supplement 1. Characterization of behavior after learned helplessness. (a).** Left, summary data showing the percentage of failures to escape an escapable aversive shock across phases of learning (Baseline, LH, and LH+ Saline). Right, same as left, but for latency to escape.  $n = 5$  animals. One-way ANOVA, Sidak's multiple comparison test, LH vs LH+ KET, % Failures,  $p = 0.5299$ , latency to escape,  $p = 0.7027$ . **(b).** Left, summary data showing the percentage of failures to escape an escapable aversive shock in learning and novel contexts (LH, and LH+ KET). Right, same as left, but for latency to escape.  $n = 5$  animals. Two-way ANOVA, Sidak's multiple comparison test, learning vs novel contexts, % Failures, LH,  $p = 0.5669$ , LH+ KET,  $p = 0.3924$ . Latency to escape, LH,  $p = 0.6409$ , LH+ KET,  $p = 0.5089$ . LH vs LH+ KET, % Failures, learning context,  $p^{**} = 0.0013$ , novel context,  $p^{**} = 0.0023$ . Latency to escape, learning context,  $p^{*} = 0.0219$ , novel context,  $p^{*} = 0.0336$ .

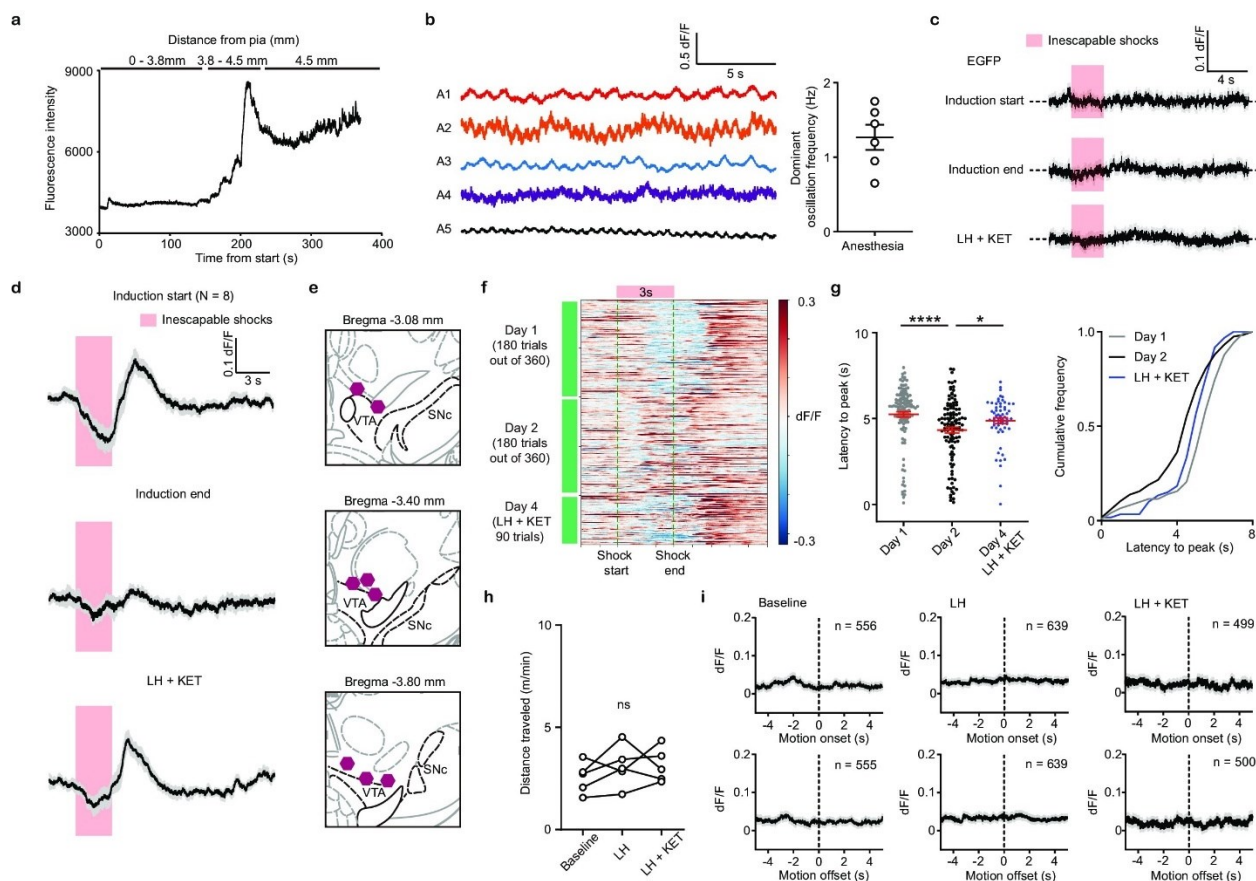


**Figure 3.1 Supplement 2. VTA DA neuron responses to anesthesia, foot shock, and motion transitions.** (a). Photometry-guided fiber implantation into the VTA. Recording began when the fiber traversed the pia. A gradual increase of fluorescence intensity was observed as the fiber tip approached GCaMP6f-expressing neurons, 3.8–4.5 mm from the pia, followed by a sharp signal increase and stabilization close to the VTA. (b). Oscillation of VTA DA  $\text{Ca}^{2+}$  transients under anesthesia. Approximately 1–2 Hz oscillations were observed in every animal. Summary data show the dominant oscillation frequencies. (c). Average neural activity-independent fluorescence transients illustrated for one EGFP-expressing animal in response to inescapable foot-shocks across learning phases. Traces are aligned to shock start time (20 trials/animal,  $n = 3$  animals). (d). Average  $\text{Ca}^{2+}$  transients (mean  $\pm$  SEM) in response to foot shocks for all animals across learning phases. Traces are aligned to shock start time (20 trials/animal, 8 animals). (e). Atlas locations showing fiber placements for data in **Figure 3.1e**. (f). Heatmap of single trial  $\text{Ca}^{2+}$  traces across learning in one mouse. Pink rectangle and green dashed lines mark the timing of shock stimuli. Colormap of  $dF/F$ , blue  $-0.3$ , red  $0.3$ , saturated for values outside this range for illustration purposes. (g). Left, latencies from shock onset to  $dF/F$  peak (averages of sequential bins of 10 traces) for subjects across learning days. Right, cumulative frequency distribution of latencies to peak.  $n = 8$  animals, one-way ANOVA,  $F(2, 258) = 9.387$ ,  $p = 0.0001$ . Sidak's multiple

comparison test, Day 1 vs Day 2,  $p = 0.0001$ , Day 2 vs LH+ KET,  $p = 0.0342$ . **(h)**. Open field locomotion (m/min) for  $n = 5$  mice across learning phases. Repeated measures one-way ANOVA,  $F(1.038, 4.153) = 1.479$ ,  $p = 0.2910$ . **(i)**. Average  $\text{Ca}^{2+}$  transients around motion onset and offset for mice in the Baseline, LH, and LH+ KET conditions. Dashed black line marks motion onset/offset. The number of onsets/offsets, as noted.  $n = 5$  animals. \* $p < 0.05$ , \*\*\*\* $p < 0.0001$ . Error bars reflect SEM.

Since the activity of DA neurons has been linked to movement<sup>400,401</sup>, one potential explanation for how aversive learning could modulate  $\text{Ca}^{2+}$  activity of VTA DA neurons involves altered locomotor behavior. While ketamine acutely changes locomotion, this effect normally occurs within tens of minutes following administration<sup>380</sup>, and resolves by the time clinically relevant changes in affective behavior are observed<sup>378,402</sup>. We found no differences in open field locomotion across phases of learning (**Figure 3.1 Supplement 2h**). Additionally, changes in VTA DA neuron activity were not associated with motion transitions, including onset and offset of locomotion (**Figure 3.1 Supplement 2i**). This result is not surprising, since movement transitions are typically associated with the activity of DA neurons in the Substantia Nigra pars Compacta rather than the VTA<sup>400,401</sup>. Together, our data demonstrate that VTA DA neuron activity is restructured by LH, which is rescued following ketamine treatment.

### **3.2.2 Outcome-specific VTA DA dynamics during weaker aversive learning and after ketamine treatment**

To better understand the relationship between VTA DA neuron activity and specific behavioral responses across phases of learning, we designed a weaker learning paradigm (wLH), which allowed us to compare  $\text{Ca}^{2+}$  transients across distinct behavioral outcomes, escapes versus failures. wLH includes a larger number of brief escapable foot shocks as the test stimuli (3 sec

long, 100 trials), with only a single day of LH induction with inescapable shocks (**Figure 3.2a**). As anticipated, a weaker form of LH, characterized by a lower average failure rate, was observed in this paradigm compared to stronger LH (sLH, as in **Figure 3.1**) (Two-way ANOVA for sLH and wLH across behavioral states, Sidak's multiple comparison, sLH 78% vs wLH 48%,  $p = 0.0022$ ). Again, escape behavior recovered after ketamine treatment, compared to saline-treated animals (**Figure 3.2b, right panel**). Another group of control animals underwent test sessions but no induction; they showed no changes in escape behavior over the time of the experiment (one-way ANOVA,  $p = 0.9882$ ).

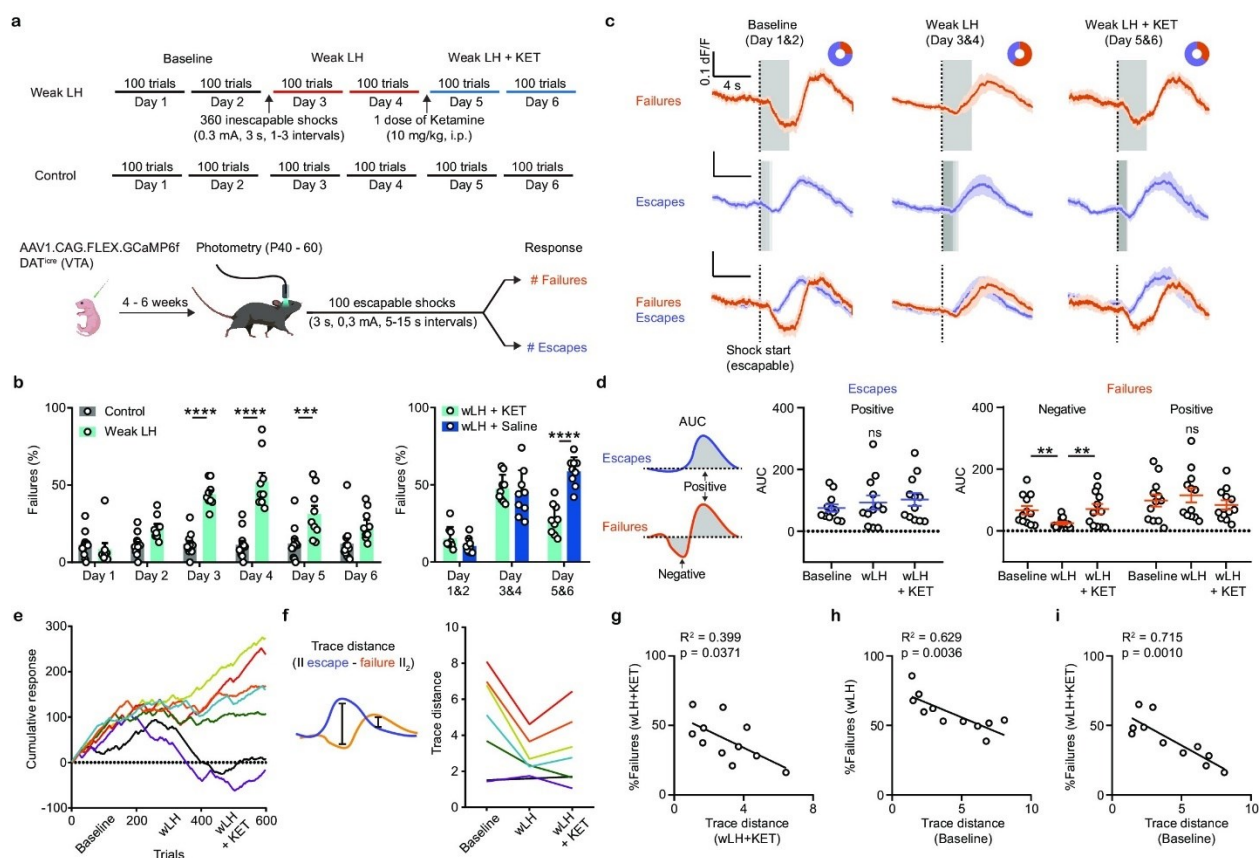


**Figure 3.2. Weak learning analysis links DA activity, behavioral outcomes, and response to ketamine.** (a). Top, schematic of experimental timeline for weak LH (wLH). Bottom, schematic of viral transduction, test trial description, and timing of photometry recording. (b). Left, summary

data showing the percentage of failures to escape an escapable aversive shock across 6 days for two groups (Gray bar, controls; Cyan, wLH). Right, summary of behavioral data for wLH mice with KET or Saline treatment. Left, responses across days, two-way ANOVA, Sidak's multiple comparison test, Control vs wLH, Day 1,  $p = 0.9934$ , Day 2,  $p = 0.1147$ , Days 3 and 4,  $p < 0.0001$ , Day 5,  $p = 0.0007$ , and D6,  $p = 0.0691$ . Control,  $n = 12$ ; wLH,  $n = 9$  animals. Right, two-way ANOVA, Sidak's multiple comparison test, wLH+ KET vs wLH+ Saline, Days 1 and 2,  $p = 0.6403$ , Days 3 and 4,  $p = 0.8715$ , Days 5 and 6,  $p < 0.0001$ .  $n = 9$  animals/group. **(c)**. Fiber photometry recordings of VTA DA  $Ca^{2+}$  transients, separated by behavioral response and aligned to shock start time (purple, escape; orange, failure; average dF/F across animals). Gray rectangles mark shock length in time, which is constant for failures to escape but variable for successful escapes and is shaded proportionally. Donut plots depict proportion of behavioral responses.  $n = 8$  animals, baseline: 1405 trials, 25% failure 75% escape; wLH: 1459 trials, 60% failure 40% escape; wLH+ KET: 1403 trials, 36% failure, 64% escape. **(d)**. Left, schematic illustration for measured variables. Middle, summary data for AUC of the positive  $Ca^{2+}$  transient peaks in escapes across learning phases. Right, same but AUC for both positive and negative peaks in failures, as shown in the schematic.  $n = 12$  animals, AUC (Escapes), positive peak, repeated measures one-way ANOVA,  $F(1.897, 20.87) = 1.881$ ,  $p = 0.1787$ . AUC (Failures), negative peak, repeated measures one-way ANOVA,  $F(1.852, 20.38) = 9.260$ ,  $p = 0.0017$ , Holm-Sidak's multiple comparison test, Baseline vs wLH,  $p = 0.0069$ , wLH vs wLH+ KET,  $p = 0.0069$ . Positive peak, repeated measures one-way ANOVA,  $F(1.540, 16.94) = 2.541$ ,  $p = 0.1181$ . **(e)**. Learning curves for individual animals.  $n = 7$  animals, 600 trials/animal. **(f)**. Left, schematic illustration for the measured variable, Euclidean norm of the difference between mean escape and failure-associated  $Ca^{2+}$  transients for each subject. Right, trace distances for each subject across learning phases with subject specific colors as in e. **(g)**. Correlation between trace distance and the percentage of failures in wLH+ KET.  $n = 11$  animals. **(h)**. Correlation between trace distance in the baseline condition and the percentage of failures in wLH.  $n = 11$  animals. **(i)**. Correlation between trace distance in the baseline condition and the percentage of failures in wLH+ KET.  $n = 11$  animals. \*\* $p < 0.01$ , \*\*\* $p < 0.001$ , \*\*\*\* $p < 0.0001$ . Error bars reflect SEM.

A three-state transition model depicts the probability of transitioning between behavioral responses, allowing us to compare patterns of response sequences across learning (**Figure 3.2 Supplement 1a**). In addition to escapes and failures, responses were labeled 'spontaneous' when the animal spontaneously ran to the other side of the chamber during the random length pretrial time. Baseline and post ketamine sequences of behavioral responses were more similar to each

other than either was to wLH. In addition to changing the average probabilities of pairs of responses, wLH also altered longer sequences of outcomes within animals, reflected in decreased probability and length of successive escapes, as well as increased successive failures. Ketamine treatment partially recovered the probability and length of successive escapes, while a more prominent effect was observed on decreasing successive failures back to baseline levels (**Figure 3.2 Supplement 1b**). Altogether, these analyses suggest that ketamine specifically restructures behavioral sequences that are altered by wLH learning.

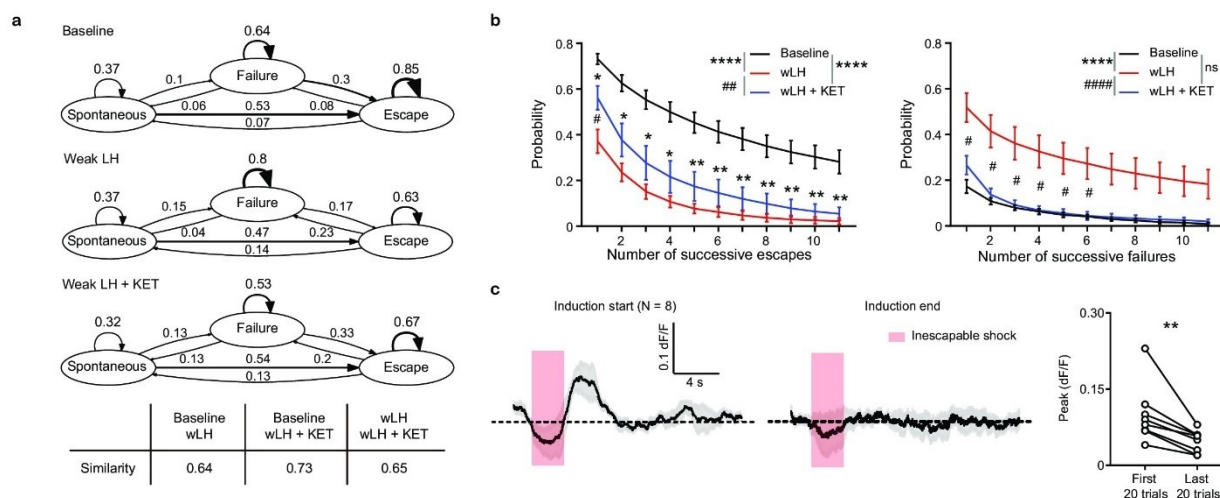


**Figure 3.2 Supplement 1. Characterization of behavioral sequences and dampened VTA DA activity in weak learned helplessness (wLH) paradigm. (a).** Graphs depicting transition probabilities between behavioral responses during baseline (top), wLH (middle), and wLH+ KET (bottom). Arrow sizes are proportional to transition probability, noted numerically. Table, Frobenius norms of differences between graphs for each graph pair.  $n = 7$  animals, 1400 trials/condition. **(b).** Summary data showing the probability of successive responses of different lengths (1-11) for escape (left) and failure (right) across learning states. Two-way ANOVA, Sidak's multiple comparison test. Escape main effect, Baseline vs wLH and Baseline vs wLH+ KET,  $p < 0.0001$ , wLH vs wLH+ KET,  $p = 0.0031$ . Failure main effect, Baseline vs wLH and wLH vs wLH+ KET,  $p < 0.0001$ , Baseline vs wLH+ KET,  $p = 0.3291$ . For comparison within specific length of responses, \* $p < 0.05$  \*\* $p < 0.01$  vs Baseline, # $p < 0.05$  vs wLH,  $n = 7$  animals. **(c).** Left, average  $\text{Ca}^{2+}$  transients in response to foot shocks during wLH induction (mean  $\pm$  SEM). Right, Peak (dF/F) vs First 20 trials and Last 20 trials. \*\* indicates significant difference.

Traces are aligned to shock start time (20 trials/animal, 8 animals). Right, quantification of peak  $\text{Ca}^{2+}$  transient amplitude of first and last 20 trials during induction. Two-tailed paired t-test,  $p = 0.009$ . \* $p < 0.05$ , \*\* $p < 0.01$ , \*\*\*\* $p < 0.0001$ . # $p < 0.05$ , ## $p < 0.01$ , ##### $p < 0.0001$ . Error bars reflect SEM.

The weaker LH paradigm, along with a large number of escapable foot shocks as the test stimuli, enabled broad sampling of  $\text{Ca}^{2+}$  transients during both escape and failure trials across conditions. Similar reductions in VTA DA responses to inescapable foot shocks were observed during wLH induction, as for strong LH (**Figure 3.2 Supplement 1c**). For escapable shocks, separately plotting VTA DA neuron activity for trials where the animal escaped or failed to escape revealed that each behavioral response is associated with distinct  $\text{Ca}^{2+}$  transient shapes (**Figure 3.2c**). Failure trial transients were biphasic, where fluorescence decreased during the shock and increased afterwards. In contrast, monophasic transients accompanied escape trials, with an increase in fluorescence following successful transitions to the other side of the box. After learning, an increase in the similarity of the activity patterns between escape and failure trials was observed (**Figure 3.2c, d**). For successful escape responses, VTA DA  $\text{Ca}^{2+}$  transients did not change in wLH and wLH + ketamine. The increased similarity of  $\text{Ca}^{2+}$  transients between outcomes after learning was explained by the reduction in negative transients associated with failures. These failure-linked negative transients recovered following ketamine treatment (**Figure 3.2d**). The timing of peaks in failure outcomes varied across conditions (**Figure 3.2 Supplement 2a, b**). Outcome-specific GCaMP6f transients, for either successful escapes or failures, did not vary across days in control mice without wLH induction, suggesting that the exposure to inescapable shocks is necessary to shape the responses of VTA DA neurons (**Figure 3.2**

**Supplement 3a, b).** In a separate control group, saline treatment did not change DA transients in either escape or failure trials after wLH (**Figure 3.2 Supplement 4a, b**).

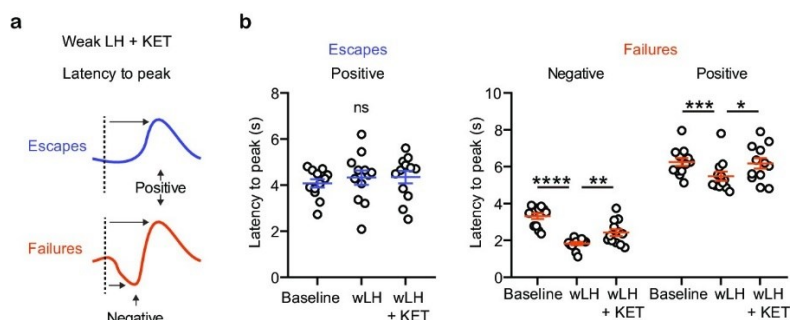


**Figure 3.2 Supplement 2. Outcome-specific VTA DA responses in wLH paradigm. (a).** Schematic illustration for the measured variables. **(b).** Left, summary data for latency to peak of the positive Ca<sup>2+</sup> transient peaks in escapes across learning phases. Right, same but for both positive and negative peaks in failures, as shown in the schematic.  $n = 12$  animals, Escapes, positive peak, repeated measures one-way ANOVA,  $F(1.902, 20.92) = 0.622$ ,  $p = 0.5388$ . Failures, negative peak, repeated measures one-way ANOVA,  $F(1.784, 19.62) = 36.23$ ,  $p < 0.0001$ , Holm-Sidak's multiple comparison test, Baseline vs wLH,  $p < 0.0001$ , wLH vs wLH+ KET,  $p = 0.0025$ . Positive peak, repeated measures one-way ANOVA,  $F(1.301, 14.31) = 5.369$ ,  $p = 0.0286$ , Holm-Sidak's multiple comparison test, Baseline vs wLH,  $p = 0.0003$ , wLH vs wLH+ KET,  $p = 0.0446$ . \* $p < 0.05$ , \*\*  $p < 0.01$ , \*\*\*  $p < 0.001$ . Error bars reflect SEM.

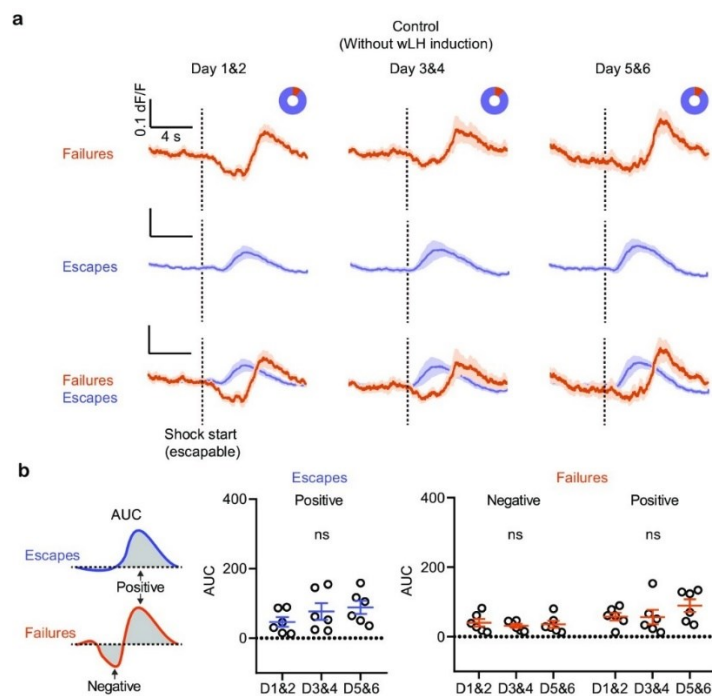


**Figure 3.2 Supplement 3. Outcome-specific VTA DA responses in control mice without wLH induction. (a).** Fiber photometry recordings of VTA DA  $Ca^{2+}$  transients, separated by behavioral response and aligned to shock start time (purple, escape; orange, failure; average  $dF/F$  across animals). Donut plots depict proportion of behavioral responses.  $n = 6$  animals, Days 1 and 2: 11 % failure, 89% escape; Days 3 and 4: 12% failure, 88% escape; Days 5 and 6: 12% failure, 88% escape. **(b).** Left, schematic illustration for measured variables. Middle, summary data for AUC of the positive  $Ca^{2+}$  transient peaks in escapes across learning phases. Right, same but AUC for both positive and negative peaks in failures, as shown in the schematic.  $n = 6$  animals, AUC (Escapes), positive peak, repeated measures one-way ANOVA,  $F(1.617, 8.084) = 2.103$ ,  $p = 0.1858$ . AUC (Failures), negative peak, repeated measures one-way ANOVA,  $F(1.422, 7.112) = 0.2283$ ,  $p = 0.7291$ , Positive peak, repeated measures one-way ANOVA,  $F(1.584, 8.918) = 1.191$ ,  $p = 0.3391$ .

In humans and other animals, individual variability in stress susceptibility and in responsiveness to neuroactive compounds is broadly acknowledged<sup>403</sup>. To visualize behavioral trajectories, learning curves were constructed by starting at 0 and incrementing by 1 for every escape trial, decrementing by 1 for every failure, and keeping constant for spontaneous transitions (**Figure 3.2e**). These learning curves highlight individual variability in learning and ketamine

responsiveness. To depict the relationship between an animal's ketamine responsiveness and VTA DA activity, we plotted the Euclidean norm of the difference between their  $\text{Ca}^{2+}$  transients during escape and failure trials ( $\|\text{escape-failure}\|_2$ ) across learning (**Figure 3.2f**, **Figure 3.2 Supplement 5a, b**). We selected this trace distance metric because it is agnostic to amplitude and kinetics of the response, specifically assaying the degree to which the activity of VTA DA neurons differentiates specific trial outcomes. **Figure 3.2g** shows a correlation between behavioral response (% failures) and trace distance following ketamine. Stronger ketamine behavioral effects were linked to more distinct  $\text{Ca}^{2+}$  transients when comparing escape and failure trials ( $R^2 = 0.399$ ). Animals characterized by a larger trace distance in the baseline were more resilient to inescapable stress during LH illustrated by fewer failures to escape after wLH (**Figure 3.2h**,  $R^2 = 0.629$ ). Intriguingly, individuals with larger differences between DA GCaMP signals on escape and failure trials in the baseline showed stronger responses to future ketamine treatment (**Figure 3.2i**,  $R^2 = 0.715$ ).

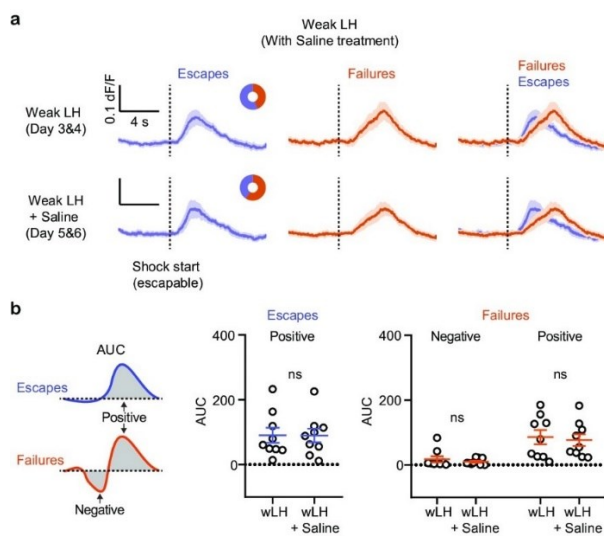


**Figure 3.2 Supplement 4. Outcome-specific VTA DA responses in wLH mice with saline treatment. (a).** Fiber photometry recordings of VTA DA  $\text{Ca}^{2+}$  transients, separated by behavioral

response and aligned to shock start time (purple, escape; orange, failure; average dF/F across animals). Donut plots depict proportion of behavioral responses.  $n = 9$  animals, wLH: 44% failure, 56% escape; wLH+ Saline: 59% failure, 41% escape. **(b)**. Left, schematic illustration for measured variables. Middle, summary data for AUC of the positive  $\text{Ca}^{2+}$  transient peaks in escapes across learning phases. Right, same but AUC for both positive and negative peaks in failures, as shown in the schematic.  $n = 9$  animals, AUC (Escapes), positive peak, two-tailed paired t-test,  $p = 0.9420$ . AUC (Failures), negative peak, two-tailed paired t-test,  $p = 0.3578$ , Positive peak, two-tailed paired t-test,  $p = 0.3988$ .

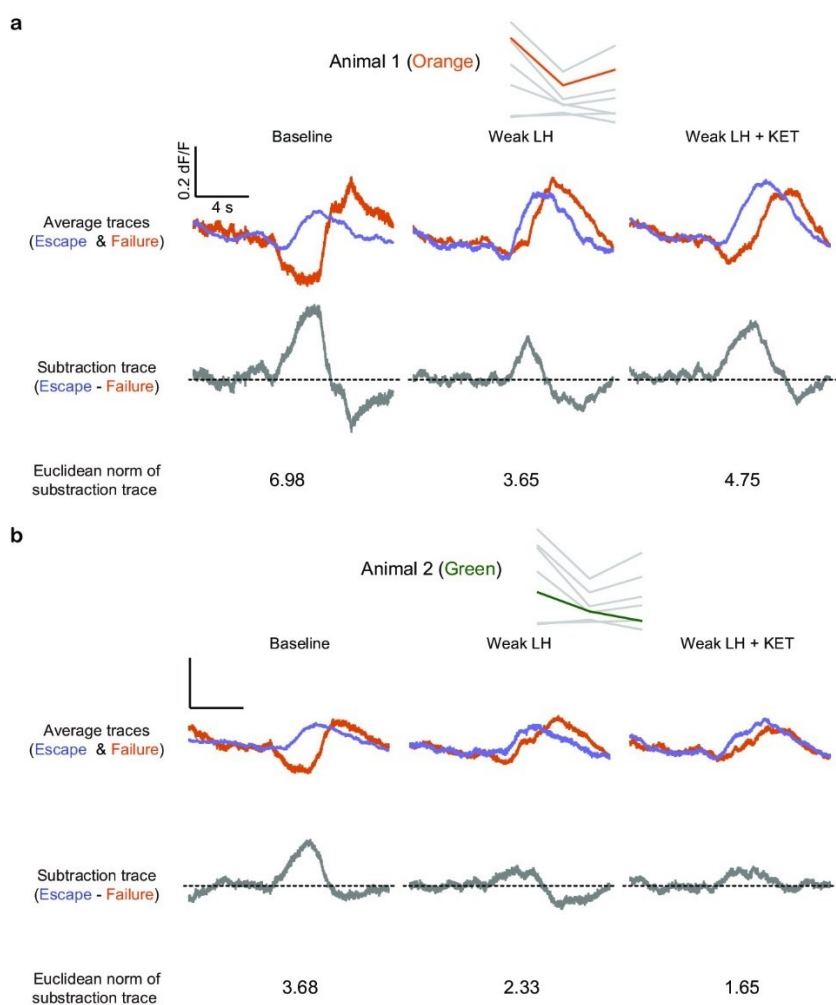


**Figure 3.2 Supplement 5. Trace distance of GCaMP transients between escape and failure trials. (a–b).** Example trace distance calculation for two animals. Top row, individual animals marked on the trace distance graph from **Figure 3.2f**. Second row, average traces of escapes and

failures across learning states. Third row, difference between the average escape and failure traces. Bottom row, Euclidean norm of subtraction traces.

### 3.2.3 DA neuron activity is necessary for behavioral effects of ketamine after LH

The association between DA transients, behavioral states, and trial outcomes raises the possibility that particular signatures of DA signals in response to aversive stimuli are required for escape actions. To test whether VTA DA activity is required for escape actions in general, or alternatively, whether it becomes important for restoring escapes after LH, we conditionally expressed an inhibitory DREADD (designer receptor exclusively activated by designer drug) hM4Di in VTA DA neurons. This engineered muscarinic receptor is activated by clozapine-N-oxide (CNO) to drive  $G\alpha_i$ -coupled pathways<sup>404-407</sup>. We used a CBA promoter driven Cre-conditional hM4Di AAV, with expression in VTA DA neurons confirmed by immunofluorescence (**Figure 3.3a**). Efficacy was evaluated using cell-attached recordings of hM4Di-mCherry<sup>+</sup> VTA DA neurons, with a flow in and a washout of 1  $\mu$ M CNO (**Figure 3.3b**).

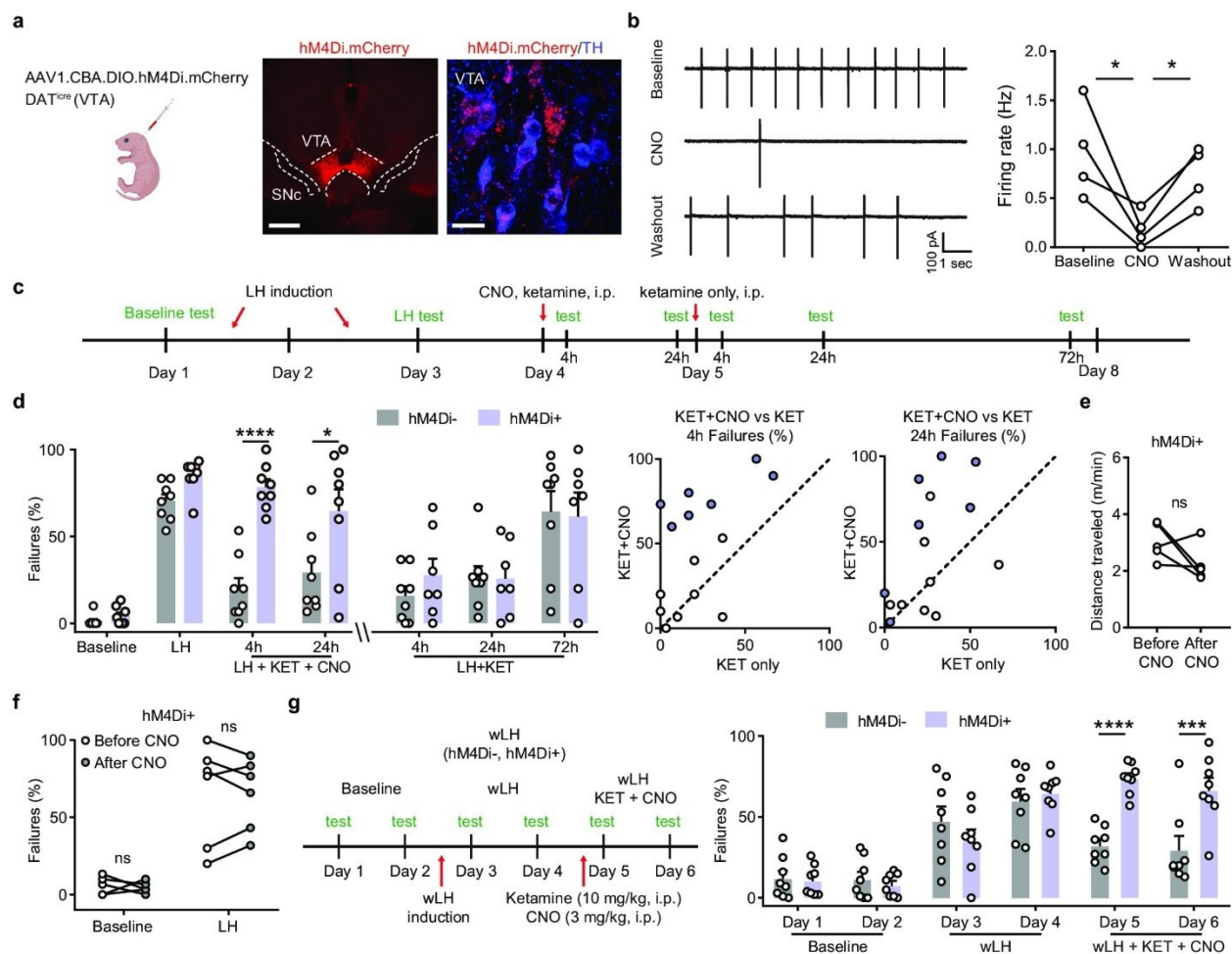


**Figure 3.3. Ketamine behavioral effects in aversive learning require VTA DA activity. (a).** Schematic for viral transduction in the VTA and hM4Di expression in VTA DA neurons (red, hM4Di.mCherry; blue, tyrosine hydroxylase (TH) immunofluorescence). Scale bars, 500  $\mu$ m and 20  $\mu$ m. **(b).** Cell-attached recording of spontaneous activity in mCherry<sup>+</sup> VTA neuron before, during, and after bath application of 1  $\mu$ M clozapine-N-oxide (CNO). Example traces (left) and summary data (right).  $n = 4$  cells from three mice, repeated measures one-way ANOVA,  $F(2, 6) = 9.634$ ,  $p = 0.0134$ , Sidak's multiple comparison test, Baseline vs CNO,  $p = 0.0104$ , CNO vs Washout,  $p = 0.0488$ . **(c).** Schematic of experimental timeline and pharmacological interventions in strong LH paradigm. **(d).** Left, summary data showing the percentage of failures to escape an escapable aversive shock across learning and treatment conditions for hM4Di AAV expressing DATiCre-positive and negative littermates. Middle, within subject summary data for behavioral responses after ketamine treatment only, compared with ketamine<sup>+</sup> CNO, 4 hr after treatment. Right, same but for 24 hr after treatment. Two-way ANOVA, Sidak's multiple comparison test, KET + CNO 4 hrs,  $p < 0.0001$ , KET + CNO 24 hr,  $p = 0.0107$ , KET only, following 4, 24, and 72

hr,  $p > 0.9$ ,  $n = 7-8$  animals. **(e)**. Total distance traveled per minute in an open field locomotion assay for hM4Di<sup>+</sup> animals before and after CNO treatment. Two-tailed paired t-test,  $p = 0.1473$ ,  $n = 5$  animals. **(f)**. Summary data showing the percentage of failures to escape an escapable aversive shock in the baseline condition, for hM4Di-expressing mice before and after CNO treatment.  $n = 5-6$  animals, Two-way ANOVA, Sidak's multiple comparison test, Baseline,  $p = 0.9538$ , LH,  $p = 0.9947$ . **(g)**. Left, schematic of experimental timeline and pharmacological interventions in weak LH paradigm. Right, summary data showing the percentage of failures to escape an escapable aversive shock across 6 days for two groups (white bar, hM4Di<sup>-</sup> controls; purple, hM4Di<sup>+</sup>). Two-way ANOVA, Sidak's multiple comparison test, hM4Di<sup>+</sup> vs hM4Di<sup>-</sup>, D1-D4,  $p > 0.5$ , D5,  $p < 0.0001$ , D6,  $p = 0.0001$ ,  $n = 8$  animals. \* $p < 0.05$ , \*\*\* $p < 0.001$ , \*\*\*\* $p < 0.0001$ . Error bars reflect SEM.

Mice conditionally expressing hM4Di in VTA DA neurons were compared to their Cre<sup>-</sup> littermate controls in the strong LH paradigm. Here, two ketamine treatments were administered on sequential days – the first one along with CNO, and the second one without (**Figure 3.3c**).

The expression of hM4Di in DA neurons did not change baseline behavior or learned helplessness induction (**Figure 3.3d**). However, inhibiting DA neurons by CNO application (3 mg/kg, b.w., i.p.) co-administered with ketamine (10 mg/kg, b.w., i.p.) blocked ketamine's rescue of escape behaviors. This effect was evident 4 hrs after CNO/Ketamine treatment and persisted at 24 hrs. Yet, when ketamine was administered alone on the following day, the behavioral rescue in hM4Di<sup>+</sup> mice was successful. Persistent LH was evident in multiple animals of both groups 72 hrs following the ketamine only treatment (last two bars, **Figure 3.3d**).

Comparing behavioral responses following ketamine alone versus ketamine plus CNO, within animals at two separate time-points, showed that the responses of hM4Di<sup>-</sup> animals lie around the unity line (**Figure 3.3d**). In contrast, hM4Di<sup>+</sup> responses were above the unity line, reflecting selective efficacy of ketamine treatment in the absence of CNO. Locomotor behavior in hM4Di-

expressing animals was not grossly altered by a single CNO administration, suggesting that the observed changes in escape actions are not due to reduced movement (**Figure 3.3e**).

Although chemogenetic inhibition of DA activity blocked the behavioral effect of ketamine after aversive learning, the administration of CNO in the absence of ketamine in separate groups of hM4Di<sup>+</sup> mice did not alter the proportion of failures to escape in the baseline condition or after sLH (**Figure 3.3f**). These data support the alternative hypothesis that the effect of ketamine after LH specifically requires the associated restoration of DA signals. Although VTA DA activity varies with behavioral outcomes before LH, innate escape actions may not fundamentally require DA activity. In addition, CNO co-administration blocked the behavioral effects of ketamine in the relatively weaker learning paradigm, as expected (wLH, **Figure 3.3g**). These data support the necessity of VTA DA signaling for the behavioral reversal of aversive learning by ketamine, rather than for native escape responses in naïve animals.

### **3.2.4 Ex vivo local effects of ketamine on VTA DA neurons**

In the next series of experiments, we sought to address the mechanisms underlying ketamine modulation of VTA DA activity and escape actions. *In vivo* ketamine treatment may modulate DA neuronal activity in a cell-autonomous manner locally in the VTA, or alternatively, indirectly, through effects on brain regions interconnected with the VTA. To determine whether ketamine application changes VTA DA GCaMP activity locally, we performed 2-photon calcium imaging of VTA DA neurons with and without *ex vivo* ketamine application. DAT<sup>icre</sup> neonates were transduced with AAV1.CAG.FLEX.GCaMP6f, and acute brain slices of VTA were

prepared and imaged 4-6 weeks after viral transduction (**Figure 3.4a, b**). We observed spontaneous  $\text{Ca}^{2+}$  oscillations of DA neurons *ex vivo* (**Figure 3.4c**), which have been shown to match action potentials in previous reports<sup>408</sup>. Further, bath application of ketamine (50  $\mu\text{M}$ ) in acute VTA brain slices did not alter the power or frequency tuning of spontaneous  $\text{Ca}^{2+}$  dynamics in DA neurons (**Figure 3.4c-f**), suggesting that the effect of *in vivo* ketamine treatment on VTA DA  $\text{Ca}^{2+}$  dynamics is not likely to be caused by direct cell-autonomous regulation. To reveal whether *ex vivo* ketamine application regulates VTA DA firing or spontaneous synaptic inputs, we also carried out cell-attached and whole-cell voltage clamp recordings from genetically targeted VTA DA neurons.  $\text{DAT}^{\text{icre}}$  neonates were transduced with AAV1.FLEX.EGFP, and EGFP-expressing cells were recorded in acute brain slices from the VTA (**Figure 3.4g**). Consistent with imaging results, *ex vivo* application of ketamine did not change spontaneous firing rate of VTA DA cells (**Figure 3.4h, i**), or the amplitudes and inter-event intervals of spontaneous EPSCs and IPSCs (**Figure 3.4j-o**). Altogether, our data suggest the *in vivo* effects of ketamine on DA activity and behavior are not likely caused by local regulation in the VTA.

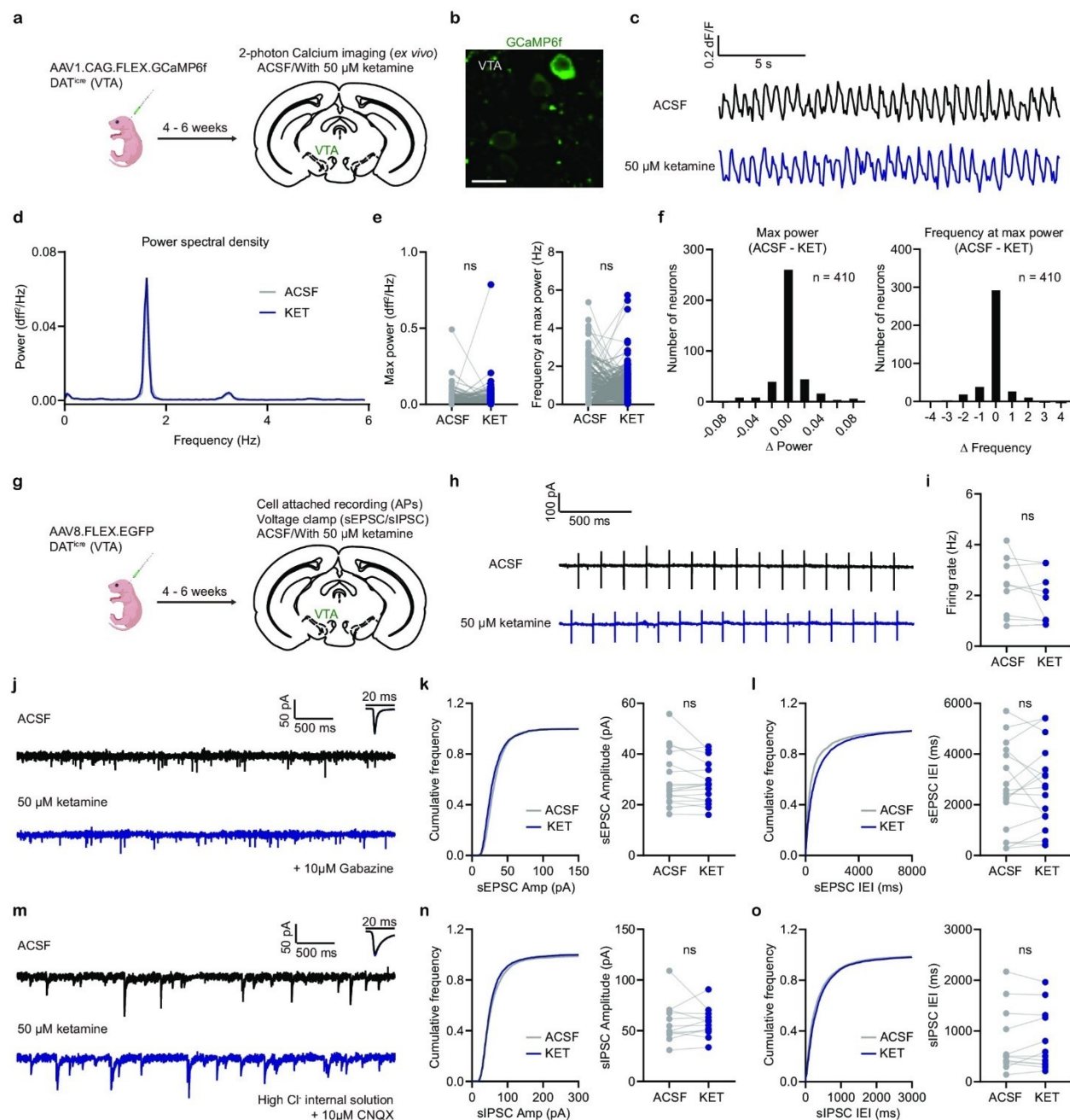


**Figure 3.4. Ex vivo ketamine application does not alter GCaMP6f transients, neuronal firing, and synaptic inputs of VTA DA neurons.** (a). Schematic illustrating viral transduction strategy and two-photon  $\text{Ca}^{2+}$  imaging of VTA DA neurons in acute brain slices. (b). Example 2PLSM image of VTA DA neurons expressing GCaMP6f. Scale bar, 20  $\mu\text{m}$ . (c). Spontaneous  $\text{Ca}^{2+}$  oscillations in one neuron with and without ketamine bath application (50  $\mu\text{M}$ ). Black, ACSF; blue, with ketamine. (d). Power spectral density of  $\text{Ca}^{2+}$  transients for the neuron in (c). (e). Left,

quantification of max power with and without ketamine treatment ( $n = 410$  neurons). Right, quantification of frequency at max power. Paired two-tailed t test, ACSF vs KET, Max power,  $p = 0.8865$ , Frequency at max power,  $p = 0.3779$ . **(f)**. Left, histogram showing the distribution of changes in max power with ketamine application. Right, same but for frequency at max power.  $n = 410$  neurons. **(g)**. Schematic illustrating viral transduction strategy and electrophysiological recording of VTA DA neurons in acute brain slices. **(h)**. Spontaneous action potentials recorded in one neuron with and without ketamine bath application ( $50 \mu\text{M}$ ). Black, ACSF; blue, with ketamine. **(i)**. Quantification of neuronal firing rate with and without ketamine treatment ( $n = 9$  neurons from three animals). Paired two-tailed t test, ACSF vs KET,  $p = 0.2561$ . **(j)**. Spontaneous EPSCs recorded in one neuron with and without ketamine bath application ( $50 \mu\text{M}$ ). Black, ACSF; blue, with ketamine. Holding membrane potential at  $-70 \text{ mV}$ ,  $10 \mu\text{M}$  Gabazine in ACSF for both conditions. **(k)**. Left, cumulative frequency distribution of sEPSCs amplitudes. Right, quantification of sEPSC amplitude in recorded neurons. Paired two-tailed t test, ACSF vs KET,  $p = 0.1958$ .  $n = 17$  neurons from three animals. **(l)**. Same as **(k)**, but for sEPSCs inter-event intervals (IEI). Paired two-tailed t test, ACSF vs KET,  $p = 0.8413$ . **(m)**. Spontaneous IPSCs recorded in one neuron with and without ketamine bath application ( $50 \mu\text{M}$ ). Black, ACSF; blue, with ketamine. Holding membrane potential at  $-70 \text{ mV}$  with high chloride internal solution,  $10 \mu\text{M}$  CNQX in ACSF for both conditions. **(n)**. Left, cumulative frequency distribution of sIPSCs amplitudes. Right, quantification of sIPSC amplitude in recorded neurons. Paired two-tailed t test, ACSF vs KET,  $p = 0.9164$ .  $n = 12$  neurons from two animals. **(o)**. Same as **(n)**, but for sIPSCs inter-event intervals (IEI). Paired two-tailed t test, ACSF vs KET,  $p = 0.5675$ .

### 3.2.5 Local mPFC ketamine infusion rescues VTA $\text{Ca}^{2+}$ transients and escape actions after LH

The absence of local modulation of DA neuron activity by ketamine supports the possibility of circuit-level mechanisms. In addition to spontaneous tonic activity, VTA DA neurons are driven by multiple sources of glutamatergic excitation, including inputs from mPFC, PPTg, and PAG, among others<sup>367</sup>. To explore whether ketamine acts through one or more among core glutamatergic VTA inputs to rescue escape actions, we locally infused ketamine into three different brain regions (mPFC, PAG, and PPTg), along with the VTA itself, in separate experiments (**Figure 3.5a**). Local infusion of ketamine into mPFC alone sufficed to rescue

escape behavior after LH (**Figure 3.5b**, **Figure 3.5 Supplement 1a**). In contrast, ketamine infusion into the periaqueductal gray (PAG) and the pedunclopontine tegmental nucleus (PPTg) did not rescue escape actions. Local VTA infusion of ketamine also failed to rescue escape behavior after LH, further supporting the idea that the *in vivo* effects of ketamine on behavior are not implemented through local regulatory mechanisms in the VTA (**Figure 3.5b**).

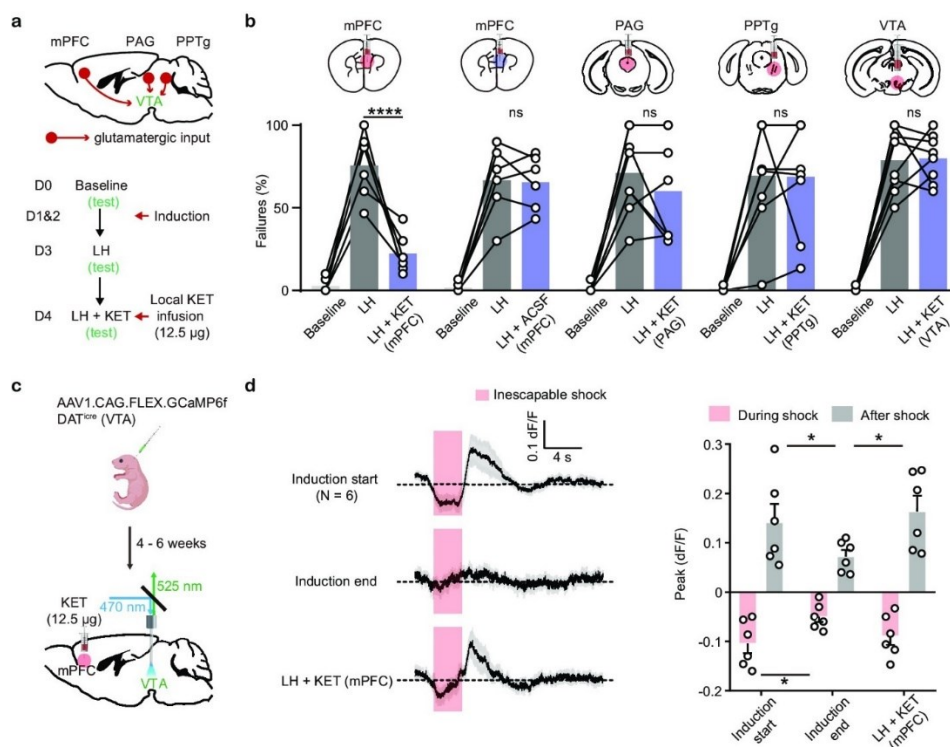


**Figure 3.5. Local ketamine infusion in mPFC rescues escape behavior and VTA DA activity after LH.** (a). Top, schematic for selected glutamatergic input regions to VTA. Bottom, experimental timeline. (b). Summary data showing the percentage of failures after local infusion of ketamine or ACSF in mPFC, and ketamine in PAG, PPTg, and VTA. Two-way ANOVA, Sidak's multiple comparison test, LH vs LH+ KET, mPFC,  $p < 0.0001$ , PAG,  $p = 0.4965$ , PPTg,  $p = 0.9998$ , VTA,  $p = 0.9986$ . LH vs LH+ ACSF (mPFC),  $p = 0.9993$ . (c). Schematic for viral transduction and VTA photometry recording of Ca<sup>2+</sup> transients with local ketamine delivery in mPFC. (d). Left, average Ca<sup>2+</sup> transients (mean ± SEM) in response to foot shocks at the start of induction, at the end of induction, and following local ketamine infusion. Traces are aligned to shock start time (20 trials/animal, 6 animals). Right, quantification of peak Ca<sup>2+</sup> transient

amplitude during and after foot shock stimuli across conditions. Both positive and negative values are quantified.  $n = 6$  animals, repeated measures one-way ANOVA, Holm-Sidak's multiple comparison test, Peak: During shock,  $F(1.948, 9.739) = 5.547$ ,  $p = 0.0252$ , Induction start vs Induction end  $p = 0.0433$ , Induction end vs LH + KET,  $p = 0.0823$ . After shock,  $F(1.468, 7.341) = 10.05$ ,  $p = 0.0105$ , Induction start vs Induction end,  $p = 0.0462$ , Induction end vs LH + KET,  $p = 0.0147$ . \* $p < 0.05$ , \*\*\*  $p < 0.001$ , \*\*\*\*  $p < 0.0001$ . Error bars reflect SEM.

To test whether local ketamine effects in mPFC rescue VTA DA dynamics after aversive learning in parallel to the behavioral changes, we infused ketamine locally into mPFC (12.5  $\mu\text{g}$ , 500 nl), with fiber photometry as a readout of VTA activity (**Figure 3.5c**). *In vivo* local infusion of ketamine into mPFC sufficed to recover  $\text{Ca}^{2+}$  activity signatures in VTA DA neurons after aversive learning, along with behavioral rescue (**Figure 3.5d**), while infusion of ACSF did not recover VTA DA activity (**Figure 3.5 Supplement 1b, c**). These data support the idea that ketamine rescues VTA DA dynamics through circuit-level effects involving mPFC.

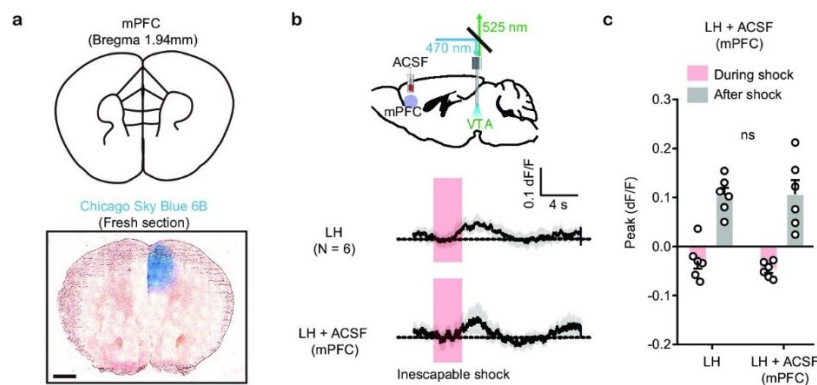


**Figure 3.5 Supplement 1. VTA DA activity after local ACSF infusion in mPFC. (a).** Atlas location and dye infusion in mPFC. Blue: Chicago Sky Blue 6B. Scale bar: 500  $\mu\text{m}$ . **(b).** Top, schematic for VTA photometry recording of  $\text{Ca}^{2+}$  transients with local ACSF delivery in mPFC. Bottom, average  $\text{Ca}^{2+}$  transients (mean  $\pm$  SEM) in response to foot shocks in LH mice before and after local ACSF infusion. Traces are aligned to shock start time (20 trials/animal, 6 animals). **(c).** Quantification of peak  $\text{Ca}^{2+}$  transient amplitude during and after foot shock stimuli across

conditions. Both positive and negative values are quantified.  $n = 6$  animals, two-tailed paired  $t$ -test, Peak: During shock,  $p = 0.3615$ ; After shock,  $p = 0.9509$ .

### **3.2.6 mPFC Drd1<sup>+</sup> neurons mediate behavioral effects of ketamine**

Next, in order to define the mPFC cell populations that project to the VTA, we combined retrograde tracing with fluorescence in situ hybridization (FISH). We injected red retrograde tracer fluorescent beads (retrobeads, RTB) into the VTA (**Figure 3.6a**) and observed red RTB fluorescence in mPFC 7-9 days after injection (**Figure 3.6b**). Results from FISH experiments demonstrate that the majority of RTB<sup>+</sup> neurons in deep layers (layers 5/6) of mPFC express Drd1a mRNA. In contrast, only a small fraction of the retrobead<sup>+</sup> neurons in layers 2/3 of mPFC have Drd1a mRNA (**Figure 3.6b, c**). To determine whether the deep layer Drd1<sup>+</sup> population in mPFC projects to the VTA, we expressed AAV8.FLEX.EGFP in Drd1Cre(FK150) animals and found that VTA neurons reside within fields of dense projections from mPFC Drd1<sup>+</sup> neurons (**Figure 3.6d**). These anatomical tracing results are consistent with previous reports showing that VTA-targeting mPFC neurons may also receive VTA DA inputs<sup>367,396</sup>.

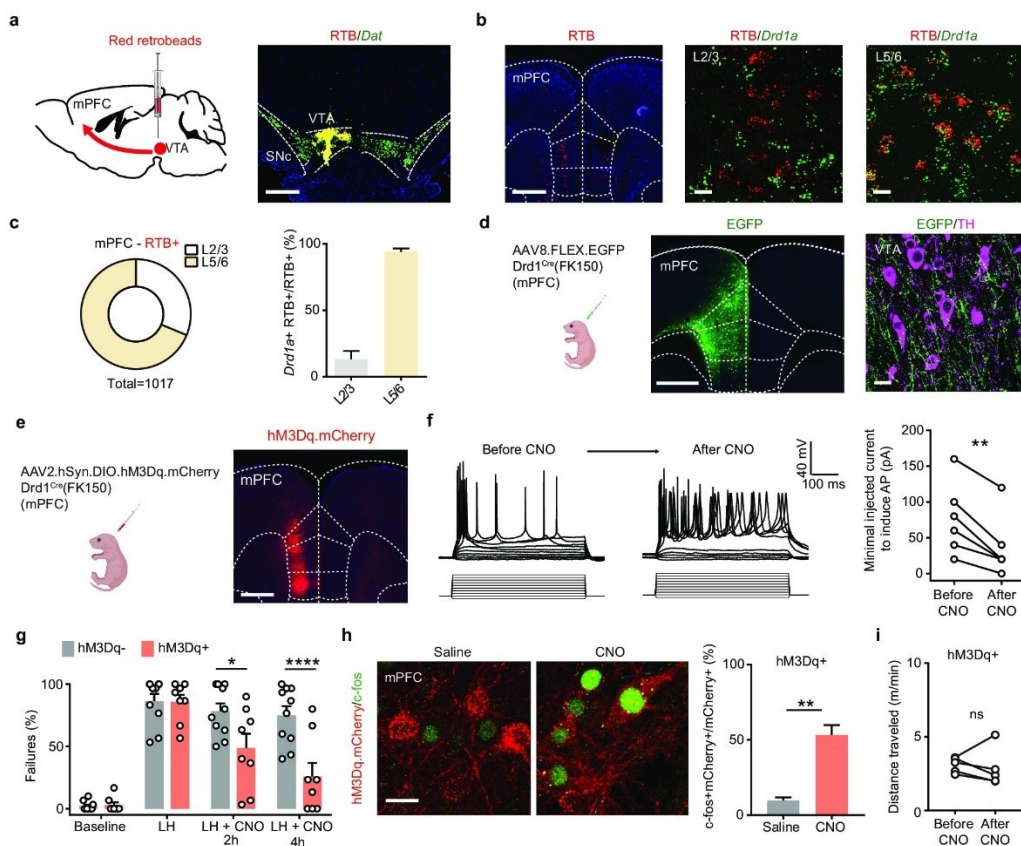


**Figure 3.6. Activation of mPFC *Drd1*<sup>+</sup> neurons rescues escape actions.** (a). Left, schematic illustrating retrograde labeling strategy. Right, coronal image of retrobead (RTB) injection site. Red, retrobeads; green, *Dat* mRNA; blue, DAPI. Scale bar, 500  $\mu$ m. (b). Left, retrobead fluorescence in mPFC (atlas overlay, dashed line). Middle and right, colocalization of RTB and *Drd1* mRNA in superficial and deep layers of mPFC. Scale bars, 500  $\mu$ m (left), 20  $\mu$ m (middle and right). (c). Left, the proportional distribution of RTB<sup>+</sup> neurons across superficial and deep cortical layers. Right, quantification of the percentage of *Drd1*<sup>+</sup> cells among RTB<sup>+</sup> cells across layers.  $n = 2$  animals, 31.3% RTB<sup>+</sup> neurons in layer 2/3, 68.7% RTB<sup>+</sup> in layer 5/6. Among those RTB<sup>+</sup> neurons, 13.2%  $\pm$  6.2% are *Drd1*<sup>+</sup> in layer 2/3,  $\pm$  2.5 are *Drd1*<sup>+</sup> in layer 5/6. (d). Left, schematic illustrating viral transduction strategy. Right, a coronal image showing the expression of EGFP (green) in the mPFC *Drd1*<sup>+</sup> neurons. Scale bar, 500  $\mu$ m. (e). Left, schematic illustrating viral transduction strategy. Right, epifluorescent image of hM3Dq-mCherry expression in mPFC. Scale bar, 500  $\mu$ m. (f). Whole-cell recording of action potentials evoked by different amplitude current injections in one mCherry<sup>+</sup> mPFC neuron before, during, and after bath application of 1  $\mu$ M CNO. Left, example traces. Right, summary data for minimal injected current sufficient to evoke action potential firing before and after CNO application.  $n = 6$  cells from two animals, two-tailed paired t-test,  $p = 0.0028$ . (g). Summary data showing the percentage of failures to escape an escapable

aversive shock in Drd1-Cre<sup>+</sup> and Drd1-Cre<sup>-</sup> mice expressing hM3Dq across phases of learning and after CNO treatment (Baseline, LH, LH+ CNO 2 hrs, and LH+ CNO 4 hrs). n = 8 animals for Cre<sup>-</sup>, n = 10 mice for Cre<sup>+</sup>, two-way ANOVA, Sidak's multiple comparison test, LH+ CNO 2 hr, p = 0.0157, LH+ CNO 4 hr, p < 0.0001, Baseline/LH, p > 0.9. **(h)**. Left, colocalization of c-fos immunolabeling in hM3Dq.mCherry<sup>+</sup> mPFC neurons in saline and CNO-treated Drd1 Cre<sup>+</sup>, hM3Dq-expressing mice. Right, the quantification of percentage of c-fos<sup>+</sup> cells among mCherry<sup>+</sup> cells. Scale bar, 20 μm. n = 3 mice/condition, two-tailed unpaired t-test, p = 0.0031. **(i)**. Total distance traveled per minute in an open-field locomotion assay for hM3Dq<sup>+</sup> animals before and after CNO treatment. Two-tailed paired t-test, p = 0.6289, n = 5 animals. \*p < 0.05, \*\*p < 0.01, \*\*\*\*p < 0.0001. Error bars reflect SEM.

To determine whether ketamine modulates the activity of DA-sensing mPFC Drd1<sup>+</sup> neurons *in vivo*, we used fiber photometry to monitor the activity of Drd1<sup>+</sup> neurons in mPFC before and after ketamine treatment. To restrict the expression of GCaMP6f, we transduced AAV1.CAG.FLEX.GCaMP6f in Drd1Cre(FK150) mice (**Figure 3.6 Supplement 1a, b**). We observed a rapid enhancement in population activity of cortical Drd1<sup>+</sup> neurons after i.p. ketamine treatment (**Figure 3.6 Supplement 1c, d**). This ketamine-induced enhancement of population activity is likely mediated by suppressing the activity of local inhibitory interneurons<sup>380,383,397</sup>. If ketamine effect on mPFC Drd1<sup>+</sup> neurons is crucial for behavioral changes, then the activation of mPFC Drd1<sup>+</sup> neurons should rescue escape actions. We used the Gαq-coupled hM3D to directly enhance the excitability of Drd1 expressing neurons in mPFC following aversive learning (**Figure 3.6e**). The expression and functional activation of hM3Dq were validated by immunohistochemistry and electrophysiology (**Figure 3.6f**). The expression of hM3Dq also did not change baseline escape/failure rates, or the magnitude of aversive learning. After LH induction, a single i.p. dose of CNO was sufficient to rescue escape behavior rapidly within 2 hours, with a larger effect observed 4 hours after CNO treatment (**Figure 3.6g**). At the end of the

experiment, the successful enhancement of neuronal activity was further validated by evaluating immediate early gene product c-fos expression in mCherry<sup>+</sup> neurons (**Figure 3.6h**). The activation of hM3Dq in Drd1-positive mPFC neurons did not alter locomotion, suggesting the rescue of escape action is not due to hyperlocomotor activity (**Figure 3.6i**). In addition to our results, a recently published study showed that optogenetic activation of Drd1<sup>+</sup> mPFC neurons decreases immobility time in the forced swim test, suggesting the possibility that these Drd1-expressing neurons may broadly regulate aversive or active coping responses<sup>409</sup>. Furthermore, consistent with prior findings<sup>409</sup>, chemogenetic inhibition of mPFC Drd1<sup>+</sup> neuronal excitability through G $\alpha_i$ -coupled hM4D blocked the behavioral effects of ketamine after LH (**Figure 3.6 Supplement 2a, b**). Altogether, our data demonstrate that mPFC serves as an action site of ketamine to rescue VTA DA dynamics, which is necessary to drive escape actions after LH.

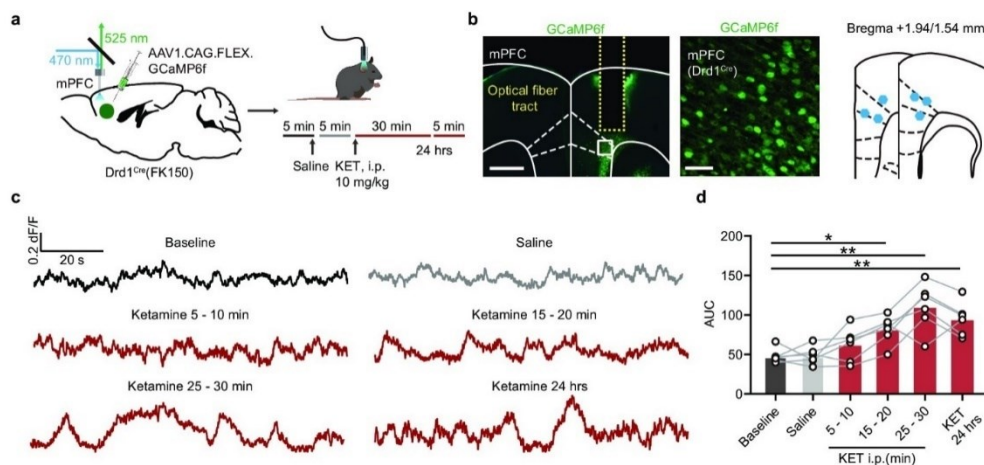


**Figure 3.6 Supplement 1. Activity of Drd1<sup>+</sup> neurons in mPFC after in vivo ketamine treatment.** (a). Left, schematic for viral transduction of GCaMP6f in the mPFC with subsequent fiber implant in Drd1<sup>Cre</sup>(FK150) mice. Right, timeline of photometry recording with saline and ketamine treatment (10 mg/kg, i.p.). (b). Left, fiber placement illustration on a coronal section through mPFC, with a close-up image of Drd1<sup>+</sup> (white dashed lines, Paxinos atlas overlay; yellow dashed lines, fiber track). Green, GCaMP6f; blue, Hoechst nucleic stain. Scale bars: 500  $\mu$ m and 50  $\mu$ m. Right, atlas location of fiber placement for each subject. (c). Example traces showing Ca<sup>2+</sup>

transients of  $Drd1^{+}$  neurons in the mPFC from one mouse in baseline, following saline treatment, and after ketamine treatment (5–10, 15–20, 25–30 min, and 24 hr). Black, baseline; gray, saline; red, after ketamine. **(d)**. Summary data showing area under the curve (AUC) of  $Ca^{2+}$  transients in 5 min bins across conditions (Baseline, Saline, 5–10, 15–20, 25–30 min, and 24 hr after ketamine).  $n = 6$  animals, repeated measures one-way ANOVA,  $F(2.498, 12.49) = 16.94$ ,  $p = 0.0002$ . Sidak's multiple comparison test vs Baseline, Saline,  $p > 0.9$ , KET 5–10 min,  $p = 0.3605$ , KET 15–20 min,  $p = 0.0131$ , KET 25–30 min,  $p = 0.0063$ , KET 24 hr,  $p = 0.0031$ . \* $p < 0.05$ , \*\*  $p < 0.01$ .

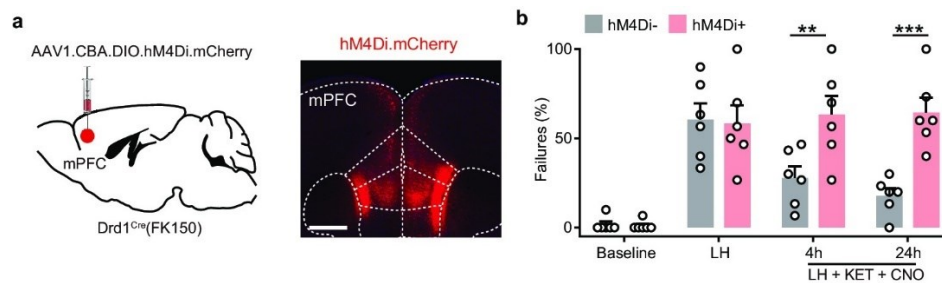


**Figure 3.6 Supplement 2. Inhibition of  $Drd1^{+}$  neurons in mPFC blocks the behavioral effects of ketamine.** **(a)**. Left, schematic illustrating viral transduction strategy. Right, epifluorescent image of hM3Dq-mCherry expression in mPFC. Scale bar, 500  $\mu$ m. **(b)**. Summary data showing the percentage of failures to escape an escapable aversive shock in  $Drd1-Cre^{+}$  and  $Drd1-Cre^{-}$  mice expressing hM4Di across phases of learning and after CNO treatment (Baseline, LH, LH+ CNO 4 hr, and LH+ CNO 24 hr).  $n = 6$  animals, two-way ANOVA, Sidak's multiple comparison test, LH+ CNO 4 hr,  $p = 0.0056$ , LH+ CNO 24 hr,  $p = 0.0002$ , Baseline/LH,  $p > 0.9$ .

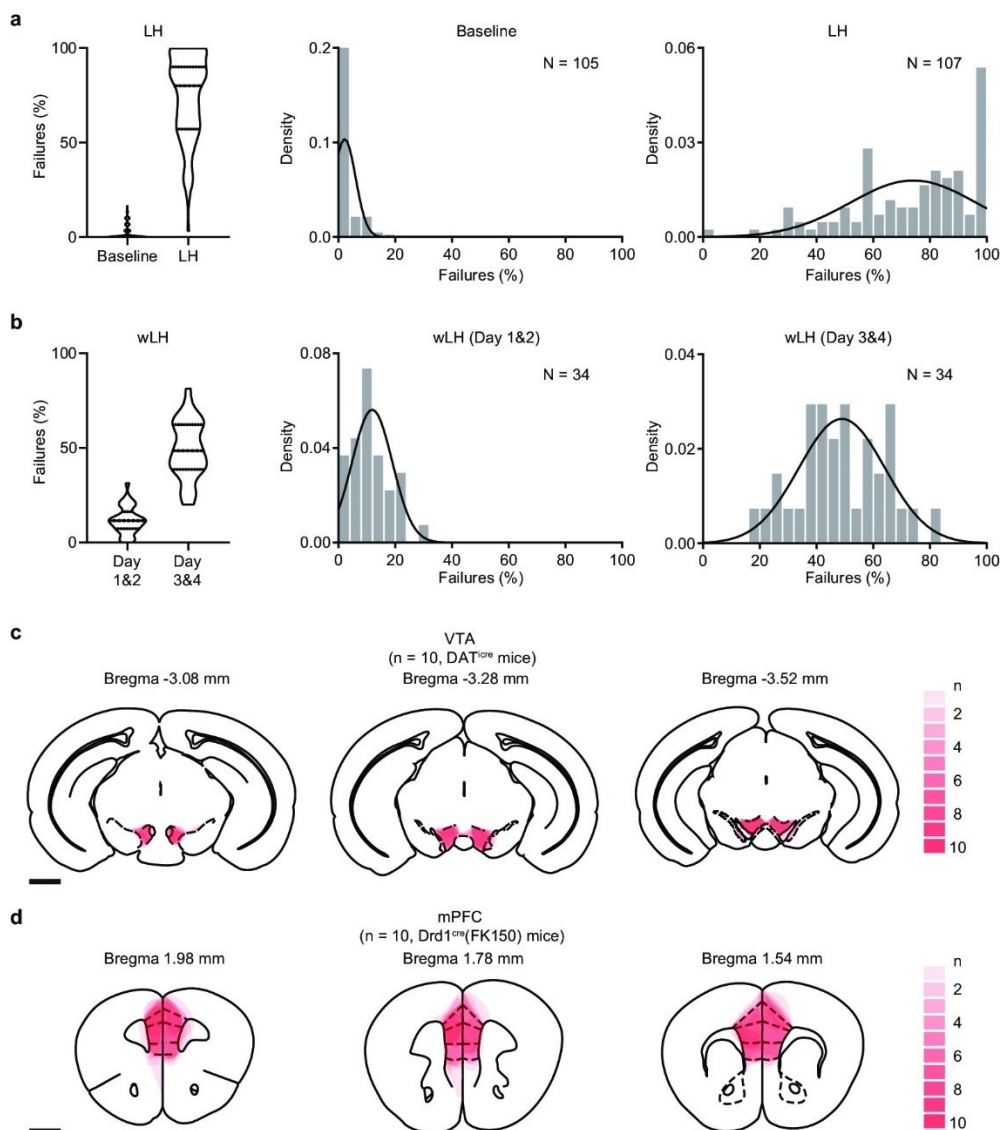


**Figure 3.6 Supplement 3. Behavioral outcomes and viral expression distributions. (a).** Left, violin plot showing the percentage of failures to escape an escapable aversive shock before and after LH induction. The width of the box indicates relative number of data points and the crossbars indicate three quartiles (Q1, Q2, Q3). Middle and right, density histograms fitted with the Gaussian distribution. Parameter estimated (Mean, SD $\pm$  error): Baseline ( $2.19 \pm 0.38$ ,  $3.844 \pm 0.27$ ), LH ( $74.02 \pm 2.15$ ,  $22.23 \pm 1.52$ ).  $n = 105$ ,  $107$  mice for baseline and LH. **(b).** Same as **(a)** but for wLH. Days 1 and 2 ( $11.88 \pm 1.22$ ,  $7.10 \pm 0.86$ ), Days 3 and 4 ( $48.91 \pm 2.60$ ,  $15.14 \pm 1.84$ ).  $n = 34$  mice/condition. **(c).** Heatmap showing viral expression in the VTA of DAT<sup>Cre</sup> mice.  $n = 10$  mice. Scale bar = 1 mm. **(d).** Same but for the mPFC of Drd1<sup>Cre</sup>(FK150) mice.  $n = 10$  mice.

### 3.2.7 Discussion

Animals must learn to avoid dangerous stimuli in order to survive, underscoring the ethological significance of aversive learning. However, overlearned responses can be maladaptive.

Prolonged exposure to stressful events can lead to learned helplessness<sup>359,360,410</sup>, where an individual fails to avoid unpleasant stimuli. Here, we demonstrate that aversive learning restructures neuronal activity in the VTA DA system, associated with a shift in behavioral outcome distribution. A single low-dose ketamine treatment suffices to temporarily normalize both DA signaling and behavior, with the efficacy of treatment correlating with VTA DA activity features prior to learning. Inhibition of somatic DA activity or consequences of DA release abolishes the behavioral effects of ketamine. We identify mPFC as a key action site that mediates ketamine's effects on VTA DA dynamics, where the activation of mPFC *Drd1*<sup>+</sup> neurons is sufficient to rescue escape actions.

#### Individual variability in VTA DA activity and behavioral susceptibility

Multivalenced encoding of information by VTA DA neurons and their projections is now well established<sup>353,367,411–413</sup>. Prior reports demonstrate that stress and aversive learning change DA neuron activity in both acute and chronic paradigms<sup>366,371,375,414,415</sup>. Our findings here show that VTA GCaMP transients are shaped both by trial outcomes—escape or failure to escape from an avoidable stimulus—as well as by the general behavioral state induced by LH learning and ketamine treatment. This malleability and multifaceted activity of DA signaling opens the possibility that particular patterns and levels of VTA DA activity map to specific behavioral outcome distributions. In this framework, differences in VTA DA activity between success and failure outcomes map to the tendency to escape aversive stimuli. Accordingly, decreases in the

differences between VTA DA activity on escape and failure trials after aversive learning are associated with increased failures to escape avoidable stressful stimuli. Future behavioral responses to ketamine are correlated with trace distances between escape and failure-associated GCaMP transients before learning occurs. Building on these correlative observations, chemogenetic inhibition of VTA DA neuron activity supports a causal relationship between learning, DA activity, and ketamine effects. These data demonstrate that DA activity changes in LH paradigms and perturbations of DA dynamics shape behavioral outcomes in escape behavior.

The question of what key biological parameters distinguish resilient and susceptible animals remains enigmatic. In this study, we observe substantial individual variability of behavioral expression after LH. Other studies have mapped this type of variability to a binary structure of resilience and susceptibility<sup>375,416–419</sup>. While there is some utility in forcing a binary behavioral outcome, in this relatively large dataset ( $n > 130$  mice), we noted a broad (and not bimodal) variance in LH outcomes for both strong and weaker LH, reflecting the diversity of individual learning experiences (**Figure 3.6 Supplement 3a, b**). Notably, we also observe biologically significant variability in VTA DA responses, correlated with future behavioral outcomes after learning and ketamine treatment. The biological nature of this variability may relate to resilience or susceptibility to stress. One interesting possibility is that projections and activity profiles of DA neuron subgroups could be related to early-life and adolescent experience<sup>419–422</sup>, resulting in variability of the overall low-dimensional activity pattern of the VTA DA population recorded using photometry. Based on this observation, it is expected that task specific VTA DA activity may serve as a potential biomarker for the degree of susceptibility to stressful events. In the context of human populations, PET studies have been used to measure aspects of DA system

function<sup>423–426</sup>. Importantly, genetic variability which can drive differences in DA signaling<sup>423</sup>, could provide additional biomarkers to predict clinical ketamine efficacy.

Animals used in this study derive from a genetically homogenous background, and one can expect larger variances in DA-associated genes in the human population. DA signaling has been associated with positive and negative emotionality and related to variability in psychopathology<sup>427</sup>. Polymorphisms in DA genes regulate DA transmission throughout the brain, influencing depression-related phenotypes<sup>428–430</sup>. Variance in DA genes and their interactors, along with early life experience, may shape activity patterns of DA neurons and DA release in response to stressful events, defining depression susceptibility in humans.

#### Circuit-level mechanisms underlying the effects of ketamine on behavior

Multiple studies demonstrate that mPFC is broadly involved in the rapid and lasting behavioral effects of ketamine. NMDA receptor antagonists, including ketamine, have been shown to rapidly enhance neuronal and dendritic activity of cortical pyramidal neurons through disinhibition<sup>380,383,397,431,432</sup>. Further, on a relative longer timescale, increases in cortical dendritic spine density, induced by ketamine, maintain behavioral effects after ketamine clearance *in vivo*<sup>392,433</sup>. The enhancement in cortical spinogenesis requires mTORC1, BDNF, subtypes of glutamate receptors, as well as dopaminergic signaling<sup>380,387,394,433–435</sup>. Optogenetic stimulation of mPFC neurons reverses depressive-like behaviors<sup>388,436,437</sup>. Evidence from this study and others has consistently demonstrated that the activation of mPFC Drd1 neurons is important for ketamine's behavioral effects. Consistent with diverse outputs of mPFC, local ketamine actions there may subsequently change the activity of multiple downstream brain regions, including the

VTA, but also basolateral amygdala, nucleus accumbens, and lateral habenula, among others. These brain regions likely contribute to specific behavioral effects of ketamine observed in different behavioral paradigms<sup>259,361,409,437</sup>.

Besides modulating mPFC *Drd1*<sup>+</sup> neurons, DA signaling in many brain regions regulates escape actions and avoidance behaviors. For example, the release and postsynaptic function of DA in the NAc and amygdala have been extensively studied in conditioned avoidance learning<sup>438-444</sup>. In this study, we found that VTA DA activity is not necessarily critical for innate escape actions, since chemogenetic suppression of VTA DA activity does not increase failures to escape from shock stimuli in the absence of prior learning. Importantly, after LH, the responses of VTA DA neurons to both inescapable and escapable shocks are significantly changed. Since DA release has been shown to be highly correlated with somatic DA neuronal activity<sup>371,445</sup>, we predict that downstream DA release in the NAc and amygdala are also modulated after LH and ketamine treatment.

Which specific projections carry information about different aversive stimuli (e.g., conditioned cues or unpredicted aversive events) and whether they derive from the same or different subpopulations of VTA DA neurons, remains an active area of research<sup>259,371,396,414,415</sup>. VTA DA neurons are highly heterogeneous based on their input/output anatomy and transcriptional profiles<sup>367,396</sup>. Prior studies have demonstrated that VTA DA neurons respond to foot shocks differently, based on the brain regions they project to<sup>371</sup>. In this study, we do not distinguish responses of DA neurons based on their projections or transcriptional profiles. Thus, the observed effects are sufficiently powerful to be seen on the background of a mixed DA population that maintains projection target diversity.

### Ketamine effects on DA activity and mPFC-VTA recurrent circuit hypothesis

Given the absence of local ketamine effects on VTA DA neurons, as shown in *ex vivo* calcium imaging and electrophysiological recordings, along with *in vivo* infusion experiments, the modulation of VTA DA activity by ketamine *in vivo* must depend on changes in the activity of projections from other brain regions. Based on evidence from electron microscopy reconstructions and anatomical tracing, VTA DA neurons that project to mPFC receive inputs from mPFC pyramidal neurons, forming excitatory connections<sup>396,446</sup>. Trans-synaptic tracing analyses and optogenetic assays provide evidence that mPFC pyramidal neurons send excitatory glutamatergic projections to VTA<sup>259,396,447,448</sup>. Prior data from our lab<sup>448</sup> and others<sup>396,446,449</sup> confirm that VTA DA neurons receive excitatory mPFC inputs. Glutamate release from mPFC terminals elicits excitatory responses in VTA DA neurons<sup>437,450-452</sup>, driving synchronized activity across VTA and mPFC, as well as other limbic structures<sup>437</sup>. Although the mPFC and VTA are the not only brain regions that control escape behaviors, the enhanced activity within these two brain regions is likely one important mechanism underlying behavioral effects of ketamine. Our data show that local mPFC ketamine infusion rescues both VTA DA activity and behavior (**Figure 3.5**). *In vivo* ketamine treatment rapidly enhances Drd1 neuronal activity in mPFC (**Figure 3.6 Supplement 1**) and chemogenetic activation of mPFC Drd1<sup>+</sup> neurons rescues escape behaviors (**Figure 3.6g**). Moreover, in recently published work, we show that DA signaling through Drd1 activation is necessary for ketamine's action on restoring glutamate-evoked dendritic spinogenesis in mPFC<sup>394</sup>, which has been shown to maintain the lasting behavioral effects of ketamine after corticosterone treatment<sup>392</sup>. Chemogenetic activation of Gas-coupled signaling cascades downstream of Drd1 activation in mPFC also rescues escape behavior after

LH<sup>394</sup>. Based on the sum of these data across multiple laboratories and experimental modalities, we hypothesize that the initial enhancement of activity induced by ketamine in mPFC may be amplified within recurrent mPFC-VTA circuit, which may help extend ketamine behavioral effects beyond its *in vivo* bioavailability. Future studies are necessary to explicitly test this model.

Other potential circuit mechanisms for ketamine's enhancement of VTA DA activity may involve ventral hippocampal inputs to nucleus accumbens and lateral habenula projections to the VTA, both of which are modulated by stressful experience and ketamine<sup>259,361,453-455</sup>. One such potential mechanism could involve actions in the lateral habenula, which sends glutamatergic inputs to GABAergic neurons that suppress VTA DA activity<sup>456</sup>. Excitatory synapses onto VTA-projecting lateral habenula neurons are potentiated in rats in behavioral and genetic models of LH<sup>454</sup>. Ketamine could disinhibit VTA DA neurons by suppressing the activity of lateral habenula glutamatergic neurons<sup>259</sup>. Rapid and lasting behavioral effects of ketamine likely result from synergistic actions across many brain regions, involving multiple molecular pathways.

#### Clinical implications in co-morbidity

Drugs that modulate the dopaminergic system represent first line therapies for a large number of diverse neurological and mental health conditions that are comorbid with major depressive disorder, including Parkinson's disease, schizophrenia, OCD, ADHD, and eating disorders<sup>457-461</sup>. The recent FDA approval of esketamine for the treatment of major depressive disorder is a major expansion of its clinical use. Our results on dopaminergic mediation of ketamine's effects on behavior and plasticity suggest the possibility of ketamine's differential clinical effects in

patients receiving exogenous DA precursors (e.g., L-DOPA), re-uptake inhibitors, and dopaminergic receptor agonists and antagonists.

### **3.3 Methods**

#### Mouse strains and genotyping.

Animals were handled according to protocols approved by the Northwestern University Animal Care and Use Committee. Weanling and young adult male and female mice (postnatal days 40-80) were used in this study. Approximately equal numbers of males and females were used for every experiment. All mice were group-housed, with standard feeding, 12-hour light and 12-hour dark cycle (6:00 or 7:00 lights on), and enrichment procedures. Littermates were randomly assigned to conditions. C57BL/6 mice used for breeding and backcrossing were acquired from Charles River (Wilmington, MA), and all other mouse lines were acquired from the Jackson Laboratory (Bell Harbor, ME) and bred in house.

B6.SJL-Slc6a3tm1.1(cre)Bkmn/J mice, which express Cre recombinase under control of the dopamine transporter promoter, are referred to as DAT<sup>iCre</sup><sup>462</sup>; B6.FVB(Cg)-Tg(Drd1-cre)FK150Gsat/Mmucd mice, which express Cre recombinase under control of the dopamine Drd1a receptor promoter, are referred to as Drd1Cre(FK150)<sup>463</sup>. All transgenic animals were backcrossed to C57BL/6 for several generations. Heterozygous Cre<sup>+</sup> mice were used in experiments. Standard genotyping primers are available on the Jackson Lab website.

#### Stereotactic injections and optic fiber implants

Conditional expression of target genes in Cre-containing neurons was achieved using recombinant adeno-associated viruses (AAVs) using the FLEX cassette or encoding a double-floxed inverted open reading frame (DIO) of target genes, as described previously<sup>406</sup>. For fiber photometry and *ex vivo* 2-photon calcium imaging experiments in the VTA, DAT<sup>iCre</sup> mice were transduced with AAV1.CAG.FLEX.GCaMP6f.WPRE-SV40 (1.33 x 10<sup>13</sup> GC/ml) from the UPenn viral core (Philadelphia, PA, a gift from the Genetically Encoded Neuronal Indicator and Effector Project (GENIE) and Douglas Kim; Addgene viral prep #100835-AAV1)<sup>464</sup> or AAV8.CAG.FLEX.EGFP (3.1 x 10<sup>12</sup> GC/ml, UNC vector core, Dr. Ed Boyden). For fiber photometry experiments in the mPFC, Drd1Cre(FK150) mice were transduced with AAV1.CAG.FLEX.GCaMP6f.WPRE.SV40 (1.33 x 10<sup>13</sup> GC/ml). For chemogenetic experiments in mPFC, Drd1Cre(FK150) mice were transduced with AAV2.hSyn.DIO.hM3Dq.mCherry (8.6 x 10<sup>12</sup> GC/ml, Addgene viral prep #44361-AAV2, Dr. Bryan Roth)<sup>465</sup>. For chemogenetic experiments in VTA, DAT<sup>iCre</sup> mice were transduced with a custom built AAV1.CBA.DIO.hM4Di.mCherry (1.28 x 10<sup>13</sup> GC/ml, Vigene Biosciences, Rockville, MD, plasmid a gift from Dr. Bernardo Sabatini)<sup>466</sup>. For retrograde labeling, mice were intracranially injected with Red Retrobeads<sup>TM</sup> (Lumafluor Inc) in VTA.

Neonatal viral transduction was carried out to minimize invasiveness and increase surgical efficiency<sup>405,406,467-469</sup>. P3-6 mice were cryoanesthetized, received ketoprofen for analgesia, and were placed on a cooling pad. Virus was delivered at a rate of 100 nl/min for up to 150-200 nl using an UltraMicroPump (World Precision Instruments, Sarasota, FL). Medial prefrontal cortex (mPFC) was targeted in the neonates by directing the needle immediately posterior to the eyes, 0.3 mm from midline, and 1.8 mm ventral to skin surface. Ventral tegmental area (VTA) was

targeted in the neonates by directing the needle approximately  $\pm 0.2$  mm lateral from Lambda and 3.8 mm ventral to skin surface. Coordinates were slightly adjusted based on pup age and size.

Following the procedure, pups were warmed on a heating pad and returned to home cages.

For intracranial injections, mice were anesthetized with isoflurane (3% for induction value, 1.5-2% for maintenance) or ketamine:xylazine (100:12.5 mg/kg b.w.), received ketoprofen for analgesia, and were placed on a small animal stereotax frame (David Kopf Instruments, Tujunga, CA). AAVs or retrobeads were delivered through a pulled glass pipette at a rate of 100 -150 nl/min using an UltraMicroPump (World Precision Instruments, Sarasota, FL). Ketamine, ACSF, or Chicago Sky Blue 6B were delivered intracranially at a rate of 150 nl/min using the UltraMicroPump. Injection coordinates for VTA, 2.8 mm posterior to bregma, 0.4 mm lateral, and 4.3 - 4.5 mm below the pia; for mPFC, 2.3 mm anterior to bregma, 0.4 mm lateral, and 1.3 - 1.6 mm below the pia; for PAG, 4.2 mm posterior to bregma, 0.1 mm lateral, and 2.2 below the pia; for PPTg, 4.5 mm posterior to bregma, 1.2 mm lateral, and 2.5 below the pia. Pipettes were held at the injection location for 15 min following AAV or retrobead release. Coordinates were slightly adjusted based on mouse age and size.

For photometry fiber placement in the VTA or mPFC, mice were implanted with a 400  $\mu$ m diameter 0.48 NA single mode optical fiber (Doric lenses, Quebec City, QC, Canada) directly above the VTA at -2.8 mm (AP); +0.4 mm (ML); 4.3 - 4.5 mm (DV), mPFC +2.0 mm (AP); +0.4 mm (ML); 1.3 - 1.6 mm (DV), four to six weeks after viral transduction. Coordinates for mPFC fiber placement were +2.0 mm (AP), +0.4 mm (ML), and 1.3 - 1.6 mm (DV). Behavioral experiments were conducted 7-12 days after implantation. Real-time photometry recording was performed during optical fiber implant above the VTA, for optimal targeting. When the fiber tip

approached the VTA region, a continuous increase of fluorescence intensity was observed. The final position of implantation was determined by the cessation of further increases in fluorescence intensity. Mice recovered for 7-9 days after implantation.

### Behavior assays

Aversive learning. P40-60 mice were used for behavioral assays with fiber photometry and chemogenetics experiments. The strong learned helplessness procedure consisted of two induction sessions (1 session per day; 360 inescapable foot shocks per session; 0.3 mA, 3 sec; random 1-15 sec inter-shock intervals). Active/Passive Avoidance Shuttle Boxes from MazeEngineers (Boston, MA) were used for the experiment. To assess the degree of aversive learning, test sessions (30 escapable foot shocks per session; 0.3 mA, 10 sec; random 5-30 sec inter-shock intervals) were conducted before induction, 24 hrs after the last induction session, and following pharmacological manipulations. The testing was performed in a shuttle box (18 × 18 × 20 cm) equipped with a grid floor and a gate separating the two compartments. No conditioned stimulus was delivered either before or after the shocks. Escapes were scored when the animal shuttled between compartments during the shock. Escape latency was measured as the time from the start of the shock to the escape. The shock automatically terminated when the animal shuttled to the other compartment. Failures were scored when the animal failed to escape before the shock end. All behavioral assays were conducted during the active phase of the circadian cycle. Schematics with mice were made using BioRender.

To evaluate learned helplessness behavior in a novel context, another shuttle box with different decorative designs was used. In addition to a differently designed gate, decorations with black

and white patterns (bars and circles) were applied to the walls. To evaluate the effect of ketamine on learned helplessness behavior, a single dose of ketamine (10 mg/kg b.w., i.p.) was given 48 hrs after the last induction session, with the test session performed 4 hrs later. For chemogenetic activation in mPFC, 48 hrs after the last induction session, Clozapine N-oxide (CNO) was administered i.p., followed by test sessions 2 hrs and 4 hrs later. For chemogenetic inhibition in VTA, the first CNO dose (3 mg/kg, i.p.) was co-administered with ketamine 48 hrs after the last induction, followed by test sessions 4 and 24 hrs later. Then, immediately following the last test session ketamine was administered alone, followed by test sessions 4, 24, and 72 hrs later.

For the weak aversive learning procedure, a single induction session (360 inescapable foot shocks; 0.3 mA, 3 sec; random 1-15 sec intershock intervals) was performed at the end of the 2nd day. Six test sessions were performed (1 session per day; 100 escapable foot shocks per session; 0.3 mA, 3 sec; random 5-15 sec intershock intervals). A single dose of ketamine (10 mg/kg b.w., i.p.) was given 4 hrs before the 5th test session. The final test session was performed 24 hrs after ketamine treatment. Age-matched controls were given six test sessions, in the absence of induction sessions or ketamine treatment.

Locomotion test. To assess the locomotor activity, mice were placed in the center of a plastic chamber (48 cm × 48 cm × 40 cm) or in the shuttle box in a dimly lit room. Mice explored the arena for 15 min, with video (30 fps) and photometry recording performed during the final 10 min.

#### Fiber photometry

Hardware was created based on open-source resources made available by Dr. Thomas Davidson (<https://drive.google.com/drive/folders/0B7FioEJA1B1aNmdPOEsxTjhxajg>)<sup>470</sup>. Briefly, a custom-built setup was created combining Doric fluorescence mini-cube (Doric, Westport, CT) and a 2151 Femtowatt photoreceiver with a lensed adapter (Newport, Irvine, CA). All downstream hardware including fiberoptic cannulas and patch cords, except for LEDs and drivers (Thorlabs, Newton, NJ), are readily available from Doric. A conventional single-cell electrophysiology recording system (DAQ+software) was used to acquire signal and drive the LED, with a modified version of MATLAB-based Scanimage<sup>471</sup> adapted for electrophysiology recordings by Dr. Bernardo Sabatini (<https://github.com/bernardosabatini/lab>). Signals were sampled at 1 kHz and downsampled to 250 Hz for time-locked and to 10 Hz for non-time-locked analyses. Fluorescence signal was baseline adjusted in non-overlapping 100 sec windows as  $(\text{signal} - \text{median}(\text{signal})) / \text{median}(\text{signal})$ , denoted as  $dF/F$ . Recordings were made during a subset of the sessions of LH and open field locomotion, as noted in the text. Additional analyses details and link to analysis code are below.

#### Acute slice preparation and electrophysiology

Coronal brain slice preparation was modified from previously published procedures<sup>405,406,472</sup>. Animals were deeply anesthetized by inhalation of isoflurane, followed by a transcardial perfusion with ice-cold, oxygenated artificial cerebrospinal fluid (ACSF) containing (in mM) 127 NaCl, 2.5 KCl, 25 NaHCO<sub>3</sub>, 1.25 NaH<sub>2</sub>PO<sub>4</sub>, 2.0 CaCl<sub>2</sub>, 1.0 MgCl<sub>2</sub>, and 25 glucose (osmolarity 310 mOsm/L). After perfusion, the brain was rapidly removed, and immersed in ice-cold ACSF equilibrated with 95%O<sub>2</sub>/5%CO<sub>2</sub>. Tissue was blocked and transferred to a slicing chamber containing ice-cold ACSF, supported by a small block of 4% agar (Sigma-Aldrich).

Bilateral 250 or 300  $\mu\text{m}$ -thick slices were cut on a Leica VT1000s (Leica Biosystems, Buffalo Grove, IL) in a rostro-caudal direction and transferred into a holding chamber with ACSF, equilibrated with 95%O<sub>2</sub>/5%CO<sub>2</sub>. Slices were incubated at 34°C for 30 min prior to electrophysiological recording and 2-photon calcium imaging. Slices were transferred to a recording chamber perfused with oxygenated ACSF at a flow rate of 2–4 ml/min at room temperature.

To assess spontaneous firing rate of dopaminergic neurons in the VTA, cell-attached recordings were performed. Cell-attached recording electrode pipettes were filled with the internal solution for voltage clamp recordings to monitor spontaneous break in, with pipette resistance varying between 3 and 7 M $\Omega$ . To assess spontaneous synaptic inputs (sEPSC/sIPSC), voltage clamp recordings were performed. Dopaminergic neurons were identified by the expression of mCherry or GFP in DAT<sup>iCre</sup> mice. Recording electrodes contained the following (in mM): Cell-attached recordings and voltage clamp for sEPSCs: 120 CsMeSO<sub>4</sub>, 15 CsCl, 10 HEPES, 10 Na-phosphocreatine, 2 MgATP, 0.3 NaGTP, 10 QX314, and 1 EGTA (pH 7.2-7.3, ~295 mOsm/L); Voltage clamp for sIPSCs (high chloride internal solution): 100 CsCl, 35 CsF, 4 MgCl<sub>2</sub>, 10 HEPES, 10 Na-phosphocreatine, 4 MgATP, 0.4 Na<sub>2</sub>GTP, and 1 EGTA (pH 7.2, 295 mOsm/L). In voltage clamp recordings, cells were held at -70mV. Recordings were made using 700B amplifiers (Axon Instruments, Union City, CA); data were sampled at 10 kHz and filtered at 4 kHz with a MATLAB-based acquisition script (MathWorks, Natick, MA). Offline analysis of electrophysiology data was performed using MATLAB (Mathworks, Natick, MA), and Clampfit 11.2 (Molecular Devices, San Jose, CA).

### Two-photon GCaMP6f imaging

Calcium sensor imaging was accomplished on a custom-built microscope combining two-photon laser-scanning microscopy (2PLSM), as previously described<sup>405,406,448,472,473</sup>. A mode-locked Ti:Sapphire laser (Mai Tai eHP and Mai Tai eHP DeepSee, Spectra-Physics, Santa Clara, CA) were tuned to 910 nm for GCaMP6f. The intensity of each laser was independently controlled by Pockels cells (Conoptics, Danbury, CT). A modified version of Scanimage software was used for data acquisition<sup>471</sup>. Calcium imaging of GCaMP6f expressing DA neurons in acute brain slices of the VTA was done at 910 nm and sampled at 12 Hz. Spontaneous activity was imaged for 5 min in the baseline at 34°C, followed by a 5 min recording after *ex vivo* ketamine application (50 µM, with 15 - 40 min delay).

### Pharmacology

Pharmacological agents were acquired from Vedco (St. Joseph, MO) or Sigma-Aldrich (St. Louis, MO). *In vivo* injections included intraperitoneal and subcutaneous injections of ketamine (10 mg/kg, Vedco, St. Joseph, MO) and Clozapine N-oxide (3 mg/kg *in vivo*, 1 µM *in vitro*, Sigma-Aldrich); intracranial injections of ketamine (12.5 µg in 500 nl ACSF) and Chicago Sky Blue 6B (50 µg in 500 nl ACSF, Tocris, Bristol, United Kingdom). *Ex vivo* applications included SR95531 (Gabazine, 10 µM, Tocris), CNQX (10 µM, Tocris), and ketamine (50 µM).

### Tissue processing and immunohistochemistry

Mice were deeply anaesthetized with isoflurane and transcardially perfused with 4% paraformaldehyde (PFA) in 0.1 M phosphate buffered saline (PBS). Brains were post-fixed for 1-5 days and washed in PBS, prior to sectioning at 50-100 µm on a vibratome (Leica Biosystems). Sections were pretreated in 0.2% Triton X-100 for an hour at RT, then blocked in

10% bovine serum albumin (BSA, Sigma-Aldrich, ST Louis, MO):PBS with 0.05% Triton X-100 for two hours at RT, and incubated for 24-48 hrs at 4°C with primary antibody solution in PBS with 0.2% Triton X-100. On the following day, tissue was rinsed in PBS, reacted with secondary antibody for 2 hrs at RT, rinsed again, then mounted onto Superfrost Plus slides (ThermoFisher Scientific, Waltham, MA). Sections were dried and coverslipped under ProLong Gold antifade reagent with DAPI (Molecular Probes, Life Technologies, Carlsbad, CA) or under glycerol:TBS (9:1) with Hoechst 33342 (2.5µg/ml, ThermoFisher Scientific). Primary antibodies used in the study were rabbit anti-tyrosine hydroxylase (1:1000; AB152, Millipore, Burlington, MA), mouse anti-tyrosine hydroxylase (1:1000; AB129991, Abcam, Cambridge, UK), rabbit anti-RFP (1:500, 600-401-379, Rockland, Limerick, PA), and rabbit anti-c-Fos (1:5000; Synaptic Systems, Goettingen, Germany). Alexa Fluor 488-, Fluor 594-, or Fluor 647-conjugated secondary antibodies against rabbit, mouse, or chicken (Life Technologies, Carlsbad, CA) were diluted 1:500. Whole sections were imaged with an Olympus VS120 slide scanning microscope (Olympus Scientific Solutions Americas, Waltham, MA). Confocal images were acquired with a Leica SP5 confocal microscope (Leica Microsystems). Depth-matched z-stacks of 2 µm-thick optical sections were analyzed in ImageJ (FIJI)<sup>474,475</sup>. For c-fos quantification, every four adjacent z stack slices were combined, for a total of 6 µm thickness. mCherry signal was used to localize cell bodies of hM3Dq-expressing neurons. Laser intensity and all imaging parameters were held constant across samples, and the same threshold was applied for subtracting background immunofluorescence. C-fos<sup>+</sup> neurons were identified by an experimenter blind to the conditions.

#### Quantitative fluorescence in situ hybridization

Quantitative fluorescence in situ hybridization (FISH) was conducted following previously published procedures<sup>448,472</sup>. Mice were deeply anesthetized by inhalation of isoflurane and decapitated. Brains were quickly removed and frozen in tissue-freezing medium on a mixture of dry ice and ethanol for 5 - 15 min prior to storage at 80° C. Brains were subsequently cut on a cryostat (Leica CM1850, Leica Biosystems) into 20 µm-thick sections, adhered to Superfrost Plus slides, and frozen at 80° C. Samples were fixed with 4% PFA in 0.1 M PBS at 4° C for 15 min, processed according to the manufacturer's instructions in the RNAscope Fluorescent Multiplex Assay manual for fresh frozen tissue (Advanced Cell Diagnostics, Newark, CA), and coverslipped with ProLong Gold antifade reagent with DAPI (Molecular Probes). Drd1a receptor channel 2 (Drd1a) or Slc6a3 (Dat) probes were added to slides in combination, and Amp4-b fluorescent amplification reagent was used for all experiments. Sections were subsequently imaged on a Leica SP5 confocal microscope in four channels with a 40x objective lens at a zoom of 1.4 and resolution of 512 x 512 pixels with 1.0 µm between adjacent z sections.

FISH images were analyzed using FIJI<sup>474</sup>. Briefly, every four adjacent z stack slices were combined, for a total of 3 µm thickness, in order to minimize missed colocalization, while decreasing false positive colocalization driven by signal from cells at a different depth in a similar x-y position. All channels were thresholded. Cellular ROIs were defined using the retrobead<sup>+</sup> channel information to localize cell bodies. FISH molecule puncta were counted within established cell boundaries. Whether a cell was considered positive for a given marker was determined by setting a transcript-dependent threshold of the number of puncta (e.g., over 5 puncta/soma for Drd1a<sup>+</sup>). These stringent parameters for co-localization and the challenges of

quantifying low abundance receptor transcripts likely lead to underestimation of receptor-positive populations.

### Quantification of behavior

For evaluating locomotor behavior, Toxtrac<sup>476</sup> was used to track the animal's position, defined by its body center position, and quantify the distance travelled in each session. To detect motion onset/offset, movement was defined by the body center moving  $> 30$  mm/sec for at least 0.5 sec. The associated  $\text{Ca}^{2+}$  transients were then aligned to transitions between motion start and stop times and averaged across all animals. Video was recorded and the mouse was tracked with Toxtrac.

Three state transition models were constructed for a given condition and behavioral response, by counting the occurrence of each of the 3 possible 2-response sequences in all animals and then dividing by the total number of the given response. For example, an escape can be followed by another escape, a failure, or a premature trial. The probability of a failure following an escape was calculated by counting the number of failures that followed escapes and dividing it by the total number of escape trials. The graphs for the transition models were constructed using GraphViz<sup>477</sup>. The similarity between transition models was calculated as one minus the Frobenius norm (the Euclidean norm of a matrix) of the difference between models ( $1 - \text{norm}(\text{model}_a - \text{model}_b)$ ). To depict individual learning trajectories, starting at zero, trajectory value incremented by 1 for each escape trial, decremented by 1 for each failure trial, and kept constant for spontaneous transitions in the shuttle box. For the analysis of distributions of % failure to escape, the density histograms of percentage of failures were generated with a bin

width = 4. Density histograms were fitted with the Gaussian distribution using `fitdistrplus` R package using a maximum likelihood estimation.

#### Quantification of fiber photometry data

The heatmap of  $\text{Ca}^{2+}$  transients was constructed by plotting single trial transients with signal amplitude depicted by color. The latency to peak was defined as the time from shock onset to the maximum  $\text{Ca}^{2+}$  transient value within 8 sec of shock onset. The negative and positive area under the curve (AUC) was calculated based on the direction of the peaks. Peaks were omitted from analyses if they were less than 5% of the distance from minimum to maximum  $\text{dF}/\text{F}$  or less than 3 times the standard deviation of the baseline period. The baseline was chosen by using the mean  $\text{dF}/\text{F}$  of the 5 sec segment before the shock onset. For behavioral response-specific  $\text{Ca}^{2+}$  transients, the transients for each behavioral response were averaged within a single subject, and then these data were averaged across all animals. The distance between escape and failure traces for each animal was computed as the Euclidean norm of the difference between the average of all their  $\text{Ca}^{2+}$  transients on escape trials and the average of all their  $\text{Ca}^{2+}$  transients on failure trials ( $\|\text{mean}(\text{escape trials}) - \text{mean}(\text{failure trials})\|_2$ ).

#### Quantification of two-photon $\text{Ca}^{2+}$ sensor imaging

ROIs of dopaminergic neuron somata were defined manually. Raw fluorescence intensity for all frames during 5 min recording sessions was extracted using FIJI<sup>474</sup>. For each neuron, the power spectral density of its baseline adjusted fluorescence was computed using Welch's method<sup>478</sup> with a Hann window and 50% overlap.

#### Statistical analyses

Required sample sizes were estimated based on previous publications and past experience. The number of replicates were reported, and several internal replications are present in the study. No data were excluded after analyses. Animals were randomly assigned to treatment groups. Group statistical analyses were done using GraphPad Prism 7 and 8 software (GraphPad, LaJolla, CA). For N sizes, the number of trials or cells recorded, as well as the number of animals are provided. All data are expressed as mean  $\pm$  SEM, or individual plots. Probabilities are expressed as aggregate probabilities within individuals. For two-group comparisons, statistical significance was determined by two-tailed Student's t-tests. For multiple group comparisons, one-way or two-way analysis of variance (ANOVA) tests were used for normally distributed data, followed by post hoc analyses. For non-normally distributed data, non-parametric tests for the appropriate group numbers were used. Pearson regression was used to detect the correlation between two groups of data.  $p < 0.05$  was considered statistically significant. All computer code generated in the current study is available at [https://github.com/KozorovitskiyLaboratory/Wu\\_et\\_al\\_2021](https://github.com/KozorovitskiyLaboratory/Wu_et_al_2021).

## **Chapter 4 – Wireless multilateral devices for optogenetic studies of individual and social behaviors**

This work was the result of a collaboration between the Kozorovitskiy Lab and the group of Dr. John Rogers. A version of this chapter is published in:

Yiyuan Yang, Mingzheng Wu, Abraham Vázquez-Guardado, Amy J. Wegener, Jose G. Grajales-Reyes, Yujun Deng, Taoyi Wang, Raudel Avila, Justin A. Moreno, Samuel Minkowicz, Vasin Dumrongprechachan, Jungyup Lee, Shuangyang Zhang, Alex A. Legaria, Yuhang Ma, Sunita Mehta, Daniel Franklin, Layne Hartman, Wubin Bai, Mengdi Han, Hangbo Zhao, Wei Lu, Yongjoon Yu, Xing Sheng, Anthony Banks, Xinge Yu, Zoe R. Donaldson, Robert W. Gereau IV, Cameron H. Good, Zhaoqian Xie, Yonggang Huang, Yevgenia Kozorovitskiy & John A. Rogers. *Nature neuroscience*. 24.7 (2021): 1035-1045. <https://doi.org/10.1038/s41593-021-00849-x>

### **Abstract**

Advanced technologies for controlled delivery of light to targeted locations in biological tissues are essential to neuroscience research that applies optogenetics in animal models. Fully implantable, miniaturized devices with wireless control and power-harvesting strategies offer an appealing set of attributes in this context, particularly for studies that are incompatible with conventional fiber-optic approaches or battery-powered head stages. Limited programmable

control and narrow options in illumination profiles constrain the use of existing devices. The results reported here overcome these drawbacks via two platforms, both with real-time user programmability over multiple independent light sources, in head-mounted and back-mounted designs. Engineering studies of the optoelectronic and thermal properties of these systems define their capabilities and key design considerations. Neuroscience applications demonstrate that induction of interbrain neuronal synchrony in the medial prefrontal cortex shapes social interaction within groups of mice, highlighting the power of real-time subject-specific programmability of the wireless optogenetic platforms introduced here.

## 4.1 Introduction

Understanding the functional organization of the central nervous system is a major goal in modern neuroscience research<sup>479</sup>. *In-vivo* optogenetics facilitates this goal by modulating neuronal activity using light stimulation of genetically targeted excitatory or inhibitory opsins<sup>480,481,482</sup>. However, the most common approach—using optical fibers to deliver light from external sources<sup>483,484</sup>—results in steric constraints that can interfere with animals' natural movements and impede the investigation of neural circuits underlying complex behaviors<sup>485,486,487</sup>. Recently developed, battery-free wireless devices that incorporate microscale light emitting diodes ( $\mu$ -ILEDs) and radiofrequency (RF) strategies for wireless power delivery enable fully implantable, tether-free optogenetics studies<sup>485,486,488,489</sup>. The most advanced system variants provide control over optical intensity, pulse duration, and stimulation frequency, with some multimodal operation<sup>488</sup>; yet, they rely on passive modulation of the RF source or deterministic pre-loaded programs in microcontrollers. These control mechanisms limit real-time

modification of stimulation protocols during an experiment. Moreover, the geometrical designs of current wireless platforms allow for only single or dual-probe placement with fixed spacing<sup>486,487,488</sup>, restricting flexible targeting in the brain and periphery. Finally, while subdermal mounting on the head of the animal is straightforward, the location imposes severe constraints on the area available for circuit components and receiver antennas.

These collective limitations are significant for many experimental protocols, including those that require control capabilities for independent modulation of neuronal activity patterns across regions<sup>490,491,492,493</sup> and/or real-time programmability of light delivery to interrogate the casual relationships between neuronal activity and behavioral phenotypes<sup>494,495,496,497</sup>. Also, independent wireless control over multiple individual animals within the same physical space could create unique opportunities to investigate social behavior<sup>498,499</sup>. The overall capabilities of the technology introduced here address these requirements, along with potential for low cost production using advanced manufacturing processes, adapted from the flexible printed circuit board industry, suggesting a strong potential for widespread adoption across the neuroscience community.

## **4.2 Results and discussion**

### **4.2.1 Head mounted and back mounted multilateral optogenetic devices**

The devices described here summarize both head mounted (HM) and back mounted (BM) designs (**Fig. 4.1, Figure 4.1 Supplement 1a**). The devices are wirelessly powered using magnetic inductive coupling provided by a primary dual-loop RF transmission antenna driven at

13.56 MHz wrapped around the experimental enclosure (~ 30 x 30 cm). The user interface controls the near field communication (NFC) protocol that allows independent wireless communication to each device through the same transmission antenna in real-time. **Figure 4.1a** shows an expanded schematic illustration of the HM device (10 x 12 mm, ~1.2 mm thick). The small size allows implantation directly over the top of the skull, underneath the skin, in animal models as small as mice. The device contains laser ablated receiver antenna with soldered electronic components to provide power and active control.  $\mu$ -ILEDs affixed at the tip ends of the penetrating probes provide localized illumination for stimulation or inhibition. Bilateral probes connected to the electronics platform via independent serpentine traces provide large degrees of freedom in positioning during the surgical processes. Parylene (~14  $\mu$ m)/polydimethylsiloxane (PDMS; ~ 30  $\mu$ m at probes and serpentine traces, and ~ 200–800  $\mu$ m elsewhere) bilayer encapsulates the device and provide soft contact with surrounding tissues. The advanced HM device platform (**Fig. 4.1b**) incorporates an analog filter, an NFC system-on-a-chip (SoC), and a micro-controller for dynamically programmable operation (**Fig. 4.1 Supplement 1b**) of two independent channels. Simplified versions of these devices selectively support voltage regulation (**Fig. 4.1 Supplement 1c**) for experiments that only require synchronized bilateral stimulation at fixed intensity.

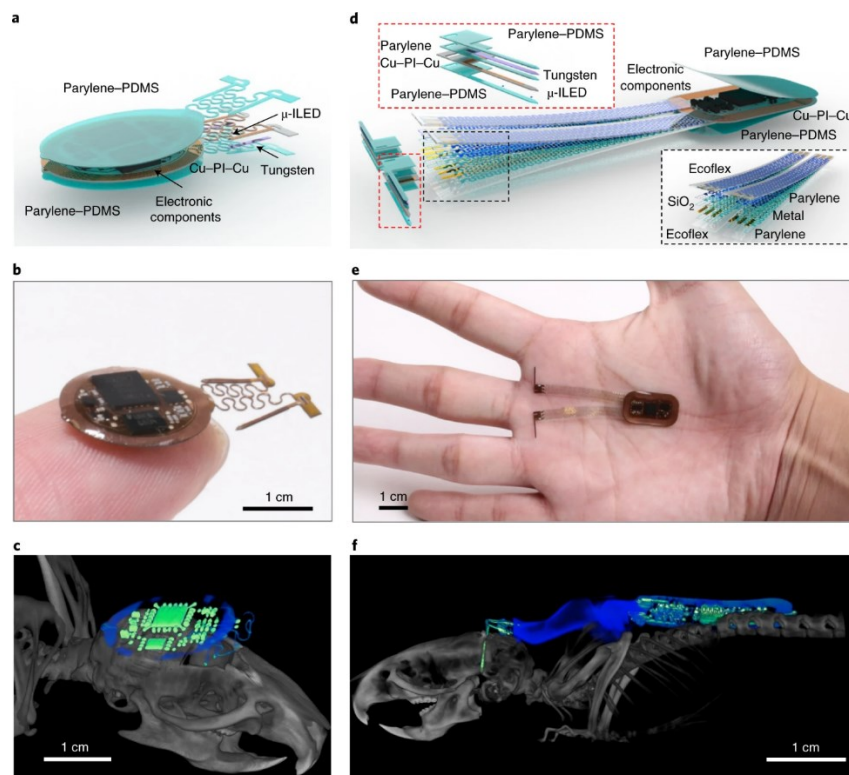


**Figure 4.1. Device layout and implantation.** **a**, Layered schematic illustration of an HM, subdermal device for optogenetic research in untethered animals with dynamically programmable operation. PI, polyimide. **b**, Photograph of the HM device. **c**, CT image of an HM device (**b**) in a mouse model. **d**, Layered schematic illustration of a similar device with a BM, subdermal design. **e**, Photograph of the BM device. **f**, CT image of a BM device (**e**) in a mouse model.

The lateral dimensions of HM devices cannot exceed the top surface of the skull of the animal ( $\sim 100 \text{ mm}^2$  for mice), restricting advanced embodiments of larger sizes and power requirements. A solution that largely circumvents these considerations utilizes the broad space on the back of the animal. Here, BM subdermal implants can include relatively large receiver coils (11 x 19 mm) and complex electronics encapsulated in parylene/PDMS bilayer similar to HM devices. The penetrating probes connect to electronic platform through thin ( $\sim 390 \text{ nm}$ ) serpentine metallic traces encapsulated in soft elastomers ( $\sim 200 \mu\text{m}$ ) to yield mechanics compatible with the

implantation procedure and natural motion of the animal, without adverse effects (**Fig. 4.1d**). An example device illustrating this design offers dynamically programmable operation (**Fig. 4.1 Supplement 1b**) with four independent  $\mu$ -ILEDs (**Fig. 4.1e**). The layouts can be further extended to  $\mu$ -ILED arrays that integrate injectable probes or compliant substrates at additional interface locations, including peripheral nerves, heart, spinal cord, and others. Microscale computed tomography (CT) images of mice with the HM or BM implants are in **Fig. 4.1c** and **Fig. 4.1f**. Studies indicate chronic stability in operation for >9 weeks, the longest tested period.

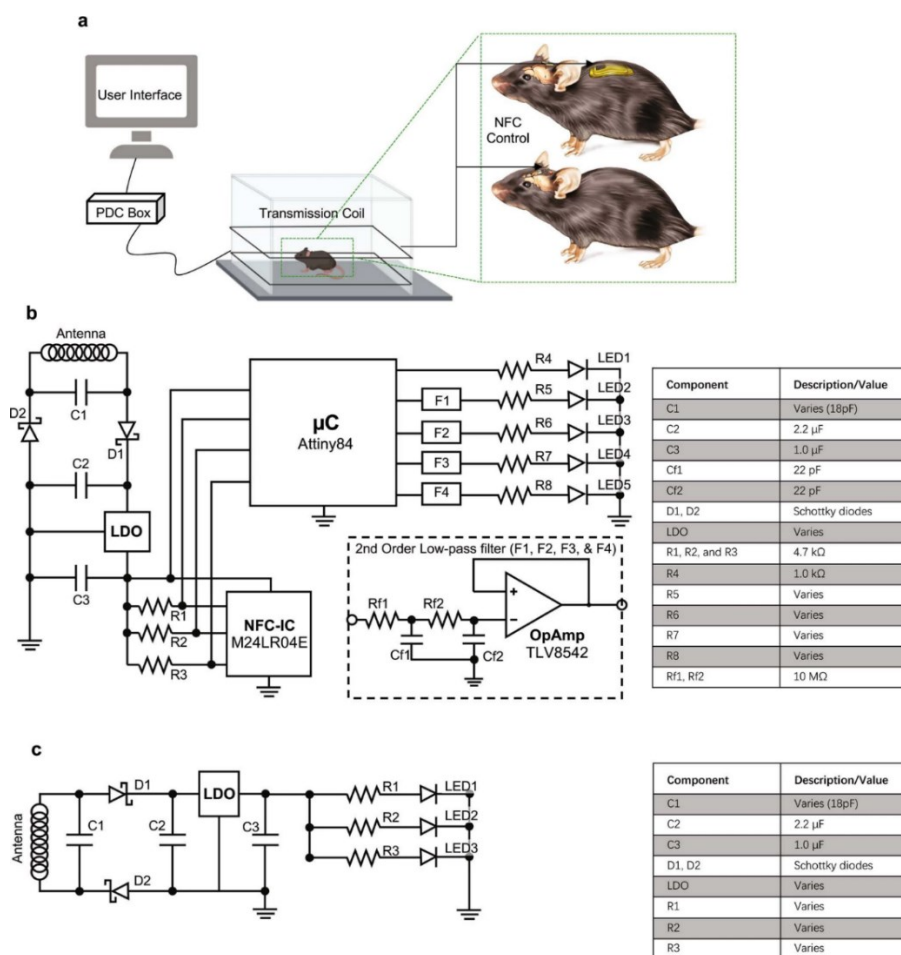


**Figure 4.1 Supplement 1. Electrical circuit implemented in the NFC-enabled platform. a**, The experimental platform includes the implanted device, transmission antenna, power distribution

(PDC) box, and PC with user interface. The device is wirelessly programmed using a PC in a real-time manner through near field communication (NFC) control over the stimulation parameters. **b**, The NFC corresponds to an RF addressable memory chip supporting ISO15693 protocol. The microcontroller interfaces to the NFC memory via the I2C communication protocol. Up to four channels are supported by the microcontroller's firmware, independently controlled by the end user. Each channel is filtered using a second order low-pass passive filter whose output is coupled by a high impedance voltage follower that drives the  $\mu$ -ILED. The number of channels to be used depends on the type of implant: two for head mounted devices or four for back mounted devices. **c**, Simple voltage regulation circuit that implements a low dropout regulator (LDO) that passes current directly to the  $\mu$ -ILEDs and resistor after rectification. The component bill of materials is also shown.

#### 4.2.2 Mechanical characterization for multilateral optogenetic devices

The electrical connections between the electronics and the probes for BM devices must support a wide range of continuous motion across the back and neck regions during natural movement.

Video graphic analysis using DeepLabCut<sup>500</sup> yields quantitative estimates of the range of deformations associated with natural mouse motion at the head, neck, back, and tail regions (**Fig. 4.2a** and methods), defining compliance requirements in the interconnect structures. Specifically, changes in distance from head-to-neck and neck-to-back determine the magnitudes of compression and elongation. Variations in the circumradius of the head-neck-back triangle determine the levels of bending. The probability distribution in **Fig. 4.2b** shows ranges of ~30% for compression and ~60% for elongation. **Figure 4.2c** shows the corresponding probability distribution for bending ranging from ~1 cm to ~30 cm.

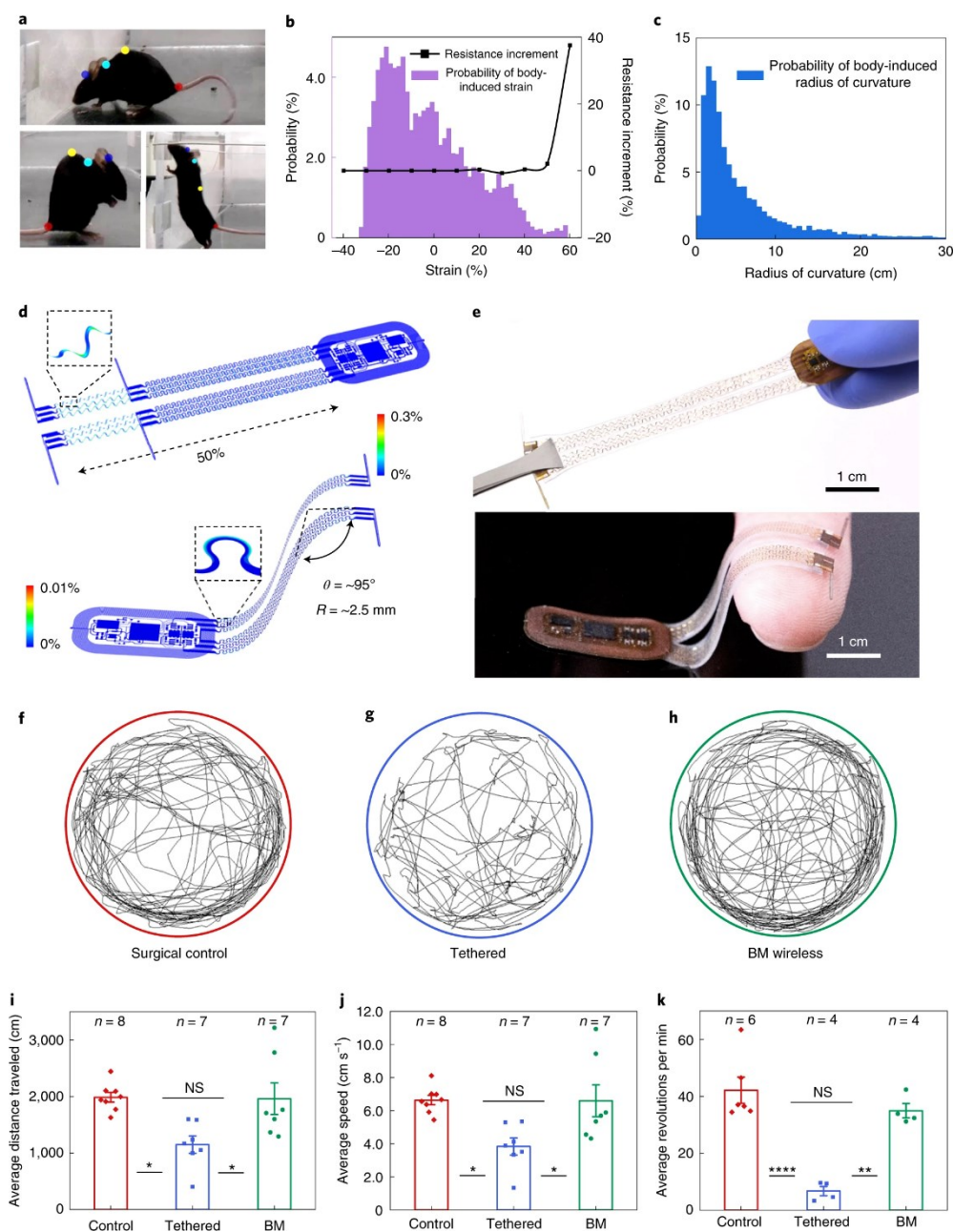


**Figure 4.2. Characterization of mechanical properties and effects on animal locomotor behavior.** **a**, Photograph of the curvature of the body of a mouse and changes in this curvature during natural movements. The colored dots mark points on the head, neck, back and tail of the mouse for characterizing these changes as the mouse moves in an enclosure. **b**, Probability distribution of tensile strains (that is, compressing and stretching) associated with routine activities and benchtop tests of changes in resistance of the stretchable interconnects used for the BM-device platform after 10,000 cycles of stretching and compressing (black line) at 1 Hz. **c**, Corresponding

probability distribution of bending deformations (that is, radius of curvature). **d**, FEA simulations of a stretched and bent BM device. **e**, Photographs of a stretched and bent device. **f–h**, Results of motion tracking (5 min in a circular arena) for independent, freely moving mice (surgical control), for mice implanted with bilateral optical fibers (tethered) and for mice implanted with BM devices (BM wireless). **i,j**, The same cohorts of biologically independent animals (control,  $n = 8$ ; tethered,  $n = 7$ ; BM wireless,  $n = 7$ ) were used to derive these results over three independent experiments. **i**, Average distance traveled over 5 min in the circular arena (one-way ANOVA, Tukey's multiple-comparisons test; control versus tethered,  $P = 0.01$ ; tethered versus BM wireless,  $P = 0.02$ ; control versus BM wireless,  $P = 0.99$ ). NS, not significant. **j**, Average movement speed over 5 min in the circular arena (one-way ANOVA, Tukey's multiple-comparisons test; control versus tethered,  $P = 0.02$ ; tethered versus BM wireless,  $P = 0.02$ ; control versus BM wireless,  $P = 0.99$ ). **k**, Average revolutions per minute when running on a wheel over a 60-min period (one-way ANOVA, Tukey's multiple-comparisons test; control versus tethered,  $P < 0.0001$ ; tethered versus BM wireless,  $P = 0.0014$ ; control versus BM wireless,  $P = 0.40$ ). Biologically independent animals (control,  $n = 6$ ; tethered,  $n = 4$ ; BM wireless,  $n = 4$ ) were used to derive these results over three independent experiments. All data are represented as mean  $\pm$  s.e.m. \* $P < 0.05$ , \*\* $P < 0.01$ , \*\*\*\* $P < 0.0001$ .

The designs of the interconnects of the BM devices support repetitive deformations across these ranges. Finite element analysis (FEA) and experimental results (**Fig. 4.2d**) show that the constituent materials of the interconnects remain in an elastic response regime for uniaxial stretching of up to 50% and for 95° bending at a radius of curvature of 2.5 mm (**Fig. 4.2d-e**). The equivalent strains in the metals are less than their yield strains ( $\sim 0.3\%$ )<sup>501</sup>, as are the strains in the polymers. Systematic experimental studies using cyclic tests (10,000 cycles, 1 Hz) at different stretching levels define transition threshold from elastic to plastic deformation. In the elastic region, the electrical resistance of the interconnects remains nearly unchanged. Plastic deformations lead to notable increases in resistance. The results, highlighted in **Fig. 4.2b** (black line), define an elastic range that extends to a stretch of  $\sim 50\%$  (resistance change  $< 3\%$ ), consistent with FEA results (**Fig. 4.2d**). Unlike for the BM devices, the serpentine traces in the HM devices can be plastically deformed to target positions during implantation because they

remain fixed in these positions by anchoring to the skull with dental cement. **Figure 4.2 Supplement 1** shows typical mechanical deformations for the HM devices during and after implantation, which remain well below the fracture point<sup>502</sup>.

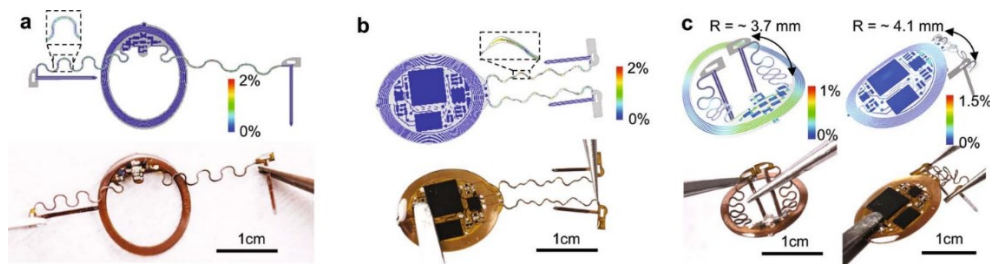


**Figure 4.2 Supplement 1. Mechanical deformations for head mounted devices. a, b,** FEA simulations and photographs of 30% stretching of different head mounted devices. **c,** FEA simulations and photographs of these devices deformed into various configurations after implantation.

For both classes of devices, the impact on locomotor behaviors is negligible. Natural behavior patterns of mice implanted with HM devices are similar to those of mice without implantation (**Figure 4.2 Supplement 2**), consistent with previous studies<sup>503</sup>. **Figures 4.2f-h** present representative single mouse movement tracks over a five-minute period in an open-field environment. Reductions in the average distance traveled (**Fig. 4.2i**; ANOVA;  $F = 6.607$ ;  $P = 0.0066$ ) and average speed during movements (**Fig. 4.2j**; ANOVA;  $F = 6.418$ ;  $P = 0.0074$ ) are seen in mice implanted with, and tethered by, optical fibers. Meanwhile, mice implanted with BM devices exhibit near identical travel distances (NS;  $P = 0.99$ ) and movement speeds (NS;  $P = 0.99$ ) compared to surgical controls. Additional tests examine mobility across the groups ( $n = 4-6$ ) using a running wheel experiment. Mice implanted with BM devices exhibit similar average revolutions per minute as controls over a 60-minute period (NS;  $P = 0.40$ ), while tethered mice

run less than control and BM groups (**Fig. 4.2k**, ANOVA;  $F = 23.12$ ;  $P = 0.0001$ ). Collectively, these experiments demonstrate that the BM devices do not restrict animal's natural movement and maintain function during routine activity.

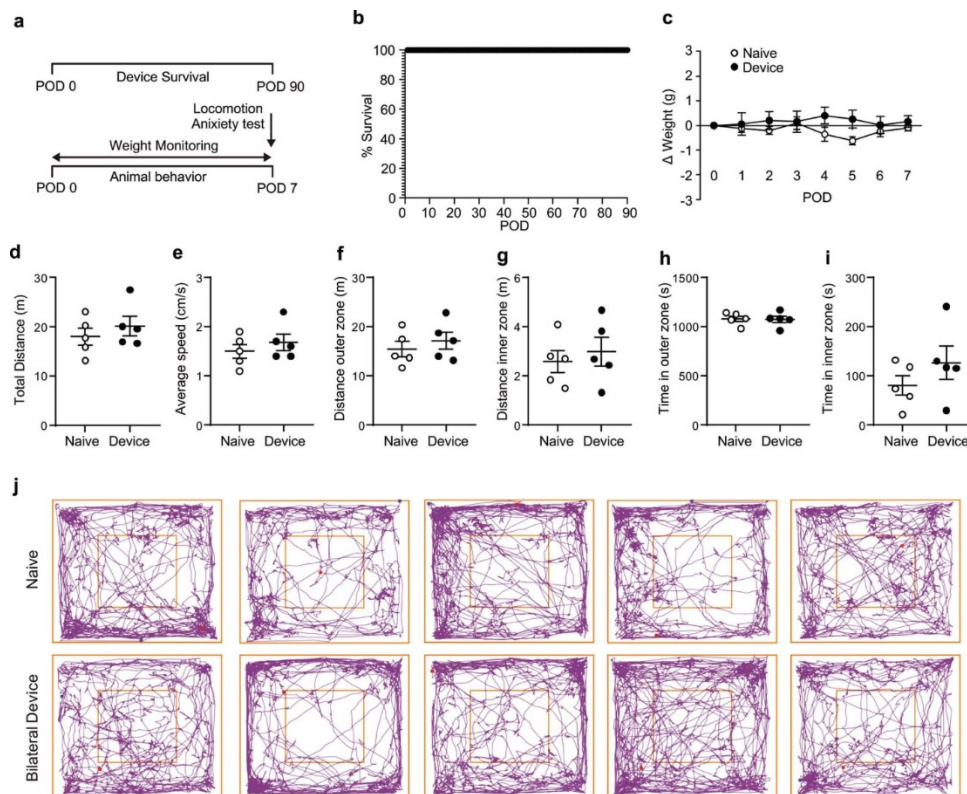


**Figure 4.2 Supplement 2. Device longevity and behavioral outcomes for head mounted devices.** **a**, Cartoon representation of the timeline for monitoring device longevity and animal postoperative behavior. **b**, Routine testing of head mounted devices for 90 days ( $n = 5$  animals). **c**, Normalized weight assessment for 7 postoperative days (POD) after implantation of head mounted device (two-way ANOVA Sidak's multiple comparison test; POD1  $P = 0.9998$ , POD2  $P = 0.9491$ , POD3  $P > 0.9999$ , POD4  $P = 0.3731$ , POD5  $P = 0.2038$ , POD6  $P = 0.9966$ , POD7  $P = 0.9966$ ;  $n = 5$  naïve &  $n = 5$  device animals). **d**, Total distance traveled ( $P = 0.6905$ ), **e**, Average speed ( $P = 0.5952$ ), **f**, Distance in the outer zone ( $P = 0.6905$ ), **g**, Distance in the inner zone ( $P > 0.9999$ ), **h**, Time in the outer zone ( $P > 0.9999$ ), **i**, Time in the inner zone ( $P = 0.5476$ ). (**d-i**), Locomotion effects of implantation were assessed using the open field test and a variety of parameters were measured (two-tailed unpaired t-test, Mann Whitney test;  $n = 5$  naïve &  $n = 5$  device animals). **j**, Graphical representation of individual animal behavior, implanted animals (top row) versus naïve

controls (bottom row) in the open field test. Outer and inner squares represent the two zones. All data are represented as mean  $\pm$  s.e.m.

### 4.2.3 Biocompatibility characterization for multilateral optogenetic devices

Additional experiments assess biocompatibility of the implantable device components, including the injectable probes with tungsten stiffeners and BM subdermal implants. Immunohistochemical markers of glial cells, microglia, and hemoglobin yield insights into implantation-associated gliosis and hemorrhage (see Methods). Mice implanted with wireless probes or 200  $\mu$ m diameter optical fibers show similar astrocytic and microglial activation (**Figure 4.2 Supplement 3a-e**). No difference in hemoglobin immunoreactivity between conditions is observed (**Figure 4.2 Supplement 3f**). The wireless probe does not induce significant damage to the brain, as the ratio of measured damage and estimated damage is  $\sim$ 1 (**Figure 4.2 Supplement 3g**). These data suggest that the biocompatibility of wireless probes with encapsulated tungsten is similar to optical fiber.

To determine whether BM implants induce erosion of proximal tissue or spinal impact, BM implanted, and sham surgery control mice were compared 40 days after implantation (**Figure 4.2 Supplement 3h**, see Method for process detail). No significant differences in morphology of surrounding muscles and skins, evidenced by H&E staining, were observed in implanted mice compared to controls (**Figure 4.2 Supplement 3i-k**). MicroCT imaging results confirm no significant changes in bone density associated with the implants (**Figure 4.2 Supplement 3l**).

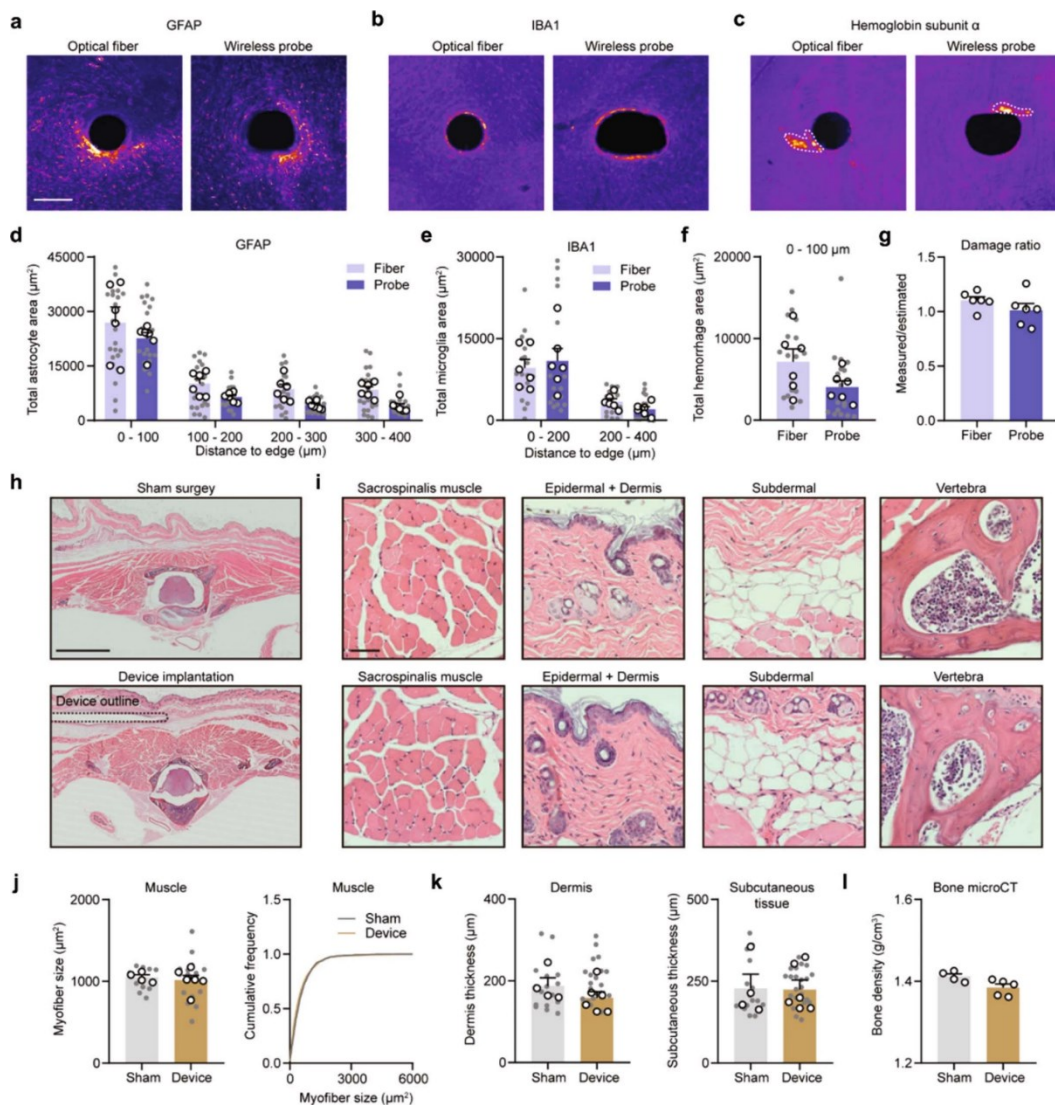


**Figure 4.2 Supplement 3. Biocompatibility of injectable probes and back mounted implants.**

**a**, Astrocytic (GFAP) immunoreactivity surrounding the implantation site of an optical fiber (left) and a wireless probe (right). Scale bar, 200  $\mu\text{m}$ . **b-c**, Same as **(a)**, but for microglia (IBA1) and hemorrhage (hemoglobin subunit  $\alpha$ ). **d**, Summary data showing total astrocyte dense (GFAP) area at different distances from the edge of implantation. Two-way ANOVA, Sidak's multiple comparisons test (Fiber vs Probe), 0-100  $\mu\text{m}$ ,  $P = 0.3477$ , 100-200  $\mu\text{m}$ ,  $P = 0.4931$ , 200-300  $\mu\text{m}$ ,  $P = 0.3285$ , 300-400  $\mu\text{m}$ ,  $p = 0.3022$ .  $n = 22 - 23$  slices from 6 brains/group. **e**, Same as **(d)**, but for microglia (IBA1). Two-way ANOVA, Sidak's multiple comparisons test (Fiber vs Probe), 0-200  $\mu\text{m}$ ,  $P = 0.7692$ , 200-400  $\mu\text{m}$ ,  $P = 0.7414$ .  $n = 18$  slices from 6 brains/group. **f**, Same as **(d)**, but for hemorrhage (hemoglobin subunit  $\alpha$ ). Two-tailed unpaired t-test,  $P = 0.1054$ .  $n = 18$  slices from 6 brains/group. **g**, Summary data show the ratio between measured brain damage and

estimated brain damage, based on probe size. Two-tailed unpaired t-test ANOVA,  $P = 0.2191$ .  $n = 6$  brains/group. **h-i**, H&E staining images show the morphology of the back tissues in mice that went through sham surgery or BM device implantation. Scale bar, 5 mm and 20  $\mu\text{m}$ . **j**, Left, summary data showing average sacrospinalis myofiber size in BM implant and control mice. Two-tailed unpaired t-test,  $P = 0.6714$ . Right, cumulative frequency of myofiber size.  $n = 10$  slices from 4 animals (Sham),  $n = 17$  slices from 6 animals (Device). **k**, Summary data showing the thickness of dermis (left) and subcutaneous tissue (right) in mice after BM implantation of sham surgery. Two-tailed unpaired t-test, Dermis,  $P = 0.2650$ , Subcutaneous tissue,  $P = 0.9517$ .  $n = 16$  slices from 4 animals (Sham),  $n = 24$  slices from 6 animals (Device). **l**, Summary data for bone density in mice after sham surgery or BM implantation. Mann Whitney test,  $P = 0.0635$ .  $n = 4-5$  animals/group. **d-f, j, and k**, white open circles: average value for each animal, grey filled circles: value for individual ROIs/brain slices.

#### 4.2.4 Dynamically programmable multichannel operation

The technology introduced here supports bidirectional wireless communication, qualitatively expanding device functionality. The result provides full, continuous, and nondeterministic real-time wireless control over all relevant optogenetics stimulation parameters, including intensity, frequency, and duty cycle. Additional capabilities, crucial for neuroscience research, include arbitrary implementation of multichannel operation: unilateral or bilateral stimulation, and control over multiple devices within the same enclosed space. The elements that enable these capabilities are NFC read/write random access memory (M24LR04E, ST-Microelectronics) and an 8-bit microcontroller (ATtiny84, Atmel Corp.). **Figure 4.1 Supplement 1** shows the generic electronic diagram. The user addresses the microcontroller firmware using a personal computer running a customized graphical user interface (GUI) that interfaces with the RF power and communication module, supporting the ISO15693 NFC protocol (LRM2500-A, Feig Electronic). Upon a wireless command, the microcontroller reads operational parameters from the NFC memory—period, duty cycle, intensity, and mode of operation—which are then updated into the

firmware to operate up to four channels independently (**Fig. 4.3a**). **Figure 4.3b** shows the mice implanted with HM and BM devices inside the cage.

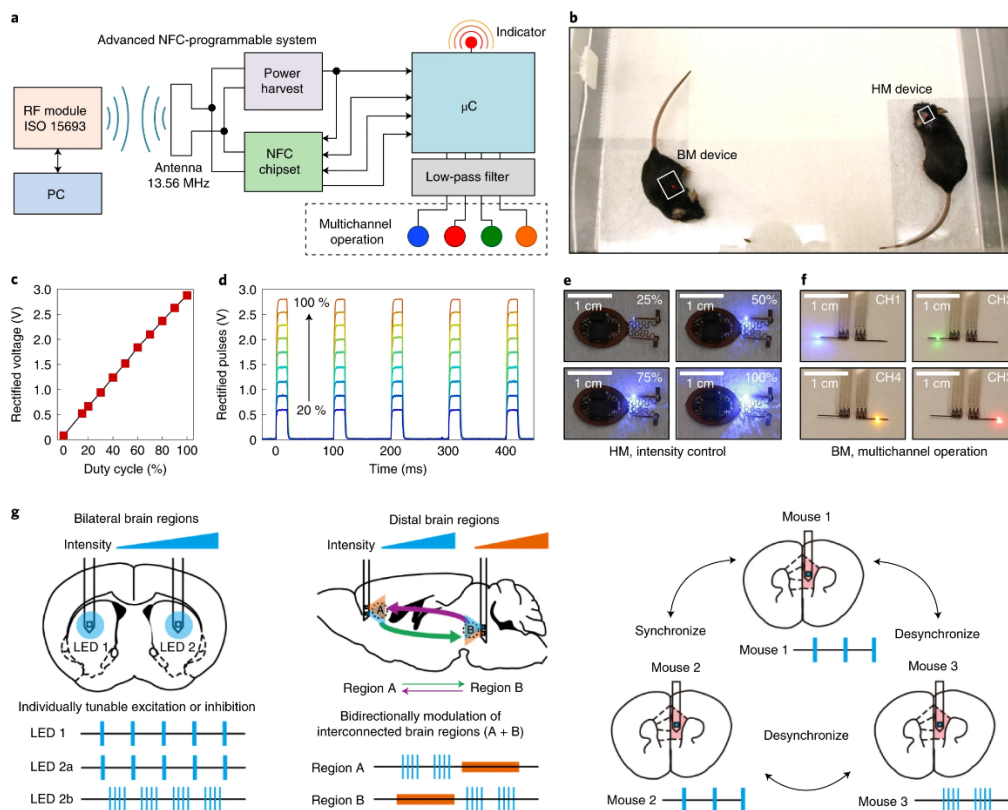


**Figure 4.3. Designs, operational features and use cases for dynamically programmable NFC electronics.** **a**, Block diagram of an NFC-enabled platform for independent, programmable control over operational parameters. Microcontroller firmware coupled with this electronic module allows multichannel selection and control over the period ( $T$ ), duty cycle and intensity of the  $\mu$ -ILEDs. PC, personal computer;  $\mu$ C, microcontroller. **b**, Photograph of HM and BM devices implemented with dynamically programmable NFC electronics, operating after implantation in mice. **c**, Filter output voltage as a function of duty cycle of the intensity-encoding carrier waveform (Extended Data Fig. 5b). **d**, Time dependence of output waveforms with a period of 100 ms and a duty cycle of 20% at various peak voltage magnitudes. The carrier frequency is 2 kHz, and the duty cycle varies from 20% to 100%. **e**, Sequence of photographs of an HM device operated at different duty cycles of the carrier waveform, to control the intensity of one of the two  $\mu$ -ILEDs. **f**, Sequence of photographs of a BM device showing multichannel operation. **g**, Schematic illustrations of several potential applications of this technology in optogenetic studies, including tunable modulation of

bilateral brain regions (left), bidirectional modulation of distal regions (middle) and multi-brain synchrony manipulation (right).

Each channel in the microcontroller supports an amplitude modulated digital signal (AM-DS) at its general purpose input/output (GPIO), which controls dynamics for optical stimulation and the optical intensity of the corresponding  $\mu$ -ILED. **Figure 4.3 Supplement 1a** shows schematic illustrations of time traces of the AM-DS. Here, a low frequency signal (signal: period,  $T1$ ; duty cycle,  $DC1$ ) modulates a high frequency signal (carrier: period,  $T2$ ; duty cycle,  $DC2$ ). The former encodes the pulse duration and frequency of the stimulation, while the latter encodes voltage control. These parameters are extracted using a second-order passive low-pass filter that performs digital to analog conversion in the time domain. Consider an arbitrary AM-DS, as depicted in **Figure 4.3 Supplement 1a**, where the time dependent amplitude  $A(t)$  can be described in a Fourier series as

$$A(t) = A_0 \sum_{n1=-\infty}^{\infty} C_{n1} e^{-i\omega_{n1}t} \sum_{n2=-\infty}^{\infty} C_{n2} e^{-i\omega_{n2}t}$$

where  $A_0$  is the amplitude,  $n_{1,2}$ ,  $C_{n1,2}$  and  $\omega_{n1,2}$  ( $= 2\pi n_1 f_{n1}$ ,  $2\pi n_2 f_{n2}$ ) are the indices, coefficients and frequency harmonics of the signal (1) and carrier (2), respectively. The fundamental frequencies are  $f_{01} = 1/T1$  and  $f_{02} = 1/T2$ . A low-pass filter with cut-off frequency,  $f_c$ , larger than the signal ( $f_c > f_{01}$ ) but smaller than the carrier ( $f_c < f_{02}$ ), filters out the fundamental and higher harmonics of the carrier, while its direct current ( $dc$ ) component and the signal remain, as graphically illustrated in **Figure 4.3 Supplement 1b**. For a square wave, the  $dc$  component is equal to the

duty cycle,  $C_{02} = DC2$ . Thus, the AM-DS becomes a low frequency signal whose amplitude is determined by DC2:

$$A(t) \approx A_0 C_{02} \sum_{n1=-\infty}^{\infty} C_{n1} e^{-i\omega_{n1}t}$$

The microcontroller firmware, running at 1 MHz, supports signals with periods between 1 and 65000 ms and duty cycles between 1 and 100%; and carriers with periods between 0.5 and 65 ms and duty cycles between 15 and 100%. The cut-off frequency of the second order passive filter is designed to 700 Hz and the carrier frequency implemented in the AM-DS is 2 kHz. **Figure 4.3c** shows the analog voltage waveform of a filtered AM-DS, where the period and duty cycle of the signal are  $P1 = 100$  ms (10 Hz) and  $DC1 = 20$  %, respectively. **Figure 4.3d** shows the corresponding voltage traces at different voltage levels, and the pre- and post-filtered voltage traces, respectively. These results illustrate that individual channels can be driven at different voltage levels, as observed in the intensity of the blinking  $\mu$ -ILED. **Figure 4.3e** displays images of an HM device with a blue  $\mu$ -ILED operating at different optical intensities. **Figure 4.3f** presents images of a BM device with four different  $\mu$ -ILEDs individually activated wirelessly in an experimental enclosure.

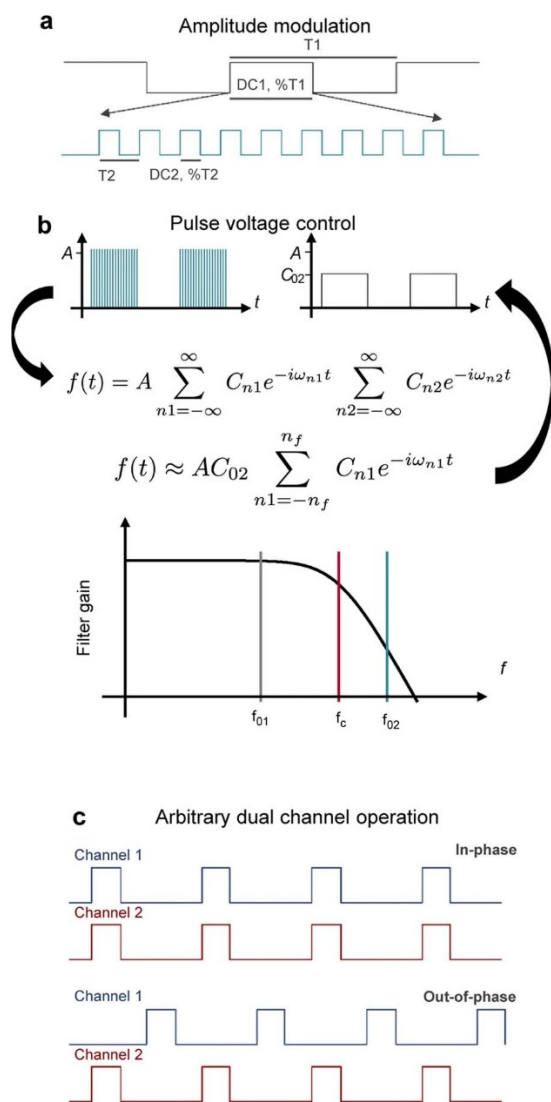


**Figure 4.3 Supplement 1. Dynamically programmable platform operation with intensity control.** **a**, Generic time diagram that depicts the dynamic parameters accessible via NFC programming. Each channel supports amplitude modulation with signal/carrier defined by period  $T1/T2$  and duty cycle  $DC1/DC2$ , respectively. **b**, Voltage control implemented by amplitude modulation and its frequency interaction with a passive low-pass filter with cut-off frequency at  $f_c$ . While the information signal contained in its low order harmonics,  $f_{01} < f_c$ , passes almost unchanged, the high frequency carrier,  $f_{02} > f_c$ , is filtered to its direct current component, which is proportional to the duty cycle of the carrier. **c**, Multichannel operation mode representation. This platform allows single channel operation addressed individually, dual operation of any arbitrary channel combination with two modes, in-phase and out-of-phase.

The introduced dynamic programmable NFC system offers accurate real-time wireless control over frequency ( $\pm 1.5\%$  accuracy) with pulse width as short as 3 ms. The pulse limit can be further shortened down to 234  $\mu$ s at the expense of removing the intensity control capability. In this manner, the low frequency component of the AM-DS involves a 1 ms temporal window that allows a single low duty cycle oscillation of the high frequency component (1 kHz). This mode of operation also enables programmable burst stimulation where the low frequency component determines the burst cycles and the high frequency component dictates the illumination dynamics.

The optogenetic device firmware allows selection across different  $\mu$ -ILEDs with wide-ranging control over patterns of illumination. For example, in the HM device, four illumination configurations are possible with two independent  $\mu$ -ILED channels: single channel (unilateral) or dual channel in-phase or 180° out-of-phase (bilateral), as graphically depicted in **Figure 4.3 Supplement 1c**. With arbitrary pulse width and frequency selection, the out-of-phase mode operation also supports variable delay operation, *i.e.* controlling the bilateral stimulation time delay as described in **Figure 4.3 Supplement 1c**. The increased available area for electronic components and harvesting power in the BM device enables operating four independent  $\mu$ -ILEDs. Sixteen modes of operation are possible: four unilateral, six out-of-phase and six in-phase bilateral. Another feature of this technology is device addressing capability. Each NFC chip is hardware encoded with a 64-bit unique identifier (UID) code that individually address a targeted device upon each command. The RF NFC reader can discover up to 256 devices simultaneously and communicate with any device with a known UID.

Our technology expands possibilities for advanced stimulation protocols in optogenetics. Several examples are schematized in **Fig. 4.3g**. The simplest case is synchronized excitation or inhibition of bilateral or distal brain regions (**Fig. 4.3g**). Additional possibilities (**Fig. 4.1b**) follow from regulation of neuronal activity by controlling the stimulation dynamics of  $\mu$ -ILED channels independently within the same subject. Individually tunable excitation and inhibition lines provide further controls over stimulation modes, frequencies, and pulse durations, with real-time user control (**Fig. 4.3g**, left). With  $\mu$ -ILEDs of different wavelengths tailored to corresponding opsins, studies of the interactions of different brain regions in a behavioral context might exploit desynchronized patterns of optogenetic excitation or inhibition. Moreover, additional power and space provided by BM devices (**Fig. 4.1e**) allow for bidirectional modulation of interconnected brain regions, where independent, dynamic control over at least four  $\mu$ -ILEDs is important (**Fig. 4.3g**, middle). Finally, the capacity of real-time reprogramming and independent control over multiple devices enable the possibility of studying complex social behavior involving multiple animals, with individualized stimulation parameters (**Fig. 4.3g** right). Additional options follow from full use of the GPIO of the microcontroller for operation of up to eight channels. See Methods for hardware implementation and customized software operation of control system for behavior experiments.

#### **4.2.5 Optical and Thermal Characterization of the $\mu$ -ILEDs**

The illumination intensity and excitation volume for given operational parameters, as well as the associated thermal loads on the adjacent tissue are discussed in this section. The energy

conversion efficiency (ECE) of the  $\mu$ -ILEDs determines the thermal power generated. The ECE of blue (460 nm), green (535 nm), orange (590 nm) and red (630 nm)  $\mu$ -ILEDs are 36.1%, 6.6%, 6.4% and 26.7%, respectively. These parameters, together with the electrical power wirelessly harvested by the device, determine stimulation intensities. Present studies consider RF power applied through an antenna on a standard 30 cm (w) x 30 cm (l) x 12 cm (h) experimental cage, in a double loop configuration at heights of 3 and 9 cm from the base (**Fig. 4.4a**). Simulated results for the magnetic field intensity distribution at the plane in the middle between the double loop antenna (**Fig. 4.4a**) reveal a spatially inhomogeneous magnetic field. Active voltage regulation implemented in the devices yields constant power delivery to  $\mu$ -ILEDs throughout the experimental enclosure.

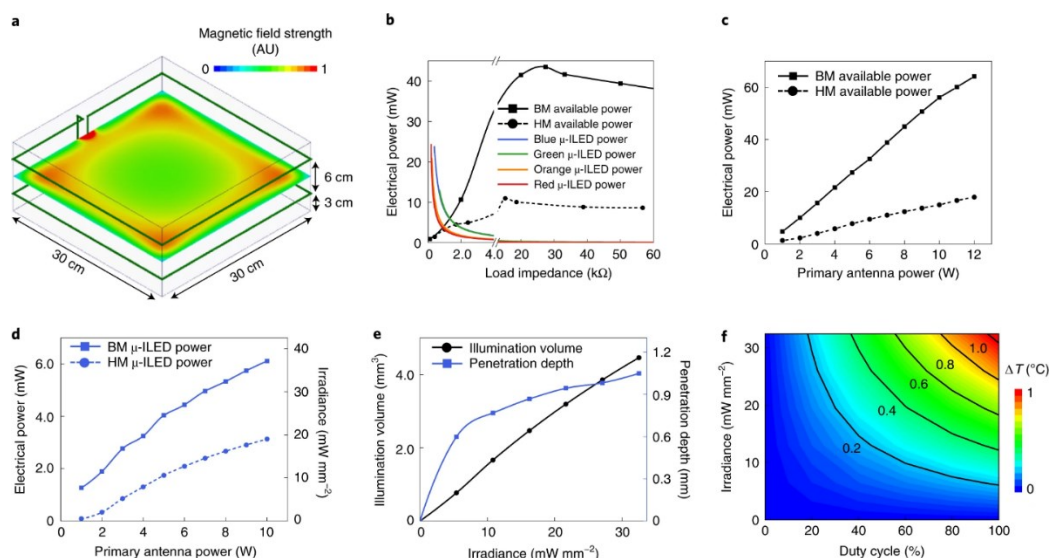


**Figure 4.4. Characterization of optical and thermal properties.** **a**, Simulated magnetic-field-intensity distribution at the central plane of a cage (dimensions, 30 cm (length)  $\times$  30 cm (width)  $\times$  15 cm (height)) surrounded by a double-loop antenna at heights of 3 cm and 9 cm. AU, arbitrary units. **b**, Electrical power supplied to HM and BM coils and different  $\mu$ -ILEDs (460 nm, 535 nm, 595 nm, 630 nm) as a function of internal working impedance at 8 W of RF power applied to the transmission antenna. **c**, Maximum harvested power as a function of RF power applied to

the transmission antenna for HM and BM coils. **d**, Maximum electrical and optical power for a single blue  $\mu$ -ILED (460 nm) as a function of RF power applied to the transmission antenna for HM and BM devices. **e**, Illumination volume and penetration depth as a function of the output irradiance of the blue  $\mu$ -ILED (460 nm) (cutoff intensity,  $0.1 \text{ mW mm}^{-2}$ ). **f**, Temperature change ( $\Delta T$  ( $^{\circ}\text{C}$ )) at the interface between the  $\mu$ -ILED and brain tissue as a function of operational irradiance of the blue  $\mu$ -ILED (460 nm) and its duty cycle at a frequency of 20 Hz.

HM and BM devices have different power harvesting capabilities due to differences in the size of the receiver coils. The IV characteristics of the  $\mu$ -ILEDs define relationships between their electrical power and their internal impedance during operation (**Fig. 4.4b**  $\mu$ -ILED). The maximum power to the  $\mu$ -ILED results when its impedance finds equilibrium with that of the receiver coil, as observed as the intersection between power-impedance characteristics curves in **Fig. 4.4b**. The power from the receiver coil also depends on the RF power applied to the transmission antenna. **Figure 4.4c** summarizes the maximum electrical power that can be harvested by HM and BM devices as a function of power to the transmission antenna. The maximum electrical power and corresponding optical irradiance that each blue  $\mu$ -ILED can reach with respect to the power to the transmission antenna for HM and BM devices appears in **Fig. 4.4d**. Corresponding thermal powers are in **Figure 4.4 Supplement 1a**. Similar information for other  $\mu$ -ILEDs are in **Figure 4.4 Supplement 1b-e, g, i**. The power not consumed by the  $\mu$ -ILEDs can be exploited for the control electronic system and for future applications in biosensing or for novel illumination schemes that rely on arrays of  $\mu$ -ILEDs.

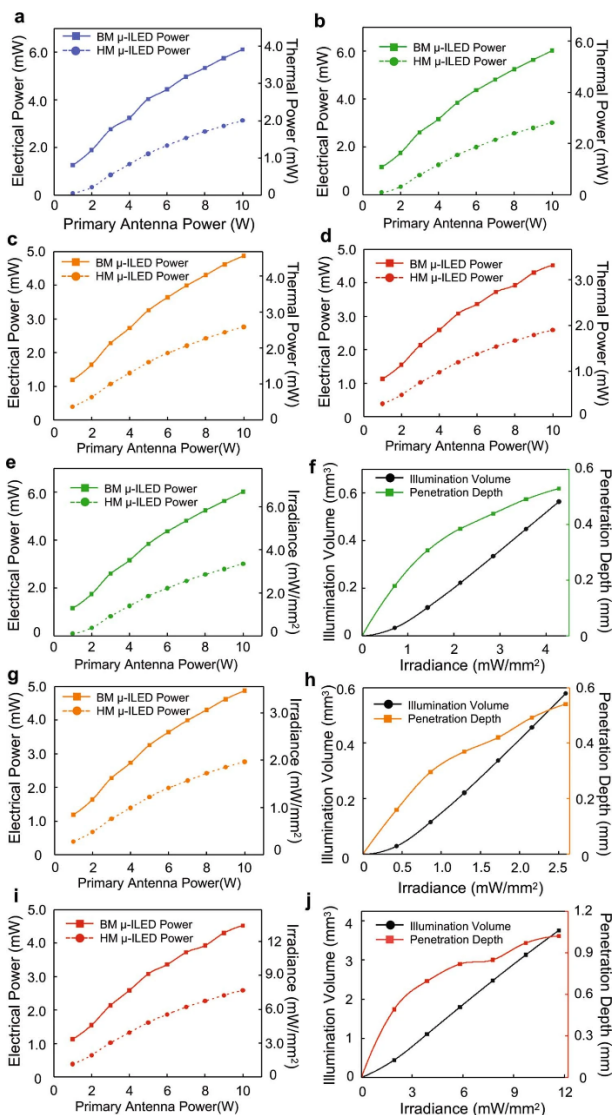


**Figure 4.4 Supplement 1. Thermal power, irradiance, illumination volume, and penetration depth of  $\mu$ -ILEDs.** **a**, Maximum electrical and thermal power for a single blue  $\mu$ -ILED (460 nm) as a function of RF power applied to the transmission antenna for HM and BM devices. **b**, **c**, **d**, Same measurements as reported in **(a)** for green (535 nm), orange (590 nm), and red (630 nm)  $\mu$ -ILEDs respectively. **e**, Maximum electrical and optical irradiance for a single green  $\mu$ -ILED (535 nm) as a function of RF power applied to the transmission antenna for HM and BM devices. **f**, Illumination volume and penetration depth as a function of optical irradiance from a green  $\mu$ -ILED (535 nm; cutoff intensity 0.1 mW/mm<sup>2</sup>). **g**, **h**, Same measurements and simulations as reported in **(e)** and **(f)** respectively for an orange  $\mu$ -ILED (590 nm). **i**, **j**, Same measurements and simulations as reported in **(e)** and **(f)** respectively for a red  $\mu$ -ILED (630 nm).

The optical and thermal power levels described above serve as the basis for numerical simulations of the illumination and temperature profiles through adjacent biological tissues, as detailed in the Methods. The transport of light through the brain depends on wavelength-dependent scattering and absorption coefficients, input power, as well as spatial and angular emission profiles. Dynamic voltage control further enables users to program the  $\mu$ -ILED optical power and thus the illumination volume and penetration depth. **Figure 4.4e** shows this capability as a function of input optical power of a blue  $\mu$ -ILED. Examples for other  $\mu$ -ILEDs are in **Figure 4.4 Supplement 1f, h, j**.

Numerical simulations of the temperature distributions on surrounding brain tissue rely on the thermal power dissipation in the  $\mu$ -ILED, optical absorption, and thermal properties of the device and surrounding biological tissue. Highest temperatures occur at the surface above the  $\mu$ -ILED that directly contacts the brain tissue. **Figure 4.4f** shows this temperature increment for a range of irradiances and duty cycles, for a typical stimulation frequency of 20 Hz for a blue  $\mu$ -ILED (additional wavelengths in **Figure 4.4 Supplement 2**). The results presented here provide accurate guidelines for choosing  $\mu$ -ILED power and duty cycle without overheating the brain (See Methods for details on simulation model and results).

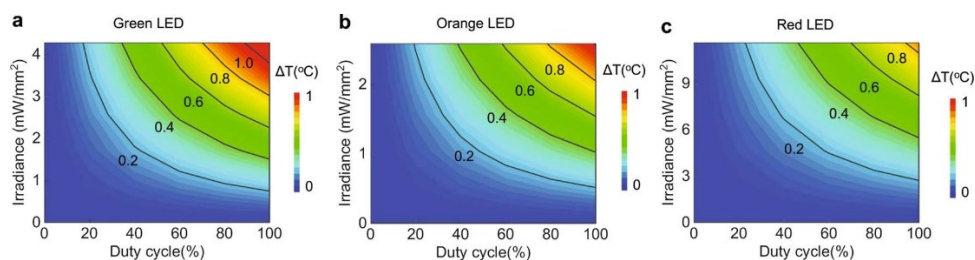


**Figure 4.4 Supplement 2. Temperature increment vs irradiance and duty cycle at 20 Hz frequency.** a, Temperature change at the interface between the encapsulated  $\mu$ -ILED and brain

tissue as a function of operational irradiance of green  $\mu$ -ILED (535 nm) and its duty cycle at 20 Hz frequency. **b, c**, Same simulation as reported in **(a)** for orange (590 nm) and red (630 nm)  $\mu$ -ILEDs, respectively.

#### **4.2.6 Applications of bilateral stimulation and subject-specific programmability for wireless control of place preference and social behavior**

Next, we evaluate the function of the newly developed devices in a series of behavioral assays. Demonstrations of the functionality for the bilateral devices involve experiments on a group of midbrain dopaminergic (DA) neurons in the ventral tegmental area (VTA), a brain region linked to the processing of reward<sup>367,366</sup>. The bilateral design enables surgical implantation of  $\mu$ -ILEDs into the two hemispheres of the brain in a single surgical operation. Stimulation probes with  $\mu$ -ILEDs were positioned posterior to bilateral VTA, in DAT<sup>icre</sup> animals, neonatally transduced with Cre-dependent ChR2-EYFP adeno-associated viral vector (AAV) in midbrain DA neurons (**Figure 4.5 Supplement 1a-b**). Probe placement and the expression of ChR2-EYFP were verified by histology after behavioral experiments (**Figure 4.5 Supplement 1c**).

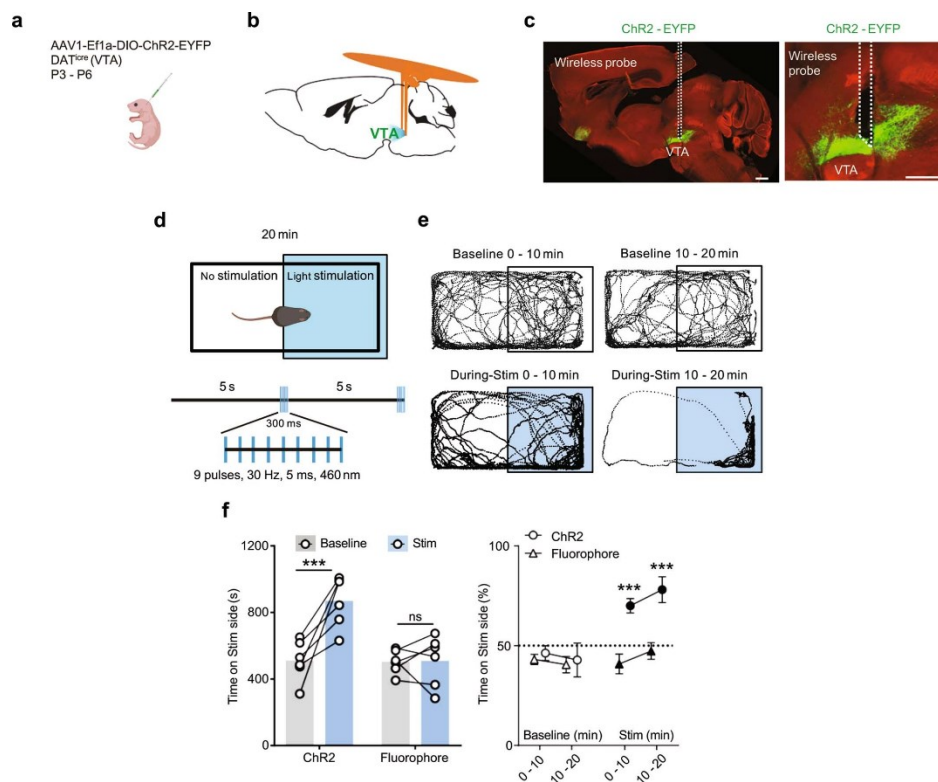


**Figure 4.5 Supplement 1. Bilateral burst wireless stimulation of midbrain dopaminergic neurons regulates place preference.** **a**, Schematic illustration of neonatal virus transduction in DATiCre animals. **b**, Schematic image of implanted position of bilateral wireless device posterior to the VTA. **c**, Left: sagittal brain section showing the expression of ChR2.EYFP in the VTA and the track of wireless probe. Right: Close up image of the VTA. Scale bar: 500  $\mu$ m. **d**, Top: schematic showing the arena of real-time place preference (RTPP) and the stimulation area (blue). Bottom: burst pattern of wireless optogenetic stimulation. **e**, Example traces showing the tracks of positions in different test periods from one animal. Top: baseline condition without stimulation in the first and last 10 min of the testing session. Bottom: same period of test session, but with light stimulation (460 nm). **f**, Left: summary data showing the total time spent on the antenna side in baseline and stimulation conditions. Two-way ANOVA, Sidak's multiple comparisons test (Baseline vs Stim), ChR2,  $P = 0.001$ , Fluorophore,  $P = 0.9962$ . Right: percentage of time spent on the antenna side in different testing period. Two-way ANOVA, Sidak's multiple comparisons (Stim, ChR2 vs Fluorophore), 0 – 10 min,  $P = 0.0008$ , 10 – 20 min,  $P = 0.0005$ .  $N = 6$  mice/group. All data are represented as mean  $\pm$  s.e.m. \*\*\* $P < 0.001$ . ns: not significant.

The first test uses a well-established paradigm of reward-based behavior, termed real-time place preference (RTPP). In this paradigm, burst excitation of DA neurons in the VTA and consequent dopamine release promote the animal's preference for the side of the enclosure associated with optogenetic stimulation<sup>486,369</sup> (**Figure 4.5 Supplement 1d**). Consistent with previous reports<sup>486,369</sup>, burst wireless photostimulation (Stim) significantly increases the time animals spent on the stimulated side, in contrast to the absence of place preference in the baseline condition before stimulation (**Figure 4.5 Supplement 1e, f**). Wireless photostimulation shows no effect on preference in control animals expressing a static fluorophore (**Figure 4.5 Supplement 1f**). Further tests include the use of bilateral devices in a social interaction paradigm that involves a choice between a novel same-sex conspecific and an inanimate object, since the activation of VTA DA neurons promotes social behavior<sup>498</sup> (**Fig. 4.5a**). Compared to the baseline and fluorophore controls, time spent in the social interaction zone (14 x 26 cm) increases during light stimulation in ChR2-expressing animals, while interaction with the inanimate object remained unchanged (**Fig. 4.5b-c**).

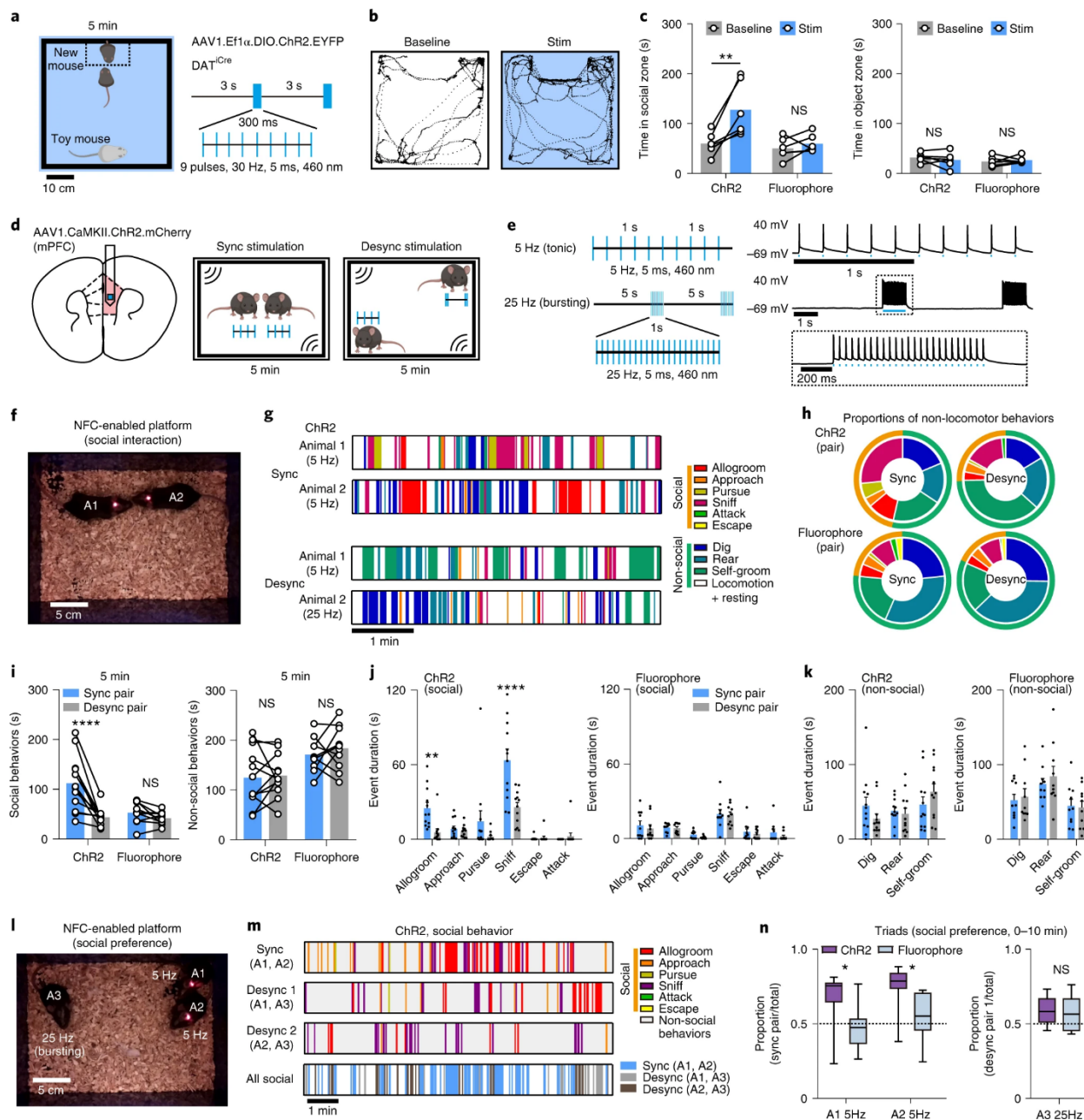


**Figure 4.5. Bilateral stimulation and subject-specific programmability for wireless optogenetic control of social behavior.** **a**, Left: schematic of the arena for the social preference task and the stimulation area. Right: burst pattern of wireless light stimulation (460 nm). **b**, Example traces show position tracks in baseline and bilateral stimulation conditions from one animal. **c**, Left: summary data for total time spent in the social-interaction zone in baseline and stimulation conditions. Two-way ANOVA, Sidak's multiple-comparisons test (baseline versus stim), ChR2,  $P = 0.0016$ ; fluorophore,  $P = 0.7763$ . Right: total time spent in the object interaction

zone. Two-way ANOVA, Sidak's multiple-comparisons test (baseline versus stim), ChR2,  $P = 0.6208$ ; fluorophore,  $P = 0.8363$ .  $n = 6$  animals per group. **d**, Left: schematic of viral transduction and probe implantation in the mPFC. Right: the arena and experimental design for the free social-interaction assay. Sync, synchronized; desync, desynchronized. **e**, Left: stimulation patterns used to induce synchronized and desynchronized activity. Right: example traces from a current-clamp recording of a ChR2–mCherry<sup>+</sup> mPFC pyramidal neuron during optogenetic activation with blue light, as noted. **f**, Photograph of two mice interacting during synchronized wireless light stimulation. **g**, Behavioral sequences recorded in individual mice receiving synchronized or desynchronized stimulation during free social interaction. **h**, Proportion of time spent engaging in non-locomotor behaviors for mice expressing ChR2 or fluorophore controls, receiving synchronized or desynchronized stimulation. Proportions of time spent engaging in social behavior: ChR2 synchronized, 46.5%; ChR2 desynchronized, 25.9%; fluorophore synchronized, 23.5%; fluorophore desynchronized, 18.4%.  $n = 10$ – $12$  pairs per group. **i**, Left: summary data show the total time spent in social interaction for paired mice during synchronized and desynchronized stimulation. Two-way ANOVA, Sidak's multiple-comparisons test (synchronized pair versus desynchronized pair), ChR2,  $P < 0.0001$ ; fluorophore,  $P = 0.6198$ . Right: total time spent engaging in non-social behaviors, exclusive of locomotion. Two-way ANOVA, Sidak's multiple-comparisons test (synchronized pair versus desynchronized pair), ChR2,  $P = 0.9526$ ; fluorophore,  $P = 0.6608$ .  $n = 10$ – $12$  pairs per group. **j**, Left: summary data for social event durations for paired ChR2-expressing mice during synchronized and desynchronized stimulation. Right: same as left but for fluorophore control mouse pairs. Two-way ANOVA, Holm–Sidak's multiple-comparisons test (synchronized pair versus desynchronized pair). ChR2: allogroom,  $P = 0.0027$ ; approach,  $P = 0.9517$ ; sniff,  $P < 0.0001$ ; pursue,  $P = 0.0939$ ; escape,  $P = 0.9517$ ; attack,  $P = 0.9517$ . Fluorophore: allogroom,  $P = 0.8903$ ; approach,  $P = 0.9541$ ; sniff,  $P = 0.9541$ ; pursue,  $P = 0.8996$ ; escape,  $P = 0.9092$ ; attack,  $P = 0.788$ .  $n = 12$  pairs for ChR2 and  $n = 10$  pairs for the fluorophore. **k**, Left: summary data for non-social event durations for paired ChR2-expressing mice during synchronized and desynchronized stimulation. Right: same as left but for fluorophore control mouse pairs. Two-way ANOVA, Holm–Sidak's multiple-comparisons test (synchronized pair versus desynchronized pair). ChR2: dig,  $P = 0.1941$ ; rear,  $P = 0.6816$ ; self-groom,  $P = 0.1941$ . Fluorophore: dig,  $P = 0.822$ ; rear,  $P = 0.5568$ ; self-groom,  $P = 0.822$ .  $n = 12$  pairs for ChR2 and  $n = 10$  pairs for the fluorophore. **l**, Photograph of three mice receiving 5-Hz or 25-Hz stimulation in the social-interaction arena, forming three synchronized or desynchronized pairs. **m**, Example social behavior sequences in synchronized or desynchronized pairs during free social interaction. **n**, Left: the proportion of social interactions for a focal animal in a triad with the synchronously stimulated one, over the total social-interaction time, in animals receiving 5-Hz optogenetic stimulation. Two-way ANOVA, Sidak's multiple-comparisons test, ChR2 versus fluorophore, animal (A)1,  $P = 0.0145$ ; A2,  $P = 0.0198$ . One-sample t-test, ChR2 versus random chance (0.5, dotted line), A1,  $P = 0.0066$ ; A2,  $P = 0.0003$ . Right: the proportion of social interactions for the focal animal receiving 25-Hz stimulation in a triad, desynchronized from both

other present conspecifics, over the total social-interaction time. Unpaired two-tailed t-test, ChR2 versus fluorophore,  $P = 0.7207$ .  $n = 8-10$  experiments per group. Data represent mean  $\pm$  s.e.m. in bar graphs; box-and-whisker plots show quantiles and medians. \* $P < 0.05$ , \*\* $P < 0.01$ , \*\*\*\* $P < 0.0001$ .

For a direct evaluation of the unique properties of the new generation wireless optogenetic devices—subject-specific programming and real-time adjustment—we tested the intriguing hypothesis emerging from recent imaging studies<sup>504,505</sup>, which suggests that interbrain neuronal activity synchrony in the medial prefrontal cortex (mPFC) may be sufficient to drive social interactions and social preference within groups of animals. This study would be challenging to carry out with traditional optical fibers, or large overhead devices, because tangling fibers would affect the animals' natural social grooming and other emergent behaviors.

To directly manipulate interbrain activity across subjects, mice were virally transduced with AAV1.CaMKII.ChR2.mCherry in mPFC pyramidal neurons, followed by subsequent implantation of wireless optogenetic devices targeting mPFC (**Fig. 4.5d**). Synchronized (Sync) interbrain activity was generated using the same stimulation pattern for two mice (5 Hz, tonic stimulation), while distinct stimulation patterns (5 Hz tonic vs 25 Hz bursting) were used to induce desynchronized (Desync) activity across animals (**Fig. 4.5e**). We selected 5 Hz stimulation to induce synchronization, based on prior work reporting interbrain synchrony in the theta range as relevant for emergent interactive behaviors<sup>506,507</sup>. The ability of mPFC pyramidal neurons to follow selected stimulation patterns was validated using current clamp recordings of mPFC neurons in an acute slice preparation, with temporally matched light stimulation using 470 nm whole field LED illumination (**Fig. 4.5e**). We also validated increased excitability *in vivo* using c-Fos immunofluorescent labeling (**Figure 4.5 Supplement 2a-c**). Mice receiving *in vivo*

stimulation were allowed to interact with each other freely in an open-field arena (18 cm x 25 cm) (**Fig. 4.5f**), with social and non-social behaviors scored for each subject or pair (**Fig. 4.5g**, see Methods for details). The proportion of social behavior in Chr2-expressing mice during synchronized optogenetic stimulation was 46.5% (n = 12 pairs), compared to 25.9% during desynchronized stimulation. In fluorophore expressing control mice (n = 10 pairs), the proportion of social behavior was 23.5% for Syn pairs and 18.4% for Desyn pairs (**Fig. 4.5h**). **Figure 4.5h-j** exclude locomotion from analysis to highlight the rarer behavioral events.

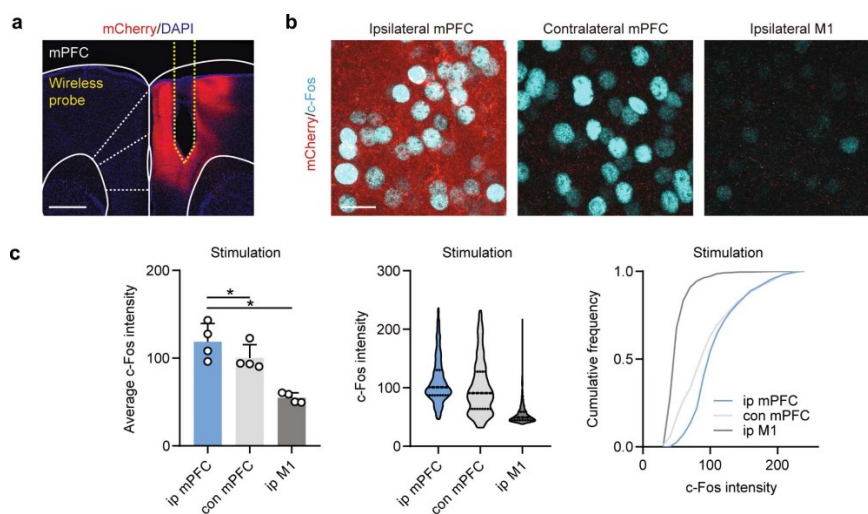


**Figure 4.5 Supplement 2. Increased excitability of mPFC pyramidal neurons after stimulation.** **a**, Image of viral expression of Chr2.mCherry and probe placement. Scale bar, 500  $\mu$ m. **b**, Images of c-Fos immunoreactivity in ipsilateral mPFC, interconnected contralateral mPFC, and ipsilateral M1 as a control region. Scale bar, 20  $\mu$ m. **c**, Summary data show average c-Fos intensity in individual mice (left), the distribution of c-Fos neuronal particle intensities (middle), and cumulative frequency of c-Fos particle intensities. RM one-way ANOVA,  $P = 0.0025$ , Sidak's multiple comparisons test, ipsilateral (ip) mPFC vs ipsilateral M1,  $P = 0.0201$ , contralateral (con) mPFC vs ipsilateral M1,  $P = 0.0370$ .  $N = 4$  mice/group. Data represent mean  $\pm$  s.e.m.; dashed lines in the violin plot show quartiles and median. \* $P < 0.05$ .

For ChR2-expressing mouse pairs, synchronized stimulation induced greater amount of time spent engaged in social interaction than desynchronized stimulation, while the total social interaction time was not significantly different between two stimulation conditions for fluorophore control mice (**Fig. 4.5i**). Among social behaviors, the affiliative actions of social grooming and sniffing were significantly increased during synchronized stimulation, contributing to the overall greater amount of social interaction time for ChR2-expressing mouse pairs (**Fig. 4.5j**). No significant differences were observed in scored non-social behaviors across all conditions (**Fig. 4.5i, k**). Thus, in the context of dyadic social interactions, synchronized stimulation enhances social interaction but not non-social behaviors.

To further evaluate whether interbrain synchrony may shape social preference in more complex social contexts, we leveraged the individualized programmability of NFC-based wireless devices during dynamic social interactions involving three mice at the same time. Two animals were stimulated (tonically) at 5 Hz to form a synchronized pair, while another animal was receiving stimulus-number-matched 25 Hz bursting stimulation, in order to form an imposed desynchronized pairing with the other two mice (**Fig. 4.5l**). In the fluorophore control mice, we first observed that individuals spent more time engaged in social behaviors in triads, compared to dyads (**Figure 4.5 Supplement 3a**). This increase in social interaction in more complex contexts likely reflects both an increase in the amount of time required to process social stimuli associated with multiple individuals and as a probabilistic function of increased density occurring with three mice rather than two in the same size arena. Evaluating the latter assumption, we simulated the conditions involving interacting dyads and triads in a virtual experimental space (18 x 25 cm open field). Our modeling result showed that individuals spent more time in proximity to another

subject in triads compared to dyads (**Figure 4.5 Supplement 3b**), consistent with experimental observations (**Figure 4.5 Supplement 3a**). We next assessed the distribution of social interaction among the three possible pairs within the triad and found that, for ChR2-expressing triads, more social interactions were observed within the synchronized pair (**Fig. 4.5m, Figure 4.5 Supplement 3c**). Focal animals, considered individually, spent more time with their synchronized pair than fluorophore controls, or than would be dictated by chance. Animals who could only partake in desynchronized pairs did not distinguish between interaction partners and did not deviate from chance (**Fig. 4.5n**). The social interaction events were more evenly distributed across animal pairs in fluorophore controls, and no salient preference were observed for individuals (**Fig. 4.5n, Figure 4.5 Supplement 3c**). Non-social behaviors were similar for mice receiving different stimulation patterns in all conditions (**Figure 4.5 Supplement 3d**).

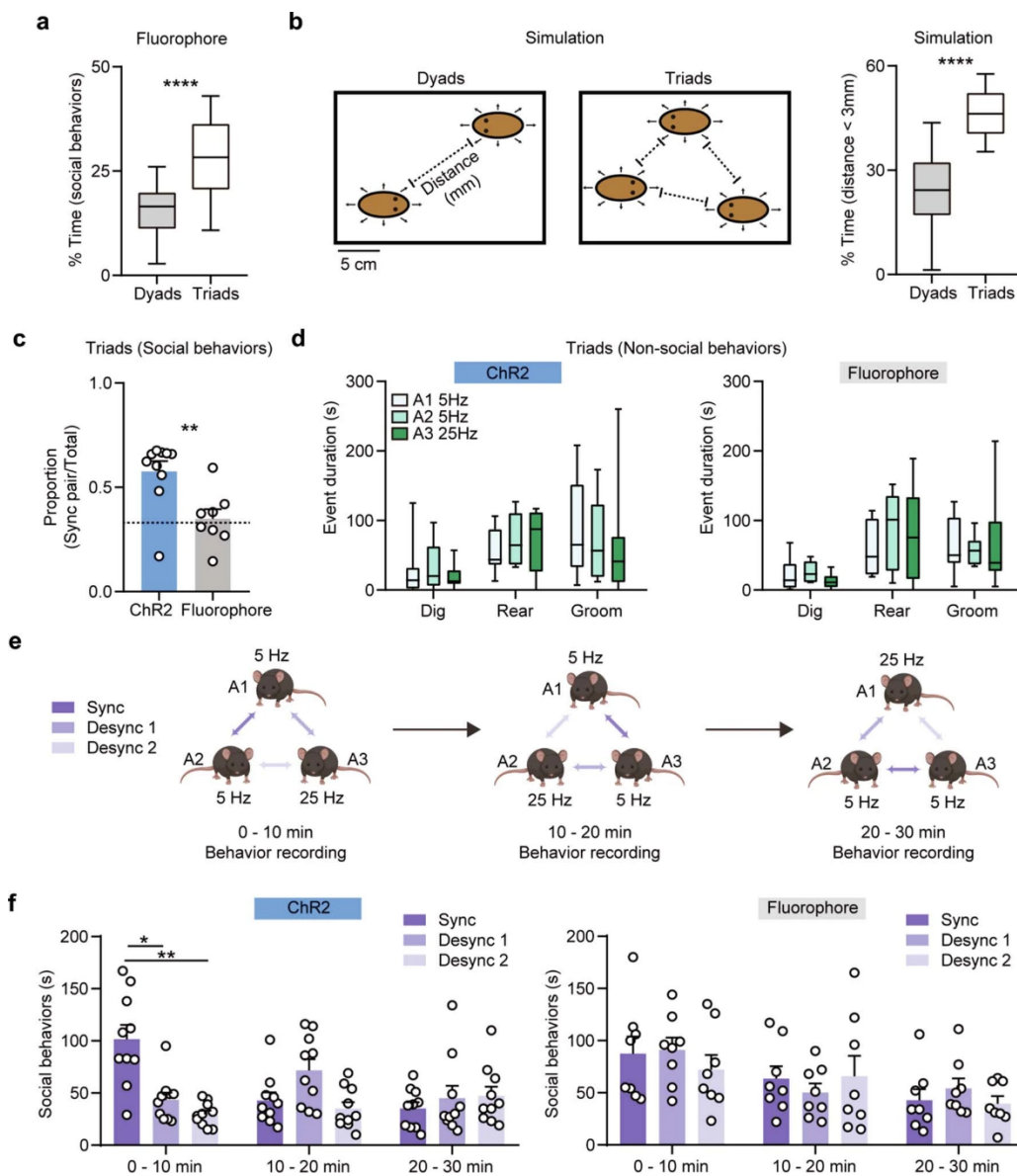


**Figure 4.5 Supplement 3. Wireless control of social behavior in dyads and triads.** **a**, Summary data show the percentage of time spent in social interaction for individual mice in dyads and triads, unpaired two-tailed t-test,  $P < 0.0001$ .  $N = 10$  independent experiments (Dyads),  $N = 8$  independent experiments (Triads). **b**, Left, Schematic illustrating simulation of subject proximity in dyads and triads. Right, estimated percent of time spent in proximity to another subject (distance  $< 3$  mm) for simulated individual in dyads and triads. Unpaired two-tailed t-test,  $P < 0.0001$ .  $N = 30$ /group. **c**, Summary data show the proportion of time spent in social interactions within the synchronized pair, over the total social interaction time for each experiment. Unpaired two-tailed t-test, ChR2 vs Fluorophore,  $P = 0.0044$ .  $N = 10$  independent experiments (ChR2),  $N = 8$

independent experiments (Fluorophore). **d**, Summary data for non-social event durations for ChR2-expressing (left) and fluorophore control (right) mice. Two-way ANOVA, Sidak's multiple comparisons test (main column effect), ChR2: A1 vs A2,  $P = 0.9991$ , A1 vs A3,  $P = 0.8996$ , A2 vs A3,  $P = 0.8420$ . Fluorophore: A1 vs A2,  $P = 0.7711$ , A1 vs A3,  $P = 0.9661$ , A2 vs A3,  $P = 0.9586$ .  $N = 10$  independent experiments (ChR2),  $N = 8$  independent experiments (Fluorophore). **e**, Schematic showing experimental design for 3 mouse social preference and real-time switching of synchronized pairs. **f**, Summary data for the total time spent engaged in social interactions for synchronized or desynchronized pairs across all test sessions. Two-way ANOVA, Sidak's multiple comparisons test, ChR2 0 – 10 min, Sync vs Desync 1,  $P = 0.0198$ , Sync vs Desync 2,  $P = 0.0022$ , other comparisons,  $P > 0.1$ .  $N = 10$  independent experiments (ChR2),  $N = 8$  independent experiments (Fluorophore). Data represent mean  $\pm$ s.e.m. in bar graphs; box and whisker plots show quartiles and median. \*  $P < 0.05$ , \*\* $P < 0.01$ , \*\*\*\* $P < 0.0001$ .

To determine whether these arbitrarily imposed pairings are stable, we tested whether the optogenetically established social preference can be switched by changing stimulation patterns across pairs, in three 10 min long intervals. At the end of each interval, synchronized stimulation was arbitrarily re-assigned to another pair (**Figure 4.5 Supplement 3e**). During the first period, as described, social preference was established in the synchronized pair, but no new pair preference could be induced during the following session. No significant preference was observed in any fluorophore control pairs (**Figure 4.5 Supplement 3f**). Altogether, these data demonstrate the advantages of NFC-based wireless devices in the study of social behaviors, supporting the hypothesis that imposed interbrain synchrony shapes social interaction and social preference in mice.

#### 4.2.7 Discussion

Real-time control over optical stimulation patterns is essential for many existing and emerging types of optogenetic studies in free-moving animals, particularly important for difficult to reach brain regions or complex behavioral tasks. The technology presented here employs well-developed NFC power transfer infrastructure and communication protocols, that, when aligned with commercial low-cost electronic components and scalable manufacturing techniques, yields a robust and flexible platform. Recent developments in application-specific integrated circuits (ASICs) offer the opportunity to further integrate this customized multi-component electronic system into a single specialized chip. This approach would share most of the digital and analog operations this platform supports in the context of user configurable optogenetics protocols, in a miniaturized form factor for minimally invasive *in vivo* applications<sup>508,509</sup>.

*In vivo* optogenetic experiments illustrate powerful application opportunities for the new devices in behavioral neuroscience research<sup>505</sup>. Our wireless optogenetic platform provides a unique opportunity in unconstrained naturalistic behavior, especially in the context of social interactions involving multiple free-moving subjects in the same environment. Programmability features enabled by the NFC platform support real-time manipulation of interbrain dynamics in a multi-brain framework experiment. Emerging evidence from multiple human<sup>510,511,512</sup> and several rodent and bat<sup>504,513</sup> studies suggest that interbrain neural synchrony arising during ongoing social interactions are associated with shared social variables among individuals. We were able to leverage the new NFC-based wireless optogenetic platform to directly test the hypothesis that interbrain synchrony specifically shapes social interactions in pairs or groups of mice. We observed paired mice display more social behaviors when they were receiving synchronized

optogenetic stimulation of mPFC pyramidal neurons at 5 Hz, within the range of the theta band frequency (4-7 Hz) previously reported for interbrain synchronization<sup>505,506,507</sup>. Moreover, within a group context, social preference arises within pairs that receive synchronized stimulation, but not between individuals with distinct stimulation pattern (5 Hz tonic vs 25 Hz burst). Our results suggest that imposed interbrain synchronization of neural process can causally shape ongoing social interaction and demonstrate the utility of our system to disentangle complex social phenomena.

Among other applications, next generation wireless neural devices with added functionalities will continue to deepen our understanding of social behaviors in the multi-brain level framework, potentially providing valuable mechanistic insights into atypical social behaviors (*e.g.*, as in autism). A natural extension of this technology available with the current hardware is the implementation of closed-loop *in vivo* behavioral studies. External events, such as sensor readouts or real-time video feeds, can be used to conditionally TTL-trigger the modification of optogenetic stimulation/inhibition protocols in real-time, dramatically expanding the space of applications for this technology. In addition, future possibilities enabled by the current advancements include multimodal functionality in sensing and other diverse applications.

## 4.3 Methods

### Device design:

#### Fabrication of the flexible circuit and probe

Patterned laser ablation (ProtoLaser U4, LPKF Laser & Electronics) of a flexible substrate of a copper-polyimide-copper laminate (18, 75 and 18  $\mu\text{m}$ ; Dupont, Pyralux) defined the circuit interconnects, the bonding pads for the electronic components and the geometry of the probe. Flexible printed circuit board with customized designs offered by commercial companies (e.g. PCBWay) would also work. Conductive pastes (Leitsilber 200 Silver Paint) filled plated via holes through the substrate to electrically connect circuits on the top and bottom sides. Hot air soldering using low temperature solder (Indium Corporation) bonded packaged components and  $\mu$ -ILEDs (TR2227, CREE, for emission at 460 nm and 535 nm; TCE12, III-V Compounds, for emission at 590 nm and 630 nm) to the respective pads. Chemical vapor deposition (Specialty Coating Systems<sup>TM</sup> Inc.) formed conformal coatings of parylene (14  $\mu\text{m}$ ) to encapsulate the devices. Laser cut tungsten stiffeners (50  $\mu\text{m}$ ; Sigma-Aldrich) bonded onto the back sides of the probes with a thin layer of epoxy (DEVCON) to provide enhanced mechanical rigidity for controlled implantation into the brain. A second layer of parylene (14  $\mu\text{m}$ ) and a dip-coated layer of poly(dimethylsiloxane) (PDMS; Sylgard<sup>TM</sup> 184, Dow Inc.) completed the formation of a soft encapsulation structure. The BM devices required extra assembly steps before dip coating with PDMS, as described subsequently.

#### Fabrication of mechanically compliant interconnects for back subdermal devices

Fabrication began with spin coating a layer of poly(methylmethacrylate) (3000 rpm, 30s; PMMA A8, MicroChem Corp) on a silicon wafer substrate. Chemical vapor deposition formed a film of parylene (5  $\mu\text{m}$ ) over the PMMA. Electron beam evaporation (AJA International Inc.) yielded a multilayer stack of Ti (20 nm)/Cu (300 nm)/Ti (20 nm)/Au (50 nm), from bottom to top.

Photolithography (MLA 150, Heidelberg Instrument) and wet chemical etching defined patterns

in this metallic stack in the serpentine geometries of the interconnection traces. Chemical vapor deposition formed a second film of parylene (5  $\mu\text{m}$ ) on these patterned metal traces. Sputter deposition (AJA International Inc.), photolithography and reactive ion etching (RIE; Samco Inc.) patterned a layer of  $\text{SiO}_2$  (60 nm) as an etch mask. RIE of the exposed parylene to define geometries that matched those of the serpentine, with exposed contact pads for electric connections. The entire structure was transferred from the substrate to water soluble tape (AQUASOL) upon dissolving the PMMA by immersion in acetone. Sputter deposition formed a uniform layer of  $\text{SiO}_2$  (30 nm) on the system while on the tape. Exposing the  $\text{SiO}_2$  and a thin layer of silicone elastomer (Ecoflex 00-30, Smooth-On Inc.) to ultraviolet induced ozone (UVO Cleaner Model 144AX; Jelight Company Inc.) created surface hydroxyl termination on both surfaces. Physically laminating the two and then baking at 70  $^\circ\text{C}$  for 10 min in a convection oven (Isotemp Microbiological Incubator, Fisherbrand) created a strong adhesive bond. Immersion in warm water dissolved the tape to complete the fabrication process. Several companies can carry some of the fabrication steps. For example, Special Coating Systems<sup>TM</sup> Inc. offers chemical vapor deposition of parylene. Thinfilms Inc. offers sputter deposition that yields thin metal multilayers and  $\text{SiO}_2$ . In addition, most research universities offer micro-fabrication services toward science community. In this case, photolithography, wet chemical etching, and RIE can be achieved upon order.

#### Assembly of back mounted subdermal devices

Laser ablation of a film of polyimide (75  $\mu\text{m}$ ; Argon Masking Inc.) created shadow masks that covered the parylene-encapsulated probes and flexible circuits and left the contact pads for electric connections exposed to allow removal of parylene in these regions by reactive ion

etching. Hot air soldering with a low temperature solder electrically bonded the probes, interconnection serpentines, and flexible circuits. Dip coating with epoxy and PDMS further mechanically secured the joints and encapsulated the probes and flexible circuit. The final step involved encapsulation of the serpentine interconnects with a dip coated layer of a low modulus silicone (Ecoflex, 00-30).

### Electronic device components

An RF harvesting module, built with a matching capacitor, high-speed Schottky diodes in a half-cycle regulation configuration, and a smoothing capacitor, supplied power to the system. The 0201 package configuration for these and other components minimized the overall size. A linear voltage regulator (NCP161, ON Semiconductors, 1x1 mm<sup>2</sup>) ensured a constant voltage supply. A low power, 8-bit microcontroller, (4x4 mm<sup>2</sup>, ATtiny84, Atmel) operating with preprogrammed firmware served as the control system. A dynamic NFC-accessible EEPROM (2x3 mm<sup>2</sup>, M24LR04E-R, ST) provided external data storage and access by a microcontroller on a write-in-progress event basis to update the device operation. Finally, control of intensity from the  $\mu$ -ILEDs was implemented with a passive second order low pass filter coupled with a high impedance, ultra-low power operational amplifier (1.5x1.5 mm<sup>2</sup>, TLV8542, Texas Instruments).

### Optical intensity measurement

An integrating sphere (OceanOptics FOIS-1) calibrated with a standard diffusive light source (OceanOptics HL-3 plus) enabled accurate measurements of optical output for all of the  $\mu$ -ILEDs examined here. A semiconductor device analyzer (Keysight S1500A) supplied current to the  $\mu$ -ILEDs, from 100  $\mu$ A to 2 mA with a 100  $\mu$ A interval, through a probe station (SIGNATONE

1160) during optical measurement. Corresponding software (OceanView) generated an output as irradiance flux over the wavelength spectrum from 350 to 1000 nm. A MATLAB integration script yielded the total optical output power at each current value.

### Mechanical modeling

The commercial software ABAQUS (ABAQUS Analysis User's Manual 2016) was used to design and optimize the shapes of the serpentine structures and material layouts of the interconnects in multilateral optogenetic devices to improve their mechanical performance and facilitate surgical implantation. For the HM devices (Fig.4a-c), PDMS, parylene, copper, PI, and tungsten layers were modeled by composite shell elements (S4R). For the BM devices (Fig. 4d-f), the Ecoflex substrate was modeled by solid hexahedron elements (C3D8R), while other layers were modeled by composite shell elements (S4R), similar to the HM devices. Convergence tests of the mesh size were performed to ensure accuracy. The elastic modulus and Poisson's ratio values used in the simulations were 119 GPa and 0.34 for Cu; 2.1 GPa and 0.34 for parylene; 2.5 GPa and 0.34 for PI; 79 GPa and 0.42 for Au; 110 GPa and 0.34 for Ti; 60 kPa and 0.49 for Ecoflex.

### Electromagnetic modeling

The commercial software Ansys HFSS (Ansys HFSS 13 User's guide) was used to design and optimize the configuration of the double loop antenna to achieve relatively large, uniform magnetic fields in the cages for behavior experiments (Fig. 2a). The adaptive mesh (tetrahedron elements) together with a spherical surface (1000 mm in radius) as the radiation boundary, was adopted to ensure computational accuracy. The relative permittivity, relative permeability and

conductivity of copper used for the simulations were 1, 0.999991 and  $5.8 \times 10^7 \text{ S} \cdot \text{m}^{-1}$ , respectively.

### Optical and thermal modeling

The light distribution and temperature change caused by continuous operation of implanted  $\mu$ -ILEDs was simulated to quantify key functional parameters (i.e. penetration depth, illumination volume, temperature change) that describe the physiological interaction with the brain. Finite element analysis (FEA) was implemented with the commercial software COMSOL 5.2a (Equation Based Modeling User's guide) for propagation of light emitted by blue, green, orange, and red  $\mu$ -ILEDs with wavelengths  $\lambda = 460, 535, 590$  and  $630 \text{ nm}$ , respectively, into mouse brain tissue, according to the Helmholtz equation,

$$\nabla(-c\nabla\phi) + \mu_a\phi = f \quad (1)$$

where  $\phi$  represents the light fluence rate in the brain,  $c$  is the diffusion coefficient,  $\mu_a$  is absorption coefficient, and  $f$  is the source term. The isotropic diffusion coefficient can be written as<sup>514</sup>.

$$c = \frac{1}{3(\mu_a + \mu'_s)} \quad (2)$$

where  $\mu'_s$  is the reduced scattering coefficient. The absorption and reduced scattering coefficients of the fresh brain, implanted probe materials, and  $\mu$ -ILEDs are given in supplementary Table S2 and S3.

Similarly for the heat transfer analysis, finite element analysis was also implemented with the commercial software COMSOL 5.2a (Heat-Transfer Modeling User's Guide) to compute the temperature change ( $\Delta T$ ) caused by the light emitted from the  $\mu$ LEDs, heat generated by thermal power of  $\mu$ -ILEDs, brain's metabolism, and blood perfusion to account for the physiological heat transfer phenomenon in the brain. The Pennes' bio-heat equation describes the heat-transfer problem as <sup>515,516</sup>.

$$\rho C_p \frac{\partial T}{\partial t} + \nabla \cdot (-k \nabla T) = \rho_b C_b \omega_b (T_b - T) + Q_{met} + Q_{the} + \phi \mu_a \quad (3)$$

where  $T$  is temperature,  $t$  is time;  $k$ ,  $\rho$ , and  $C_p$  are the thermal conductivity, mass density and heat capacity of the brain, and  $\rho_b$  and  $C_b$  are the mass density and specific heat capacity of the blood, respectively.  $\omega_b$  denotes the blood perfusion rate <sup>515</sup> and  $T_b$  is the arterial blood temperature <sup>515</sup>.  $Q_{met}$  is the heat source from metabolism in the brain,  $Q_{the}$  is the heat generated by thermal power of  $\mu$ -ILEDs, and  $\phi$  corresponds to the light fluence rate of the  $\mu$ LEDs calculated in the optical simulation. The thermal properties of the implanted probe and bio-heat input parameters used in the simulation are given in supplementary Table S4 and S5.

The brain tissue, implanted probe geometry, and the  $\mu$ -ILEDs were modeled using 4-node tetrahedral elements. Convergence tests of the mesh size were performed to ensure accuracy. The total number of elements in the models was approximately 905,000.

## **In vivo studies:**

### Animals

All experiments used adult male wild-type C57BL/6J mice (6-12 weeks old and 20-30 g at start of experiments; Jackson Labs), maintained at ~25 °C and humidity ranged of 30% to 70%. Mice were maintained on a 12-h light/dark cycle (lights on at 9:00 PM, reverse light cycle) and fed *ad libitum*. Mice were group housed (two to four per cage) prior to surgery, after which mice were individually housed in a climate-controlled vivarium. All experimental procedures were conducted in accordance with the National Institutes of Health standards and were approved by the Institutional Animal Care and Use Committee (IACUC) of the US Army Medical Research Institute of Chemical Defense (MRICD) and Washington University.

#### Surgical procedures

Animals were anesthetized using isoflurane and their head and back fur was shaved. Mice were then mounted in a stereotactic frame with a heating pad, and an incision was made down the center of the scalp to expose the skull. Burr holes for implantation of the optogenetic probes were drilled in the skull using a variable speed surgical drill. Using the attachment flag, the optogenetic probes were stereotactically lowered into the designated brain region at a rate of ~100  $\mu\text{m/s}$  until appropriately positioned. The probes were then affixed to the skull using cyanoacrylate to prevent further movement. For the BM devices, a second ~10 mm incision was made midway down and across the back. The subcutaneous fascia between the scalp and back incision was separated, and the wireless device was then pulled from the scalp incision posteriorly until it rested above the spine. Serpentine wires connecting the two optogenetic probes to the thin and flexible wireless antenna traveled subcutaneously through the neck to connect the two components. The incisions were sutured closed and animals were monitored and

allowed to recover for several hours before transfer back to the cage area facility for appropriate post-surgical monitoring.

DAT<sup>iCre</sup> neonates (P3-6) were transduced with AAV1.EF1a.DIO.hChR2(H134R).eYFP (3.55x10<sup>13</sup> GC/ml), (Addgene viral prep # 20297/20298-AAV1, Dr. Karl Deisseroth) or AAV8-CAG-FLEX-GFP (3.1x10<sup>12</sup> GC/ml, UNC vector core, Dr. Ed Boyden). Six weeks after virus transduction, wireless probes were positioned posterior to the VTA (referenced from bregma: - 3.1 mm anteroposterior, ± 1.5 mm medio-lateral and - 4.7 mm dorsoventral). C57BL/6 Mice (~P60) were transduced with AAV1.CaMKIIa.hChR2(H134R).mCherry (1.2x10<sup>13</sup> GC/ml, Addgene viral prep # 26975-AAV1, Dr. Karl Deisseroth). Two weeks after virus transduction, wireless probes were positioned anterior to the mPFC (referenced from bregma: + 2.2 mm anteroposterior, + 0.5 mm medio-lateral and - 1.5 – 2.0 mm dorsoventral). Mice recovered for at least 5 days before behavioral experiments.

### Histology

For hematoxylin and eosin (H&E) staining, standard protocols were followed. Four µm thick issue sections adhered to slides were dewaxed and cleared with xylene, hydrated through incubation in a series of decreasing concentrations of alcohols (100-70%), stained with filtered hematoxylin, treated with an alkaline solution, and counterstained with eosin. Subsequently, sections were dehydrated in several changes of alcohol, cleared, and coverslipped. Sections were imaged using an Olympus VS120 microscope in brightfield mode. Colored bright field images of back tissue sections were automatically acquired and stitched by using automated slide scanner and a 40x objective.

For immunofluorescent c-Fos labeling, 50-80  $\mu\text{m}$  thick sections were incubated with primary antibody with rabbit anti-c-Fos in 0.5% triton X-100 PBS overnight at 4°C (1:10000; Cat. No. 226003, Synaptic Systems, Goettingen, Germany). For evaluation of biocompatibility, rabbit anti-GFAP (1:1000, ab7260, abcam, Cambridge, United Kingdom), rabbit anti-IBA1 (1:1000, ab178846, abcam), and rabbit anti-Hemoglobin subunit alpha (1:500, ab92492, abcam) were used. On the following day, tissues were rinsed three times with PBS, reacted with anti-rabbit Alexa Fluor 647 secondary antibody (1:500, Thermo Fisher, Waltham, MA) for 2hrs at RT, rinsed again for three times in PBS. Sections were mounted on Superfrost Plus slides (Thermo Fisher, Waltham, MA), air dried, and cover slipped under glycerol:TBS (9:1) with Hoechst 33342 (2.5  $\mu\text{g}/\text{ml}$ , Thermo Fisher Scientific). For c-Fos quantification,  $\sim 30$   $\mu\text{m}$  stacks with 2  $\mu\text{m}$ -step size were acquired with a Leica SP5 confocal microscope for the following regions including ipsilateral mPFC, contralateral mPFC, and ipsilateral M1. All imaging parameters were constant across all samples and each channel was imaged sequentially with a 40x objective. Analysis was carried out in FIJI<sup>474</sup> using autothresholding and particle analysis scripts. The same analysis parameters were applied across all regions of interest.

### Electrophysiology

Coronal brain slice preparation was modified from previously published procedures<sup>472,448,517</sup>. Animals were deeply anesthetized by inhalation of isoflurane, followed by a transcardial perfusion with ice-cold, oxygenated artificial cerebrospinal fluid (ACSF) containing (in mM) 127 NaCl, 2.5 KCl, 25 NaHCO<sub>3</sub>, 1.25 NaH<sub>2</sub>PO<sub>4</sub>, 2.0 CaCl<sub>2</sub>, 1.0 MgCl<sub>2</sub>, and 25 glucose (osmolarity 310 mOsm/L). After perfusion, the brain was rapidly removed, and immersed in ice-cold ACSF equilibrated with 95%O<sub>2</sub>/5%CO<sub>2</sub>. Tissue was blocked and transferred to a slicing

chamber containing ice-cold ACSF, supported by a small block of 4% agar (Sigma-Aldrich). Bilateral 250  $\mu\text{m}$ -thick mPFC slices were cut on a Leica VT1000s (Leica Biosystems, Buffalo Grove, IL) in a rostro-caudal direction and transferred into a holding chamber with ACSF, equilibrated with 95% $\text{O}_2$ /5% $\text{CO}_2$ . Slices were incubated at 34°C for 30 min prior to electrophysiological recording. Slices were transferred to a recording chamber perfused with oxygenated ACSF at a flow rate of 2–4 ml/min at room temperature.

Current clamp whole-cell recordings were obtained from neurons visualized under infrared DIC contrast video microscopy using patch pipettes of  $\sim$ 2–5  $\text{M}\Omega$  resistance. mPFC neurons expressing ChR2 were identified by the expression of mCherry. To activate ChR2-expressing pyramidal neurons in the mPFC, tonic light pulses at 5 Hz or bursting light pulses at 25 Hz (1s-long burst every 5s) were delivered at the recording site using whole-field illumination through a 60X water-immersion objective (Olympus, Tokyo, Japan) with a PE4000 CoolLED illumination system (CoolLED Ltd., Andover, UK). Recording electrodes contained the following (in mM): 135 K-gluconate, 4 KCl, 10 HEPES, 10 Na-phosphocreatine, 4 MgATP, 0.4  $\text{Na}_2\text{GTP}$ , and 1 EGTA (pH 7.2, 295 mOsm/L). Recordings were made using 700B amplifiers (Axon Instruments, Union City, CA); data were sampled at 10 kHz and filtered at 4 kHz with a MATLAB-based acquisition script (MathWorks, Natick, MA).

#### Experimental setup for behavioral studies.

A host computer supports a customized graphical user interface (GUI), developed in MATLAB, and connected to the RF power module and NFC reader that operates the ISO15693 NFC communication protocol (LRM2500-A, FEIG Electronics). The computer connects to the RF

power module via RS232 serial communication (a RS232 to USB converter was used in order to compensate the lack of physical RS232 ports in modern computers). The power module (Neurolux Inc.) drives a dual loop antenna that wraps around the experimental enclosure. An antenna tuner (Neurolux Inc.) provides impedance matching between the RF power module and the antenna to efficiently transmit power and communication signaling (Supplementary Fig. S11a). The customized GUI controls the information flow via write/read commands to the NFC optogenetic devices via the NFC reader (Supplementary Fig. S11b). Up to four devices can be addressed independently using their unique device identifier codes. A straightforward modification to the GUI can support additional devices. The write/read commands allow modification of illumination parameters, activation/deactivation of the  $\mu$ -ILEDs, or activation of two devices simultaneously. In addition, this interface permits control of the RF module such as the power output. Although not implemented here, further on-demand activation of a target device via external signal controls such as TTL represents a natural extension of this system.

#### Real-time place preference

Mice were placed in a custom two-compartment conditioning apparatus (61 x 30.5 x 30.5 cm) as described previously<sup>518,519</sup>. Mice underwent a 20 min trial where entry into one compartment triggered a burst of wirelessly powered photostimulation of 300 ms at 30 Hz (5 ms pulse width). Burst stimulations were delivered every 5 s while a mouse remained in the stimulation-paired chamber. Departure from the stimulation-paired side and entry into the other chamber side resulted in the cessation of photostimulation. The stimulation side was decorated with vertical grating pattern and the no-stimulation side with horizontal gratings. Mice were excluded from the study if they showed preference for either side in the baseline condition without

photostimulation. The video recorded in each session was analyzed by Toxtrac<sup>520</sup>. Time spent in each side was quantified as a measurement of place preference. Data were analyzed blind to conditions.

#### Social preference with DA stimulation

Mice underwent the social interaction test during a 5 min episode. A same-sex novel mouse was placed in a plastic mesh cage (10 x 6 cm) on one side of the open field (44 x 44 cm). A mouse-shaped object was placed on the opposite side. The experimental mouse was allowed to freely explore the open field for 2 min before a novel mouse and object were placed into the arena. Videos analyzed by Toxtrac<sup>520</sup> were used to measure the amount of time the experimental mouse spent in the ‘interaction zone’ (14 x 26 cm around the center of mesh cage or object). One day following a baseline session without stimulation, burst light stimulation (300 ms burst every 3 s, 9 pulses at 30 Hz in each burst, 5 ms pulse width) was delivered during the test period, and the interaction times with the new mouse and the inanimate object were measured. Data were analyzed blind to conditions.

#### Social interaction and preference with interbrain synchrony

In paired mice social interaction experiments, two male mice implanted with wireless optogenetic devices were placed in an open-field arena (18 x 25 cm) for free social interaction. For paired mice social interaction experiments, pairs were receiving synchronized or desynchronized stimulation for 5 min period. During synchronized session, two mice were simultaneously stimulated at 5 Hz (5 ms pulse width). During desynchronized session, one mouse was stimulated at 5 Hz, while the other mouse was receiving bursting optogenetic

stimulation (1 s burst every 5 s, 25 pulses at 25 Hz in each burst, 5 ms pulse width). The order of synchronized and desynchronized sessions was randomized for pairs. All animals were habituated to the open-field arena for 5 min before testing. For triple-mice social preference, each experiment was consisted of three sequential sessions (10 min for each). During each session, two mice were simultaneously stimulated at 5 Hz and the third mouse received bursting stimulation at 25 Hz. At the end of each session, stimulation patterns and the synchronized pair were reassigned.

The videos recorded at 25 fps were analyzed by Behavioral Observation Research Interactive Software (BORIS)<sup>521</sup>. Behaviors were manually scored for individual animals or pairs, as noted in the results and figures. Investigators were not blinded to the stimulation patterns displayed by the indicator LEDs. Behavioral events were converted into binary vectors for each type of behavior using 1 sec bins to generate behavioral sequences. A total of nine social and non-social behaviors were quantified. Social behaviors included allo-grooming, approach, pursue, sniff, attack, and escape. Non-social behaviors included self-grooming, digging, and rearing. Total time spent engaged in social interaction and non-social behaviors were calculated for comparisons among conditions.

#### Simulation of subject proximity

Mice were modeled as ellipses with a 60 mm major and 30 mm minor axis. Their movement was simulated in a 250 by 180 mm arena. For each movement, each object's speed was sampled from a Gaussian distribution with a mean of 0.09 mm/ms and standard deviation of 0.06 mm/ms, matching the distribution of reported mouse speeds<sup>522</sup>. Movement duration was chosen to be on

average  $1/5^{\text{th}}$  of body length, fixed at 133.33 ms. The simulated objects were initially placed equidistantly across the arena width, at half the arena height. The first movement direction was sampled from a uniform distribution over  $0, 2\pi$ . Each subsequent movement was sampled from a Gaussian distribution centered at the object's previous heading direction with a standard deviation of  $\pi/4$ . If the object encountered a wall, its movement direction was then sampled from a uniform distribution over  $0, 2\pi$ . Objects were not allowed to overlap. Objects were considered interacting if their perimeters were  $< 3$  mm from each other.

### MicroCT imaging

Animals were anaesthetized with isoflurane and placed inside a preclinical microPET/CT imaging system (Mediso nanoScan scanner). Data were acquired with 'medium' magnification,  $33 \mu\text{m}$  focal spot,  $1 \times 1$  binning, with 720 projection views over a full circle, with a 300 ms exposure time. Three images were acquired, using 35 kVp, 50 kVp and 70 kVp (where kVp is peak kilovoltage). The projection data was reconstructed with a voxel size of  $34 \mu\text{m}$  using filtered (Butterworth filter) back-projection software from Mediso Nucline (v2.01). Throughout imaging, respiratory signals were monitored using a digital system developed by Mediso (Mediso-USA). Advanced imaging studies used five 25-30 g C57BL/6 mice (C57BL/6NCrl) and three 250-300 g Sprague Dawley rats from Charles River. In mice, the ventral tegmental area was targeted for probe placement (referenced from bregma: -3.3 mm anteroposterior,  $\pm 0.5$  mm medio-lateral and -4.4 mm dorsoventral). In the rats, the probes were placed -5.0 mm anteroposterior,  $\pm 2.4$  mm medio-lateral and -5.0 mm dorsoventral. Data were analyzed with Amira (v2020.2, Thermo Fisher Scientific) Bone density was calculated from Mean (Hu) acquired with 50 kVp.

**Mobility studies:**Stereotaxic surgery

Mice were anesthetized in an induction chamber (3% isoflurane) and then placed in a stereotaxic frame (Kopf) where they were maintained at 1-2% isoflurane. All surgeries were performed using aseptic conditions. Meloxicam (0.5 mg mL<sup>-1</sup>, subcutaneous injection) and lidocaine (0.25-0.5%, intradermal injection) were given as preoperative analgesia. After a stable plane of anesthesia was reached, a midline incision was made to expose the skull. Two burr holes were drilled at the site of viral injection (all groups) and probe placement (for tethered and wireless subjects). Surgical controls only received viral injections; no probes were implanted. All mice were injected bilaterally with 200 nL per side of AAV-CaMKII $\alpha$ -hChR2-EYFP (UNC Vector Core, Dr. Karl Deisseroth) at a rate of 100 nL min<sup>-1</sup> via microsyringe pump (UMP3; WPI) and controller (Micro4; WPI). After 5 minutes, the injection needles (10  $\mu$ L NanoFil with 33 ga needles; WPI) were raised 300  $\mu$ m and left in place for an additional 3 minutes to allow for diffusion of the virus throughout the tissue. Mice were then implanted bilaterally with fiber optic ferrules (1.25 mm, stainless steel; Thorlabs) that contained the implanted optical multimode fibers (200  $\mu$ m, 0.22 NA; Thor Labs) or wireless  $\mu$ LED optogenetic probes using a stereotaxic holder (PH-300, ASI Scientific) and affixed with dental cement (fibers) or cyanoacrylate (wireless). Mice were allowed to recover for 2.5 weeks before acclimation to tethering and/or handling began. All animals gained weight post-surgery and readily built nests in their new cages.

### Open field test

The novel open field tests were carried out during the more active dark cycle (9:00 AM-9:00 PM) between 10:00 AM and 11:00 AM in a sound-attenuated lab maintained at 23°C. All tests were performed in a 908-cm<sup>2</sup> (34 cm diameter) circular cage that was novel for the animals to encourage exploratory activity and maximize movement. For fiber optogenetic probe tethering, a 1x2 step-index multimode fiber optic coupler (105 µm, 0.22 NA; Thor Labs) was connected to a low torque hybrid rotary joint (0.22 NA; Doric Lenses Inc.) and to the bilateral implanted ferrules in the mouse skull. No extra connections were required for mice implanted with wireless probes or the surgical controls. All mice were gently handled for three days before behavioral tests to acclimate the subjects to the experimenter and to reduce stress. Additionally, fiber-implanted mice were habituated to fiber optic tethering in their home cages for 3 days before behavioral experiments to prevent acute stress from interfering with their behavior on test days. For testing, mice ( $n = 6-8$  per group) were placed in the center of the open field and allowed to roam freely for 1 hr. Movements were video-recorded and motion analysis was performed offline using Ethovision® 11 software. Distance traveled, velocity, and number of stops and starts were calculated in 1 and 5 minute bins for the duration of the recording and statistically compared amongst groups using an ANOVA.

### Running wheel

Similar to the open field tests, these experiments were carried out during the more active dark cycle to promote higher activity. Animals were placed in a circular cage containing a Med-Associates Low-Profile Running Wheel that measures revolutions per minute of running activity.

All animals had access to running wheel enrichment devices in their home cages to acclimate them to the device prior to recording. Animals were run for three consecutive days to further promote consistent activity and minimize potential negative effects from acute tethering of the fiber optic group. Data reported are from the third day of recording using time bins from 5 to 65 minutes.

#### Positional tracking of the mice

Tracking the position of four body parts of a mouse during natural behaviors provided estimates for the requirements on mechanical deformations of soft interconnects mounted subdermally on the back. The procedure used a mouse in a transparent chamber (30 cm x 30 cm), recorded from one side for one hour (Raspberry Pi, 25 frames per second). Tracking information was determined using DeepLabCut<sup>523</sup>. Manually marking four body parts (head, neck, back, and tail) in 200 representative frames generated a training set for a convolutional neural network designed to locate these four body parts on a frame-by-frame basis. A subset of frames (~9000) with the animal's major axis oriented perpendicular to the camera were used to compute the deformation of the body regions. Estimates of mechanical compression and stretching used the combined distance from head to neck and neck to back. The bending curvature was represented as the radius of the arc formed by the points of head, neck, and back. All data points were compared to the medians of the data set (referenced as the non-deformed state) to indicate the level of device deformation during natural activity.

#### Statistical analyses

Group statistical analyses were performed using GraphPad Prism 7 software (GraphPad, LaJolla, CA). For N sizes, the number of animals is provided. No statistical methods were used to pre-determine sample sizes but our sample sizes are similar to those reported in previous publications<sup>394,519,524</sup>. All samples were randomly allocated into experimental groups. Data from failed devices were excluded from the analysis. All data are expressed as mean  $\pm$  SEM, or individual plots. Data distribution was assumed to be normal, but this was not formally tested. For two-group comparisons, statistical significance was determined by two-tailed Student's t-tests. For multiple group comparisons, analysis of variance (ANOVA) tests were used, followed by post hoc analyses.  $P < 0.05$  was considered statistically significant.

#### Data availability

The raw unanalyzed data generated during the current study are available from the corresponding author on reasonable request. The data analyzed during the current study are available

[https://github.com/A-VazquezGuardado/Real-time\\_control\\_Optogenetics](https://github.com/A-VazquezGuardado/Real-time_control_Optogenetics)

#### Code and software availability

All computer code and customized software generated during and/or used in the current study is available [https://github.com/A-VazquezGuardado/Real-time\\_control\\_Optogenetics](https://github.com/A-VazquezGuardado/Real-time_control_Optogenetics)

## Chapter 5 – Conclusions and future directions

During grooming, rodents perform a highly stereotyped, four-phase grooming sequence called syntactic grooming<sup>34,319</sup>. While syntactic grooming was originally reported to occur frequently, we did not find syntactic grooming to be prevalent in our data (<5% of grooming sequences; unpublished). A recent publication on self-grooming behavior in rats also found that syntactic grooming sequences accounted for <7% of grooming sequences<sup>116</sup>. Interestingly, the authors reported that rats frequently performed slightly modified syntactic grooming sequences where the first phase of rapid elliptical strokes over the snout were replaced by licking and stroking of the forepaws. Although complicated by its rare occurrence, syntactic-like grooming remains an attractive behavior to understand neural control of an innate, evolutionarily conserved, structured behavior. This line of research could build on our work described in **Chapter 2** and address key remaining questions. Do striatal ensembles encode phases of syntactic grooming? Does the striatum encode innate movement sequences in a hierarchical manner, similar to the encoding of learned movement sequences<sup>181</sup>?

One difficulty in studying syntactic grooming lies in identifying when each grooming phase occurs. Specifically, automated segmentation of behaviors performed by a mouse in a 2-hour recording session would be unlikely to yield segments that correspond to each grooming phase, since they comprise such a small fraction of the behavioral repertoire. However, taking an iterative approach by first identifying the times of grooming and then segmenting those time regions might yield segments corresponding to the grooming phases. Within our dataset, one could decompose the 3D keypoint positions during identified grooming sequences using a

dimensionality reduction method like t-SNE<sup>525</sup> or UMAP<sup>526</sup> to identify grooming phases.

Behaviors can be identified in an unsupervised manner using Motion Mapper<sup>527</sup>, B-SOID<sup>528</sup>, VAME<sup>529</sup>, or the newly released keypoint-MoSeq<sup>530</sup>. Alternatively, a supervised approach can be used to identify grooming phases, using for example the algorithm developed by Kwak et al<sup>531</sup>.

Donald Hebb's original formulation of neural ensembles was derived from known properties of cortical circuits<sup>195</sup>. Since then, the majority of data on neural ensembles and related theory have come from recordings in the hippocampus<sup>200,251,252,532,533</sup> and neocortex<sup>199,250,534-536</sup>, regions comprised of predominantly glutamatergic neurons. Comparatively less is known about ensembles in subcortical, predominantly GABAergic structures, such as the striatum. How could inhibitory neurons be wired together to form ensembles? Are striatal ensembles simply formed by shared cortical inputs among a group of striatal neurons? Data from Ca<sup>2+</sup> imaging slice experiments demonstrate that excitatory input, likely from the cortex and thalamus, drives striatal ensemble activity<sup>255</sup>. Yet, local inhibition is necessary for striatal ensemble dynamics, since these dynamics are absent when GABA receptors are blocked. Burke et al. propose that striatal ensembles are comprised of groups of d- and i-SPNs that are driven by cortical and thalamic inputs. Within this framework, the dSPNs within each ensemble facilitate a given movement, while the iSPNs inhibit both d- and iSPNs in other ensembles to inhibit competing movements and prevent other ensembles from inhibiting the desired movement<sup>537</sup>. While this model is consistent with known striatal circuitry and activity during behavior, it remains to be validated experimentally. Further, the role of striatal interneurons in striatal ensembles has not been elaborated. Our data suggest that FSIs are part of ensembles together with SPNs. FSIs could play a similar role to the proposed function of iSPNs in inhibiting other ensembles. Additionally,

given the importance of dopamine and other neuromodulators in the configuration of neural circuits<sup>263,538,539</sup> (**Chapter 3**), it remains to be determined how striatal neuromodulatory tone contribute to the formation and maintenance of striatal ensembles.

Our current data on striatal ensembles during grooming has been limited to passive recording of ensemble activity. Perturbations of striatal activity during grooming behavior would provide additional insight into their function. In **chapter 4** we describe the design of wireless devices for optogenetics that can be used to perturb striatal activity while adding minimal external interference with the behavior. In our experiments described in **chapter 2**, the electrophysiology implant was tethered to our recording system. Thus, mouse movement was somewhat impeded even though they could move freely within the arena and a commutator relieved torque buildup in the recording wire. For example, one common component of rodent self-grooming is body-licking<sup>318,319</sup> where rodents lower their head and lick their torso. This grooming movement is virtually absent in tethered mice as the wire prevents them from lowering their head to their torso. A wireless system for perturbation or recording neural activity would enable us to study the full, unobstructed grooming behavior<sup>540</sup>. Further, wireless systems would provide the ability to transition from studying neural control of self-grooming in single animals to also studying neural control of social grooming or allogrooming between animals. Allogrooming is a highly conserved behavior<sup>31,49,50,541–547</sup> that serves to care for the outer body surface and is important for the regulation of social relationships.

Given the evolutionary conservation of both grooming behavior and the basal ganglia, a comparative study of the basal ganglia control of grooming could yield insights into conserved and specialized roles of the basal ganglia in the control of an innate behavior.

## References

1. Szebenyi, A. L. Cleaning behaviour in *Drosophila melanogaster*. *Animal Behaviour* **17**, 641–651 (1969).
2. Farish, D. J. The evolutionary implications of qualitative variation in the grooming behaviour of the hymenoptera (insecta). *Animal Behaviour* **20**, 662–676 (1972).
3. Dawkins, R. & Dawkins, M. Hierarchical organization and postural facilitation: Rules for grooming in flies. *Animal Behaviour* **24**, 739–755 (1976).
4. Thelen, E. & Farish, D. J. An Analysis of the Grooming Behavior of Wild and Mutant Strains of *Bracon Hebet* or (Braconidae : Hymenoptera). *Behav* **62**, 70–102 (1977).
5. Waldorf, E. S. Variation in Self-Grooming in Male *Sinella coeca* (Collembola: Entomobryidae). *Transactions of the American Microscopical Society* **97**, 111 (1978).
6. Lefebvre, L. Grooming in crickets: Timing and hierarchical organization. *Animal Behaviour* **29**, 973–984 (1981).
7. Smith, B. J. B. & Valentine, B. D. Phylogenetic Implications of Grooming Behavior in Cockroaches (Insecta: Blattaria). *Psyche: A Journal of Entomology* **92**, 369–385 (1985).
8. Pettis, J. S. & Pankiw, T. Grooming behavior by *Apis mellifera* L. in the presence of *Acarapis woodi* (Rennie) (Acari: Tarsonemidae). *Apidologie* **29**, 241–253 (1998).
9. Valentine, B. D. Grooming Behavior in Embioptera and Zoraptera (Insecta). *The Ohio journal of science* **86**, (1986).
10. Valentine, B. D. Grooming Behavior in Coleoptera. *The Coleopterists Bulletin* **27**, 63–73 (1973).

11. Valentine, B. D. & Glorioso, M. J. Grooming Behavior in Diplura (Insecta: Apterygota). *Psyche: A Journal of Entomology* **85**, 191–200 (1978).
12. Zack, S. Head grooming behaviour in the praying mantis. *Animal Behaviour* **26**, 1107–1119 (1978).
13. Felgenhauer, B. E. & Schram, F. R. Differential Epibiont Fouling in Relation to Grooming Behavior in *Palaemonetes kadiakensis*. *Fieldiana Zoology* **72**, 83–100 (1978).
14. Bauer, R. T. Grooming Behavior and Morphology in the Decapod Crustacea. *Journal of Crustacean Biology* **1**, 153–173 (1981).
15. Martin, J. W. & Felgenhauer, B. E. Grooming behaviour and the morphology of grooming appendages in the endemic South American crab genus *Aegla* (Decapoda, Anomura, Aeglididae). *Journal of Zoology* **209**, 213–224 (1986).
16. Bauer, R. T. Stomatopod Grooming Behavior: Functional Morphology and Amputation Experiments in *Gonodactylus Oerstedii*. *Journal of Crustacean Biology* **7**, 414–432 (1987).
17. Rowell, C. H. F. Displacement grooming in the chaffinch. *Animal Behaviour* **9**, 38–63 (1961).
18. McKinney, F. The Comfort Movements of Anatidae. *Behav* **25**, 120–220 (1965).
19. Lefebvre, L. & Joly, R. Organization rules and timing in kestrel grooming. *Animal Behaviour* **30**, 1020–1028 (1982).
20. Lefebvre, L. The organization of grooming in budgerigars. *Behavioural Processes* **7**, 93–106 (1982).
21. Delius, J. D. A Stochastic Analysis of the Maintenance Behaviour of Skylarks. *Behav* **33**, 137–177 (1969).

22. Ainley, D. G. The Comfort Behaviour of Adélie and Other Penguins. *Behav* **50**, 16–50 (1974).
23. van RHIJN, J. G. The Patterning of Preening and Other Comfort Behaviour in a Herring Gull. *Behav* **63**, 71–109 (1977).
24. Delius, J. D. Preening and Associated Comfort Behavior in Birds. *Ann NY Acad Sci* **525**, 40–55 (1988).
25. Bolles, R. C. Grooming behavior in the rat. *The Journal of Comparative and Physiological Psychology* **53**, 306–310 (1960).
26. Ewer, R. F. The Behaviour of the African Giant Rat (*Cricetomys gambianus* Waterhouse). *Zeitschrift für Tierpsychologie* **24**, 6–79 (1967).
27. Fentress, J. C. Interrupted ongoing behaviour in two species of vole (*Microtus agrestis* and *Clethrionomys britannicus*). I. Response as a function of preceding activity and the context of an apparently ‘irrelevant’ motor pattern. *Animal Behaviour* **16**, 135–153 (1968).
28. Fentress, J. C. Interrupted ongoing behaviour in two species of vole (*Microtus agrestis* and *Clethrionomys britannicus*). II. Extended analysis of motivational variables underlying fleeing and grooming behaviour. *Animal Behaviour* **16**, 154–167 (1968).
29. Russell, E. Observations on the behaviour of the red Kangaroo (*Megaleia rufa*) in captivity. *Zeitschrift für Tierpsychologie* **27**, 385–404 (1970).
30. Stanley, M. An Ethogram of the Hopping mouse, *Notomys alexis*. *Zeitschrift für Tierpsychologie* **29**, 225–258 (1971).
31. Steiner, A. L. Self- and allo-grooming behavior in some ground squirrels (*Sciuridae*), a descriptive study. *Can. J. Zool.* **51**, 151–161 (1973).

32. Simonsen, H. B. Grooming behaviour of domestic cattle. *Nord Vet Med* **31**, 1–5 (1979).
33. Hart, B. L., Hart, L. A., Mooring, M. S. & Olubayo, R. Biological basis of grooming behaviour in antelope: the body-size, vigilance and habitat principles. *Animal Behaviour* **44**, 615–631 (1992).
34. Berridge, K. C. Comparative fine structure of action: rules of form and sequence in the grooming patterns of six rodent species. *Behaviour* **113**, 21–56 (1990).
35. Colonnese, M. T., Stallman, E. L. & Berridge, K. C. Ontogeny of action syntax in altricial and precocial rodents: grooming sequences of rat and guinea pig pups. *Behaviour* **133**, 1165–1195 (1996).
36. Mooring, M. Grooming in impala: Role of oral grooming in removal of ticks and effects of ticks in increasing grooming rate. *Physiology & Behavior* **59**, 965–971 (1996).
37. Ferron, J. & Lefebvre, L. Comparative Organization of Grooming Sequences in Adult and Young Sciurid Rodents. *Behaviour* **81**, 110–127 (1982).
38. Richmond, G. & Sachs, B. D. Grooming in Norway Rats : The Development and Adult Expression of a Complex Motor Pattern. *Behaviour* **75**, 82–96 (1980).
39. Eckstein, R. A. & Hart, B. L. The organization and control of grooming in cats. *Applied Animal Behaviour Science* **68**, 131–140 (2000).
40. Young, R. K. & Thiessen, D. D. Washing, Drying, and Anointing in Adult Humans (Homo sapiens): Commonalities With Grooming Sequences in Rodents. *Journal of Comparative Psychology* **105**, 340–344 (1991).
41. Golani, I. & Fentress, J. C. Early Ontogeny of Face Grooming in Mice. *Developmental Psychobiology* **18**, 529–544 (1985).

42. Bolles, R. C., Woods, P. J. & College, H. The ontogeny of behaviour in the albino rat. *Animal Behaviour* **12**, 427–441 (1964).
43. Small, W. S. Notes on the Psychic Development of the Young White Rat. *The American Journal of Psychology* **11**, 80 (1899).
44. Thiessen, D., Pendergrass, M. & Young, R. K. Development and expression of autogrooming in the Mongolian gerbil, *Meriones unguiculatus*. *Journal of comparative psychology* **97**, 187–190 (1983).
45. Altman, J. & Sudarshan, K. Postnatal development of locomotion in the laboratory rat. *Animal Behaviour* **23**, 896–920 (1975).
46. Westerga, J. & Gramsbergen, A. The development of locomotion in the rat. *Developmental Brain Research* **57**, 163–174 (1990).
47. Borchelt, P. L., Griswold, J. G. & Brancheck, R. S. An analysis of sandbathing and grooming in the kangaroo rat (*Dipodomys merriami*). *Animal Behaviour* **24**, 347–353 (1976).
48. Griswold, J. G., Borchelt, P. L., Brancher, R. S. & Bensko, J. A. Condition of the pelage regulates sandbathing and grooming behaviour in the kangaroo rat (*Dipodomys merriami*). *Animal Behaviour* **25**, 602–608 (1977).
49. Spruijt, B. M., van Hooff, J. A. & Gispen, W. H. Ethology and neurobiology of grooming behavior. *Physiological Reviews* **72**, 825–852 (1992).
50. Reber, A., Purcell, J., Buechel, S. D., Buri, P. & Chapuisat, M. The expression and impact of antifungal grooming in ants: Grooming in ants. *Journal of Evolutionary Biology* **24**, 954–964 (2011).

51. Vincent, C. M. & Bertram, S. M. Crickets groom to avoid lethal parasitoids. *Animal Behaviour* **79**, 51–56 (2010).
52. Hart, B. L. Behavioral adaptations to pathogens and parasites: Five strategies. *Neuroscience & Biobehavioral Reviews* **14**, 273–294 (1990).
53. Brown, N. S. The Effect of Louse Infestation, Wet Feathers, and Relative Humidity on the Grooming Behavior of the Domestic Chicken. *Poultry Science* **53**, 1717–1719 (1974).
54. Bąk, B. & Wilde, J. Grooming behavior by worker bees of various subspecies of honey bees to remove *Varroa destructor* mites. *Journal of Apicultural Research* **54**, 207–215 (2015).
55. Snowball, G. The effect of self-licking by cattle on infestations of cattle tick, *Boophilus microplus* (Canestrini). *Aust. J. Agric. Res.* **7**, 227 (1956).
56. Bennett, G. F. *Boophilus microplus* (Acarina: Ixodidae): Experimental infestations on cattle restrained from grooming. *Experimental Parasitology* **26**, 323–328 (1969).
57. Weisbroth, S. H., Friedman, S., Powell, M. & Scher, S. The parasitic ecology of the rodent mite *Myobia musculi*. I. Grooming factors. *Laboratory Animal Science* **24**, 510–516 (1974).
58. Koch, H. G. Suitability of Birds and Mammals as Hosts for Immature Stages of the Lone Star Tick, *Amblyomma Americanum* (Acari: Ixodidae)<sup>12</sup>. *Journal of Medical Entomology* **18**, 93–98 (1981).
59. Koch, H. G. Suitability of White-Tailed Deer, Cattle, and Goats as Hosts for the Lone Star Tick, *Amblyomma americanum* (Acari: Ixodidae). *Journal of the Kansas Entomological Society* **61**, 251–257 (1988).

60. Olubayo, R. O., Jono, J., Orinda, G., Groothenhuis, J. G. & Hart, B. L. Comparative differences in densities of adult ticks as a function of body size on some East African antelopes. *African J Ecol* **31**, 26–34 (1993).
61. Franklin, Benjamin. *Experiments and observations on electricity*. (1769).
62. Robinson, K. W. & Morrison, P. R. The reaction to hot atmospheres of various species of australian marsupial and placental animals. *J. Cell. Comp. Physiol.* **49**, 455–478 (1957).
63. Higginbotham, A. C. & Koon, W. E. Temperature Regulation in the Virginia Opossum. *American Journal of Physiology* **181**, 69–71 (1955).
64. Adolph, E. F. Tolerance to heat and dehydration in several species of mammals. *American Journal of Physiology-Legacy Content* **151**, 564–575 (1947).
65. Hainsworth, F. R. Saliva spreading, activity, and body temperature regulation in the rat. *American Journal of Physiology* 1288–1292 (1967) doi:10.1007/978-3-642-16472-9-24.
66. Stricker, E. M. & Hainsworth, F. R. Evaporative cooling in the rat: interaction with heat loss from the tail. *Exp Physiol* **56**, 231–241 (1971).
67. Tanaka, H., Kanosue, K., Nakayama, T. & Shen, Z. Grooming, body extension, and vasomotor responses induced by hypothalamic warming at different ambient temperatures in rats. *Physiology and Behavior* **38**, 145–151 (1986).
68. Kennedy, G. Y. Harderoporphyrin: A new porphyrin from the Harderian glands of the rat. *Comparative Biochemistry and Physiology* **36**, 21–36 (1970).
69. Otsuru, O. *et al.* The Characterization of 2,3-Alkanediol Diacyl Esters Obtained from the Harderian Glands of Mongolian Gerbil (*Meriones unguiculatus*)<sup>1</sup>. *The Journal of Biochemistry* **94**, 2049–2054 (1983).

70. Carriere, R. Ultrastructural visualization of intracellular porphyrin in the rat Harderian gland. *Anat. Rec.* **213**, 496–504 (1985).
71. Otsuka, H. *et al.* Stereochemistry of 2,3-Alkanediols Obtained from the Harderian Gland of Mongolian Gerbil (*Meriones unguiculatus*). *The Journal of Biochemistry* **99**, 1339–1344 (1986).
72. Thiessen, D. D., Pendergrass, M. & Harriman, A. E. The thermoenergetics of coat colour maintenance by the mongolian gerbil, *Meriones unguiculatus*. *Journal of Thermal Biology* **7**, 51–56 (1982).
73. Pendergrass, M. L. & Thiessen, D. D. Body temperature and autogrooming in the mongolian gerbil, *Meriones unguiculatus*. *Behavioral and Neural Biology* **33**, 524–528 (1981).
74. Thiessen, D. D. Body Temperature and Grooming in the Mongolian Gerbil. *Annals of the New York Academy of Sciences* **525**, 27–39 (1988).
75. Ritter, R. C. & Epstein, A. N. Saliva lost by grooming: A major item in the rat's water economy. *Behavioral Biology* **11**, 581–585 (1974).
76. Ferkin, M. H., Sorokin, E. S. & Johnston, R. E. Self-grooming as a sexually dimorphic communicative behaviour in meadow voles, *Microtus pennsylvanicus*. *Animal Behaviour* **51**, 801–810 (1996).
77. Ferkin, M. H., Leonard, S. T., Heath, L. A. & C, G. P.-M. Self-Grooming as a Tactic Used by Prairie Voles *Microtus ochrogaster* to Enhance Sexual Communication. *Ethology* **107**, 939–949 (2001).
78. Lai, S.-C. & Johnston, R. E. Individual Odors in Djungarian Hamsters (*Phodopus campbelli*). *Ethology* **96**, 117–126 (2010).

79. Castelli, F. R. Aspects of Olfactory Communication in the Dwarf Hamster (*Phodopus sungorus*) and the Naked Mole-Rat (*Heterocephalus glaber*). (Cornell University, 2017).
80. Paz-Y-Miño C, G., Leonard, S. T., Ferkin, M. H. & Trimble, J. F. Self-grooming and sibling recognition in meadow voles, *Microtus pennsylvanicus*, and prairie voles, *M. Ochrogaster*. *Animal Behaviour* **63**, 331–338 (2002).
81. Ferkin, M. H. & Leonard, S. T. Self-grooming as a form of olfactory communication in meadow voles and prairie voles (*Microtus spp.*). in *Neurobiology of Grooming Behavior* (eds. Kalueff, A. V., La Porte, J. L. & Bergner, C. L.) 19–45 (Cambridge University Press, 2010). doi:10.1017/CBO9780511676109.003.
82. Böröczky, K., Wada-Katsumata, A., Batchelor, D., Zhukovskaya, M. & Schal, C. Insects groom their antennae to enhance olfactory acuity. *Proc. Natl. Acad. Sci. U.S.A.* **110**, 3615–3620 (2013).
83. Baillie, P. & Morrison, S. D. The nature of the suppression of food intake by lateral hypothalamic lesions in rats. *The Journal of Physiology* **165**, 227–245 (1963).
84. van Erp, A. M. M., Kruk, M. R., Meelis, W. & Willekens-Bramer, D. C. Effect of environmental stressors on time course, variability and form of self-grooming in the rat: Handling, social contact, defeat, novelty, restraint and fur moistening. *Behavioural Brain Research* **65**, 47–55 (1994).
85. Continella, G., Drago, F., Auditore, S. & Scapagnini, U. Quantitative alteration of grooming behavior in aged male rats. *Physiology & Behavior* **35**, 839–841 (1985).
86. Kametani, H., Osada, H. & Inoue, K. Increased novelty-induced grooming in aged rats: a preliminary observation. *Behavioral and Neural Biology* **42**, 73–80 (1984).

87. Kametani, H. Analysis of Age-related Changes in Stress-induced Grooming in the Rat: Differential Behavioral Profile of Adaptation to Stress. *Ann NY Acad Sci* **525**, 101–113 (1988).
88. Van Iersel, J. J. A. & Angela Bol, A. C. Preening of Two Tern Species. a Study On Displacement Activities. *Behav* **13**, 1–87 (1958).
89. Andrew, R. J. Normal and irrelevant toilet behaviour in *Emberiza* Spp. *The British Journal of Animal Behaviour* **4**, 85–91 (1956).
90. Huxley, J. S. The Courtship habits of the Great Crested Grebe (*Podiceps cristatus*); with an addition to the Theory of Sexual Selection. *Proceedings of the Zoological Society of London* **84**, 491–562 (1914).
91. Tinbergen, N. On the Analysis of Social Organization Among Vertebrates, with Special Reference to Birds. *American Midland Naturalist* **21**, 210 (1939).
92. Tinbergen, N. ‘Derived’ Activities; Their Causation, Biological Significance, Origin, and Emancipation During Evolution. *The Quarterly Review of Biology* **27**, 1–32 (1952).
93. Van Iersel, J. J. A. & Tinbergen, N. ‘Displacement Reactions’ in the Three-Spined Stickleback. *Behav* **1**, 56–63 (1947).
94. Pflumm, W. Consecutive antenna grooming as displacement activity of the honeybee in collecting differently concentrated sucrose solutions. *Ins. Soc* **32**, 435–444 (1985).
95. Holmquist, J. G. The Grooming Behavior of the Terrestrial Amphipod *Talitroides Alluaudi*. *Journal of Crustacean Biology* **5**, 334–340 (1985).
96. Grant, E. C. An Analysis of the Social Behaviour of the Male Laboratory Rat. *Behav* **21**, 260–281 (1963).

97. Durant, P., Dole, J. W. & Fisler, G. F. Agonistic behavior of the California ground squirrel, *Spermophilus beecheyi*, at and artificial food source. *The Great Basin Naturalist* **48**, 19–24 (1988).
98. Jolles, J., Rompa-Barendregt, J. & Gispen, W. H. ACTH-induced excessive grooming in the rat: The influence of environmental and motivational factors. *Hormones and Behavior* **12**, 60–72 (1979).
99. Jolles, J., Rompa-Barendregt, J. & Gispen, W. H. Novelty and grooming behavior in the rat. *Behavioral and Neural Biology* **25**, 563–572 (1979).
100. Scucchi, S., Maestriperi, D. & Schino, G. Conflict, displacement activities, and menstrual cycle in long-tailed macaques. *Primates* **32**, 115–118 (1991).
101. Maestriperi, D., Schino, G., Aureli, F. & Troisi, A. A modest proposal: displacement activities as an indicator of emotions in primates. *Animal Behaviour* **44**, 967–979 (1992).
102. Sevenster, P. A Causal Analysis of a Displacement Activity (Fanning in *Gasterosteus Aculeatus* L.). *Behaviour. Supplement* **9**, 1–170 (1961).
103. Delius, J. D. Displacement Activities and Arousal. *Nature* **214**, 1259–1260 (1967).
104. Komorowska, J. & Pellis, S. M. Regulatory mechanisms underlying novelty-induced grooming in the laboratory rat. *Behavioural processes* **67**, 287–293 (2004).
105. Kalueff, A. V. *et al.* Neurobiology of rodent self-grooming and its value for translational neuroscience. *Nature Reviews Neuroscience* **17**, 45–59 (2016).
106. Fentress, J. C. Specific and Nonspecific Factors in the Causation of Behavior. in *Perspectives in Ethology* (eds. Bateson, P. P. G. & Klopfer, P. H.) 155–224 (Springer US, 1973). doi:10.1007/978-1-4615-7569-6\_6.

107. Sherrington, C. S. *The Integrative Action of the Nervous System*. (Yale University Press, 1906).
108. Berridge, K. & Fentress, J. Contextual control of trigeminal sensorimotor function. *J. Neurosci.* **6**, 325–330 (1986).
109. Berridge, K. C. & Fentress, J. C. Deafferentation does not disrupt natural rules of action syntax. *Behavioural Brain Research* **23**, 69–76 (1987).
110. Fentress, J. C. The tonic hypothesis and the patterning of behavior. *Ann NY Acad Sci* **290**, 370–395 (1977).
111. Fentress, J. C. Development of Grooming in Mice with Amputated Forelimbs. *Science* **179**, 704–705 (1973).
112. Berridge, K. C. & Fentress, J. C. Disruption of natural grooming chains after striatopallidal lesions. *Psychobiology* **15**, 336–342 (1987).
113. Berridge, K. C. Substantia nigra 6-OHDA lesions mimic striatopallidal disruption of syntactic grooming chains: A neural systems analysis of sequence control. *Psychobiology* **17**, 377–385 (1989).
114. Cromwell, H. C. & Berridge, K. C. Implementation of action sequences by a neostriatal site: a lesion mapping study of grooming syntax. *The Journal of neuroscience* **16**, 3444–58 (1996).
115. Aldridge, J. W., Berridge, K. C., Herman, M. & Zimmer, L. Neuronal Coding of Serial Order: Syntax of Grooming in the Neostriatum. *Psychological Science* **4**, 391–395 (1993).
116. Sjöbom, J., Tamtè, M., Halje, P., Brys, I. & Petersson, P. Cortical and striatal circuits together encode transitions in natural behavior. *Sci. Adv.* **6**, eabc1173 (2020).

117. Corbit, V. L. *et al.* Dissociable roles of central striatum and anterior lateral motor area in initiating and sustaining naturalistic behavior. *bioRxiv* (2020)  
doi:10.1101/2020.01.08.899070.
118. Hintiryan, H. *et al.* The mouse cortico-striatal projectome. *Nat Neurosci* **19**, 1100–1114 (2016).
119. Foster, N. N. *et al.* The mouse cortico–basal ganglia–thalamic network. *Nature* **598**, 188–194 (2021).
120. Alexander, G. E., DeLong, M. R. & Strick, P. L. Parallel Organization of Functionally Segregated Circuits Linking Basal Ganglia and Cortex. *Annu. Rev. Neurosci.* **9**, 357–381 (1986).
121. Hunnicutt, B. J. *et al.* A comprehensive excitatory input map of the striatum reveals novel functional organization. *eLife* **5**, 1–32 (2016).
122. Parent, A. & Hazrati, L.-N. Functional anatomy of the basal ganglia. I. The cortico-basal ganglia-thalamo-cortical loop. *Brain Research Reviews* **20**, 91–127 (1995).
123. Albin, R. L., Young, A. B. & Penney, J. B. The functional anatomy of basal ganglia disorders. *Trends in Neurosciences* **12**, 366–375 (1989).
124. Montaron, M. F., Deniau, J. M., Menetrey, A., Glowinski, J. & Thierry, A. M. Prefrontal cortex inputs of the nucleus accumbens-nigro-thalamic circuit. *Neuroscience* **71**, 371–382 (1996).
125. Berendse, H. W., Graaf, Y. G.-D. & Groenewegen, H. J. Topographical organization and relationship with ventral striatal compartments of prefrontal corticostriatal projections in the rat. *J. Comp. Neurol.* **316**, 314–347 (1992).

126. Nakano, K., Kayahara, T. & Chiba, T. Afferent Connections to the Ventral Striatum from the Medial Prefrontal Cortex (Area 25) and the Thalamic Nuclei in the Macaque Monkey. *Annals NY Acad Sci* **877**, 667–670 (1999).
127. Voorn, P., Jorritsma-Byham, B., Van Dijk, C. & Buijs, R. M. The dopaminergic innervation of the ventral striatum in the rat: A light- and electron-microscopical study with antibodies against dopamine. *J. Comp. Neurol.* **251**, 84–99 (1986).
128. Nicola, S. M., Surmeier, D. J. & Malenka, R. C. Dopaminergic Modulation of Neuronal Excitability in the Striatum and Nucleus Accumbens. *Annu. Rev. Neurosci.* **23**, 185–215 (2000).
129. Azcorra, M. *et al.* Unique functional responses differentially map onto genetic subtypes of dopamine neurons. *bioRxiv* (2022) doi:10.1101/2022.12.19.521076.
130. Smith, Y., Bevan, M. D., Shink, E. & Bolam, J. P. Microcircuitry of the Direct and Indirect Pathways of the Basal Ganglia. *Neuroscience* **86**, 353–387 (1998).
131. Alexander, G. E. & Crutcher, M. D. Functional architecture of basal ganglia circuits: neural substrates of parallel processing. *Trends in Neurosciences* **13**, 266–271 (1990).
132. Kravitz, A. V. *et al.* Regulation of parkinsonian motor behaviours by optogenetic control of basal ganglia circuitry. *Nature* **466**, 622–626 (2010).
133. Cui, G. *et al.* Concurrent activation of striatal direct and indirect pathways during action initiation. *Nature* **494**, 238–242 (2013).
134. Klaus, A. *et al.* The Spatiotemporal Organization of the Striatum Encodes Action Space. *Neuron* **95**, 1171–1180 (2017).

135. Parker, J. G. *et al.* Diametric neural ensemble dynamics in parkinsonian and dyskinetic states. *Nature* **557**, 177–182 (2018).
136. Markowitz, J. E. *et al.* The Striatum Organizes 3D Behavior via Moment-to-Moment Action Selection. *Cell* **174**, 44–49.e17 (2018).
137. Calabresi, P., Picconi, B., Tozzi, A., Ghiglieri, V. & Di Filippo, M. Direct and indirect pathways of basal ganglia: a critical reappraisal. *Nat Neurosci* **17**, 1022–1030 (2014).
138. Stock, D. W. & Whitt, G. S. Evidence from 18 S Ribosomal RNA Sequences that Lampreys and Hagfishes form a Natural Group. *Science* **257**, 787–789 (1992).
139. Grillner, S. & Robertson, B. The Basal Ganglia Over 500 Million Years. *Current Biology* **26**, R1088–R1100 (2016).
140. Kumar, S. & Hedges, S. B. A molecular timescale for vertebrate evolution. *Nature* **392**, 917–920 (1998).
141. Stephenson-Jones, M., Ericsson, J., Robertson, B. & Grillner, S. Evolution of the basal ganglia: Dual-output pathways conserved throughout vertebrate phylogeny. *Journal of Comparative Neurology* **520**, 2957–2973 (2012).
142. Gerfen, C. R. *et al.* D1 and D2 Dopamine Receptor-regulated Gene Expression of Striatonigral and Striatopallidal Neurons. *Science* **250**, 1429–1432 (1990).
143. Gerfen, C. R. & Surmeier, D. J. Modulation of Striatal Projection Systems by Dopamine. *Annu. Rev. Neurosci.* **34**, 441–466 (2011).
144. Gerfen, C. R. Molecular effects of dopamine on striatal-projection pathways. *Trends in Neurosciences* **23**, S64–S70 (2000).

145. Carlsson, A. Evidence for a role of dopamine in extrapyramidal functions. *Acta Neurovegetativa* **26**, 484–493 (1964).
146. Robbins, T. W. & Everitt, B. J. Functions of dopamine in the dorsal and ventral striatum. *Seminars in Neuroscience* **4**, 119–127 (1992).
147. Ehringer, H. & Hornykiewicz, O. Verteilung Von Noradrenalin Und Dopamin (3-Hydroxytyramin) Im Gehirn Des Menschen Und Ihr Verhalten Bei Erkrankungen Des Extrapyramidalen Systems. *Klin Wochenschr* **38**, 1236–1239 (1960).
148. Poirier, L. J. & Sourkes, T. L. Influence of the Substantia Nigra on the Catecholamine Content of the Striatum. *Brain* **88**, 181–192 (1965).
149. Calabresi, P., Centonze, D., Gubellini, P., Pisani, A. & Bernardi, G. Acetylcholine-mediated modulation of striatal function. *Trends in Neurosciences* **23**, 120–126 (2000).
150. Oldenburg, I. A. & Ding, J. B. Cholinergic modulation of synaptic integration and dendritic excitability in the striatum. *Current Opinion in Neurobiology* **21**, 425–432 (2011).
151. Svenningsson, P. Distribution, biochemistry and function of striatal adenosine A2A receptors. *Progress in Neurobiology* **59**, 355–396 (1999).
152. Steinbusch, H. W. M. Distribution of serotonin-immunoreactivity in the central nervous system of the rat—Cell bodies and terminals. *Neuroscience* **6**, 557–618 (1981).
153. Mathur, B. N. & Lovinger, D. M. Serotonergic action on dorsal striatal function. *Parkinsonism & Related Disorders* **18**, S129–S131 (2012).
154. Cavaccini, A. *et al.* Serotonergic Signaling Controls Input-Specific Synaptic Plasticity at Striatal Circuits. *Neuron* **98**, 1–16 (2018).

155. Ellender, T. J., Huerta-Ocampo, I., Deisseroth, K., Capogna, M. & Bolam, J. P. Differential Modulation of Excitatory and Inhibitory Striatal Synaptic Transmission by Histamine. *J. Neurosci.* **31**, 15340–15351 (2011).
156. Bolam, J. P. & Ellender, T. J. Histamine and the striatum. *Neuropharmacology* **106**, 74–84 (2016).
157. Howe, M. *et al.* Coordination of rapid cholinergic and dopaminergic signaling in striatum during spontaneous movement. *eLife* **8**, e44903 (2019).
158. Kita, H., Kosaka, T. & Heizmann, C. W. Parvalbumin-immunoreactive neurons in the rat neostriatum: a light and electron microscopic study. *Brain Research* **536**, 1–15 (1990).
159. Koós, T. & Tepper, J. M. Inhibitory control of neostriatal projection neurons by GABAergic interneurons. *Nature Neuroscience* **2**, 467–472 (1999).
160. Kawaguchi, Y., Wilson, C. J., Augood, S. J. & Emson, P. C. Striatal interneurons: chemical, physiological and morphological characterization. *Trends in Neurosciences* **18**, 527–535 (1995).
161. Aosaki, T., Kimura, M. & Graybiel, A. M. Temporal and spatial characteristics of tonically active neurons of the primate's striatum. *Journal of Neurophysiology* **73**, 1234–1252 (1995).
162. Bennett, B. D. & Wilson, C. J. Spontaneous Activity of Neostriatal Cholinergic Interneurons In Vitro. *J. Neurosci.* **19**, 5586–5596 (1999).
163. Guzman, M. S. *et al.* Elimination of the Vesicular Acetylcholine Transporter in the Striatum Reveals Regulation of Behaviour by Cholinergic-Glutamatergic Co-Transmission. *PLoS Biol* **9**, e1001194 (2011).

164. Higley, M. J. *et al.* Cholinergic Interneurons Mediate Fast VGluT3-Dependent Glutamatergic Transmission in the Striatum. *PLoS ONE* **6**, e19155 (2011).
165. Gonzales, K. K. & Smith, Y. Cholinergic interneurons in the dorsal and ventral striatum: anatomical and functional considerations in normal and diseased conditions: Striatal cholinergic interneurons in disease. *Ann. N.Y. Acad. Sci.* **1349**, 1–45 (2015).
166. Zhou, F.-M., Liang, Y. & Dani, J. A. Endogenous nicotinic cholinergic activity regulates dopamine release in the striatum. *Nat Neurosci* **4**, 1224–1229 (2001).
167. Lapper, S. R. & Bolam, J. P. Input from the frontal cortex and the parafascicular nucleus to cholinergic interneurons in the dorsal striatum of the rat. *Neuroscience* **51**, 533–545 (1992).
168. Ding, J. B., Guzman, J. N., Peterson, J. D., Goldberg, J. A. & Surmeier, D. J. Thalamic gating of corticostriatal signaling by cholinergic interneurons. *Neuron* **67**, 294–307 (2010).
169. Zhou, F.-M., Wilson, C. J. & Dani, J. A. Cholinergic interneuron characteristics and nicotinic properties in the striatum. *J. Neurobiol.* **53**, 590–605 (2002).
170. Cowan, R. L., Wilson, C. J., Emson, P. C. & Heizmann, C. W. Parvalbumin-containing gabaergic interneurons in the rat neostriatum. *J. Comp. Neurol.* **302**, 197–205 (1990).
171. Fukuda, T. Network Architecture of Gap Junction-Coupled Neuronal Linkage in the Striatum. *Journal of Neuroscience* **29**, 1235–1243 (2009).
172. Bennett, B. D. & Bolam, J. P. Synaptic Input and Output of Parvalbumin-Immunoreactive Neurons in the Neostriatum of the Rat. *Neuroscience* **62**, 707–719 (1994).
173. Vuillet, J., Kerkerian, L., Kachidian, P., Bosler, O. & Nicoullon, A. Ultrastructural correlates of functional relationships between nigral dopaminergic or cortical afferent fibers

- and neuropeptide Y-containing neurons in the rat striatum. *Neuroscience Letters* **100**, 99–104 (1989).
174. Petryszyn, S., Beaulieu, J.-M., Parent, A. & Parent, M. Distribution and morphological characteristics of striatal interneurons expressing calretinin in mice: A comparison with human and nonhuman primates. *Journal of Chemical Neuroanatomy* **59–60**, 51–61 (2014).
175. Gurney, K., Prescott, T. J. & Redgrave, P. A computational model of action selection in the basal ganglia. I. A new functional anatomy. *Biol Cybern* **84**, 401–410 (2001).
176. Stephenson-Jones, M., Samuelsson, E., Ericsson, J., Robertson, B. & Grillner, S. Evolutionary Conservation of the Basal Ganglia as a Common Vertebrate Mechanism for Action Selection. *Current Biology* **21**, 1081–1091 (2011).
177. Mink, J. W. The Basal Ganglia: Focused Selection and Inhibition of Competing Motor Programs. *Progress in Neurobiology* **50**, 381–425 (1996).
178. Frank, M. J. Computational models of motivated action selection in corticostriatal circuits. *Current Opinion in Neurobiology* **21**, 381–386 (2011).
179. Graybiel, A. M. The basal ganglia and chunking of action repertoires. *Neurobiology of Learning and Memory* **70**, 119–136 (1998).
180. Jin, X. & Costa, R. M. Start/stop signals emerge in nigrostriatal circuits during sequence learning. *Nature* **466**, 457–462 (2010).
181. Jin, X., Tecuapetla, F. & Costa, R. M. Basal ganglia subcircuits distinctively encode the parsing and concatenation of action sequences. *Nature Neuroscience* **17**, 423–430 (2014).
182. Geddes, C. E., Li, H. & Jin, X. Optogenetic Editing Reveals the Hierarchical Organization of Learned Action Sequences. *Cell* **174**, 32–43.e15 (2018).

183. Mink, J. W. Basal ganglia dysfunction in Tourette's syndrome: a new hypothesis. *Pediatric Neurology* **25**, 190–198 (2001).
184. Singer, H. S. *et al.* Elevated Intrasympaptic Dopamine Release in Tourette's Syndrome Measured by PET. *AJP* **159**, 1329–1336 (2002).
185. Segawa, M. Neurophysiology of Tourette's syndrome: pathophysiological considerations. *Brain and Development* **25**, S62–S69 (2003).
186. Itard, J.-M. G. Memoire sur quelques fonctions involontaires des appareils de la locomotion de la prehension et de la voix. *Archiv Generale Medecine* **8**, 385–407 (1825).
187. Rapoport, J. L. Obsessive compulsive disorder and basal ganglia dysfunction. *Psychol. Med.* **20**, 465–469 (1990).
188. Talland, G. A. & Schwab, R. S. Performance with multiple sets in Parkinson's disease. *Neuropsychologia* **2**, 45–53 (1964).
189. Agostino, R., Berardelli, A., Formica, A., Accornero, N. & Manfredi, M. Sequential arm movements in patients with parkinson's disease, huntington's disease and dystonia. *Brain* **115**, 1481–1495 (1992).
190. Benecke, R., Rothwell, J. C., Dick, J. P. R., Day, B. L. & Marsden, C. D. Disturbance of sequential movements in patients with parkinson's disease. *Brain* **110**, 361–379 (1987).
191. Harrington, D. L. & Haaland, K. Y. Sequencing in Parkinson's disease: Abnormalities in programming and controlling movement. *Brain* **114**, 99–115 (1991).
192. Horne, D. J. D. L. Sensorimotor control in Parkinsonism. *Journal of Neurology, Neurosurgery & Psychiatry* **36**, 742–746 (1973).

193. Phillips, J. G., Chiu, E., Bradshaw, J. L. & Iansak, R. Impaired movement sequencing in patients with Huntington's disease: A kinematic analysis. *Neuropsychologia* **33**, 365–369 (1995).
194. Berardelli, A., Curra, A., Fabbrini, G., Gilio, F. & Manfredi, M. Pathophysiology of tics and Tourette syndrome. *Journal of Neurology* **250**, 781–787 (2003).
195. Hebb, D. O. *The organization of Behavior: A Neuropsychological Theory*. (Wiley, 1949).
196. Milner, P. M. The cell assembly: Mark II. *Psychological Review* **64**, 242–252 (1957).
197. Wallis, J. D. Decoding Cognitive Processes from Neural Ensembles. *Trends in Cognitive Sciences* **22**, 1091–1102 (2018).
198. Peyrache, A., Benchenane, K., Khamassi, M., Wiener, S. I. & Battaglia, F. P. Principal component analysis of ensemble recordings reveals cell assemblies at high temporal resolution. *J Comput Neurosci* **29**, 309–325 (2010).
199. Hamm, J. P., Shymkiv, Y., Han, S., Yang, W. & Yuste, R. Cortical ensembles selective for context. *Proc. Natl. Acad. Sci. U.S.A.* **118**, e2026179118 (2021).
200. Johnson, A. & Redish, A. D. Neural Ensembles in CA3 Transiently Encode Paths Forward of the Animal at a Decision Point. *J. Neurosci.* **27**, 12176–12189 (2007).
201. See, J. Z., Atencio, C. A., Sohal, V. S. & Schreiner, C. E. Coordinated neuronal ensembles in primary auditory cortical columns. *eLife* **7**, e35587 (2018).
202. Maltese, M., March, J. R., Bashaw, A. G. & Tritsch, N. X. Dopamine differentially modulates the size of projection neuron ensembles in the intact and dopamine-depleted striatum. *eLife* **10**, e68041 (2021).

203. Averbeck, B. B. & Lee, D. Coding and transmission of information by neural ensembles. *Trends in Neurosciences* **27**, 225–230 (2004).
204. Lin, L. *et al.* Identification of network-level coding units for real-time representation of episodic experiences in the hippocampus. *Proc. Natl. Acad. Sci. U.S.A.* **102**, 6125–6130 (2005).
205. Lin, L., Osan, R. & Tsien, J. Z. Organizing principles of real-time memory encoding: neural clique assemblies and universal neural codes. *Trends in Neurosciences* **29**, 48–57 (2006).
206. Camhi, J. M. & Levy, A. The code for stimulus direction in a cell assembly in the cockroach. *J. Comp. Physiol.* **165**, 83–97 (1989).
207. Angulo-Garcia, D., Berke, J. D. & Torcini, A. Cell Assembly Dynamics of Sparsely-Connected Inhibitory Networks: A Simple Model for the Collective Activity of Striatal Projection Neurons. *PLoS Computational Biology* **12**, 1–29 (2016).
208. Buzsáki, G. Neural Syntax: Cell Assemblies, Synapsembles, and Readers. *Neuron* **68**, 362–385 (2010).
209. Berger, D., Borgelt, C., Louis, S., Morrison, A. & Grün, S. Efficient Identification of Assembly Neurons within Massively Parallel Spike Trains. *Computational Intelligence and Neuroscience* **2010**, 1–18 (2010).
210. van der Plas, T. L. *et al.* Neural assemblies uncovered by generative modeling explain whole-brain activity statistics and reflect structural connectivity. *eLife* **12**, e83139 (2023).
211. Gerstein, G. L., Bedenbaugh, P. & Aertsen, A. M. H. J. Neuronal assemblies. *IEEE Trans. Biomed. Eng.* **36**, 4–14 (1989).

212. Angotzi, G. N. *et al.* SiNAPS: An implantable active pixel sensor CMOS-probe for simultaneous large-scale neural recordings. *Biosensors and Bioelectronics* **126**, 355–364 (2019).
213. Dimitriadis, G. *et al.* Why not record from every electrode with a CMOS scanning probe? *bioRxiv* (2018) doi:10.1101/275818.
214. Lopez, C. M. *et al.* A 966-electrode neural probe with 384 configurable channels in 0.13 $\mu$ m SOI CMOS. in *2016 IEEE International Solid-State Circuits Conference (ISSCC)* 392–393 (IEEE, 2016). doi:10.1109/ISSCC.2016.7418072.
215. Frey, U. *et al.* Switch-Matrix-Based High-Density Microelectrode Array in CMOS Technology. *IEEE J. Solid-State Circuits* **45**, 467–482 (2010).
216. Berdondini, L. *et al.* High-density electrode array for imaging in vitro electrophysiological activity. *Biosensors and Bioelectronics* **21**, 167–174 (2005).
217. Eversmann, B. *et al.* A 128 x 128 cmos biosensor array for extracellular recording of neural activity. *IEEE J. Solid-State Circuits* **38**, 2306–2317 (2003).
218. Du, J., Blanche, T. J., Harrison, R. R., Lester, H. A. & Masmanidis, S. C. Multiplexed, High Density Electrophysiology with Nanofabricated Neural Probes. *PLoS ONE* **6**, e26204 (2011).
219. Shim, E., Chen, Y., Masmanidis, S. & Li, M. Multisite silicon neural probes with integrated silicon nitride waveguides and gratings for optogenetic applications. *Sci Rep* **6**, 22693 (2016).
220. Steinmetz, N. A. *et al.* Neuropixels 2.0: A miniaturized high-density probe for stable, long-term brain recordings. *Science* **372**, eabf4588 (2021).

221. Jun, J. J. *et al.* Fully integrated silicon probes for high-density recording of neural activity. *Nature* **551**, 232–236 (2017).
222. Zhang, Y. *et al.* Fast and sensitive GCaMP calcium indicators for imaging neural populations. *Nature* (2023) doi:10.1038/s41586-023-05828-9.
223. Jacob, A. D. *et al.* A Compact Head-Mounted Endoscope for In Vivo Calcium Imaging in Freely Behaving Mice. *Current Protocols in Neuroscience* **84**, e51 (2018).
224. Aharoni, D., Khakh, B. S., Silva, A. J. & Golshani, P. All the light that we can see: a new era in miniaturized microscopy. *Nat Methods* **16**, 11–13 (2019).
225. Dong, Z. *et al.* Minian, an open-source miniscope analysis pipeline. *eLife* **11**, e70661 (2022).
226. Skocek, O. *et al.* High-speed volumetric imaging of neuronal activity in freely moving rodents. *Nat Methods* **15**, 429–432 (2018).
227. de Groot, A. *et al.* NINscope, a versatile miniscope for multi-region circuit investigations. *eLife* **9**, e49987 (2020).
228. Barbera, G., Liang, B., Zhang, L., Li, Y. & Lin, D.-T. A wireless miniScope for deep brain imaging in freely moving mice. *Journal of Neuroscience Methods* **323**, 56–60 (2019).
229. Liberti, W. A., Perkins, L. N., Leman, D. P. & Gardner, T. J. An open source, wireless capable miniature microscope system. *J. Neural Eng.* **14**, 045001 (2017).
230. Scott, B. B. *et al.* Imaging Cortical Dynamics in GCaMP Transgenic Rats with a Head-Mounted Widefield Macroscopic. *Neuron* **100**, 1045-1058.e5 (2018).
231. Ghosh, K. K. *et al.* Miniaturized integration of a fluorescence microscope. *Nature Methods* **8**, 871–878 (2011).

232. Scherrer, J. R., Lynch, G. F., Zhang, J. J. & Fee, M. S. An optical design enabling lightweight and large field-of-view head-mounted microscopes. *Nat Methods* (2023) doi:10.1038/s41592-023-01806-1.
233. Siegle, J. H. *et al.* Open Ephys: an open-source, plugin-based platform for multichannel electrophysiology. *J. Neural Eng.* **14**, 045003 (2017).
234. Putzeys, J. *et al.* Neuropixels Data-Acquisition System: A Scalable Platform for Parallel Recording of 10 000+ Electrophysiological Signals. *IEEE Trans. Biomed. Circuits Syst.* **13**, 1635–1644 (2019).
235. Lee, J. H. *et al.* YASS: Yet Another Spike Sorter. in *Advances in Neural Information Processing Systems* (eds. Guyon, I. *et al.*) vol. 30 (Curran Associates, Inc., 2017).
236. Pachitariu, M., Steinmetz, N. A., Kadir, S. N., Carandini, M. & Harris, K. D. Fast and accurate spike sorting of high-channel count probes with KiloSort. *Advances in Neural Information Processing Systems (NIPS)* 4448–4456 (2016) doi:10.2108/zsj.30.135.
237. Buccino, A. P. *et al.* SpikeInterface, a unified framework for spike sorting. *eLife* **9**, e61834 (2020).
238. Chung, J. E. *et al.* A Fully Automated Approach to Spike Sorting. *Neuron* **95**, 1381-1394.e6 (2017).
239. Yger, P. *et al.* A spike sorting toolbox for up to thousands of electrodes validated with ground truth recordings in vitro and in vivo. *eLife* **7**, e34518 (2018).
240. Hilgen, G. *et al.* Unsupervised Spike Sorting for Large-Scale, High-Density Multielectrode Arrays. *Cell Reports* **18**, 2521–2532 (2017).

241. Jun, J. J. *et al.* Real-time spike sorting platform for high-density extracellular probes with ground-truth validation and drift correction. *bioRxiv* (2017) doi:10.1101/101030.
242. Diggelmann, R., Fiscella, M., Hierlemann, A. & Franke, F. Automatic spike sorting for high-density microelectrode arrays. *Journal of Neurophysiology* **120**, 3155–3171 (2018).
243. Chen, X. *et al.* Brain-wide Organization of Neuronal Activity and Convergent Sensorimotor Transformations in Larval Zebrafish. *Neuron* **100**, 876-890.e5 (2018).
244. Avitan, L. *et al.* Spontaneous Activity in the Zebrafish Tectum Reorganizes over Development and Is Influenced by Visual Experience. *Current Biology* **27**, 2407-2419.e4 (2017).
245. Weissbourd, B. *et al.* A genetically tractable jellyfish model for systems and evolutionary neuroscience. *Cell* **184**, 5854-5868.e20 (2021).
246. Pérez-Ortega, J. *et al.* Parallel processing of natural images by overlapping retinal neuronal ensembles. *bioRxiv* (2021) doi:10.1101/2021.02.22.432289.
247. Kogan, A. B. Intercellular relationships in elementary neuronal ensembles. *Neurosci Behav Physiol* **16**, 410–416 (1986).
248. Kampa, B. Representation of visual scenes by local neuronal populations in layer 2/3 of mouse visual cortex. *Front. Neural Circuits* **5**, (2011).
249. Bathellier, B., Ushakova, L. & Rumpel, S. Discrete Neocortical Dynamics Predict Behavioral Categorization of Sounds. *Neuron* **76**, 435–449 (2012).
250. Narayanan, N. S., Kimchi, E. Y. & Laubach, M. Redundancy and Synergy of Neuronal Ensembles in Motor Cortex. *J. Neurosci.* **25**, 4207–4216 (2005).

251. Eichenbaum, H., Wiener, S., Shapiro, M. & Cohen, N. The organization of spatial coding in the hippocampus: a study of neural ensemble activity. *J. Neurosci.* **9**, 2764–2775 (1989).
252. Harris, K. D., Csicsvari, J., Hirase, H., Dragoi, G. & Buzsáki, G. Organization of cell assemblies in the hippocampus. *Nature* **424**, 552–556 (2003).
253. Adler, A. *et al.* Temporal Convergence of Dynamic Cell Assemblies in the Striato-Pallidal Network. *Journal of Neuroscience* **32**, 2473–2484 (2012).
254. Barbera, G. *et al.* Spatially Compact Neural Clusters in the Dorsal Striatum Encode Locomotion Relevant Information. *Neuron* **92**, 202–213 (2016).
255. Carrillo-Reid, L. *et al.* Encoding Network States by Striatal Cell Assemblies. *Journal of Neurophysiology* **99**, 1435–1450 (2008).
256. Packer, A. M., Russell, L. E., Dalgleish, H. W. P. & Häusser, M. Simultaneous all-optical manipulation and recording of neural circuit activity with cellular resolution in vivo. *Nat Methods* **12**, 140–146 (2015).
257. Carrillo-Reid, L., Yang, W., Bando, Y., Peterka, D. S. & Yuste, R. Imprinting and recalling cortical ensembles. *Science* **353**, 691–694 (2016).
258. Mardinly, A. R. *et al.* Precise multimodal optical control of neural ensemble activity. *Nat Neurosci* **21**, 881–893 (2018).
259. Yang, W., Carrillo-Reid, L., Bando, Y., Peterka, D. S. & Yuste, R. Simultaneous two-photon imaging and two-photon optogenetics of cortical circuits in three dimensions. *eLife* **7**, e32671 (2018).
260. Rabadan, M. A. *et al.* An in vitro model of neuronal ensembles. *Nat Commun* **13**, 3340 (2022).

261. Bakhurin, K. I., Mac, V., Golshani, P. & Masmanidis, S. C. Temporal correlations among functionally specialized striatal neural ensembles in reward-conditioned mice. *Journal of Neurophysiology* **115**, 1521–1532 (2016).
262. Roberts, B. M., White, M. G., Patton, M. H., Chen, R. & Mathur, B. N. Ensemble encoding of action speed by striatal fast-spiking interneurons. *Brain Struct Funct* **224**, 2567–2576 (2019).
263. Prinz, A. A., Bucher, D. & Marder, E. Similar network activity from disparate circuit parameters. *Nature Neuroscience* **7**, 1345–1352 (2004).
264. Marder, E., O’Leary, T. & Shruti, S. Neuromodulation of Circuits with Variable Parameters: Single Neurons and Small Circuits Reveal Principles of State-Dependent and Robust Neuromodulation. *Annual Review of Neuroscience* **37**, 329–346 (2014).
265. Carrillo-Reid, L., Hernández-López, S., Tapia, D., Galarraga, E. & Bargas, J. Dopaminergic Modulation of the Striatal Microcircuit: Receptor-Specific Configuration of Cell Assemblies. *J. Neurosci.* **31**, 14972–14983 (2011).
266. Gerstein, G. L., Perkel, D. H. & Subramanian, K. N. Identification of functionally related neural assemblies. *Brain Research* **140**, 43–62 (1978).
267. Wright, W. E. Gravitational clustering. *Pattern Recognition* **9**, 151–166 (1977).
268. Adams, W., Graham, J. N., Han, X. & Rieke, H. Top-down inputs drive neuronal network rewiring and context-enhanced sensory processing in olfaction. *PLoS Comput Biol* **15**, e1006611 (2019).
269. Bartoszek, E. M. *et al.* Ongoing habenular activity is driven by forebrain networks and modulated by olfactory stimuli. *Current Biology* **31**, 3861-3874.e3 (2021).

270. Panier, T. *et al.* Fast functional imaging of multiple brain regions in intact zebrafish larvae using Selective Plane Illumination Microscopy. *Front. Neural Circuits* **7**, (2013).
271. Laubach, M., Shuler, M. & Nicolelis, M. A. L. Independent component analyses for quantifying neuronal ensemble interactions. *Journal of Neuroscience Methods* **94**, 141–154 (1999).
272. Laubach, M., Wessberg, J. & Nicolelis, M. A. L. Cortical ensemble activity increasingly predicts behaviour outcomes during learning of a motor task. *Nature* **405**, 567–571 (2000).
273. Chapin, J. K. & Nicolelis, M. A. L. Principal component analysis of neuronal ensemble activity reveals multidimensional somatosensory representations. *Journal of Neuroscience Methods* **94**, 121–140 (1999).
274. Lopes-dos-Santos, V., Conde-Ocazonez, S., Nicolelis, M. A. L., Ribeiro, S. T. & Tort, A. B. L. Neuronal Assembly Detection and Cell Membership Specification by Principal Component Analysis. *PLoS ONE* **6**, e20996 (2011).
275. Lopes-dos-Santos, V., Ribeiro, S. & Tort, A. B. L. Detecting cell assemblies in large neuronal populations. *Journal of Neuroscience Methods* **220**, 149–166 (2013).
276. Carrillo-Reid, L., Miller, J. -e. K., Hamm, J. P., Jackson, J. & Yuste, R. Endogenous Sequential Cortical Activity Evoked by Visual Stimuli. *Journal of Neuroscience* **35**, 8813–8828 (2015).
277. Pietri, T. *et al.* The Emergence of the Spatial Structure of Tectal Spontaneous Activity Is Independent of Visual Inputs. *Cell Reports* **19**, 939–948 (2017).
278. Mu, Y. *et al.* Glia Accumulate Evidence that Actions Are Futile and Suppress Unsuccessful Behavior. *Cell* **178**, 27-43.e19 (2019).

279. Romano, S. A. *et al.* Spontaneous Neuronal Network Dynamics Reveal Circuit's Functional Adaptations for Behavior. *Neuron* **85**, 1070–1085 (2015).
280. Mölter, J., Avitan, L. & Goodhill, G. J. Detecting neural assemblies in calcium imaging data. *BMC Biol* **16**, 143 (2018).
281. Abeles, M. & Gerstein, G. L. Detecting spatiotemporal firing patterns among simultaneously recorded single neurons. *Journal of Neurophysiology* **60**, 909–924 (1988).
282. Pipa, G., Wheeler, D. W., Singer, W. & Nikolić, D. NeuroXidence: reliable and efficient analysis of an excess or deficiency of joint-spike events. *J Comput Neurosci* **25**, 64–88 (2008).
283. Picado-Muiño, D., Borgelt, C., Berger, D., Gerstein, G. & Grün, S. Finding neural assemblies with frequent item set mining. *Front. Neuroinform.* **7**, (2013).
284. Torre, E., Picado-Muiño, D., Denker, M., Borgelt, C. & Grün, S. Statistical evaluation of synchronous spike patterns extracted by frequent item set mining. *Front. Comput. Neurosci.* **7**, (2013).
285. Gansel, K. S. & Singer, W. Detecting Multineuronal Temporal Patterns in Parallel Spike Trains. *Front. Neuroinform.* **6**, (2012).
286. Quaglio, P., Yegenoglu, A., Torre, E., Endres, D. M. & Grün, S. Detection and Evaluation of Spatio-Temporal Spike Patterns in Massively Parallel Spike Train Data with SPADE. *Front. Comput. Neurosci.* **11**, 41 (2017).
287. Shimazaki, H., Amari, S., Brown, E. N. & Grün, S. State-Space Analysis of Time-Varying Higher-Order Spike Correlation for Multiple Neural Spike Train Data. *PLoS Comput Biol* **8**, e1002385 (2012).

288. Russo, E. & Durstewitz, D. Cell assemblies at multiple time scales with arbitrary lag constellations. *eLife* **6**, e19428 (2017).
289. Abeles, M. & Gat, I. Detecting precise firing sequences in experimental data. *Journal of Neuroscience Methods* **107**, 141–154 (2001).
290. Driscoll, L. N., Golub, M. D. & Sussillo, D. Computation through Cortical Dynamics. *Neuron* **98**, 873–875 (2018).
291. Gallego, J. A., Perich, M. G., Miller, L. E. & Solla, S. A. Neural Manifolds for the Control of Movement. *Neuron* **94**, 978–984 (2017).
292. Jazayeri, M. & Afraz, A. Navigating the Neural Space in Search of the Neural Code. *Neuron* **93**, 1003–1014 (2017).
293. Saxena, S. & Cunningham, J. P. Towards the neural population doctrine. *Current Opinion in Neurobiology* **55**, 103–111 (2019).
294. Sussillo, D. Neural circuits as computational dynamical systems. *Current Opinion in Neurobiology* **25**, 156–163 (2014).
295. Sussillo, D. & Barak, O. Opening the black box: Low-dimensional dynamics in high-dimensional recurrent neural networks. *Neural Computation* **25**, 626–649 (2013).
296. Yuste, R. From the neuron doctrine to neural networks. *Nat Rev Neurosci* **16**, 487–497 (2015).
297. Minkowicz, S. *et al.* Striatal ensemble activity in an innate naturalistic behavior. *eLife* **12**, RP87042 (2023).
298. Wu, M. *et al.* Attenuated dopamine signaling after aversive learning is restored by ketamine to rescue escape actions. *eLife* **10**, e64041 (2021).

299. Yang, Y. *et al.* Wireless multilateral devices for optogenetic studies of individual and social behaviors. *Nat Neurosci* **24**, 1035–1045 (2021).
300. Wu, M., Minkowicz, S., Dumrongprechachan, V., Hamilton, P. & Kozorovitskiy, Y. Ketamine Rapidly Enhances Glutamate-Evoked Dendritic Spinogenesis in Medial Prefrontal Cortex Through Dopaminergic Mechanisms. *Biological Psychiatry* **89**, 1096–1105 (2021).
301. Janet M. Kemp & Powell, T. P. S. The structure of the caudate nucleus of the cat: light and electron microscopy. *Phil. Trans. R. Soc. Lond. B* **262**, 383–401 (1971).
302. Rymar, V. V., Sasseville, R., Luk, K. C. & Sadikot, A. F. Neurogenesis and stereological morphometry of calretinin-immunoreactive GABAergic interneurons of the neostriatum. *J. Comp. Neurol.* **469**, 325–339 (2004).
303. Jaidar, O. *et al.* Dynamics of the Parkinsonian Striatal Microcircuit: Entrainment into a Dominant Network State. *Journal of Neuroscience* **30**, 11326–11336 (2010).
304. Mathis, A. *et al.* DeepLabCut: markerless pose estimation of user-defined body parts with deep learning. *Nature Neuroscience* **21**, 1281–1289 (2018).
305. Karashchuk, P. *et al.* Anipose: A toolkit for robust markerless 3D pose estimation. *Cell Reports* **36**, 109730 (2021).
306. Berke, J. D., Okatan, M., Skurski, J. & Eichenbaum, H. B. Oscillatory Entrainment of Striatal Neurons in Freely Moving Rats. *Neuron* **43**, 883–896 (2004).
307. Gage, G. J., Stoetzner, C. R., Wiltschko, A. B. & Berke, J. D. Selective Activation of Striatal Fast-Spiking Interneurons during Choice Execution. *Neuron* **67**, 466–479 (2010).
308. Dhawale, A. K., Wolff, S. B. E., Ko, R. & Ölveczky, B. P. The basal ganglia control the detailed kinematics of learned motor skills. *Nat Neurosci* **24**, 1256–1269 (2021).

309. Hotelling, H. Analysis of a complex of statistical variables into principal components. *Journal of Educational Psychology* **24**, 417–441 (1933).
310. Ozden, I., Lee, H. M., Sullivan, M. R. & Wang, S. S.-H. Identification and Clustering of Event Patterns From In Vivo Multiphoton Optical Recordings of Neuronal Ensembles. *Journal of Neurophysiology* **100**, 495–503 (2008).
311. Aldridge, J. W. & Berridge, K. C. Coding of serial order by neostriatal neurons: a ‘natural action’ approach to movement sequence. *J Neurosci* **18**, 2777–2787 (1998).
312. Oh, S. W. *et al.* A mesoscale connectome of the mouse brain. *Nature* **508**, 207–214 (2014).
313. Berke, J. D. Functional Properties of Striatal Fast-Spiking Interneurons. *Front. Syst. Neurosci.* **5**, (2011).
314. Tepper, J. M., Tecuapetla, F., Koós, T. & Ibáñez-Sandoval, O. Heterogeneity and Diversity of Striatal GABAergic Interneurons. *Frontiers in Neuroanatomy* **4**, 1–18 (2010).
315. Berke, J. D. Uncoordinated Firing Rate Changes of Striatal Fast-Spiking Interneurons during Behavioral Task Performance. *Journal of Neuroscience* **28**, 10075–10080 (2008).
316. Kim, N., Barter, J. W., Sukharnikova, T. & Yin, H. H. Striatal firing rate reflects head movement velocity. *Eur J Neurosci* **40**, 3481–3490 (2014).
317. Freeze, B. S., Kravitz, A. V., Hammack, N., Berke, J. D. & Kreitzer, A. C. Control of Basal Ganglia Output by Direct and Indirect Pathway Projection Neurons. *Journal of Neuroscience* **33**, 18531–18539 (2013).
318. Fentress, J. C. & Stilwell, F. P. Grammar of a movement sequence in inbred mice. *Nature* **244**, 52–53 (1973).

319. Berridge, K. C., Fentress, J. C. & Parr, H. Natural syntax rules control action sequence of rats. *Behavioural Brain Research* **23**, 59–68 (1987).
320. McFarland, D. J. Time-Sharing as a Behavioral Phenomenon. in *Advances in the Study of Behavior* 201–225 (1974).
321. Krakauer, J. W., Ghazanfar, A. A., Gomez-Marin, A., Maciver, M. A. & Poeppel, D. Neuroscience Needs Behavior: Correcting a Reductionist Bias. *Neuron* **93**, 480–490 (2017).
322. Fürth, D. *et al.* An interactive framework for whole-brain maps at cellular resolution. *Nat Neurosci* **21**, 139–149 (2018).
323. R Core Team. R: A Language and Environment for Statistical Computing. (2017).
324. Wang, Q. *et al.* The Allen Mouse Brain Common Coordinate Framework: A 3D Reference Atlas. *Cell* **181**, 936-953.e20 (2020).
325. Freda, S. N. *et al.* Brainwide input-output architecture of paraventricular oxytocin and vasopressin neurons. *bioRxiv* (2022) doi:10.1101/2022.01.17.476652.
326. Nath, T. *et al.* Using DeepLabCut for 3D markerless pose estimation across species and behaviors. *Nat Protoc* **14**, 2152–2176 (2019).
327. Insafutdinov, E., Pishchulin, L., Andres, B., Andriluka, M. & Schiele, B. DeeperCut: A Deeper, Stronger, and Faster Multi-person Pose Estimation Model. in *Computer Vision – ECCV 2016* (eds. Leibe, B., Matas, J., Sebe, N. & Welling, M.) vol. 9910 34–50 (Springer International Publishing, 2016).
328. He, K., Zhang, X., Ren, S. & Sun, J. Deep Residual Learning for Image Recognition. in *2016 IEEE Conference on Computer Vision and Pattern Recognition (CVPR)* 770–778 (IEEE, 2016). doi:10.1109/CVPR.2016.90.

329. Segalin, C. *et al.* The Mouse Action Recognition System (MARS) software pipeline for automated analysis of social behaviors in mice. *eLife* **10**, e63720 (2021).
330. VideoLan. VLC media player. (2006).
331. Mederi. Time v3.2. (2012).
332. Andrei Hutu. Speed Controller. (2021).
333. Arthur, D. & Vassilvitskii, S. k-means++: The Advantages of Careful Seeding.
334. Dombeck, D. A., Graziano, M. S. & Tank, D. W. Functional Clustering of Neurons in Motor Cortex Determined by Cellular Resolution Imaging in Awake Behaving Mice. *Journal of Neuroscience* **29**, 13751–13760 (2009).
335. Rousseeuw, P. J. Silhouettes: A graphical aid to the interpretation and validation of cluster analysis. *Journal of Computational and Applied Mathematics* **20**, 53–65 (1987).
336. Lee, D. D. & Seung, H. S. Learning the parts of objects by non-negative matrix factorization. *Nature* **401**, 788–791 (1999).
337. Van Rossum, Guido & Drake, Fred L. *Python 3 Reference Manual*. (CreateSpace, 2009).
338. Harris, C. R. *et al.* Array programming with NumPy. *Nature* **585**, 357–362 (2020).
339. Virtanen, P. *et al.* SciPy 1.0: fundamental algorithms for scientific computing in Python. *Nat Methods* **17**, 261–272 (2020).
340. Hunter, J. D. Matplotlib: A 2D Graphics Environment. *Comput. Sci. Eng.* **9**, 90–95 (2007).
341. Pedregosa, F. *et al.* Scikit-learn: Machine Learning in Python. *MACHINE LEARNING IN PYTHON* (2011).
342. The pandas development team. pandas-dev/pandas: Pandas. (2020).

343. McKinney, W. Data Structures for Statistical Computing in Python. in 56–61 (2010).  
doi:10.25080/Majora-92bf1922-00a.
344. Foster, I. Globus Online: Accelerating and Democratizing Science through Cloud-Based Services. *IEEE Internet Comput.* **15**, 70–73 (2011).
345. Allen, B. *et al.* Software as a service for data scientists. *Commun. ACM* **55**, 81–88 (2012).
346. Luxem, K. *et al.* Open-source tools for behavioral video analysis: Setup, methods, and best practices. *eLife* **12**, e79305 (2023).
347. Rottenberg, J., Gross, J. J. & Gotlib, I. H. Emotion context insensitivity in major depressive disorder. *Journal of Abnormal Psychology* **114**, 627–639 (2005).
348. Rottenberg, J. Emotions in Depression: What Do We Really Know? *Annual Review of Clinical Psychology* **13**, 241–263 (2017).
349. Bylsma, L. M., Morris, B. H. & Rottenberg, J. A meta-analysis of emotional reactivity in major depressive disorder. *Clinical Psychology Review* vol. 28 676–691 (2008).
350. Rottenberg, J. & Hindash, A. C. Emerging evidence for emotion context insensitivity in depression. *Current Opinion in Psychology* vol. 4 1–5 (2015).
351. Abler, B., Erk, S., Herwig, U. & Walter, H. Anticipation of aversive stimuli activates extended amygdala in unipolar depression. *Journal of Psychiatric Research* **41**, 511–522 (2007).
352. Heldt, S. A., Stanek, L., Chhatwal, J. P. & Ressler, K. J. Hippocampus-specific deletion of BDNF in adult mice impairs spatial memory and extinction of aversive memories. *Molecular Psychiatry* **12**, 656–670 (2007).

353. Nestler, E. J. & Carlezon, W. A. The Mesolimbic Dopamine Reward Circuit in Depression. *Biological Psychiatry* **59**, 1151–1159 (2006).
354. Proulx, C. D., Hikosaka, O. & Malinow, R. Reward processing by the lateral habenula in normal and depressive behaviors. *Nature Neuroscience* **17**, 1146–1152 (2014).
355. Beyer, D. K. E. & Freund, N. Animal models for bipolar disorder: from bedside to the cage. *International Journal of Bipolar Disorders* vol. 5 (2017).
356. Abramson, L. Y., Seligman, M. E. & Teasdale, J. D. Learned helplessness in humans: Critique and reformulation. *Journal of Abnormal Psychology* **87**, 49–74 (1978).
357. Maier, S. F. & Seligman, M. E. Learned helplessness: Theory and evidence. *Journal of Experimental Psychology: General* **105**, 3–46 (1976).
358. Seligman, M. E. & Maier, S. F. Failure to escape traumatic shock. *Journal of Experimental Psychology* **74**, 1–9 (1967).
359. Maier, S. F. & Seligman, M. E. P. Learned helplessness at fifty: Insights from neuroscience. *Psychological Review* **123**, 1–19 (2016).
360. Chourbaji, S. *et al.* Learned helplessness: Validity and reliability of depressive-like states in mice. *Brain Research Protocols* **16**, 70–78 (2005).
361. Belujon, P. & Grace, A. A. Restoring mood balance in depression: Ketamine reverses deficit in dopamine-dependent synaptic plasticity. *Biological Psychiatry* **76**, 927–936 (2014).
362. Krishnan, V. & Nestler, E. J. Animal models of depression: molecular perspectives. *Current topics in behavioral neurosciences* **7**, 121–47 (2011).
363. Belujon, P. & Grace, A. A. Dopamine System Dysregulation in Major Depressive Disorders. *International Journal of Neuropsychopharmacology* **20**, 1036–1046 (2017).

364. Eley, T. C. *et al.* Gene–environment interaction analysis of serotonin system markers with adolescent depression. *Molecular Psychiatry* **9**, 908–915 (2004).
365. Nutt, D. J. *et al.* Consensus statement and research needs: the role of dopamine and norepinephrine in depression and antidepressant treatment. *The Journal of clinical psychiatry* **67 Suppl 6**, 46–9 (2006).
366. Lammel, S., Lim, B. K. & Malenka, R. C. Reward and aversion in a heterogeneous midbrain dopamine system. *Neuropharmacology* vol. 76 351–359 doi: 10.1016/j.neuropharm.2013.03.019 (2014).
367. Morales, M. & Margolis, E. B. Ventral tegmental area: Cellular heterogeneity, connectivity and behaviour. *Nature Reviews Neuroscience* **18**, 73–85 (2017).
368. Tan, K. R. *et al.* GABA Neurons of the VTA Drive Conditioned Place Aversion. *Neuron* **73**, 1173–1183 (2012).
369. Tsai, H.-C. *et al.* Phasic Firing in Dopaminergic Neurons Is Sufficient for Behavioral Conditioning. *Science* **324**, 1080–1084 (2009).
370. Watabe-Uchida, M., Eshel, N. & Uchida, N. Neural Circuitry of Reward Prediction Error. *Annual Review of Neuroscience* **40**, 373–394 (2017).
371. de Jong, J. W. *et al.* A Neural Circuit Mechanism for Encoding Aversive Stimuli in the Mesolimbic Dopamine System. *Neuron* **101**, 133-151.e7 (2019).
372. Grace, A. A. Dysregulation of the dopamine system in the pathophysiology of schizophrenia and depression. *Nature Reviews Neuroscience* **17**, 524–532 (2016).
373. Hollon, N. G., Burgeno, L. M. & Phillips, P. E. M. Stress effects on the neural substrates of motivated behavior. *Nature Neuroscience* **18**, 1405–1412 (2015).

374. Russo, S. J. & Nestler, E. J. The brain reward circuitry in mood disorders. *Nature Reviews Neuroscience* **14**, 609–625 (2013).
375. Chaudhury, D. *et al.* Rapid regulation of depression-related behaviours by control of midbrain dopamine neurons. *Nature* **493**, 532–536 (2013).
376. Tye, K. M. *et al.* Dopamine neurons modulate neural encoding and expression of depression-related behaviour. *Nature* **493**, 537–541 (2012).
377. Walker, E. R., McGee, R. E. & Druss, B. G. Mortality in mental disorders and global disease burden implications a systematic review and meta-analysis. *JAMA Psychiatry* **72**, 334–341 (2015).
378. Berman, R. M. *et al.* Antidepressant effects of ketamine in depressed patients. *Biological Psychiatry* **47**, 351–354 (2000).
379. Daly, E. J. *et al.* Efficacy and safety of intranasal esketamine adjunctive to oral antidepressant therapy in treatment-resistant depression: A randomized clinical trial. *JAMA Psychiatry* **75**, 139–148 (2018).
380. Ali, F. *et al.* Ketamine disinhibits dendrites and enhances calcium signals in prefrontal dendritic spines. *Nature Communications* **11**, 1–15 (2020).
381. Chatterjee, M., Verma, R., Ganguly, S. & Palit, G. Neurochemical and molecular characterization of ketamine-induced experimental psychosis model in mice. *Neuropharmacology* **63**, 1161–1171 (2012).
382. Duman, R. S. Ketamine and rapid-acting antidepressants: a new era in the battle against depression and suicide. *F1000Research* **7**, 659 (2018).

383. Hare, B. D., Pothula, S., DiLeone, R. J. & Duman, R. S. Ketamine increases vmPFC activity: Effects of (R)- and (S)-stereoisomers and (2R,6R)-hydroxynorketamine metabolite. *Neuropharmacology* **166**, 107947 (2020).
384. Lorrain, D. S., Baccei, C. S., Bristow, L. J., Anderson, J. J. & Varney, M. A. Effects of ketamine and n-methyl-d-aspartate on glutamate and dopamine release in the rat prefrontal cortex: modulation by a group II selective metabotropic glutamate receptor agonist LY379268. *Neuroscience* **117**, 697–706 (2003).
385. Zanos, P. *et al.* NMDAR inhibition-independent antidepressant actions of ketamine metabolites. *Nature* **533**, 481–486 (2016).
386. Duman, R. S., Aghajanian, G. K., Sanacora, G. & Krystal, J. H. Synaptic plasticity and depression: New insights from stress and rapid-acting antidepressants. *Nature Medicine* **22**, 238–249 (2016).
387. Duman, R. S. & Aghajanian, G. K. Synaptic dysfunction in depression: potential therapeutic targets. *Science (New York, N.Y.)* **338**, 68–72 (2012).
388. Fuchikami, M. *et al.* Optogenetic stimulation of infralimbic PFC reproduces ketamine's rapid and sustained antidepressant actions. *Proceedings of the National Academy of Sciences* **112**, 8106–8111 (2015).
389. Harmer, C. J., Duman, R. S. & Cowen, P. J. How do antidepressants work? New perspectives for refining future treatment approaches. *The Lancet Psychiatry* **4**, 409–418 (2017).

390. Kokkinou, M., Ashok, A. H. & Howes, O. D. The effects of ketamine on dopaminergic function: Meta-Analysis and review of the implications for neuropsychiatric disorders. *Molecular Psychiatry* **23**, 59–69 (2018).
391. Li, N. *et al.* mTOR-Dependent Synapse Formation Underlies the Rapid Antidepressant Effects of NMDA Antagonists. *Science (New York, N.Y.)* **329**, 959–964 (2010).
392. Moda-Sava, R. N. *et al.* Sustained rescue of prefrontal circuit dysfunction by antidepressant-induced spine formation. *Science (New York, N.Y.)* **364**, eaat8078 (2019).
393. Shirayama, Y. & Hashimoto, K. Effects of a single bilateral infusion of R-ketamine in the rat brain regions of a learned helplessness model of depression. *European Archives of Psychiatry and Clinical Neuroscience* **267**, 177–182 (2017).
394. Wu, M., Minkowicz, S., Dumrongprechachan, V., Hamilton, P. & Kozorovitskiy, Y. Ketamine rapidly enhances glutamate-evoked dendritic spinogenesis in medial prefrontal cortex through dopaminergic mechanisms. *Biological Psychiatry* **0**, (2021).
395. Ng, L. H. L. *et al.* Ketamine and selective activation of parvalbumin interneurons inhibit stress-induced dendritic spine elimination. *Translational Psychiatry* **8**, 272 (2018).
396. Beier, K. T. *et al.* Circuit Architecture of VTA Dopamine Neurons Revealed by Systematic Input-Output Mapping. *Cell* **162**, 622–634 (2015).
397. Homayoun, H. & Moghaddam, B. NMDA receptor hypofunction produces opposite effects on prefrontal cortex interneurons and pyramidal neurons. *The Journal of neuroscience : the official journal of the Society for Neuroscience* **27**, 11496–500 (2007).

398. Beurel, E., Song, L. & Jope, R. S. Inhibition of glycogen synthase kinase-3 is necessary for the rapid antidepressant effect of ketamine in mice. *Molecular Psychiatry* vol. 16 1068–1070 (2011).
399. Maeng, S. *et al.* Cellular Mechanisms Underlying the Antidepressant Effects of Ketamine: Role of  $\alpha$ -Amino-3-Hydroxy-5-Methylisoxazole-4-Propionic Acid Receptors. *Biological Psychiatry* **63**, 349–352 (2008).
400. da Silva, J. A., Tecuapetla, F., Paixão, V. & Costa, R. M. Dopamine neuron activity before action initiation gates and invigorates future movements. *Nature* **554**, 244–248 (2018).
401. Howe, M. W. & Dombeck, D. A. Rapid signalling in distinct dopaminergic axons during locomotion and reward. *Nature* **535**, 505–510 (2016).
402. Peltoniemi, M. A. *et al.* Ketamine: A Review of Clinical Pharmacokinetics and Pharmacodynamics in Anesthesia and Pain Therapy. *Clinical Pharmacokinetics* **55**, (2016).
403. Honey, G. D. *et al.* Individual differences in psychotic effects of ketamine are predicted by brain function measured under placebo. *The Journal of neuroscience : the official journal of the Society for Neuroscience* **28**, 6295–303 (2008).
404. Armbruster, B. N., Li, X., Pausch, M. H., Herlitze, S. & Roth, B. L. Evolving the lock to fit the key to create a family of G protein-coupled receptors potently activated by an inert ligand. *Proceedings of the National Academy of Sciences* **104**, 5163–5168 (2007).
405. Kozorovitskiy, Y., Saunders, A., Johnson, C. A., Lowell, B. B. & Sabatini, B. L. Recurrent network activity drives striatal synaptogenesis. *Nature* **485**, 646–650 (2012).

406. Kozorovitskiy, Y., Peixoto, R., Wang, W., Saunders, A. & Sabatini, B. L. Neuromodulation of excitatory synaptogenesis in striatal development. *eLife* **4**, e10111 (2015).
407. Roth, B. L. DREADDs for Neuroscientists. *Neuron* **89**, 683–694 (2016).
408. Engelhard, B. *et al.* Specialized and spatially organized coding of sensory, motor, and cognitive variables in midbrain dopamine neurons. *Nature* (2019) doi:10.1101/456194.
409. Hare, B. D. *et al.* Optogenetic stimulation of medial prefrontal cortex Drd1 neurons produces rapid and long-lasting antidepressant effects. *Nature Communications* **10**, 223 (2019).
410. Maier, S. F. Learned helplessness and animal models of depression. *Progress in neuro-psychopharmacology & biological psychiatry* **8**, 435–46 (1984).
411. Berridge, K. C. & Kringelbach, M. L. Pleasure Systems in the Brain. *Neuron* **86**, 646–664 (2015).
412. Lammel, S., Lim, B. K. & Malenka, R. C. Reward and aversion in a heterogeneous midbrain dopamine system. *Neuropharmacology* vol. 76 351–359. doi: 10.1016/j.neuropharm.2013.03.019 (2014).
413. Schultz, W. Dopamine reward prediction-error signalling: a two-component response. *Nature Reviews Neuroscience* **17**, 183–195 (2016).
414. Lammel, S., Ion, D. I., Roeper, J. & Malenka, R. C. Projection-Specific Modulation of Dopamine Neuron Synapses by Aversive and Rewarding Stimuli. *Neuron* **70**, 855–862 (2011).

415. Lammel, S. *et al.* Input-specific control of reward and aversion in the ventral tegmental area. *Nature* **491**, 212–217 (2012).
416. Bagot, R. C. *et al.* Ketamine and Imipramine Reverse Transcriptional Signatures of Susceptibility and Induce Resilience-Specific Gene Expression Profiles. *Biological Psychiatry* **81**, 285–295 (2017).
417. Friedman, A. K. *et al.* Enhancing Depression Mechanisms in Midbrain Dopamine Neurons Achieves Homeostatic Resilience. *Science (New York, N.Y.)* **344**, 313–319 (2014).
418. Wang, Q., Timberlake, M. A., Prall, K. & Dwivedi, Y. The recent progress in animal models of depression. *Progress in Neuro-Psychopharmacology and Biological Psychiatry* vol. 77 99–109 (2017).
419. Peña, C. J. *et al.* Early life stress alters transcriptomic patterning across reward circuitry in male and female mice. *Nature Communications* **10**, 1–13 (2019).
420. Wahlstrom, D., Collins, P., White, T. & Luciana, M. Developmental changes in dopamine neurotransmission in adolescence: Behavioral implications and issues in assessment. *Brain and Cognition* vol. 72 146–159 doi: 10.1016/j.bandc.2009.10.013 (2010).
421. Peña, C. J. *et al.* Early life stress confers lifelong stress susceptibility in mice via ventral tegmental area OTX2. *Science (New York, N.Y.)* **356**, 1185–1188 (2017).
422. O'Donnell, P. Adolescent maturation of cortical dopamine. *Neurotoxicity Research* vol. 18 306–312 (2010).
423. Jönsson, E. G. *et al.* Polymorphisms in the dopamine D2 receptor gene and their relationships to striatal dopamine receptor density of healthy volunteers. *Molecular Psychiatry* **4**, 290–296 (1999).

424. MacDonald, S. W. S., Karlsson, S., Rieckmann, A., Nyberg, L. & Backman, L. Aging-Related Increases in Behavioral Variability: Relations to Losses of Dopamine D1 Receptors. *Journal of Neuroscience* **32**, 8186–8191 (2012).
425. Okubo, Y. *et al.* Decreased prefrontal dopamine D1 receptors in schizophrenia revealed by PET. *Nature* **385**, 634–636 (1997).
426. Volkow, N. D. *et al.* PET Evaluation of the Dopamine System of the Human Brain. *Journal of Nuclear Medicine* **37**, (1996).
427. Felten, A., Montag, C., Markett, S., Walter, N. T. & Reuter, M. Genetically determined dopamine availability predicts disposition for depression. *Brain and Behavior* **1**, 109–118 (2011).
428. Frisch, A. *et al.* Association of unipolar major depressive disorder with genes of the serotonergic and dopaminergic pathways. *Molecular Psychiatry* **4**, 389–392 (1999).
429. Haeffel, G. J. *et al.* Association between polymorphisms in the dopamine transporter gene and depression: evidence for a gene-environment interaction in a sample of juvenile detainees. *Psychological science* **19**, 62–9 (2008).
430. Pearson-Fuhrhop, K. M. *et al.* Dopamine Genetic Risk Score Predicts Depressive Symptoms in Healthy Adults and Adults with Depression. *PLoS ONE* **9**, e93772 (2014).
431. Picard, N., Takesian, A. E., Fagiolini, M. & Hensch, T. K. NMDA 2A receptors in parvalbumin cells mediate sex-specific rapid ketamine response on cortical activity. *Molecular Psychiatry* **1** (2019) doi:10.1038/s41380-018-0341-9.
432. Zanos, P. & Gould, T. D. Mechanisms of ketamine action as an antidepressant. *Molecular Psychiatry* **23**, 801–811 (2018).

433. Li, S. C., Lindenberger, U. & Bäckman, L. Dopaminergic modulation of cognition across the life span. *Neuroscience and Biobehavioral Reviews* vol. 34 625–630. doi: 10.1016/j.neubiorev.2010.02.003 (2010).
434. Liu, R. J. *et al.* GSK-3 inhibition potentiates the synaptogenic and antidepressant-like effects of subthreshold doses of ketamine. *Neuropsychopharmacology* **38**, 2268–2277 (2013).
435. Sarkar, A. & Kabbaj, M. Sex Differences in Effects of Ketamine on Behavior, Spine Density, and Synaptic Proteins in Socially Isolated Rats. *Biological Psychiatry* **80**, 448–456 (2016).
436. Covington, H. E. *et al.* Antidepressant effect of optogenetic stimulation of the medial prefrontal cortex. *Journal of Neuroscience* **30**, 16082–16090 (2010).
437. Kumar, S. *et al.* Cortical control of affective networks. *Journal of Neuroscience* **33**, 1116–1129 (2013).
438. Antunes, G. F. *et al.* Dopamine modulates individual differences in avoidance behavior: A pharmacological, immunohistochemical, neurochemical and volumetric investigation. *Neurobiology of Stress* **12**, 100219 (2020).
439. Darvas, M., Fadok, J. P. & Palmiter, R. D. Requirement of dopamine signaling in the amygdala and striatum for learning and maintenance of a conditioned avoidance response. *Learning and Memory* **18**, 136–143 (2011).
440. McCullough, L. D., Sokolowski, J. D. & Salamone, J. D. A neurochemical and behavioral investigation of the involvement of nucleus accumbens dopamine in instrumental avoidance. *Neuroscience* **52**, 919–925 (1993).

441. Oleson, E. B., Gentry, R. N., Chioma, V. C. & Cheer, J. F. Subsecond dopamine release in the nucleus accumbens predicts conditioned punishment and its successful avoidance. *Journal of Neuroscience* **32**, 14804–14808 (2012).
442. Oleson, E. B. & Cheer, J. F. On the role of subsecond dopamine release in conditioned avoidance. *Frontiers in Neuroscience* **7**, 96 (2013).
443. Stelly, C. E. *et al.* Pattern of dopamine signaling during aversive events predicts active avoidance learning. *Proceedings of the National Academy of Sciences of the United States of America* **116**, 13641–13650 (2019).
444. Wenzel, J. M. *et al.* Phasic Dopamine Signals in the Nucleus Accumbens that Cause Active Avoidance Require Endocannabinoid Mobilization in the Midbrain. *Current Biology* **28**, 1392-1404.e5 (2018).
445. Patriarchi, T. *et al.* Ultrafast neuronal imaging of dopamine dynamics with designed genetically encoded sensors. *Science* **360**, eaat4422 (2018).
446. Carr, D. B. & Sesack, S. R. Projections from the rat prefrontal cortex to the ventral tegmental area: Target specificity in the synaptic associations with mesoaccumbens and mesocortical neurons. *Journal of Neuroscience* **20**, 3864–3873 (2000).
447. Lodge, D. J. The medial prefrontal and orbitofrontal cortices differentially regulate dopamine system function. *Neuropsychopharmacology : official publication of the American College of Neuropsychopharmacology* **36**, 1227–36 (2011).
448. Xiao, L., Priest, M. F. & Kozorovitskiy, Y. Oxytocin functions as a spatiotemporal filter for excitatory synaptic inputs to VTA dopamine neurons. *eLife* **7**, e33892 (2018).

449. Geisler, S., Derst, C., Veh, R. W. & Zahm, D. S. Glutamatergic afferents of the ventral tegmental area in the rat. *Journal of Neuroscience* **27**, 5730–5743 (2007).
450. Gariano, R. F. & Groves, P. M. Burst firing induced in midbrain dopamine neurons by stimulation of the medial prefrontal and anterior cingulate cortices. *Brain research* **462**, 194–8 (1988).
451. Tong, Z. Y., Overton, P. G. & Clark, D. Stimulation of the prefrontal cortex in the rat induces patterns of activity in midbrain dopaminergic neurons which resemble natural burst events. *Synapse (New York, N.Y.)* **22**, 195–208 (1996).
452. You, Z. B., Wang, B., Zitzman, D., Azari, S. & Wise, R. A. A role for conditioned ventral tegmental glutamate release in cocaine seeking. *Journal of Neuroscience* **27**, 10546–10555 (2007).
453. Bagot, R. C. *et al.* Ventral hippocampal afferents to the nucleus accumbens regulate susceptibility to depression. *Nature Communications* **6**, 1–9 (2015).
454. Li, B. *et al.* Synaptic potentiation onto habenula neurons in the learned helplessness model of depression. *Nature* **470**, 535–539 (2011).
455. Pignatelli, M. *et al.* Cooperative synaptic and intrinsic plasticity in a disynaptic limbic circuit drive stress-induced anhedonia and passive coping in mice. *Molecular Psychiatry* 1–20 (2020) doi:10.1038/s41380-020-0686-8.
456. Gonçalves, L., Segó, C. & Metzger, M. Differential projections from the lateral habenula to the rostromedial tegmental nucleus and ventral tegmental area in the rat. *The Journal of Comparative Neurology* **520**, 1278–1300 (2012).

457. Biederman, J., Mick, E. & Faraone, S. V. Depression in attention deficit hyperactivity disorder (ADHD) children: 'True' depression or demoralization? *Journal of Affective Disorders* **47**, 113–122 (1998).
458. Corcos, M. *et al.* Alexithymia and depression in eating disorders. *Psychiatry Research* **93**, 263–266 (2000).
459. Masellis, M., Rector, N. A. & Richter, M. A. Quality of life in OCD: Differential impact of obsessions, compulsions, and depression comorbidity. *Canadian Journal of Psychiatry* **48**, 72–77 (2003).
460. Mayeux, R., Stern, Y., Rosen, J. & Leventhal, J. Depression, intellectual impairment, and Parkinson disease. *Neurology* **31**, 645–645 (1981).
461. Siris, S. G. Depression in schizophrenia: Perspective in the era of 'atypical' antipsychotic agents. *American Journal of Psychiatry* vol. 157 1379–1389 (2000).
462. Bäckman, C. M. *et al.* Characterization of a mouse strain expressing Cre recombinase from the 3' untranslated region of the dopamine transporter locus. *Genesis* **44**, 383–390 (2006).
463. Gong, S. *et al.* Targeting Cre recombinase to specific neuron populations with bacterial artificial chromosome constructs. *The Journal of neuroscience : the official journal of the Society for Neuroscience* **27**, 9817–23 (2007).
464. Chen, T.-W. *et al.* Ultrasensitive fluorescent proteins for imaging neuronal activity. *Nature* **499**, 295–300 (2013).
465. Krashes, M. J. *et al.* Rapid, reversible activation of AgRP neurons drives feeding behavior in mice. *Journal of Clinical Investigation* **121**, 1424–1428 (2011).

466. Hou, X. H. *et al.* Central Control Circuit for Context-Dependent Micturition. *Cell* **167**, 73-86.e12 (2016).
467. He, C. X., Arroyo, E. D., Cantu, D. A., Goel, A. & Portera-Cailliau, C. A Versatile Method for Viral Transfection of Calcium Indicators in the Neonatal Mouse Brain. *Frontiers in Neural Circuits* **12**, (2018).
468. Bariselli, S. *et al.* SHANK3 controls maturation of social reward circuits in the VTA. *Nature Neuroscience* **19**, 926–934 (2016).
469. Peixoto, R. T., Wang, W., Croney, D. M., Kozorovitskiy, Y. & Sabatini, B. L. Early hyperactivity and precocious maturation of corticostriatal circuits in Shank3B<sup>-/-</sup> mice. *Nature Neuroscience* **19**, 716–724 (2016).
470. Lerner, T. N. *et al.* Intact-Brain Analyses Reveal Distinct Information Carried by SNc Dopamine Subcircuits. *Cell* **162**, 635–647 (2015).
471. Pologruto, T. A., Sabatini, B. L. & Svoboda, K. ScanImage: Flexible software for operating laser scanning microscopes. *BioMedical Engineering OnLine* **2**, 13 (2003).
472. Xiao, L., Priest, M. F., Nasenbeny, J., Lu, T. & Kozorovitskiy, Y. Biased Oxytocinergic Modulation of Midbrain Dopamine Systems. *Neuron* **95**, 368-384.e5 (2017).
473. Banala, S., Arvin, M. C., Bannon, N. M., Jin, X. & Wang, Y. Development of photoactivatable drugs enables nicotinic optopharmacology. 1–26 (2018).
474. Schindelin, J. *et al.* Fiji: an open-source platform for biological-image analysis. *Nature methods* **9**, 676–82 (2012).
475. Schneider, C. A., Rasband, W. S. & Eliceiri, K. W. NIH Image to ImageJ: 25 years of image analysis. *Nature Methods* **9**, 671–675 (2012).

476. Rodriguez, A. *et al.* ToxTrac: A fast and robust software for tracking organisms. *Methods in Ecology and Evolution* **9**, 460–464 (2018).
477. Gansner, E. R. & North, S. C. Open graph visualization system and its applications to software engineering. *Software - Practice and Experience* **30**, 1203–1233 (2000).
478. Welch, P. D. The Use of Fast Fourier Transform for the Estimation of Power Spectra: A Method Based on Time Averaging Over Short, Modified Periodograms. *IEEE Transactions on Audio and Electroacoustics* **15**, 70–73 (1967).
479. Bassett, D. S. & Sporns, O. Network neuroscience. *Nature Neuroscience* **20**, 353–364 (2017).
480. Klapoetke, N. C. *et al.* Independent optical excitation of distinct neural populations. *Nature Methods* **11**, 338–346 (2014).
481. Boyden, E. S., Zhang, F., Bamberg, E., Nagel, G. & Deisseroth, K. Millisecond-timescale, genetically targeted optical control of neural activity. *Nature Neuroscience* **8**, 1263–1268 (2005).
482. Deisseroth, K. Optogenetics. *Nature Methods* **8**, 26–29 (2011).
483. Yizhar, O., Fenno, L. E., Davidson, T. J., Mogri, M. & Deisseroth, K. Optogenetics in Neural Systems. *Neuron* **71**, 9–34 (2011).
484. Park, S. *et al.* One-step optogenetics with multifunctional flexible polymer fibers. *Nature Neuroscience* **20**, 612–619 (2017).
485. Montgomery, K. L. *et al.* Wirelessly powered, fully internal optogenetics for brain, spinal and peripheral circuits in mice. *Nature Methods* **12**, 969–974 (2015).

486. Shin, G. *et al.* Flexible Near-Field Wireless Optoelectronics as Subdermal Implants for Broad Applications in Optogenetics. *Neuron* **93**, 509-521.e3 (2017).
487. Gutruf, P. & Rogers, J. A. Implantable, wireless device platforms for neuroscience research. *Current Opinion in Neurobiology* **50**, 42–49 (2017).
488. Gutruf, P. *et al.* Fully implantable optoelectronic systems for battery-free, multimodal operation in neuroscience research. *Nature Electronics* **1**, 652–660 (2018).
489. Park, S. Il *et al.* Soft, stretchable, fully implantable miniaturized optoelectronic systems for wireless optogenetics. *Nature Biotechnology* **33**, 1280–1286 (2015).
490. Gold, B. T. & Buckner, R. L. Common Prefrontal Regions Coactivate with Dissociable Posterior Regions during Controlled Semantic and Phonological Tasks. *Neuron* **35**, 803–812 (2002).
491. Crossley, N. A. *et al.* Cognitive relevance of the community structure of the human brain functional coactivation network. *Proceedings of the National Academy of Sciences* **110**, 11583–11588 (2013).
492. Marlin, B. J., Mitre, M., D’amour, J. A., Chao, M. V. & Froemke, R. C. Oxytocin enables maternal behaviour by balancing cortical inhibition. *Nature* **520**, 499–504 (2015).
493. Capelli, P., Pivetta, C., Soledad Esposito, M. & Arber, S. Locomotor speed control circuits in the caudal brainstem. *Nature* **551**, 373–377 (2017).
494. Hitchcott, P. K., Quinn, J. J. & Taylor, J. R. Bidirectional Modulation of Goal-Directed Actions by Prefrontal Cortical Dopamine. *Cerebral Cortex* **17**, 2820–2827 (2007).
495. Tye, K. M. *et al.* Amygdala circuitry mediating reversible and bidirectional control of anxiety. *Nature* **471**, 358–362 (2011).

496. Ma, T. *et al.* Bidirectional and long-lasting control of alcohol-seeking behavior by corticostriatal LTP and LTD. *Nature Neuroscience* **21**, 373–383 (2018).
497. Pashaie, R. *et al.* Optogenetic Brain Interfaces. *IEEE Reviews in Biomedical Engineering* **7**, 3–30 (2014).
498. Gunaydin, L. A. *et al.* Natural Neural Projection Dynamics Underlying Social Behavior. *Cell* **157**, 1535–1551 (2014).
499. Yizhar, O. Optogenetic Insights into Social Behavior Function. *Biological Psychiatry* **71**, 1075–1080 (2012).
500. Mathis, A. *et al.* DeepLabCut: markerless pose estimation of user-defined body parts with deep learning. *Nature Neuroscience* **21**, 1281–1289 (2018).
501. Zhang, Y. *et al.* Experimental and Theoretical Studies of Serpentine Microstructures Bonded To Prestrained Elastomers for Stretchable Electronics. *Advanced Functional Materials* **24**, 2028–2037 (2014).
502. Scott, W. W. *ASM Specialty Handbook* ® *Copper and Copper Alloys*. (2001).
503. Lu, L. *et al.* Wireless optoelectronic photometers for monitoring neuronal dynamics in the deep brain. *Proceedings of the National Academy of Sciences of the United States of America* **115**, E1374–E1383 (2018).
504. Kingsbury, L. *et al.* Correlated Neural Activity and Encoding of Behavior across Brains of Socially Interacting Animals. *Cell* **178**, 429–446.e16 (2019).
505. Kingsbury, L. & Hong, W. A Multi-Brain Framework for Social Interaction. *Trends in Neurosciences* 1–16 (2020) doi:10.1016/j.tins.2020.06.008.

506. Yun, K., Watanabe, K. & Shimojo, S. Interpersonal body and neural synchronization as a marker of implicit social interaction. *Scientific Reports* **2**, 1–8 (2012).
507. Toppi, J. *et al.* Investigating Cooperative Behavior in Ecological Settings: An EEG Hyperscanning Study. *PLOS ONE* **11**, e0154236 (2016).
508. Jia, Y. *et al.* A mm-Sized Free-Floating Wirelessly Powered. 468–470 (2018).
509. Lee, S. Y. *et al.* 22.7 A Programmable Wireless EEG Monitoring SoC with Open/Closed-Loop Optogenetic and Electrical Stimulation for Epilepsy Control. *Digest of Technical Papers - IEEE International Solid-State Circuits Conference 2019-Febru*, 372–374 (2019).
510. Montague, P. R. *et al.* Hyperscanning: Simultaneous fMRI during linked social interactions. *NeuroImage* **16**, 1159–1164 (2002).
511. Hasson, U., Ghazanfar, A. A., Galantucci, B., Garrod, S. & Keysers, C. Brain-to-brain coupling: A mechanism for creating and sharing a social world. *Trends in Cognitive Sciences* **16**, 114–121 (2012).
512. Liu, T. & Pelowski, M. A new research trend in social neuroscience: Towards an interactive-brain neuroscience. *PsyCh Journal* **3**, 177–188 (2014).
513. Zhang, W. & Yartsev, M. M. Correlated Neural Activity across the Brains of Socially Interacting Bats. *Cell* **178**, 413-428.e22 (2019).
514. Bazrafkan, S. & Kazemi, K. Modeling time resolved light propagation inside a realistic human head model. *Journal of biomedical physics & engineering* **4**, 49–60 (2014).
515. Stujenske, J. M., Spellman, T. & Gordon, J. A. Modeling the Spatiotemporal Dynamics of Light and Heat Propagation for In Vivo Optogenetics. *Cell Reports* **12**, 525–534 (2015).

516. Aronov, D. & Fee, M. S. Analyzing the dynamics of brain circuits with temperature: Design and implementation of a miniature thermoelectric device. *Journal of Neuroscience Methods* **197**, 32–47 (2011).
517. Wu, M. *et al.* Ketamine restores escape behavior by re-engaging dopamine systems to drive cortical spinogenesis. *bioRxiv* 2020.03.11.987818 (2020)  
doi:10.1101/2020.03.11.987818.
518. Tsai, H.-C. *et al.* Phasic Firing in Dopaminergic Neurons Is Sufficient for Behavioral Conditioning. *Science* **324**, 1080–1084 (2009).
519. Shin, G. *et al.* Flexible Near-Field Wireless Optoelectronics as Subdermal Implants for Broad Applications in Optogenetics. *Neuron* **93**, 509-521.e3 (2017).
520. Rodriguez, A. *et al.* *ToxTrac* : A fast and robust software for tracking organisms. *Methods in Ecology and Evolution* **9**, 460–464 (2018).
521. Friard, O. & Gamba, M. BORIS: a free, versatile open-source event-logging software for video/audio coding and live observations. *Methods in Ecology and Evolution* **7**, 1325–1330 (2016).
522. Broom, L. *et al.* A translational approach to capture gait signatures of neurological disorders in mice and humans. *Scientific Reports* **7**, 1–17 (2017).
523. Mathis, A. *et al.* DeepLabCut: markerless pose estimation of user-defined body parts with deep learning. *Nature Neuroscience* **21**, 1281–1289 (2018).
524. Kingsbury, L. *et al.* Correlated Neural Activity and Encoding of Behavior across Brains of Socially Interacting Animals. *Cell* **178**, 429-446.e16 (2019).

525. van der Maaten, L. & Hinton, G. Visualizing Data using t-SNE. *Journal of Machine Learning Research* **9**, 2579–2605 (2008).
526. McInnes, L., Healy, J. & Melville, J. UMAP: Uniform Manifold Approximation and Projection for Dimension Reduction. (2018) doi:10.48550/ARXIV.1802.03426.
527. Berman, G. J., Choi, D. M., William, B. & Shaevitz, J. W. Mapping the stereotyped behaviour of freely moving fruit flies. *Journal of The Royal Society Interface* **11**, 20140672 (2014).
528. Hsu, A. I. & Yttri, E. A. B-SOiD, an open-source unsupervised algorithm for identification and fast prediction of behaviors. *Nat Commun* **12**, 5188 (2021).
529. Luxem, K. *et al.* Identifying behavioral structure from deep variational embeddings of animal motion. *Commun Biol* **5**, 1267 (2022).
530. Weinreb, C. *et al.* Keypoint-MoSeq: parsing behavior by linking point tracking to pose dynamics. *bioRxiv* (2023) doi:10.1101/2023.03.16.532307.
531. Kwak, I. S., Guo, J.-Z., Hantman, A., Branson, K. & Kriegman, D. Detecting the Starting Frame of Actions in Video. in *2020 IEEE Winter Conference on Applications of Computer Vision (WACV)* 478–486 (IEEE, 2020). doi:10.1109/WACV45572.2020.9093405.
532. Kuperstein, M., Eichenbaum, H. & VanDeMark, T. Neural group properties in the rat hippocampus during the theta rhythm. *Exp Brain Res* **61**, (1986).
533. Eichenbaum, H. Thinking About Brain Cell Assemblies. *Science* **261**, 993–994 (1993).
534. Palm, G., Knoblauch, A., Hauser, F. & Schüz, A. Cell assemblies in the cerebral cortex. *Biol Cybern* **108**, 559–572 (2014).

535. Fujisawa, S., Amarasingham, A., Harrison, M. T. & Buzsáki, G. Behavior-dependent short-term assembly dynamics in the medial prefrontal cortex. *Nat Neurosci* **11**, 823–833 (2008).
536. Miller, J. K., Ayzenshtat, I., Carrillo-Reid, L. & Yuste, R. Visual stimuli recruit intrinsically generated cortical ensembles. *Proc. Natl. Acad. Sci. U.S.A.* **111**, (2014).
537. Burke, D. A., Rotstein, H. G. & Alvarez, V. A. Striatal Local Circuitry: A New Framework for Lateral Inhibition. *Neuron* **96**, 267–284 (2017).
538. Marder, E. & Goaillard, J.-M. Variability, compensation and homeostasis in neuron and network function. *Nature reviews. Neuroscience* **7**, 563–74 (2006).
539. Kozorovitskiy, Y., Peixoto, R., Wang, W., Saunders, A. & Sabatini, B. L. Neuromodulation of excitatory synaptogenesis in striatal development. *eLife* **4**, e10111 (2015).
540. Gutruf, P. & Rogers, J. A. Implantable, wireless device platforms for neuroscience research. *Current Opinion in Neurobiology* **50**, 42–49 (2017).
541. Hart, B. L. & Hart, L. A. Reciprocal allogrooming in impala, *Aepyceros melampus*. *Animal Behaviour* **44**, 1073–1083 (1992).
542. Sato, S., Tarumizu, K. & Hatae, K. The influence of social factors on allogrooming in cows. *Applied Animal Behaviour Science* **38**, 235–244 (1993).
543. Walker, T. N. & Hughes, W. O. H. Adaptive social immunity in leaf-cutting ants. *Biol. Lett.* **5**, 446–448 (2009).
544. Dunbar, R. I. M. Functional Significance of Social Grooming in Primates. *IJFP* **57**, 121–131 (1991).

545. Di Bitetti, M. S. Evidence for an important social role of allogrooming in a platyrrhine primate. *Animal Behaviour* **54**, 199–211 (1997).
546. Lammers, J. H. C. M., Kruk, M. R., Meelis, W. & van der Poel, A. M. Hypothalamic substrates for brain stimulation-induced attack, teeth-chattering and social grooming in the rat. *Brain Research* **449**, 311–327 (1988).
547. Croft, D. B. Behaviour of Red Kangaroos, *Macropus rufus* (Desmarest, 1822) (Macropodidae; Marsupialia) in northwestern New South Wales, Australia. *Aust. Mammalogy* **4**, 5–58 (1980).
548. Berman, R. M. *et al.* Antidepressant effects of ketamine in depressed patients. *Biological Psychiatry* **47**, 351–354 (2000).
549. Kim, J., Farchione, T., Potter, A., Chen, Q. & Temple, R. Esketamine for Treatment-Resistant Depression — First FDA-Approved Antidepressant in a New Class. *New England Journal of Medicine* **381**, 1–4 (2019).
550. Miller, O. H. *et al.* GluN2B-containing NMDA receptors regulate depression-like behavior and are critical for the rapid antidepressant actions of ketamine. *eLife* **3**, e03581 (2014).
551. Abdallah, C. G., Sanacora, G., Duman, R. S. & Krystal, J. H. Ketamine and Rapid-Acting Antidepressants: A Window into a New Neurobiology for Mood Disorder Therapeutics. *Annual Review of Medicine* **66**, 509–523 (2015).
552. Holmes, S. E. *et al.* Lower synaptic density is associated with depression severity and network alterations. *Nature Communications* **10**, 1529 (2019).

553. Wray, N. H., Schappi, J. M., Singh, H., Senese, N. B. & Rasenick, M. M. NMDAR-independent, cAMP-dependent antidepressant actions of ketamine. *Molecular Psychiatry* **24**, 1833–1843 (2019).
554. Krishnan, V. & Nestler, E. J. Animal models of depression: molecular perspectives. *Current topics in behavioral neurosciences* **7**, 121–47 (2011).
555. Popoli, M., Yan, Z., McEwen, B. S. & Sanacora, G. The stressed synapse: The impact of stress and glucocorticoids on glutamate transmission. *Nature Reviews Neuroscience* **13**, 22–37 (2012).
556. Gerhard, D. M., Wohleb, E. S. & Duman, R. S. Emerging treatment mechanisms for depression: focus on glutamate and synaptic plasticity. *Drug Discovery Today* **21**, 454–464 (2016).
557. Phoumthippavong, V., Barthas, F., Hassett, S. & Kwan, A. C. Longitudinal effects of ketamine on dendritic architecture in vivo in the mouse medial frontal cortex. *eNeuro* **3**, 91–95 (2016).
558. Krystal, J. H., Sanacora, G. & Duman, R. S. Rapid-Acting Glutamatergic Antidepressants: The Path to Ketamine and Beyond. *Biological Psychiatry* **73**, 1133–1141 (2013).
559. Krystal, J. H., Abdallah, C. G., Sanacora, G., Charney, D. S. & Duman, R. S. Ketamine: A Paradigm Shift for Depression Research and Treatment. *Neuron* **101**, 774–778 (2019).
560. Proulx, C. D., Hikosaka, O. & Malinow, R. Reward processing by the lateral habenula in normal and depressive behaviors. *Nature Neuroscience* **17**, 1146–1152 (2014).

561. Abler, B., Erk, S., Herwig, U. & Walter, H. Anticipation of aversive stimuli activates extended amygdala in unipolar depression. *Journal of Psychiatric Research* **41**, 511–522 (2007).
562. Heldt, S. A., Stanek, L., Chhatwal, J. P. & Ressler, K. J. Hippocampus-specific deletion of BDNF in adult mice impairs spatial memory and extinction of aversive memories. *Molecular Psychiatry* **12**, 656–670 (2007).
563. Luking, K. R., Pagliaccio, D., Luby, J. L. & Barch, D. M. Reward Processing and Risk for Depression Across Development. *Trends in Cognitive Sciences* vol. 20 456–468. doi: 10.1016/j.tics.2016.04.002 (2016).
564. Morales, M. & Margolis, E. B. Ventral tegmental area: Cellular heterogeneity, connectivity and behaviour. *Nature Reviews Neuroscience* **18**, 73–85 (2017).
565. Bromberg-Martin, E. S., Matsumoto, M. & Hikosaka, O. Dopamine in Motivational Control: Rewarding, Aversive, and Alerting. *Neuron* **68**, 815–834 (2010).
566. de Jong, J. W. *et al.* A Neural Circuit Mechanism for Encoding Aversive Stimuli in the Mesolimbic Dopamine System. *Neuron* **101**, 133-151.e7 (2019).
567. Vander Weele, C. M. *et al.* Dopamine enhances signal-to-noise ratio in cortical-brainstem encoding of aversive stimuli. *Nature* **563**, 397–401 (2018).
568. Dunlop, B. W. & Nemeroff, C. B. The role of dopamine in the pathophysiology of depression. *Archives of General Psychiatry* vol. 64 327–337. doi:10.1001/archpsyc.64.3.327 (2007).

569. Dailly, E., Chenu, F., Renard, C. E. & Bourin, M. Dopamine, depression and antidepressants. *Fundamental and Clinical Pharmacology* vol. 18 601–607. doi:10.1111/j.1472-8206.2004.00287.x (2004).
570. Belujon, P. & Grace, A. A. Restoring mood balance in depression: Ketamine reverses deficit in dopamine-dependent synaptic plasticity. *Biological Psychiatry* **76**, 927–936 (2014).
571. Belujon, P. & Grace, A. A. Dopamine System Dysregulation in Major Depressive Disorders. *International Journal of Neuropsychopharmacology* **20**, 1036–1046 (2017).
572. Moghaddam, B., Adams, B., Verma, A. & Daly, D. Activation of glutamatergic neurotransmission by ketamine: A novel step in the pathway from NMDA receptor blockade to dopaminergic and cognitive disruptions associated with the prefrontal cortex. *Journal of Neuroscience* **17**, 2921–2927 (1997).
573. Verma, A. & Moghaddam, B. NMDA receptor antagonists impair prefrontal cortex function as assessed via spatial delayed alternation performance in rats: Modulation by dopamine. *Journal of Neuroscience* **16**, 373–379 (1996).
574. Lindefors, N., Barati, S. & O'Connor, W. T. Differential effects of single and repeated ketamine administration on dopamine, serotonin and GABA transmission in rat medial prefrontal cortex. *Brain Research* **759**, 205–212 (1997).
575. Tseng, K. Y. & O'Donnell, P. Dopamine-glutamate interactions controlling prefrontal cortical pyramidal cell excitability involve multiple signaling mechanisms. *Journal of Neuroscience* **24**, 5131–5139 (2004).

576. Wang, J. & O'Donnell, P. D1 dopamine receptors potentiate NMDA-mediated excitability increase in layer V prefrontal cortical pyramidal neurons. *Cerebral Cortex* **11**, 452–462 (2001).
577. Gullledge, A. T. & Jaffe, D. B. Multiple Effects of Dopamine on Layer V Pyramidal Cell Excitability in Rat Prefrontal Cortex. *Journal of Neurophysiology* **86**, 586–595 (2001).
578. Chen, L., Bohanick, J. D., Nishihara, M., Seamans, J. K. & Yang, C. R. Dopamine D1/5 Receptor-Mediated Long-Term Potentiation of Intrinsic Excitability in Rat Prefrontal Cortical Neurons: Ca<sup>2+</sup>-Dependent Intracellular Signaling. *Journal of Neurophysiology* **97**, 2448–2464 (2007).
579. Kwon, H.-B. & Sabatini, B. L. Glutamate induces de novo growth of functional spines in developing cortex. *Nature* **474**, 100–104 (2011).
580. Guo, L. *et al.* Dynamic rewiring of neural circuits in the motor cortex in mouse models of Parkinson's disease. *Nature neuroscience* **18**, 1299–1309 (2015).
581. Tritsch, N. X. & Sabatini, B. L. Dopaminergic Modulation of Synaptic Transmission in Cortex and Striatum. *Neuron* **76**, 33–50 (2012).
582. Santana, N., Mengod, G. & Artigas, F. Quantitative analysis of the expression of dopamine D1 and D2 receptors in pyramidal and GABAergic neurons of the rat prefrontal cortex. *Cerebral Cortex* **19**, 849–860 (2009).
583. Waddington, J. L. Behavioural correlates of the action of selective D-1 dopamine receptor antagonists. Impact of SCH 23390 and SKF 83566, and functionally interactive D-1: D-2 receptor systems. *Biochemical Pharmacology* **35**, 3661–3667 (1986).

584. Chourbaji, S. *et al.* Learned helplessness: Validity and reliability of depressive-like states in mice. *Brain Research Protocols* **16**, 70–78 (2005).
585. Radley, J. J. *et al.* Repeated stress induces dendritic spine loss in the rat medial prefrontal cortex. *Cerebral Cortex* **16**, 313–320 (2006).
586. Radley, J. J. *et al.* Repeated stress alters dendritic spine morphology in the rat medial prefrontal cortex. *Journal of Comparative Neurology* **507**, 1141–1150 (2008).
587. Fasano, C. *et al.* Dopamine facilitates dendritic spine formation by cultured striatal medium spiny neurons through both D1 and D2 dopamine receptors. *Neuropharmacology* **67**, 432–443 (2013).
588. Saunders, A. *et al.* Molecular Diversity and Specializations among the Cells of the Adult Mouse Brain. *Cell* **174**, 1015-1030.e16 (2018).
589. Woolfrey, K. M. & Srivastava, D. P. Control of Dendritic Spine Morphological and Functional Plasticity by Small GTPases. *Neural Plasticity*. doi:10.1155/2016/3025948 (2016).
590. Stachniak, T. J., Ghosh, A. & Sternson, S. M. Chemogenetic Synaptic Silencing of Neural Circuits Localizes a Hypothalamus→Midbrain Pathway for Feeding Behavior. *Neuron* **82**, 797–808 (2014).
591. Mahler, S. V *et al.* Designer receptors show role for ventral pallidum input to ventral tegmental area in cocaine seeking. *Nature Neuroscience* **17**, 577–585 (2014).
592. Roth, B. L. DREADDs for Neuroscientists. *Neuron* **89**, 683–94 (2016).
593. Shen, W., Flajolet, M., Greengard, P. & Surmeier, D. J. Dichotomous Dopaminergic Control of Striatal Synaptic Plasticity. *Science (New York, N.Y.)* **321**, 848–851 (2008).

594. Feder, A. *et al.* Efficacy of Intravenous Ketamine for Treatment of Chronic Posttraumatic Stress Disorder. *JAMA Psychiatry* **71**, 681 (2014).
595. Peltoniemi, M. A., Hagelberg, N. M., Olkkola, K. T. & Saari, T. I. Ketamine: A Review of Clinical Pharmacokinetics and Pharmacodynamics in Anesthesia and Pain Therapy. *Clinical Pharmacokinetics* **55**, 1059–1077 (2016).
596. Veilleux-Lemieux, D., Castel, A., Carrier, D., Beaudry, F. & Vachon, P. Pharmacokinetics of ketamine and xylazine in young and old Sprague-Dawley rats. *Journal of the American Association for Laboratory Animal Science : JAALAS* **52**, 567–70 (2013).
597. Freitas, C. *et al.* Changes in Cortical Plasticity Across the Lifespan. *Frontiers in Aging Neuroscience* **3**, 1–8 (2011).
598. Spear, L. P. The adolescent brain and age-related behavioral manifestations. *Neuroscience & Biobehavioral Reviews* **24**, 417–463 (2000).
599. Kalsbeek, A., Voorn, P., Buijs, R. M., Pool, C. W. & Uylings, H. B. M. Development of the dopaminergic innervation in the prefrontal cortex of the rat. *The Journal of Comparative Neurology* **269**, 58–72 (1988).
600. Rothmond, D. A., Weickert, C. S. & Webster, M. J. Developmental changes in human dopamine neurotransmission: Cortical receptors and terminators. *BMC Neuroscience* **13**, 18 (2012).
601. Bryant, K. A., Altinay, M., Finnegan, N., Cromer, K. & Dale, R. M. Effects of Repeated Intravenous Ketamine in Treatment-Resistant Geriatric Depression. *Journal of Clinical Psychopharmacology* **39**, 158–161 (2019).

602. Konietzny, A., Bär, J. & Mikhaylova, M. Dendritic actin cytoskeleton: Structure, functions, and regulations. *Frontiers in Cellular Neuroscience* vol. 11. doi:10.3389/fncel.2017.00147 (2017).
603. Bachmann, V. A. *et al.* Reciprocal regulation of PKA and Rac signaling. *Proceedings of the National Academy of Sciences of the United States of America* **110**, 8531–8536 (2013).
604. Nagai, T. *et al.* Phosphoproteomics of the Dopamine Pathway Enables Discovery of Rap1 Activation as a Reward Signal In Vivo. *Neuron* **89**, 550–565 (2016).
605. Sariñana, J., Kitamura, T., Künzler, P., Sultzman, L. & Tonegawa, S. Differential roles of the dopamine 1-class receptors, D1R and D5R, in hippocampal dependent memory. *Proceedings of the National Academy of Sciences of the United States of America* **111**, 8245–8250 (2014).
606. Coupé, P., Munz, M., Manjón, J. V., Ruthazer, E. S. & Louis Collins, D. A CANDLE for a deeper in vivo insight. *Medical Image Analysis* **16**, 849–864 (2012).

## Appendix

### A.1 Collaboration: Ketamine rapidly enhances spinogenesis through dopaminergic mechanisms

The work in this chapter is the second part of the collaboration with Dr. Mingzheng Wu presented in Chapter 3. This work is published in:

Mingzheng Wu, Samuel Minkowicz, Vasin Dumrongprechachan, Pauline Hamilton, Yevgenia Kozorovitskiy. *Biological psychiatry*. 89.11 (2021): 1096-1105.

<https://doi.org/10.1016/j.biopsych.2020.12.022>

#### Abstract

Ketamine elicits rapid onset antidepressant effects in patients with clinical depression through mechanisms hypothesized to involve the genesis of neocortical dendritic spines and synapses. Yet, the observed changes in dendritic spine morphology usually emerge well after ketamine clearance, raising questions about the link between rapid behavioral effects of ketamine and plasticity. Here, we used two-photon glutamate uncaging/imaging to focally induce spinogenesis in the medial prefrontal cortex, directly interrogating baseline and ketamine-associated plasticity of deep layer pyramidal neurons in C57BL/6 mice. We combined pharmacological, genetic, optogenetic, and chemogenetic manipulations to interrogate dopaminergic mechanisms

underlying ketamine-induced rapid enhancement in evoked plasticity and associated behavioral changes. We found that ketamine rapidly enhances glutamate-evoked spinogenesis in the medial prefrontal cortex, with timing that matches the onset of its behavioral efficacy and precedes changes in dendritic spine density. Ketamine increases evoked cortical spinogenesis through dopamine Drd1 receptor (Drd1) activation that requires dopamine release, compensating blunted plasticity in a learned helplessness paradigm. The enhancement in evoked spinogenesis after Drd1 activation or ketamine treatment depends on postsynaptic protein kinase A activity. Furthermore, ketamine's behavioral effects are blocked by chemogenetic inhibition of dopamine release and mimicked by activating presynaptic dopaminergic terminals or postsynaptic Gas-coupled cascades in the medial prefrontal cortex. Our findings highlight dopaminergic mediation of rapid enhancement in activity-dependent dendritic spinogenesis and behavioral effects induced by ketamine.

### **A.1.1 Introduction**

Ketamine and its S-enantiomer esketamine demonstrate rapid onset and lasting antidepressant effects in clinical studies<sup>379,548</sup>; esketamine (Spravato) has been recently approved by the Food and Drug Administration for treatment-resistant depression<sup>549</sup>. Ketamine acts primarily as an antagonist at the glutamatergic N-methyl-D-aspartate (NMDA) receptors<sup>382,432,550-552</sup>, although several studies implicate mechanisms beyond direct NMDAR antagonism<sup>385,553</sup>. Ketamine has been shown to ameliorate depressive-like behaviors in animal models of stress<sup>386-389,554</sup>. Accumulating evidence implicates the enhancement of synaptic plasticity in ketamine's behavioral effects<sup>386,387,391,392,550,552,555,556</sup>. Several prior studies demonstrate that *in vivo* administration of

ketamine enhances dendritic spine density<sup>391,395,434,435,557</sup> and restores dendritic spine loss in the medial prefrontal cortex (mPFC)<sup>392</sup>. Notably, increased dendritic spine density in mPFC pyramidal neurons usually emerges 12-24 hrs after a single subanesthetic dose of ketamine<sup>391,392,434,557</sup>, yet clinical effects on behavior emerge within 2-4 hrs<sup>379,548,558</sup>. Even if ketamine's effects on plasticity are linked to its behavioral efficacy, as has been suggested<sup>391,392,434,435,559</sup>, this temporal mismatch could in principle result from a rapid enhancement of spinogenesis by ketamine, which over time leads to increased dendritic spine density. This possibility has not yet been directly examined.

Changes in hedonic, motivational, and aversive processing represent fundamental features of major depressive disorders<sup>560-563</sup>. Reward, aversion, and motivational states are strongly tied to changes in the activity of midbrain dopaminergic (DA) neurons<sup>411,412,564-567</sup>. In addition, dysregulation of DA systems has been demonstrated in clinically depressed patients<sup>568,569</sup> and in animal models of depression<sup>375,376,570,571</sup>. The reversal of deficits in the DA system usually improves depressive-like behaviors<sup>375,376,417</sup>. A recently published meta-analysis suggests that acute sub-anesthetic doses of ketamine increase DA levels in the prefrontal cortex<sup>390</sup>, reported for both *in vivo* and *ex vivo* studies<sup>381,384,572-574</sup>. Yet, little is known about the behavioral and neurobiological consequences of elevated cortical dopamine level induced by ketamine treatment. Outside the context of ketamine effects on the brain, several studies have elucidated DA modulation of intrinsic excitability and ion channel properties of mPFC pyramidal neurons<sup>575-578</sup>. Whether DA signaling regulates structural plasticity of dendritic spines in mPFC and whether changes in DA tone account for ketamine-associated plasticity remains unknown.

Here, we rely on dual laser 2-photon glutamate uncaging and imaging to directly induce *de novo* dendritic spinogenesis on mPFC pyramidal neurons. The spatiotemporal control of this assay

enables us to evaluate the capacity for spinogenesis independently from pre-existing dendritic spines. Combining this assay with pharmacological, genetic, and behavioral manipulations allows us to functionally dissect the underlying mechanism of changes in the glutamate-evoked genesis of new dendritic spines.

## **A.1.2 Results and discussion**

### **A.1.2.1 Ketamine rapidly enhances glutamate-evoked spinogenesis in mPFC pyramidal neurons**

Acute slices of mPFC were prepared from P25-40 mice of both sexes following neonatal transduction of sparse EGFP expression accomplished by a combination of AAV1.hSyn.Cre and AAV8.FLEX.EGFP. We imaged EGFP-labeled dendrites of layer 5 pyramidal neurons in mPFC using 2-photon laser scanning microscopy (2PLSM, 910 nm). A second laser was tuned to 725 nm to locally uncage MNI-glutamate near dendrites to probabilistically induce the formation of new dendritic spines (**Figure A.1.1A**), as previously described for developing neurons in the striatum and superficial layers of sensory and motor cortex<sup>406,579,580</sup>. Successful and unsuccessful induction trials of *de novo* spinogenesis were distinguished in z-stack projections through a dendritic segment before and after the brief induction protocol (< 30 sec) of up to 40 uncaging pulses (**Figure A.1.1B**). In order to be classified as newly induced dendritic spines, the new membrane protrusions had to satisfy several criteria based on location and fluorescence intensity, relative to parent dendrite and pre-existing dendritic spines (methods and **Figure A.1.1 Supplement 1A-C**).

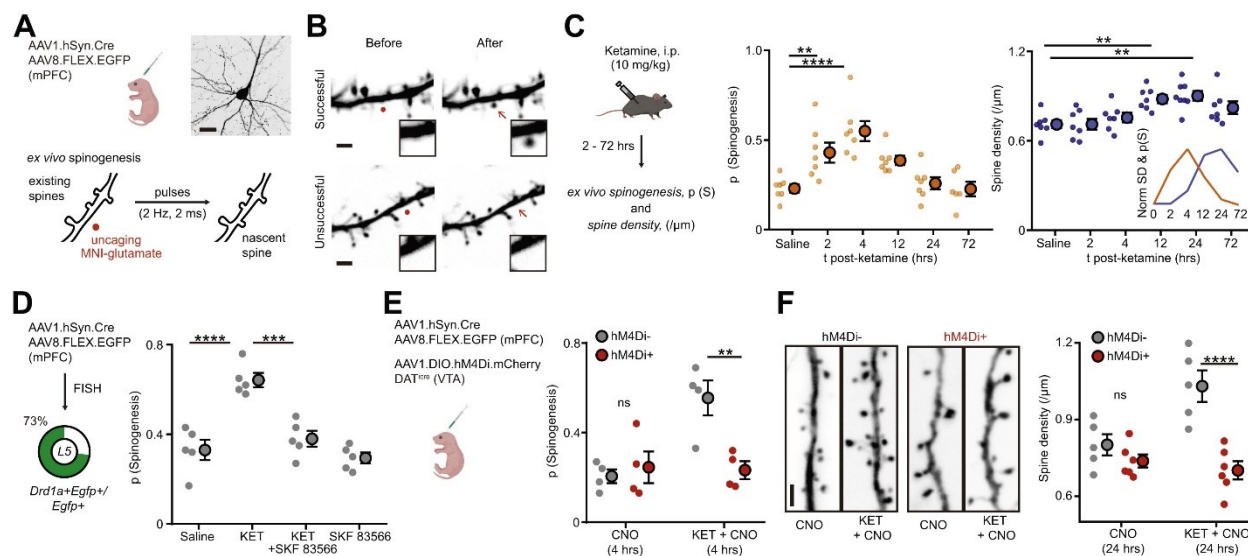


**Figure A.1.1. Ketamine regulates mPFC plasticity through a DA-dependent mechanism. (A).** Schematic illustrating glutamate-evoked de novo spinogenesis platform. Top, viral transduction and an example EGFP<sup>+</sup> pyramidal neuron in mPFC. Bottom, MNI-glutamate uncaging parameters for the induction of new dendritic spines. Scale bar, 50  $\mu\text{m}$ . **(B).** Example 2PLSM images of successful and unsuccessful induction trials of de novo spinogenesis. Red circles, uncaging sites. Black rectangle, close up images of local dendritic segments before and after glutamate uncaging. Scale bar, 2  $\mu\text{m}$ . **(C).** Left, schematic illustrating timecourse of ketamine treatments and experiments. Middle, timecourse of evoked spinogenesis probability on deep layer mPFC neurons in mice treated with either saline or ketamine (i.p. 10 mg/kg, acute slice preparation 2-72 hrs after treatment). Each small circle, aggregate probability of evoked spinogenesis from a single animal. Large circle, group data.  $n = 6 - 7$  animals/time point, 15 - 25 trials/animal, one-way ANOVA,  $F(5, 35) = 9.895$ ,  $p < 0.0001$ , Sidak's multiple comparison test vs Saline, 2 hrs  $p = 0.076$ , 4 hrs,  $p < 0.0001$ , 12 hrs,  $p = 0.0532$ , 24/72 hrs,  $p > 0.9$ . Right, same as left but for dendritic spine density.  $n = 7 - 8$  animals/time point, one-way ANOVA,  $F(5, 37) = 6.319$ ,  $p = 0.0002$ , Sidak's multiple comparison test vs Saline, 2/4 hrs  $p > 0.8$ , 12 hrs,  $p = 0.0056$ , 24 hrs,  $p = 0.0011$ , 72 hrs,  $p = 0.1271$ . Inset, normalized time course of changes in evoked spinogenesis (orange) and dendritic spine density (blue). **(D).** Left, viral transduction and percentage of Drd1a<sup>+</sup>Egfp<sup>+</sup>/Egfp<sup>+</sup> cells in layer 5 mPFC. Right, probability of glutamate-evoked spinogenesis on deep layer mPFC neurons in mice treated with Saline, KET (10 mg/kg), KET + SKF 83566 (10 mg/kg), or SKF 83566 alone. Each small circle, aggregate probability of evoked spinogenesis from a single animal. Large circle, group data. One-way ANOVA,  $p < 0.0001$ ,  $F(3, 16) = 20.29$ , Sidak's multiple comparison test, Saline vs KET,  $p < 0.0001$ , KET vs KET + SKF83566,  $p = 0.0002$ , Saline vs SKF83566,  $p = 0.8574$ . **(E).** Left, schematic illustrating triple viral transduction strategy for evoked spinogenesis with DA neuron inhibition. Right, probability of spinogenesis on deep layer mPFC neurons in

$\text{DAT}^{\text{iCre}^+}$  and  $\text{DAT}^{\text{iCre}^-}$  animals treated with CNO (3 mg/kg) across conditions (baseline, KET).  $n = 4$  animals/condition as shown in plots, two-way ANOVA, Sidak's multiple comparison test,  $\text{Cre}^-$  vs  $\text{Cre}^+$ , CNO,  $p = 0.8686$ , CNO + KET,  $p = 0.0042$ . **(F)**. Left, example confocal images of EGFP expression in dendrites of deep layer mPFC pyramidal neurons, in response to CNO and ketamine treatment, as noted. Scale, 2  $\mu\text{m}$ . Right, same as **(E)** but for dendritic spine density.  $n = 5 - 6$  animals/condition as shown in plots, two-way ANOVA, Sidak's multiple comparison test,  $\text{Cre}^-$  vs  $\text{Cre}^+$ , CNO,  $p = 0.5005$ , CNO + KET,  $p < 0.0001$ . Scale bar, 2  $\mu\text{m}$ . \*\* $p < 0.01$ , \*\*\* $p < 0.001$  \*\*\*\* $p < 0.0001$ . Error bars reflect SEM.

We carried out evoked spinogenesis assays in different mice at several time points (2-72 hours) after a single subanesthetic dose of ketamine (10 mg/kg, i.p.). *In vivo* administration of ketamine in naïve animals enhanced evoked *de novo* spinogenesis 2 and 4 hours after treatment (**Figure A.1.1C**), temporally matching the emergence of ketamine's behavioral effects<sup>382,432</sup>. This effect was transient, by 12 hours after ketamine was administered, the probability of spinogenesis decreased back to baseline levels. In addition, dendritic spine density was quantified at the same time points. In contrast to the rapid, transient changes in evoked spinogenesis, the increase in dendritic spine density was delayed until 12 hours after treatment (**Figure A.1.1C**), consistent with prior reports<sup>386,392,556,557</sup>. This temporal precedence of ketamine-associated potentiation of evoked spinogenesis suggests that changes in the potential for activity-dependent plasticity may contribute to slower, accumulating increases in spine density after ketamine treatment.

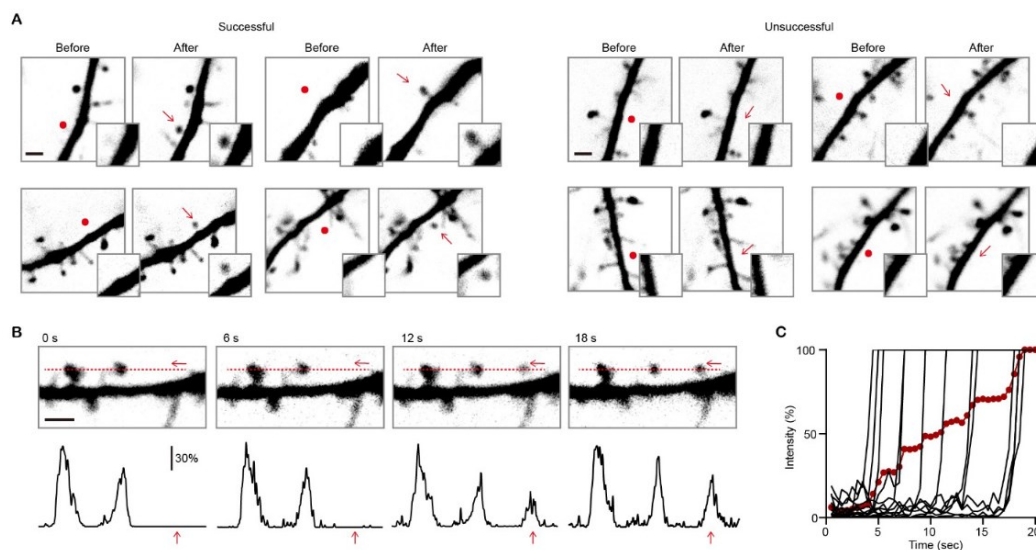


**Figure A.1.1 Supplement 1. De novo glutamate-induced spinogenesis on pyramidal neurons in mPFC.** (A). Example 2PLSM images of successful and unsuccessful induction trials of de novo spinogenesis. Red circles, uncaging sites. Inset, close up images of local dendritic segments before and after glutamate uncaging. Scale bar, 2  $\mu$ m. (B). Top, time-lapse images of spine formation during glutamate uncaging (40 pulses, 2 Hz). Red arrow, uncaging spot and nascent spine. Line-scan analysis was performed, as noted by the red dashed line. Bottom, fluorescence intensity profiles from the line-scan across pre-existing spines and uncaging spot. Scale bar, 2  $\mu$ m. (C). Time course of individual trials (2 Hz) and average (red dots) fluorescence intensity changes across a series of successful trials during glutamate uncaging.

#### A.1.2.2 Rapid enhancement in evoked spinogenesis requires Drd1-PKA signaling

Given the hypothesized links between ketamine and the DA system, we sought to determine whether ketamine's effect on evoked plasticity is mediated by the activation of DA receptors. First, we verified the expression of Drd1a receptors in EGFP-expressing neurons. Consistent with prior reports<sup>581,582</sup>, the majority of pyramidal neurons in the deep layers of mPFC express *Drd1a* mRNA (Figure A.1.1D, Figure A.1.1 Supplement 2A, B). We compared glutamate-evoked spinogenesis after administering ketamine alone, or in conjunction with a Drd1 receptor antagonist SKF 83566 (10 mg/kg i.p., 2 hours prior to *ex vivo* experiments). We found that antagonizing Drd1 receptors

blocked ketamine's potentiation of evoked spinogenesis, while the antagonist treatment alone had no effect relative to baseline (**Figure A.1.1D**). Thus, while the activation of Drd1 receptors in this neuronal population is not required for baseline glutamate-evoked plasticity, it appears to be necessary for ketamine's enhancement of evoked spinogenesis.

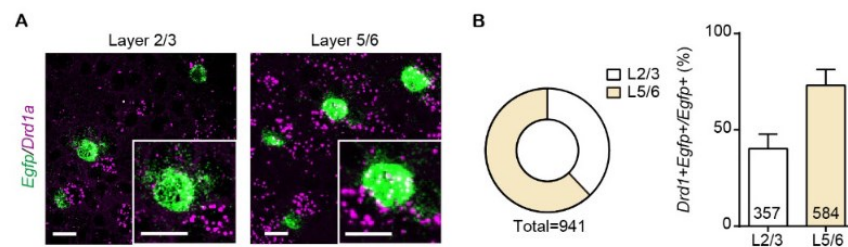


**Figure A.1.1 Supplement 2. Drd1a mRNA expression and distribution in mPFC. (A).** Fluorescence in situ hybridization (FISH) image showing Drd1a mRNA in Egfp mRNA expressing cells in layer 2/3 and layer 5/6 of mPFC. Inset, close up of a single neuron. Scale bar, 20  $\mu$ m. **(B).** Left, the proportional distribution of Egfp mRNA expression across superficial and deep cortical layers. Right, quantification of the percentage of Drd1<sup>+</sup> cells among Egfp<sup>+</sup> cells in superficial and deep cortical layers. n = 4 animals; Drd1<sup>+</sup>Egfp<sup>+</sup>/Egfp<sup>+</sup>: Layer 2/3, 40.2%  $\pm$  7.5%, layer 5/6, 73.1%  $\pm$  8.3%

Next, in order to suppress mPFC DA release without broadly altering Drd1 activation and locomotor behavior<sup>583</sup>, we used chemogenetic inhibition of VTA DA neurons; the major source of DA in mPFC. Inhibiting hM4Di<sup>+</sup> VTA DA neurons with CNO (3 mg/kg, i.p.) while administering ketamine treatment blocked ketamine's spinogenesis-enhancing effects (**Figure A.1.1E**). Yet, as for the pharmacological Drd1 receptor blockade *in vivo*, we observed no effects of CNO treatment on evoked spinogenesis in the absence of ketamine. These observations are consistent with a model where the genesis of new dendritic spines and synapses mechanistically depends on glutamate, but the enhancement of this plasticity requires the activation of PKA via G $\alpha_s$ -coupled receptors<sup>406</sup>. In

addition to blocking ketamine-mediated enhancement of evoked spinogenesis, transient inhibition of VTA DA neuron activity (a single CNO dose + ketamine) also abolished the delayed increase of spine density 24 hours after ketamine (**Figure A.1.1F**). These data show that in the absence of behavioral manipulations, *Drd1* activation and VTA DA activity regulate changes in spinogenesis and dendritic spine density, mediating the effects of ketamine on plasticity in mPFC.

The next series of experiments test whether the capacity for spinogenesis is altered in animal models of stress, where ketamine ameliorates behavior. We exposed mice to subacute uncontrollable stress by administering foot shocks over 2 days, using an adapted model of learned helplessness (LH, 3 sec inescapable, 360 shocks each day, **Figure A.1.2A**). Following repeated exposure to inescapable foot shocks, LH behavior manifests in increased failures to escape from readily avoidable shocks (10 sec escapable, 30 trials total), consistent with prior reports<sup>570,584</sup>. A single dose of ketamine 4 hours prior to the test (10 mg/kg, b.w., i.p.) is sufficient to rescue escape behavior in this paradigm (**Figure A.1.2B**). We next tested glutamate-evoked spinogenesis in the baseline, after stress exposure (LH), and following ketamine treatment (LH + KET). The probability of glutamate evoked spinogenesis decreased relative to baseline in LH mice, while ketamine treatment restored the baseline potential for plasticity (**Figure A.1.2C**). We found that 2 days of stressful experience is sufficient to decrease the potential of spinogenesis in mPFC pyramidal neurons, in contrast to changes in dendritic spine density that normally manifest after chronic stress<sup>391,585,586</sup>. No significant sex difference was observed across conditions, despite a trend towards higher evoked spinogenesis in females in the baseline condition (**Figure A.1.2 Supplement 1A-B**). To correlate individual behavioral outcomes with evoked plasticity, we performed *de novo* spinogenesis assays in animals trained with a modified, weaker LH paradigm

(wLH), with or without subsequent ketamine treatment. In the wLH paradigm, we used a larger number of brief (3 sec) escapable foot shocks to evaluate the escape behavior, following a single day of LH induction with inescapable shocks (**Figure A.1.2 Supplement 1C**). We found that the probability of evoked spinogenesis negatively correlates with the percentages of failures to escape in both conditions (wLH +/- ketamine) (**Figure A.1.2 Supplement 1D**). This result suggests that mPFC plasticity is linked to behavioral profiles of individual animals after LH and ketamine treatment.

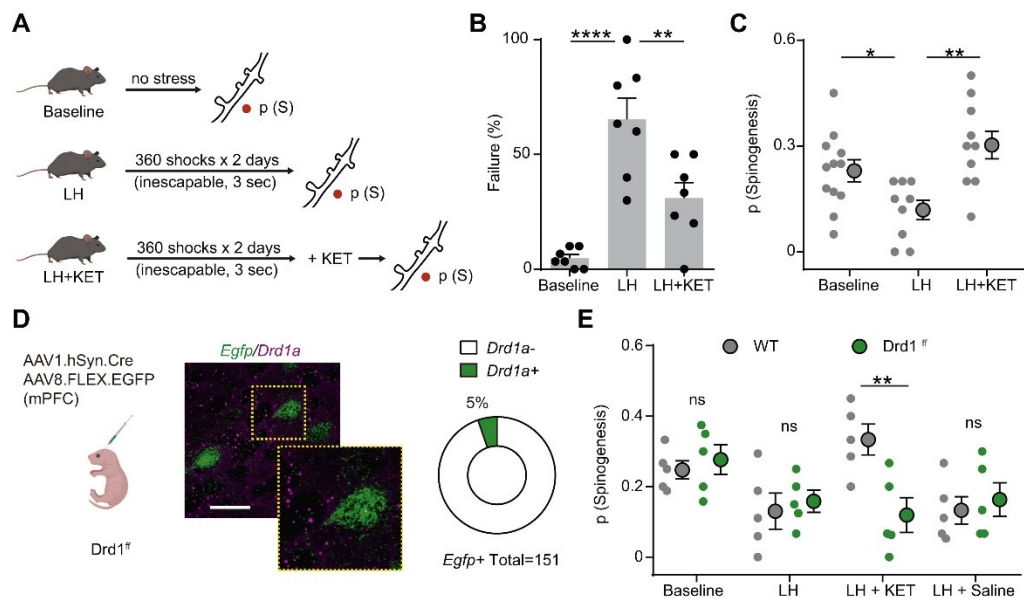


**Figure A.1.2. Ketamine rescues mPFC plasticity after stressful experience through Drd1 receptor.** (A). Left, schematic illustrating glutamate-evoked spinogenesis assay in Baseline, LH, and LH + KET conditions. (B). Summary data showing the percentage of failures to escape an escapable aversive shock, one-way ANOVA,  $F(2, 18) = 20.26$ ,  $p < 0.0001$ , Sidak's multiple comparison test, Baseline vs LH,  $p < 0.0001$ , LH vs LH + KET,  $p = 0.0041$ . (C). Probability of glutamate-evoked spinogenesis on deep layer mPFC neurons in distinct stages of aversive learning (baseline, LH, LH + KET).  $n = 9 - 12$  animals/condition as shown in plots, one-way ANOVA,  $F(2, 28) = 7.146$ ,  $p = 0.0031$ , Sidak's multiple comparison test, Baseline vs LH,  $p = 0.0496$ , LH vs

LH + KET,  $p = 0.0016$ . **(D)**. Left, schematic illustrating dual viral transduction strategy with sparse genetic manipulation of Drd1 receptor expression in Drd1<sup>ff</sup> mice. Middle, Fluorescence in situ hybridization (FISH) image confirming the absence of Drd1a mRNA expression (purple) in Egfp mRNA expressing mPFC cells (green) in Drd1<sup>ff</sup> mice. Inset, close up of a single neuron. Scale bar, 50  $\mu\text{m}$ . Right, quantification of the percentage of Drd1a<sup>+</sup> cells among Egfp<sup>+</sup> cells in mPFC. 5% Drd1a<sup>+</sup> and 95% Drd1a<sup>-</sup> among 151 Egfp<sup>+</sup> cells from 2 animals. **(E)**. Probability of glutamate-evoked spinogenesis on deep layer mPFC neurons in distinct stages of aversive learning (baseline, LH, LH + KET, LH + saline) in wild type and Drd1<sup>ff</sup> mice. Two-way ANOVA, Sidak's multiple comparison test, WT vs Drd1<sup>ff</sup>, LH + KET,  $p = 0.0043$ , Baseline, LH and LH + Saline,  $p > 0.9$ ,  $n = 5$  animals. \* $p < 0.05$ , \*\* $p < 0.01$ , \*\*\* $p < 0.001$  \*\*\*\* $p < 0.0001$ . Error bars reflect SEM.

We then tested the contribution of Drd1 receptors to ketamine related plasticity changes. To specifically manipulate Drd1 receptor expression in mPFC without affecting the global DA system, we conditionally knocked out Drd1 receptors by co-expressing Cre recombinase and Cre-dependent EGFP in Drd1-floxed mice (**Figure A.1.2D**). We validated the conditional knock-out by verifying the expression of *Drd1a* mRNA in EGFP-expressing neurons (**Figure A.1.2D**). Sparse genetic depletion of Drd1 receptor in mPFC pyramidal neurons abolished ketamine's effect on spinogenesis in LH animals, without changing the probability of spinogenesis for mice in the baseline or LH conditions (**Figure A.1.2E**).

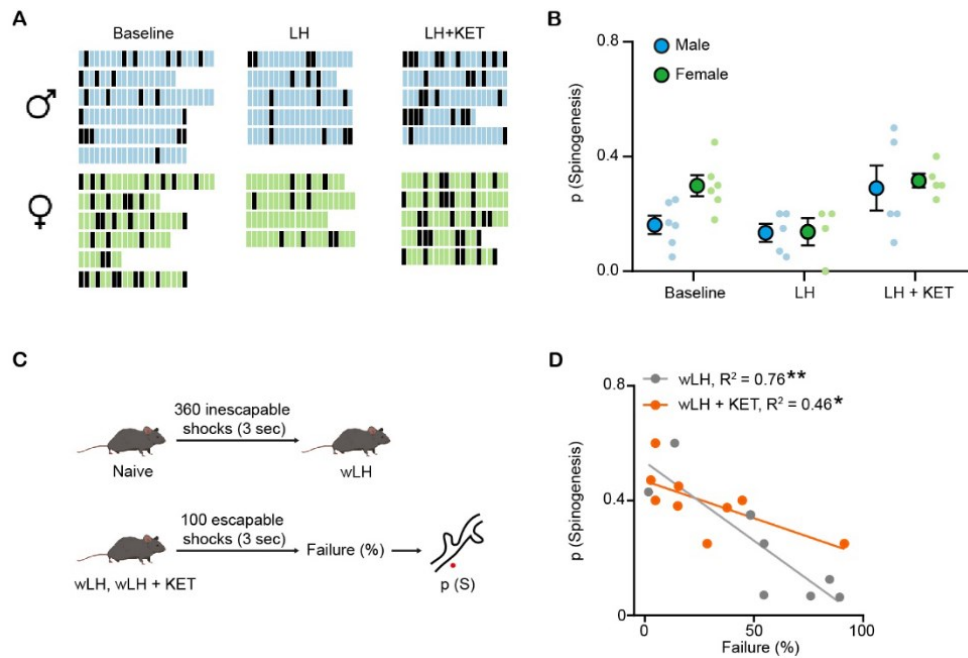


**Figure A.1.2 Supplement 1. Spinogenesis in mPFC is regulated by stress and correlates with behavioral outcomes.** (A). Binary grid plots illustrating sequences of spinogenesis induction outcomes for different mice in all conditions in **Figure A.1.2c**, separated by sex. Black, successful evoked spinogenesis trial; blue or green, unsuccessful trial for males or females, respectively. (B). Probability of glutamate-evoked spinogenesis on deep layer mPFC neurons in conditions (baseline, LH, LH + KET) in male and female mice. Two-way ANOVA, Row factor (sex),  $p = 0.1408$ . Column factor (condition),  $p = 0.0052$ . Sidak's multiple comparison test, Male vs Female, Baseline,  $p = 0.0775$ , LH and LH + KET,  $p > 0.9$ ,  $n = 4-6$  animals as shown in individual dots. Error bars reflect SEM. (C). Schematic illustrating wLH paradigm and glutamate-evoked spinogenesis assay after wLH and wLH + KET in separate groups of mice. (D). Correlation between failures to escape and the probability of spinogenesis after learning and following ketamine treatment. wLH,  $R^2 = 0.76$ ,  $p = 0.0051$ ,  $n = 8$  animals. wLH + KET,  $R^2 = 0.46$ ,  $p = 0.0439$ ,  $n = 9$  animals.

Next, we addressed the downstream signaling mechanism for DA enhancement of glutamate-evoked spinogenesis. Drd1 receptor activation is known to regulate glutamatergic synapse and dendritic spine formation in the developing striatum<sup>406,587</sup>. Yet, mPFC Drd1 receptor expression levels in single neurons are considerably lower than in the striatum (mPFC Layer 5 pyramidal

neurons: ~4/100,000 transcripts; striatum: ~110/100,000; data from DropViz<sup>588</sup>). We found that bath application of Drd1 agonist SKF 81297 (1  $\mu$ M) promotes glutamate-evoked spinogenesis in mPFC pyramidal neurons (**Figure A.1.3A, B**). This effect requires Drd1a signaling, since Drd1a cKO abolished the enhancement of spinogenesis. Suppression of PKA activity by either bath application of H-89 (10  $\mu$ M) or over-expression of endogenous PKA inhibitor (PKI $\alpha$ ) in mPFC pyramidal neurons blocked changes in spinogenesis induced by SKF 81297 (**Figure A.1.3B, C**). In addition, *in vivo* pre-treatment with ketamine (10 mg/kg, i.p.) occluded the enhancement of spinogenesis by SKF 81297 (**Figure A.1.3D**), supporting the argument that ketamine's effect on structural plasticity is mediated by Drd1 receptor. Furthermore, the plasticity-promoting effect of ketamine was blocked by over-expression of PKI $\alpha$  (**Figure A.1.3E**). Several established targets of PKA, involved in cytoskeletal remodeling, could contribute to Drd1-dependent effects of ketamine on structural plasticity<sup>589</sup> (**Figure A.1.3F**). Altogether, our results reveal that ketamine's rapid modulation of structural plasticity in mPFC pyramidal neurons requires the Drd1a-PKA signaling cascade.

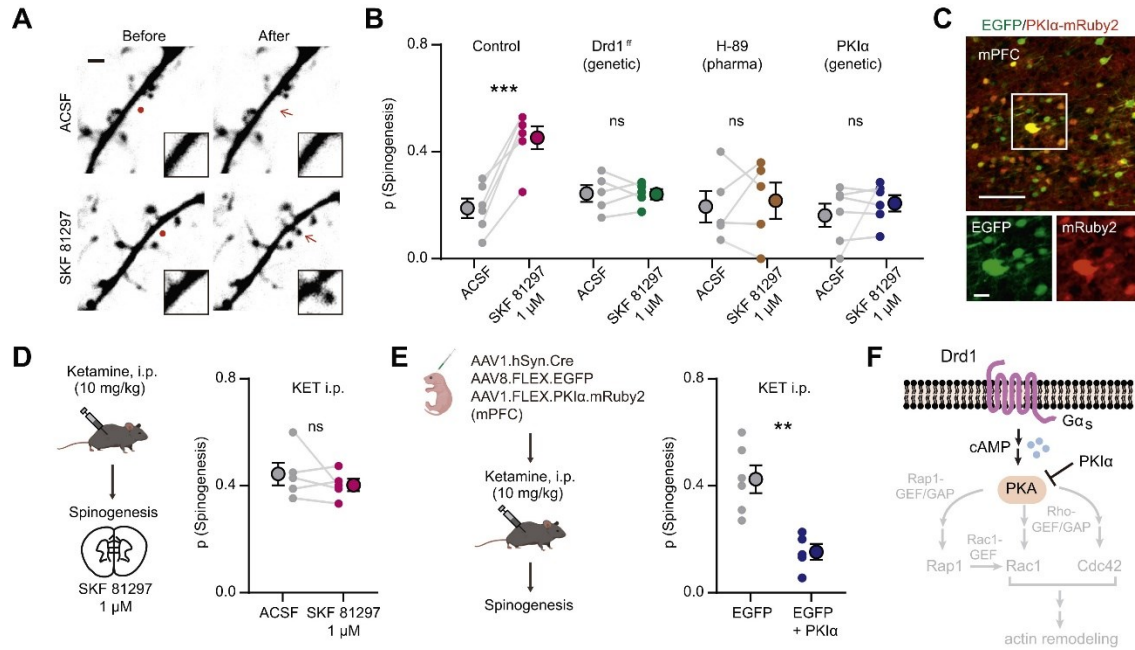


**Figure A.1.3. Drd1 activation promotes glutamate-induced spinogenesis in mPFC pyramidal neurons through PKA signaling.** (A). Example 2PLSM images of de novo spinogenesis trials with ACSF or 1  $\mu$ M SKF 81297. Red circles, uncaging sites. Black rectangle, close up images of local dendritic segments before and after glutamate uncaging. Scale bar, 2  $\mu$ m. (B). Probability of glutamate-evoked spinogenesis on deep layer mPFC neurons in brain slices with or without bath application of 1  $\mu$ M SKF 81297. Slices were treated with 10  $\mu$ M H-89 or collected from mice with genetic manipulation of GFP expressing pyramidal neurons (Drd1<sup>ff</sup> or PKI $\alpha$ ). Each small circle, aggregate probability of evoked spinogenesis from a single experiment. Large circles, group data. Paired two-tailed t test, ACSF vs SKF 81297, Control,  $p = 0.0007$ ; Drd1<sup>ff</sup>,  $p = 0.9249$ ; H-89,  $p = 0.7351$ ; PKI $\alpha$ ,  $p = 0.4$ ;  $n = 5 - 6$  experiments/group. (C). Top, colocalization of PKI $\alpha$ -mRuby2 in EGFP-expressing mPFC neurons. Bottom, close up images of EGFP and mRuby2 signals. Scale bar, 100  $\mu$ m and 20  $\mu$ m. (D). Left, schematic illustrating glutamate-evoked spinogenesis assay in slices from mice pre-treated with ketamine (10 mg/kg, i.p.). Bottom, probability of glutamate-evoked spinogenesis on deep layer mPFC neurons in brain slices with or without bath application of 1  $\mu$ M SKF 81297. Paired two-tailed t test, ACSF vs SKF 81297,  $p = 0.3745$ . (E). Left, schematic illustrating triple viral transduction strategy for PKI $\alpha$  expression. Right, probability of glutamate-evoked spinogenesis in deep layer mPFC neurons in mice with or without PKI $\alpha$  expression, injected with ketamine (10 mg/kg, i.p.). Unpaired two-tailed t test, GFP vs GFP + PKI $\alpha$ ,  $p = 0.0020$ . (F). Schematic of simplified signaling pathways downstream of Drd1-PKA involved in actin remodeling in dendritic spines. \*\* $p < 0.01$ , \*\*\* $p < 0.001$ . Error bars reflect SEM.

### **A.1.2.3 Bidirectional manipulation of mPFC DA release controls behavioral effects of ketamine**

To connect the mechanisms of ketamine-associated plasticity and its behavioral effects, we examined the role of cortical DA signaling in escape behavior after LH. To induce local dopamine release in mPFC, we optogenetically activated DA terminals in mPFC in animals with ChR2 expression restricted to VTA DA neurons. DAT<sup>icre</sup> neonates were transduced with AAV1.EF1 $\alpha$ .DIO.hChR2(H134R).eYFP, or a control fluorophore, and implanted with optical fibers 4-6 weeks after transduction (**Figure A.1.4A, B**). After LH induction, animals received a series of burst optogenetic stimuli at 20 Hz every 10 sec (10 pulses, 20 ms width, 500 ms duration) during the test session consisting of 30 avoidable foot shocks (**Figure A.1.4C**). The stimulation bursts were not timed relative to shocks and took place on either side of the shuttle box, decreasing the likelihood of forming conditioned place preference or aversion. Optogenetic activation of DA axon terminals in mPFC significantly decreased the percentage of failures after LH, as well as latencies to escape (**Figure A.1.4D**). Optogenetic stimulation did not alter locomotion behavior in either the open field or the shuttle box, suggesting the high escape tendency is not caused by hyperlocomotion (**Figure A.1.4E**). Thus, enhancing DA release in mPFC is sufficient to rescue escapes after LH.

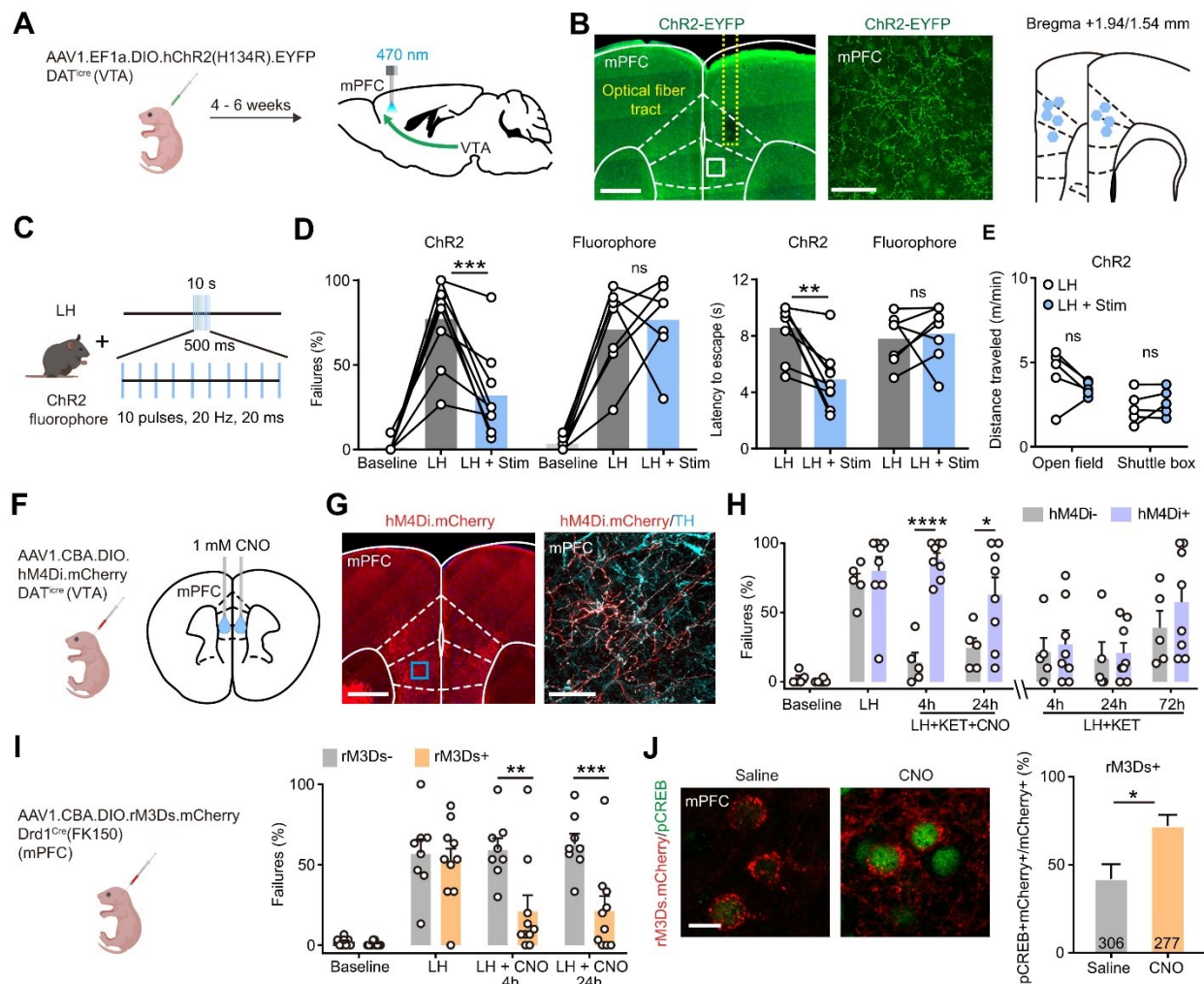


**Figure A.1.4. Activity of local DA terminals and Drd1<sup>+</sup> neurons in mPFC mediates ketamine effects on behavior after stress. (A).** Schematic for viral transduction with Cre-dependent ChR2 AAV in the VTA and subsequent optogenetic fiber implant in mPFC. **(B).** Left, fiber placement illustration on a coronal section through mPFC, with a close up image of Chr2.eYFP terminals (white dashed lines, Paxinos atlas overlay; yellow dashed lines, fiber track). Green, immunoenhanced Chr2.eYFP; blue, Hoechst nucleic stain. Scale bars: 500  $\mu$ m and 50  $\mu$ m. Right, atlas location of fiber placement for each subject. **(C).** Schematic illustrating open loop optogenetic stimulation parameters (Stim, optogenetic stimulation). **(D).** Left, summary data showing the percentage of failures to escape an escapable aversive shock in Chr2-expressing mice ( $n = 9$ ) and fluorophore-expressing controls ( $n = 7$ ) across phases of learning, Baseline, LH, and LH + Stim. Right, summary data for latency to escape in LH compared with LH + Stim conditions. Repeated measures two-way ANOVA, Sidak's multiple comparison test, LH vs LH + Stim, Chr2,  $p = 0.0002$ , Fluorophore,  $p = 0.9358$ . Latency to escape, LH vs LH + Stim, Chr2,  $p = 0.0014$ ,

Fluorophore,  $p = 0.9248$ . **(E)**. Left, locomotion in the open field and shuttle box (m/min) after learning with and without optogenetic stimulation. Repeated measures two-way ANOVA, Sidak's multiple comparison test, open field,  $p = 0.1742$ , shuttle box,  $p = 0.7503$ ,  $n = 5$  mice. **(F)**. Left, schematic illustrating viral transduction strategy. Right, local CNO infusion in mPFC (1 mM, 1  $\mu$ l). **(G)**. Left, immunoenhanced image of hM4Di.mCherry<sup>+</sup> DAT<sup>+</sup> terminals in mPFC. Right, mCherry<sup>+</sup> terminals colocalize with a subset of tyrosine hydroxylase (TH) expressing axons. Scale bars, 500  $\mu$ m and 50  $\mu$ m. **(H)**. Summary data showing the percentage of failures to escape an escapable aversive shock across learning and treatment conditions for hM4Di-expressing DAT<sup>iCre</sup> positive and negative littermates.  $n = 5$  animals for Cre<sup>-</sup>, 8 animals for Cre<sup>+</sup>, two-way ANOVA, Sidak's multiple comparison test. KET + CNO 4 hrs,  $p < 0.0001$ , KET + CNO 24 hrs,  $p = 0.0476$ , KET + only 4, 24, and 72 hrs,  $p > 0.7$ . **(I)**. Left, schematic illustrating viral transduction strategy. Right, Summary data showing the percentage of failures to escape an escapable aversive shock in Drd1-Cre<sup>+</sup> and Drd1-Cre<sup>-</sup> mice expressing rM3Ds across phases of learning and after CNO treatment (Baseline, LH, LH + CNO 4 hrs, and LH + CNO 24 hrs).  $n = 8 - 10$  animals/condition, two-way ANOVA, Sidak's multiple comparison test, Cre<sup>+</sup> vs Cre<sup>-</sup>, LH + CNO 4 hrs,  $p = 0.0018$ , LH + CNO 24 hrs,  $p = 0.0007$ , Baseline/LH,  $p > 0.9$ . **(J)**. Left, colocalization of pCREB immunolabeling and rM3Ds.mCherry expression in mPFC after Saline/CNO treatment in Drd1 Cre<sup>+</sup> mice. Right, the quantification of percentage of pCREB<sup>+</sup> cells among mCherry<sup>+</sup> cells. Scale bar, 20  $\mu$ m.  $n = 3$  animals/condition cell number as noted in each bar, two-tailed unpaired t-test,  $p = 0.0455$ . \* $p < 0.05$ , \*\* $p < 0.01$ , \*\*\* $p < 0.001$ , \*\*\*\* $p < 0.0001$ . Error bars reflect SEM.

While we find that optogenetically driven increase in mPFC DA tone mimics behavioral effects of ketamine, whether these effects require local DA release in mPFC remains unclear. To achieve local inhibition of DA release, we infused CNO into the mPFC of mice expressing hM4Di in VTA DA neurons and their terminals in mPFC to reduce axonal release of dopamine<sup>590-592</sup>. DAT<sup>iCre</sup> neonates were transduced with AAV1.CBA.DIO.hM4Di.mCherry in the VTA, and cannulae were implanted bilaterally over mPFC in order to locally deliver 1 mM CNO (1  $\mu$ l for each side) (**Figure A.1.4F and Figure A.1.4 Supplement 1A**). A high density of hM4Di.mCherry expression in mPFC terminals was observed in immunoenhanced fixed tissue sections (**Figure A.1.4G**). Local infusion of CNO in mPFC along with ketamine treatment blocked the behavioral effect of

ketamine (10 mg/kg, i.p.) in the LH paradigm, while ketamine alone was sufficient to rescue escape behavior (**Figure A.1.4H** and **Figure A.1.4 Supplement 1B**). To determine whether mPFC DA function is required to maintain the effect of ketamine on behavior, we chemogenetically inhibited DA release 24 hours after ketamine treatment (**Figure A.1.4 Supplement 1C**). This delayed manipulation had no significant effect on escape behaviors. Together, these results suggest that disruption of DA signaling is important for ketamine effects during an initial narrow time window following ketamine administration.

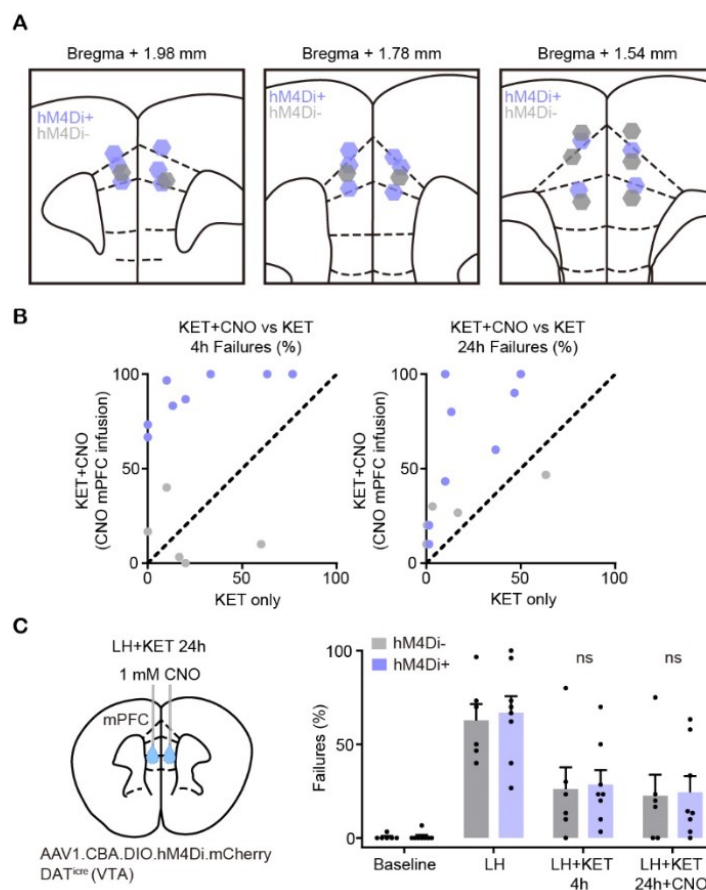


**Figure A.1.4 Supplement 1. Effects of local inhibition of DA terminals in mPFC. (A).** Atlas locations showing cannula placements for data in **Figure A.1.4H**. **(B).** Within subject summary data for behavioral responses (**Figure A.1.4H**) after ketamine treatment, compared with ketamine

+ CNO (mPFC), 4 hrs and 24 hrs after treatment,  $n = 5 - 8$  animals. **(C)**. Left, schematic illustrating local CNO infusion in mPFC 24 hrs after ketamine treatment. Right, summary data showing the percentage of failures to escape an escapable aversive shock across learning and treatment conditions for hM4Di-expressing  $\text{DAT}^{\text{iCre}}$  positive and negative animals. Behaviors were tested 2 hrs after local CNO infusion.  $n = 6$  animals for  $\text{Cre}^-$ , 8 animals for  $\text{Cre}^+$ , two-way ANOVA, Sidak's multiple comparison test,  $p > 0.9$  for all comparisons.

The activation of  $\text{Drd1}$  receptors initiates  $G\alpha_s$  mediated PKA signaling cascades, which enhance spinogenesis, synaptic transmission, and neuronal activity<sup>405,406,581,593</sup>. We therefore tested whether selective activation of  $G\alpha_s$  signaling in mPFC  $\text{Drd1}$  expressing neurons could rescue escape behavior after aversive learning. We relied on the  $G\alpha_s$ -coupled rM3D DREADD, expressing AAV1.CBA.DIO.rM3Ds.mCherry in  $\text{Drd1-Cre-FK150}$  mice (**Figure A.1.4I**). The expression of rM3Ds alone did not change baseline escape and failure rates, or the magnitude of aversive learning. After LH induction, a single i.p. dose of CNO was sufficient to rescue escape behavior 4 hours after treatment, lasting at least 24 hours (**Figure A.1.4I**). Activating  $G\alpha_s$  signaling in  $\text{Drd1}$  expressing neurons *in vivo* significantly increased phosphorylation of CREB, which is typically induced by  $G\alpha_s$ -coupled cascades (**Figure A.1.4J**). In addition to our results, a recently published study showed that optogenetic activation of  $\text{Drd1}^+$  mPFC neurons decreases immobility time in the forced swim test, suggesting that these  $\text{Drd1}$ -expressing neurons may broadly regulate aversive or active coping responses<sup>409</sup>. Altogether, our data demonstrate that mPFC DA signaling mediates both the rapid plasticity-promoting actions and behavioral effects of ketamine.

#### A.1.2.4 Discussion

Glutamate-evoked interrogation of plasticity on genetically targeted neurons offers unique strengths as a structural plasticity readout. Besides dissociating *de novo* genesis and elimination of dendritic spines and synapses, this assay facilitates pharmacological and genetic mechanism dissection and is compatible with behavioral manipulations. Our observations demonstrate a temporal precedence of spinogenesis increase relative to changes in dendritic spine density, suggesting that the changes in spine density *in vivo* can be due to a prior, accumulating change in glutamatergic activity-dependent spinogenesis. Recent work demonstrates that newly formed dendritic spines are required to maintain the behavioral effect of ketamine after chronic corticosterone administration<sup>392</sup>, establishing a causal link between the increase in new spine formation and ketamine's behavioral effects. Here, we have defined the mechanisms underlying rapid changes in spinogenesis that are required for these causal effects.

The current study explains several intriguing temporal observations about ketamine actions and reconciles previously reported temporal mismatches. First, rapid anti-depressant effects of ketamine usually begin 2-4 hours after a single dose of treatment<sup>382,548,558,594</sup>, while changes in dendritic spine morphology in mPFC are primarily observed 8-16 hours later<sup>386,391,392,434</sup>. Our results reveal that the enhancement of glutamate-induced spinogenesis occurs rapidly (2-4 hours) after ketamine treatment, corresponding to its rapid-onset behavioral effects. Second, the half-life of ketamine is estimated at 1-3 hours in humans (~1.5 hours in rodents), with a relatively short clearance time (~8-12 hours)<sup>595,596</sup>. These short clearance times stand in contrast to the lasting behavioral effects of ketamine in both humans and rodents (> 24 hours)<sup>379,548,558</sup>. Given this temporal difference, one intriguing possibility is that the timing of the clinical anti-depressant

effects of ketamine in MDD patients (~1 week following a single dose) derives from a lasting change in DA-dependent structural plasticity caused by ketamine. Exactly how new dendritic spines stabilize and contribute to behavior after ketamine treatment may further reveal how ketamine's effects last days beyond its bioavailability. Since our experiments were carried out in young animals and neural plasticity dynamics are known to change across age<sup>420,433,597</sup>, the efficacy of ketamine treatment could vary in clinical populations as a function of age, even if mechanisms of action are conserved. Since DA tone in mPFC changes through the lifespan<sup>424,598-600</sup>, the variance in ketamine's antidepressant efficacy (e.g. low efficacy and more transient effects for geriatric depression<sup>601</sup>) may be partially explained by the age-related alterations in cortical DA tone.

This work ties into a growing body of literature explicitly and implicitly linking ketamine, behavior, and plasticity. A recent study concluded that *Drd1*-positive neurons in mPFC regulate depressive-like behavior<sup>409</sup>, and our study investigated the underlying neuromodulatory and plasticity mechanisms consistent with this discovery. Together, the two studies support the idea that ketamine controls mPFC plasticity and behaviors through cortical modulation by DA. Another recent paper demonstrates that newly formed dendritic spines are required to maintain the behavioral effect of ketamine after chronic corticosterone administration<sup>392</sup>, establishing a causal link between the increase in new spine formation and ketamine's behavioral effects. These findings, together with our observations of correlated spinogenesis and escape behavior after LH, highlight the importance of new dendritic spine formation for behavioral regulation. Future experiments are required to fully understand the impact of individual variability in plasticity and neuromodulatory signaling on the anti-depressant effects of ketamine.

Our observations that DA signaling mediates of dendritic spine plasticity in mPFC after ketamine injection, may reflect broadly conserved mechanisms in the brain, where DA controls activity-induced plasticity of dendritic spines and excitatory synapse formation. Prior data demonstrate that, during development, DA regulates the formation of dendritic spines and excitatory synapses in striatal direct pathway spiny projection neurons expressing *Drd1* receptors<sup>406,587</sup>. The activation of *Drd1* receptors stimulates  $G\alpha_s$  signaling cascades, increasing cAMP production and PKA activity. Analogously, DA promotes glutamate-evoked spinogenesis on mPFC pyramidal neurons through *Drd1* receptor activation and changes in PKA activity. Given that actin dynamics are important for dendritic spine formation and shape regulation<sup>602</sup>, the mechanistic link between *Drd1*-PKA signaling and dendritic spine formation likely involves cytoskeleton remodeling proteins. Indeed, PKA modulates the activity of small GTPases (*e.g.*, Rap1, Rac1, Cdc42, among others) known to regulate dendritic spines<sup>589</sup> through guanine nucleotide exchange factors (GEFs) and GTPase-activating proteins (GAPs)<sup>603,604</sup>. Specific molecular effectors responsible for ketamine-induced changes in synaptic and dendritic spine plasticity remain to be elucidated and may provide new clinical targets.

### A.1.3 Methods

#### Mouse strains and genotyping

Animals were handled according to protocols approved by the Northwestern University Animal Care and Use Committee. Weanling and young adult male and female mice (postnatal days 25-60) were used in this study. Approximately equal numbers of males and females were used for every experiment. All mice were group-housed, with standard feeding, light-dark cycle, and enrichment procedures; littermates were randomly assigned to conditions. C57BL/6 mice used for breeding and backcrossing were acquired from Charles River (Wilmington, MA), and all other mouse lines were acquired from the Jackson Laboratory (Bell Harbor, ME) and bred in house.

B6.SJL-Slc6a3<sup>tm1.1(cre)Bkmm</sup>/J mice, which express Cre recombinase under control of the dopamine transporter promoter, are referred to as DAT<sup>iCre</sup><sup>462</sup>; B6.FVB(Cg)-Tg(Drd1-cre)FK150Gsat/Mmucd mice, which express Cre recombinase under control of the dopamine Drd1a receptor promoter, are referred to as Drd1<sup>Cre</sup>(FK150)<sup>463</sup>; Drd1<sup>tm2.1Stl</sup> floxed mutant mice that possess loxP sites flanking the single exon of the Drd1a gene, are referred to as Drd1<sup>ff</sup><sup>605</sup>. All transgenic animals were backcrossed to C57BL/6 for several generations. Heterozygous Cre<sup>+</sup> mice were used in experiments. Standard genotyping primers are available on the Jackson Lab website.

#### Behavior assays

*Learned helplessness (LH)*. P40-60 mice were used for behavioral assays with optogenetic and chemogenetic experiments. P25-40 mice were used for spinogenesis assays with behavioral

manipulations. The learned helplessness procedure consisted of two induction sessions (1 session per day; 360 inescapable foot shocks per session; 0.3 mA, 3 sec; random 1-15 sec inter-shock intervals). Active/Passive Avoidance Shuttle Boxes from MazeEngineers (Boston, MA) were used for the experiment. To assess the degree of aversive learning, test sessions (30 escapable foot shocks per session; 0.3 mA, 10 sec; random 5-30 sec inter-shock intervals) were conducted before induction, 24 hrs after the last induction session, and following pharmacological or optogenetic manipulations. The testing was performed in a shuttle box (18 × 18 × 20 cm) equipped with a grid floor and a door separating the two compartments. No conditioned stimulus was delivered either before or after the shocks. Escapes were scored when the animal shuttled between compartments during the shock. Escape latency was measured as the time from the start of the shock to the escape. The shock automatically terminated when the animal shuttled to the other compartment. Failures were scored when the animal failed to escape before the shock end. The weaker LH paradigm (wLH) consisted of one induction session, and one test session with a larger number of brief escapable shocks (100 escapable foot shocks per session; 0.3 mA, 3 sec; random 5-15 sec intershock intervals). Schematics involving mice were made using BioRender.

To evaluate the effect of ketamine on learned helplessness behavior, a single dose of ketamine (10 mg/kg b.w., i.p.) was given 48 hrs after the last induction session, and the test session was performed 4 hrs later. For chemogenetic activation of rM3Ds in mPFC, 48 hrs after the last induction session, Clozapine N-oxide (CNO) was administered i.p., followed by test sessions 4 hrs and 24 hrs later. For chemogenetic inhibition of DA terminals in mPFC, the first CNO dose (3 mg/kg, i.p.) was co-administered with ketamine 48 hrs after the last induction, followed by test sessions 4 and 24 hrs later. Then, immediately following the last test session ketamine was

administered alone, followed by test sessions 4, 24, and 72 hrs later. For optogenetic activation of DA terminals in the mPFC, 48 hrs after the last induction session a test session was performed with optogenetic stimulation. Bursts were not time-locked to behavior and consisted of ten 20 ms long pulses at 20 Hz, with 500 ms long burst duration and 10 sec inter-burst intervals. Optical power of light at the tip of fiber was  $<9 \text{ mW/mm}^2$ . Light stimulation was applied in either compartment of the shuttle box.

*Locomotion test.* To assess the locomotor activity, mice were placed in the center of a plastic chamber (48 cm  $\times$  48 cm  $\times$  40 cm) or in the shuttle box in a dimly lit room. Mice explored the arena for 15 min, with video (30 fps) and photometry recording performed during the final 10 min. All behavioral assays were conducted during the active phase of the circadian cycle.

#### Two-photon imaging with two-photon glutamate uncaging

Dendritic imaging and uncaging of MNI-glutamate for spinogenesis induction were accomplished on a custom-built microscope combining two-photon laser-scanning microscopy (2PLSM) and two-photon laser photoactivation, as previously described<sup>405,406,579</sup>. Two mode-locked Ti:Sapphire lasers (Mai Tai eHP and Mai Tai eHP DeepSee, Spectra-Physics, Santa Clara, CA) were tuned to 910 and 725 nm for exciting EGFP and uncaging MNI-glutamate, respectively. The intensity of each laser was independently controlled by Pockels cells (Conoptics, Danbury, CT). A modified version of Scanimage software was used for data acquisition<sup>471</sup>. For glutamate uncaging, 2.5 mM MNI-caged-L-glutamate (Tocris) was perfused into the slice chamber, and 725 nm light guided through a galvo scanhead was used to focally release the caging group. Secondary and tertiary dendritic branches were selected for dendritic

imaging and spinogenesis induction. MNI-glutamate was uncaged near the dendrite ( $\sim 0.5 \mu\text{m}$ ) at 2 Hz using up to forty 2 ms-long pulses. Images were continually acquired during the induction protocol at 1 Hz, and uncaging was stopped if a spinehead was visible before 40 uncaging pulses were delivered. Analysis was carried out on raw image stacks and z projections. For display purposes only, a subset of the 2-photon micrographs was processed using Candle<sup>606</sup>. A successful induction of new dendritic spine was scored when a protrusion from the dendrite in the uncaging location was observed. A newly generated dendritic spine had to satisfy the following criteria: de novo protrusion from the dendrite within  $1 \mu\text{m}$  of the uncaging site; mean spine head fluorescence matching average fluorescence of spine heads on the parent dendrite; mean spine head fluorescence exceeding 20% of intensity in the parent dendrite. Changes in fluorescence intensity were profiled using line-scan analyses. For each animal, the probability of spinogenesis is represented as the fraction of successful induction trials out of all conducted trials within the individual.

#### Quantification of dendritic spine density

Sections of mPFC were either examined with a custom-built 2PLSM or a Leica SP5 confocal microscope (Leica Microsystems). Distal apical dendritic segments were selected for analysis. For each dendritic segment, dendritic spines protruding on both sides of the dendrite were marked using a 3D reconstruction system NeuroLucida 360 (MBF Bioscience, Williston, VT). Six to eight z stacks ( $0.3 \mu\text{m}$  between each stack), at  $0.07 \mu\text{m}$  lateral pixel size, were used for reconstruction. Dendritic spine density was averaged from 8-12 dendritic segments for each animal.

### Local drug infusion

To inhibit hM4Di-expressing DA terminals by local CNO infusion in mPFC, we used internal cannulae (28 gauge, Plastics One, Roanoke, VA) with 0.5 mm long projection beyond the implanted guide-cannula, as described above. 1 mM CNO (1  $\mu$ L per side) was administered over a 2 min long injection period using a 10  $\mu$ L Hamilton syringe (Hamilton Company, Franklin, MA). Dummy cannulae with 0.2 mm projection were inserted back after the delivery of CNO. The first infusion was performed immediately before ketamine injection, and the two subsequent infusions were performed 1.5 and 3 hrs after ketamine injection. Learned helplessness behavior was assessed 4 and 24 hours after ketamine treatment. In separate groups of animals, local CNO infusion was performed 24 hours after ketamine treatment, and learned helplessness behavior was tested 2 hours after infusion.

### Acute slice preparation

Coronal brain slice preparation was modified from previously published procedures<sup>405,406,472</sup>. Animals were deeply anesthetized by inhalation of isoflurane, followed by a transcardial perfusion with ice-cold, oxygenated artificial cerebrospinal fluid (ACSF) containing (in mM) 127 NaCl, 2.5 KCl, 25 NaHCO<sub>3</sub>, 1.25 NaH<sub>2</sub>PO<sub>4</sub>, 2.0 CaCl<sub>2</sub>, 1.0 MgCl<sub>2</sub>, and 25 glucose (osmolarity 310 mOsm/L). After perfusion, the brain was rapidly removed, and immersed in ice-cold ACSF equilibrated with 95%O<sub>2</sub>/5%CO<sub>2</sub>. The tissue was blocked and transferred to a slicing chamber containing ice-cold ACSF, supported by a small block of 4% agar (Sigma-Aldrich). Bilateral 300  $\mu$ m-thick slices were cut on a Leica VT1000s (Leica Biosystems, Buffalo Grove, IL) in a rostro-caudal direction and transferred into a holding chamber with ACSF, equilibrated

with 95%O<sub>2</sub>/5%CO<sub>2</sub>. Slices were transferred to a recording chamber perfused with oxygenated ACSF at a flow rate of 2 – 4 ml/min at room temperature.

#### Tissue processing and immunohistochemistry

Mice were deeply anaesthetized with isoflurane and transcardially perfused with 4% paraformaldehyde (PFA) in 0.1 M phosphate buffered saline (PBS). Brains were post-fixed for 1-5 days and washed in PBS, prior to sectioning at 50-100  $\mu$ m on a vibratome (Leica Biosystems). Sections were pretreated in 0.2% Triton X-100 for an hour at RT, then blocked in 10% bovine serum albumin (BSA, Sigma-Aldrich, ST Louis, MO) in PBS with 0.05% Triton X-100 for two hours at RT and incubated for 24-48 hrs at 4°C with primary antibody solution in PBS with 0.2% Triton X-100. On the following day, tissue was rinsed in PBS, reacted with secondary antibody for 2 hrs at RT, rinsed again, then mounted onto Superfrost Plus slides (ThermoFisher Scientific, Waltham, MA). Sections were dried and coverslipped under ProLong Gold antifade reagent with DAPI (Molecular Probes, Life Technologies, Carlsbad, CA) or under glycerol:TBS (9:1) with Hoechst 33342 (2.5 $\mu$ g/ml, ThermoFisher Scientific). Primary antibodies used in the study were mouse anti-tyrosine hydroxylase (1:1000; AB129991, Abcam, Cambridge, UK), chicken anti-GFP (1:2000; AB13970, Abcam, Cambridge, UK), rabbit anti-RFP (1:500, 600-401-379, Rockland, Limerick, PA), and rabbit anti-pCREB S133 (1: 5000, Abcam, ab32096). Alexa Fluor 488-, Fluor 594-, or Fluor 647-conjugated secondary antibodies against rabbit, mouse, or chicken (Life Technologies, Carlsbad, CA) were diluted 1:500. Whole sections were imaged with an Olympus VS120 slide scanning microscope (Olympus Scientific Solutions Americas, Waltham, MA). Confocal images were acquired with a Leica SP5 confocal microscope (Leica Microsystems). Depth-matched z-stacks of 2  $\mu$ m-thick optical sections were

analyzed in ImageJ (FIJI)<sup>474,475</sup>. For pCREB quantification, every four adjacent z stack slices were combined, for a total of 6  $\mu\text{m}$  thickness. mCherry signal was used to localize cell bodies of rM3Ds-expressing neurons. Laser intensity and all imaging parameters were held constant across samples, and the same threshold was applied for subtracting background immunofluorescence. pCREB<sup>+</sup> neurons were identified by an experimenter blind to the conditions.

### Pharmacology

Pharmacological agents were acquired from Tocris (Bristol, UK) or Sigma-Aldrich (St. Louis, MO). In vivo injections included intraperitoneal injections of ketamine (10 mg/kg, Vedco, St. Joseph, MO), SKF 83566 (10 mg/kg, Tocris), Clozapine N-oxide (3 mg/kg in vivo, Sigma-Aldrich). SKF 81297 hydrobromide (SKF 81297, 1  $\mu\text{M}$ , Tocris), and H-89 dihydrochloride (H-89, 10  $\mu\text{M}$ , Tocris) were used in acute slice experiments, as noted.

### Quantitative fluorescence in situ hybridization

Quantitative fluorescence in situ hybridization (FISH) was conducted following previously published procedures<sup>448,472</sup>. Mice were deeply anesthetized by inhalation of isoflurane and decapitated. Brains were quickly removed and frozen in tissue-freezing medium on a mixture of dry ice and ethanol for 5 - 15 min prior to storage at 80°C. Brains were subsequently cut on a cryostat (Leica CM1850, Leica Biosystems) into 20  $\mu\text{m}$ -thick sections, adhered to Superfrost Plus slides, and frozen at 80°C. Samples were fixed with 4% PFA in 0.1 M PBS at 4°C for 15 min, processed according to the manufacturer's instructions in the RNAscope Fluorescent Multiplex Assay manual for fresh frozen tissue (Advanced Cell Diagnostics, Newark, CA), and coverslipped with ProLong Gold antifade reagent with DAPI (Molecular Probes). Enhanced

green fluorescent protein channel 1 (Egfp) and dopamine Drd1a receptor channel 2 (Drd1a) probes were added to slides in combination, and Amp4-b fluorescent amplification reagent was used for all experiments. Sections were subsequently imaged on a Leica SP5 confocal microscope in four channels with a 40x objective lens at a zoom of 1.4 and resolution of 512 x 512 pixels with 1.0  $\mu\text{m}$  between adjacent z sections. Images were taken across the entire population of mPFC Egfp-positive neurons in each brain section.

FISH images were analyzed using FIJI<sup>474</sup>. Briefly, every four adjacent z stack slices were combined, for a total of 3  $\mu\text{m}$  thickness, in order to minimize missed colocalization, while decreasing false positive colocalization driven by signal from cells at a different depth in a similar x-y position. All channels were thresholded. Cellular ROIs were defined using the Egfp<sup>+</sup> channel information to localize cell bodies. FISH molecule puncta were counted within established cell boundaries. Whether a cell was considered positive for a given marker was determined by setting a transcript-dependent threshold of the number of puncta (e.g., over 5 puncta/soma for Drd1a<sup>+</sup>). These stringent parameters for co-localization and the challenges of quantifying low abundance receptor transcripts likely lead to underestimation of receptor-positive populations.

### Statistical analyses

Group statistical analyses were done using GraphPad Prism 7 software (GraphPad, LaJolla, CA). For N sizes, the number of trials or cells recorded, as well as the number of animals are provided. All data are expressed as mean  $\pm$  SEM, or individual plots. Probabilities are expressed as aggregate probabilities within individuals. For two-group comparisons, statistical significance

was determined by two-tailed Student's t-tests. For multiple group comparisons, one-way or two-way analysis of variance (ANOVA) tests were used for normally distributed data, followed by post hoc analyses. For non-normally distributed data, non-parametric tests for the appropriate group numbers were used. Pearson regression was used to detect the correlation between two groups of data.  $p < 0.05$  was considered statistically significant.